D3.2: Final report on key technological enablers for the seamless and energy efficient ETHER Network Operation

Version: v.1.0

Work package	WP 3
Task	Tasks 3.1, 3.2, 3.3, 3.4
Due date	31/08/2025
Submission date	26/09/2025
Deliverable lead	NCSRD
Version	1.0
Editors	Fotis Lazarakis (NCSRD)
Reviewers	Victor Montilla (NCSRD) Nikolaos Pappas (LIU), Konstantinos Ntontin (UL)
Abstract	The current deliverable builds upon the results of the first deliverable of WP3, D3.1 and extends the work to fulfil all the objectives of WP3. The deliverable includes the work performed in WP3 on the following topics: i)terminal antenna design for communication with LEO satellites; ii) distributed LEO satellite precoding for communication with ground users; iii) Comparison of two versions of OTFS in a LEO-satellite communication scenario; iv) dynamic resource management leveraging the development of flexible payload framework; v) Coordinated dynamic TN-NTN spectrum management; vi Optimal LEO power control in a GEO/LEO coexistence transmission scenario; vii) Application of semantics-aware communication schemes; viii) Development of horizontal and vertical handover policies
Keywords	6G, NTN, LEO-to-User direct access, distributed satellite LEO satellite precoding, flexible payload, data analytics and semantics, horizontal and vertical handovers, OTFS

Author List

Grant Agreement No.: 101096526
Call: HORIZON-JU-SNS-2022
Topic: HORIZON-JU-SNS-2022-STREAM-B-01-03
Type of action: HORIZON-JU-RIA

Organisations	Author
UL	Konstantinos Ntontin, Ashok Bandi, Biniam Tamiru
AUTH	Marios Gatzianas, George Kalfas, Dimitrios Palianopoulos, Agapi Mesodiakaki
I2CAT	Víctor Montilla, José Ávila, Roger Pueyo Centelles, Timo Kellermann, Adrián Pérez-Portero
NBC	Angelos Antonopoulos, Godfrey Kibalya
NCSRD	Fotis Lazarakis, Aris Tsolis, Antonis Alexandridis, Anastasios Paraskevopoulos
LIU	Nikolaos Pappas
OPL	Lechosław Tomaszewski

DISCLAIMER

Co-funded by the European Union 6GSNS

ETHER (*sElf-evolving terrestrial/non-Terrestrial Hybrid nEtwoRks*) project has received funding from the **Smart Networks and Services Joint Undertaking (SNS JU)** under the European Union's **Horizon Europe research and innovation programme** under Grant Agreement No 101096526. Views and opinions expressed are however those of the author(s) only and do not necessarily reflect those of the European Union. Neither the European Union nor the granting authority can be held responsible for them.

This work has received funding from the **Swiss State Secretariat for Education, Research and Innovation (SERI)**.

COPYRIGHT NOTICE

Project co-funded by the European Commission in the Horizon Europe Programme		
Nature of the deliverable:	**Report (R)**	
Dissemination Level		
PU	*Public, fully open, e.g. web (Deliverables flagged as public will be automatically published in CORDIS project's page)*	✓
SEN	*Sensitive, limited under the conditions of the Grant Agreement*	
Classified R-UE/ EU-R	*EU RESTRICTED under the Commission Decision No2015/ 444*	
Classified C-UE/ EU-C	*EU CONFIDENTIAL under the Commission Decision No2015/ 444*	
Classified S-UE/ EU-S	*EU SECRET under the Commission Decision No2015/ 444*	

* R: Document, report (excluding the periodic and final reports)

DEM: Demonstrator, pilot, prototype, plan designs

DEC: Websites, patents filing, press & media actions, videos, etc.

DATA: Data sets, microdata, etc.

DMP: Data management plan

ETHICS: Deliverables related to ethics issues.

SECURITY: Deliverables related to security issues

OTHER: Software, technical diagram, algorithms, models, etc.

EXECUTIVE SUMMARY

This report includes the final results of WP3 on key technological enablers for the seamless and energy efficient ETHER Network Operation, serving all three ETHER Use Cases, namely:

- **Use Case 1**: *Flexible payload-enabled service provisioning to semantics aware and delay-tolerant IoT applications*.
- **Use Case 2**: *Unified RAN for direct handheld device access.*
- **Use Case 3**: *Air-space safety critical operations*.

The current deliverable builds upon the results of the first deliverable of WP3, D3.1 and extends the work to fulfil all the Objectives of WP3. Thus, the link-budget for the direct access of a user terminal with a LEO satellite is analyzed, and a terminal antenna is designed with sufficient gain to enable the direct communication. Then, the design of the antenna array that will be prototyped is detailed together with the appropriate feeding network. To tackle severe attenuation of the signal identified in the scenarios under study, ETHER investigates distributed beamforming from a swarm of LEO satellites, and specifically for multi-user scenarios. Moreover, Orthogonal Time Frequency Space modulation is evaluated in the LEO satellite environment. The above topics are addressed in Chapters 2 and 3 and contribute to Use Case 2.

The final version of the software-based flexible payload architecture is presented which offers the capability to share resources and execute distributed functionalities, addressing all three Use Cases. Then, dynamic spectrum allocation and power control techniques to mitigate interference are investigated. Dynamic spectrum allocation is realized through precoding while power control is achieved by means of a heuristic algorithm for Equivalent Power Flux-Density (EPFD). The software defined payload architecture is presented in Chapter 4.

The investigation of semantics-aware communication schemes and information handling solutions towards high energy efficiency is of great importance in ETHER and addresses Use Case 1. Version Age of Information (VAoI) at LEO nodes is analysed and its network-wide average is optimized by adopting a transmission policy at the device to reduce energy consumption as described in Chapter 5.

Finally, horizontal and vertical handovers are studied in the ETHER integrated environment of terrestrial and non-terrestrial networks, addressing respectively, Use Case 1 and Use Case 2. Horizontal handovers are studied in LEO-based Store & Forward networks and the final version of the UE Context Proxy testbed is presented. Then, the final version of the Omnet++ simulator is presented which allows the implementation and testing of Vertical Handovers algorithms and specifically SINR driven and Energy Efficiency driven algorithms. Horizontal and vertical handovers studies are included in Chapter 6.

TABLE OF CONTENTS

LIST OF FIGURES

LIST OF TABLES

ABBREVIATIONS

3GPP	3rd Generation Partnership Project
5G	5th Generation
5GC	5th Generation Core
AMF	Access & Mobility Management Function
ARM	Advanced RISC Machine
ASIC	Application Specific Integrated Circuit
AXI	Advanced eXtensible Interface
BS	Base Station
BER	Bit Error Rate
CIoT	Cellular Internet of Things
CDF	Cumulative Distribution Function
CM	Channel Model
CN	Core Network
COTS	Commercial-Off-The-Shelf
CPU	Central Processing Unit
DMA	Direct Memory Access
DSP	Digital Signal Processor
DPR	Dynamic Partial Reconfiguration
EH	Energy Harvesting
EPC	Evolved Packet Core
EPFD	Equivalent Power Flux-Density
FFT	Fast Fourier Transform
FIFO	First Input First Output buffer
FL	Feeder Link
FLOSS	Free, Libre, Open-Source Software
FPGA	Field-Programmable Gate Array
GEO	Geosynchronous Equatorial Orbit
gNB	Next Generation Node B
GPIO	General Purpose I/O
GPP	General Purpose Processor
GPU	Graphics Processing Unit
GS	Ground Station
HO	Handover
I2C	Inter-Integrated Circuit bus

IC	Integrated Circuit
ICI	Inter-Carrier-Interference
IF	Intermediate Frequency
IoT	Internet of Things
IP	Internet Protocol (if referred to as network sharing protocol)
IP	Intellectual Property (if referred to as FPGA module)
IQ	In-Phase and Quadrature
ISL	Inter-Satellite Link
LEO	Low Earth Orbit
LOS	Line of Sight
MEC	Mobile Edge Computing
MDP	Markov Decision Process
MMU	Memory Management Unit
MO	Mobile-originated
MT	Mobile-terminated
mMTC	Massive Machine-Type Communication
MMU	Memory Management Unit
NB-IoT	Narrowband Internet of Things
NFV	Network Functions Virtualization
NFVI	Network Functions Virtualization Infrastructure
NGSO	Non-Geostationary Orbit
NTN	Non-Terrestrial Network
OBC	On-Board Computer
OFDM	Orthogonal Frequency Division Multiplexing
OS	Operating System
OTFS	Orthogonal Time-Frequency Space
PCIe	Peripheral Component Interconnect Express bus
PDF	Probability Density Function
PL	Programmable Logic
PS	Processing System
RAM	Random Access Memory
RAN	Radio Access Network
RAT	Radio Access Technologies
RF	Radio Frequency
RISC	Reduced Instruction Set Computer
RMS	Root-Mean-Square

RP	Reconfigurable Partition
RTT	Round Trip Time
SAT	Satellite
S&F	Store and Forward
SDR	Software-Defined Radio
SINR	Signal-to-Interference plus Noise Ratio
SoC	System-on-chip
TCP	Transmission Control Protocol
TN	Terrestrial Network
UE	User Equipment
VHDL	Very High speed IC Description Language
VIM	Virtualised Infrastructure Manager
VM	Virtual Machine
VNF	Virtual Network Function

1 INTRODUCTION

This chapter is the introduction to the final deliverable of WP3 “Key Technological Enablers for the seamless and energy-efficient ETHER Network Operation”. First, recap is provided about positioning of WP3 in ETHER 3D Architecture, how the work in WP3 serves the implementation of ETHER Use Cases and the main achievements reported in the first deliverable, i.e., D3.1 [1]. Then, the structure of the current deliverable is provided and finally, the relation of D3.2 with other ETHER deliverables is described.

1.1 RELATIONSHIP WITH ETHER 3D ARCHITECTURE, USE CASES AND DELIVERABLE D3.1

WP3 is organised in four Tasks, namely Task 3.1: Channel Modelling, UE Antenna Design, Distributed Beamforming from LEO swarms, and Unified Waveform Design for a Unified and Sustainable RAN, Task 3.2: Dynamic spectrum management and power control leveraging software defined payload in aerial and space ETHER layers, Task 3.3: Data analytics and semantics-aware caching for high energy efficiency, Task 3.4: Horizontal and vertical handover policies guaranteeing seamless connectivity across ETHER layers. WP3 addresses “lower-level enablers” of the ETHER 3D architecture indicated with light-blue boxes in Figure 1-1 below.

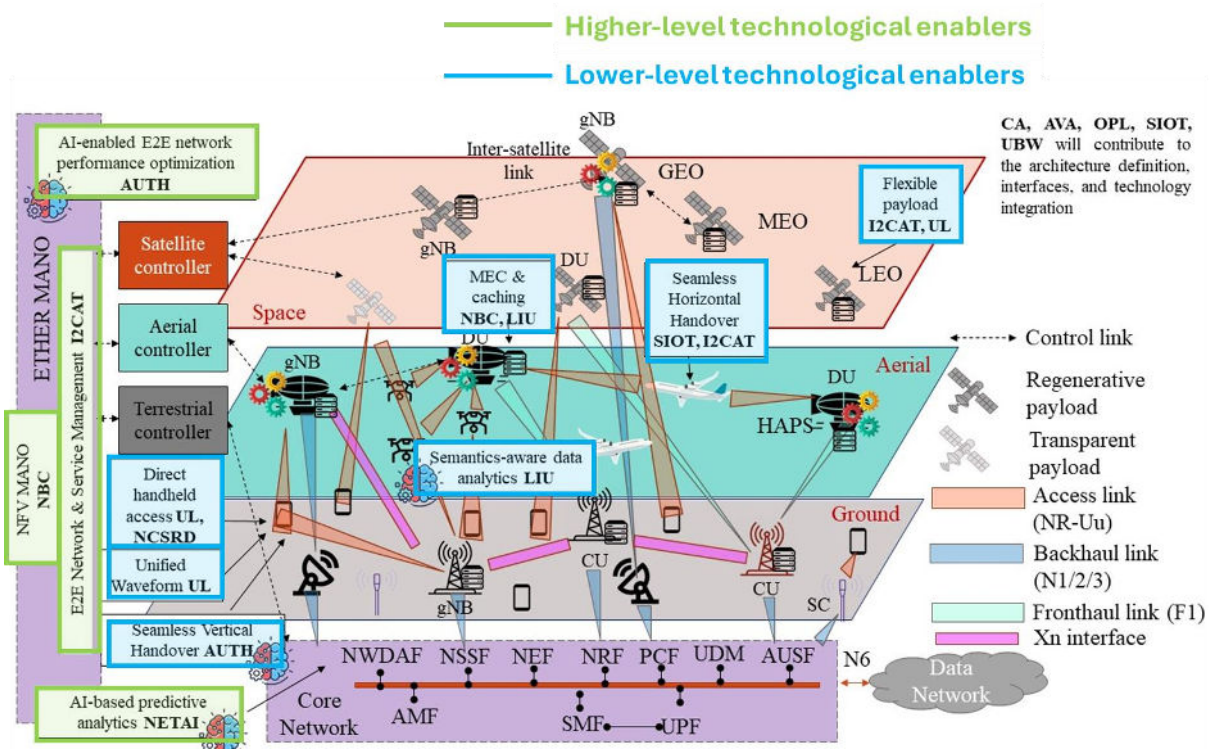

Figure 1-1: Positioning of WP3 (lower-level enablers) within ETHER 3D Architecture

ETHER technical objectives and achievements will enable the realisation of three use cases which are critical for the integration of terrestrial and non-terrestrial networks, as detailed in Deliverable D2.2 [2]. Moreover, mapping among technology enablers investigated in WP3 and corresponding Use Cases, are given in D3.1 and rewritten here for convenience together with their illustrations:

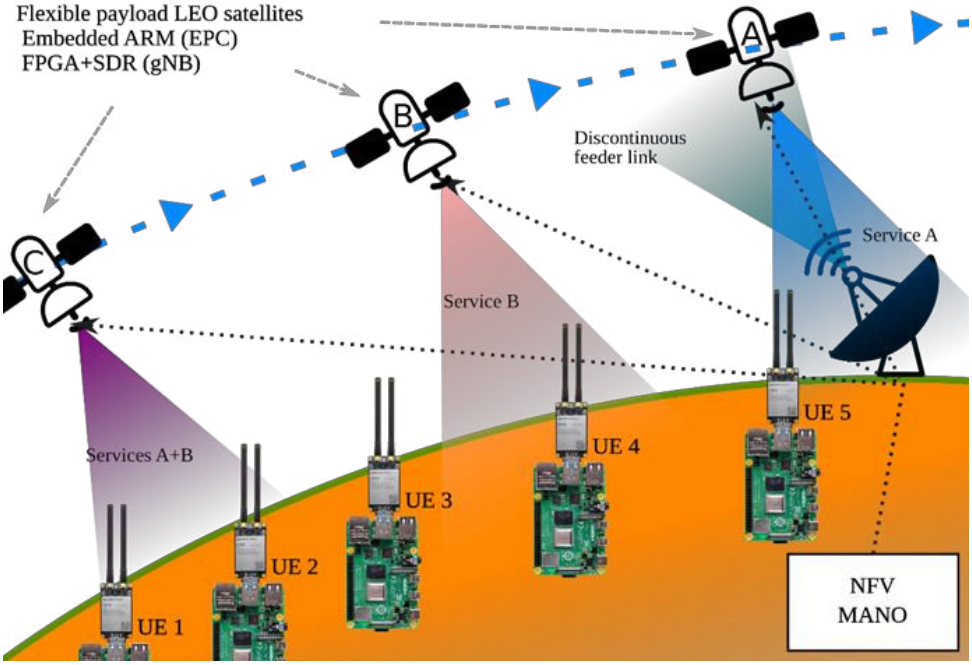

Figure 1-2: Use Case 1: Delay-tolerant IoT services

Use Case 1: Delay-tolerant Internet of Things (IoT) services

Technology Enablers

- Horizontal handovers.
- ETHER management and orchestration framework.
- Flexible payload and service orchestration.
- Semantics-aware information handling solutions.

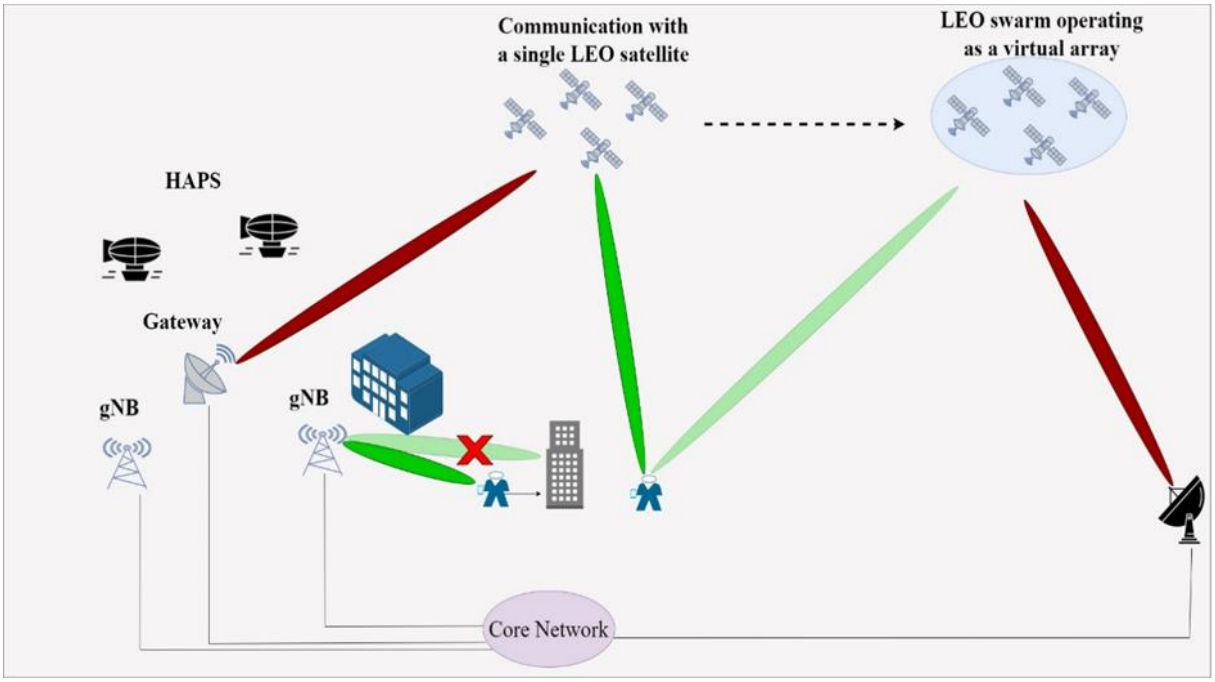

Figure 1-3: Use Case 2: Unified RAN for direct handheld device access at the Ka band

Use Case 2: Unified Radio Access Network (RAN) for direct handheld device access at the Ka band

Technology Enablers

- Distributed beamforming from LEO satellite swarms.
- Handheld device antenna design.
- Unified waveform design.
- Vertical handovers between different Radio Access Technologies (RATs).

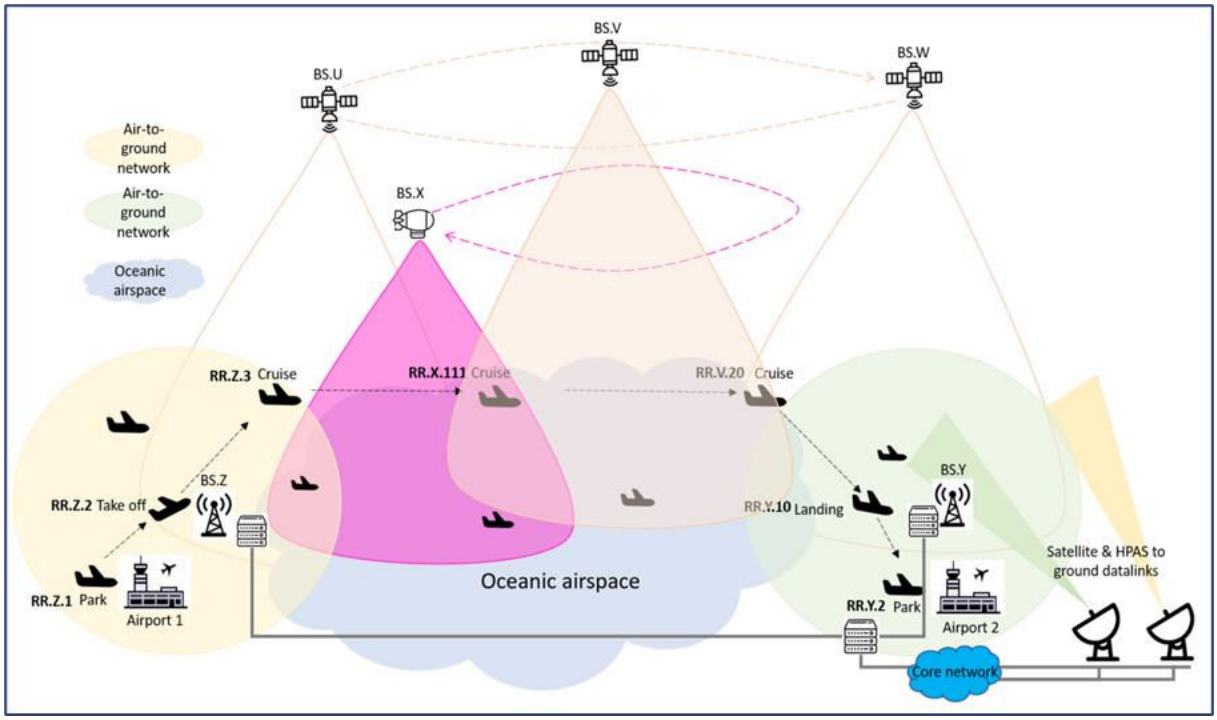

Figure 1-4: Use Case 3: Airspace safety critical operations

Use Case 3: Airspace safety critical operations

Technology Enablers

- Vertical handovers across RATs.
- ETHER MEC orchestrator.
- Predictive analytics.
- E2E network performance optimisation algorithms.

The main research results presented in D3.1 and the novel additions in D3.2 are summarized below:

- LEO-to-ground channel was investigated at 28 GHz (Ka band) and path loss due to free-space propagation and atmospheric attenuation was calculated. Multipath characteristics were investigated through ray-tracing simulations for three outdoor scenarios. The results have been exploited for the estimation of the link budget, as well as the definition of requirements for the terminal's antenna design in D3.2.
- Distributed beamforming with the cooperation of a swarm of LEO satellites was investigated as an enabler for the LEO-to-user direct access. An analytical framework was developed for the estimation of the probability distribution function of the normalised main lobe gain as the main performance metric of the scheme. Random independent phase errors are assumed to each of the satellites. Based on the distribution of the main lobe,

the maximum tolerable phase error bound that allows us to achieve the nominal target data rate, was computed. The developed methodology has been extended to multi-user scenarios and the results are presented in D3.2.

- OTFS (Orthogonal Time-Frequency Space) performance was investigated against Orthogonal Frequency-Division Multiplexing (OFDM modulation) to overcome high Doppler values observed in direct communication links between LEO satellites and users on the ground. Simulation results have shown the superiority of OFTS with respect to OFDM. D3.2 focuses in the comparison of two versions of OTFS, namely the single-step Zak transform one and the two-step conventional one.

- Software defined flexible payload architecture has been selected in ETHER to enable TNT integration. A custom OS framework was developed and integrated into experimental hardware by means of FPGA technology. The work will be continued within D3.2 towards optimization of the platform, adding HW reconfiguration capabilities and deploy additional services.

- Given the capability of software-based flexible payload, joint dynamic spectrum allocation and interference management was formulated as a NP-hard problem. A suboptimal closed form solution was extracted through a low complexity WMMSE framework. Further elaboration of the methodology is performed within D3.2.

- Power control in heterogeneous satellite networks was investigated through the “underlay” Cognitive Radio model, where secondary (LEO) users transmit concurrently with primary (GEO) users in the same spectrum. A Matlab-based tool was developed incorporating the selected algorithms. The development of the algorithms will be completed within D3.2 and the output of the tool will provide maximisation of power per LEO spot beam.

- Data analytics and semantics-aware caching for high energy efficiency has been investigated. The proposed solution is based on Version AoI (Age of Information) metric with a gossiping destination network. The objective is to model the average Version AoI for the updates stored at the destination nodes and find an optimal status update policy that minimises the average Version AoI. The proposed optimal policy leads to significant (~ 50%) reduction in the number of transmissions, compared to the greedy policy used as reference. Extending the conducted work, in D3.2 two information handling scenarios will be examined: the first with sensor data for status updating in the network and the second using Version AoI to update the context database.

- Horizontal and vertical handovers (HO) are investigated as critical enablers for the integration of terrestrial and non-terrestrial networks.

    - Horizontal handover procedure relies on the design, implementation and validation of a S&F proxying element capable of manipulating UE context in the AMF onboard a satellite. UE Context Proxy implementation is built upon Magma, a FLOSS 4G/5G CN, and validated by means of a laboratory testbed to emulate a simple NTN scenario with two LEO satellites, a Ground Segment, and different UEs. In D3.2, UE context dissemination strategies have been studied in order to determine efficient horizontal handover policies.
    - Vertical handover procedure is implemented using simulation Omnet++ after rewriting OS3 satellite library and adding critical functionality to coexist with the other Omnet++ critical libraries in order to carry out complex simulations, i.e., simulations that combine TN and NTN environments. Extensive simulations have been carried out and the functionality of the updated platform has been tested. Development of vertical handover algorithms, as well as their incorporation to the simulation platform and the evaluation of their efficiency will be presented in D3.2.

Continuing the work described above, D3.2 includes the final results of WP3 and its content is structured as follows:

Chapters 2 and 3 address the implementation of Use Case 2. Specifically, **Chapter 2** includes link-budget analysis for the LEO satellite-to-terminal user wireless channel and then, terminal antenna is designed to achieve direct access to LEO satellite. Finally, the feeding network of the antenna is analysed and different options are provided with respect to the trade-off between optimization of antenna performance and feasibility of implementation within the capacity of ETHER. **Chapter 3** is divided into two parts. The first investigates distributed beamforming from a swarm of LEO satellites, extending the results to multi-user scenarios. The second partfocuses on the Orthogonal Time Frequency Space .

Chapter 4 addresses all three Use Cases and is divided into two main parts. The first presents the software-based flexible payload architecture that integrates satellites into a cohesive multi-node cluster, capable of sharing resources and executing complex, distributed functionalities. The second part presents dynamic spectrum allocation and power control techniques to mitigate interference in aerial and space ETHER layers, exploiting the capabilities of flexible payload architecture. Dynamic spectrum allocation is addressed through precoding and the corresponding optimization problem is transformed into weighted minimum mean square estimation (WMMSE). Detailed description of WMMSE algorithm is provided and the results are compared with two reference benchmarks. Regarding power control, a heuristic algorithm for EPFD is developed that meets the ITU-R EPFD limits for any LEO constellation. The provided framework for LEO power control is a powerful tool to the satellite operator during the network provisioning stage.

Chapter 5 addresses the implementation of Use Case 1 by investigating semantics-aware communication schemes and information handling solutions towards high energy efficiency. A semantics-aware approach is employed to handling information from an energy-constrained IoT device to a network of interconnected LEO satellites. Version Age of Information (VAoI) at LEO nodes is analysed and its network-wide average is optimized by adopting a transmission policy at the device, subject to energy constraints.

Chapter 6 addresses all three Use Cases and is divided into two main parts. The first part investigates horizontal handovers in LEO-based Store & Forward networks presenting the final version of the UE Context Proxy testbed as well as the successful demonstration of the technology showcasing its evolution from laboratory proof-of-concept to a practical solution. The second part presents ETHER solution for Vertical Handovers investigation based on Omnet++ simulator using several updated libraries for the realistic representation of Terrestrial and Non-Terrestrial entities and their communication environment. SINR (Signal-to-Interference plus Noise Ratio) driven and Energy Efficiency driven Vertical HO algorithms are implemented and tested on the developed simulation platform.

Finally, according to the initial workplan, NCSRD are responsible for the design of the terminal antenna while its prototyping together with the feeding network is realized by a Subcontractor. Then, characterization of the antenna will be realized by NCSRD in their antenna far-field test site (anechoic chamber). The activity was included to WP3 results. According to timeplan, the antenna design was completed in time however, it has been proved challenging to source a subcontractor that takes over the specific task within the existing timeframe and budget limitations. As a result, NCSRD completed the design of the feeding network applying different techniques in order to simplify the implementation of the antenna. After the conclusion of that phase, NCSRD awarded the procurement to the Subcontractor which will deliver the prototype of the antenna and customized control boards to implement beam steering of the antenna pattern to predefined angles. Due to the above reasons, it was not possible to complete that part of the work within WP3.Thus, it has been decided to deliver the terminal antenna and its characterization results within WP5 and specifically Demo 2 of the Use Case 2. Details on the antenna prototyping activity are given in Section 2.2.3.

1.2 RELATIONSHIP WITH OTHER ETHER DELIVERABLES

WP3 receives input from WP2 and provides input to WP4 and WP5. Thus, the current deliverable received input from D2.1: Initial report on ETHER network architecture, interfaces and architecture evaluation, D2.2: Use cases and KPIs/KVIs, and D2.4: Final report on ETHER network architecture, interfaces and architecture evaluation. Moreover, D3.2 builds upon the work conducted in D3.1 to achieve the final results of WP3. Additionally, the work presented in D3.2 is exploited by D4.2: Final report on zero-touch data-driven network and service orchestration in the 3D ETHER architecture, in two directions, i.e., semantics-aware caching and information handling techniques as well as development of SDN architectures for efficient and scalable control of multi-domain network technologies. Furthermore, regarding WP5 this deliverable will contribute to D5.2 by integrating the upgraded WP3 technologies into the demonstration activities that will be reported in D5.3. Regarding this, the innovations that are reported in D3.2 concern both innovations that will be included in the final demonstration to be reported in D5.3 and also innovations that will not be integrated in the final demonstration, but are important for the overall ETHER architecture that was reported in D2.4. More specifically, among the presented innovations of D3.2 the ones that will be integrated in the final demonstration activities are related to **UC1: Flexible payload-enabled service provisioning to semantics-aware and delay-tolerant IoT applications** and **UC2: Unified RAN for direct handheld device access at the Ka band**. These innovations per use case that will be included in the final demonstration activities are the following:

UC1: Flexible payload-enabled service provisioning to semantics-aware and delay-tolerant IoT applications:

- Software defined payloads
- Semantics-aware information handling
- Horizontal LEO-to-LEO handovers

UC2: Unified RAN for direct handheld device access at the Ka band

- User terminal antenna design for communication with LEO satellites
- Vertical handovers

2 USER TERMINAL ANTENNA DESIGN FOR DIRECT COMMUNICATION WITH LEO SATELLITES

Introduction

This chapter is part of the work on channel modelling and terminal antenna design for direct access to LEO satellites at the Ka band, which supports ETHER Use Case 2: "Unified RAN for direct handheld device access". Specifically, channel modelling was analysed in D3.1 where free space path loss and multipath fading were studied. The results of the work conducted within D3.1 are exploited in D3.2 to perform link-budget analysis at the 28 GHz and decide the specifications of the terminal antenna that is suitable for direct access to LEO satellite. Then, the design of a 20×20 antenna array is provided and characterized through electromagnetic simulations. Moreover, the complexity of the antenna's feeding network is analysed, and an array (of smaller dimension) is selected as a realistic solution for prototyping the antenna and evaluate its main characteristics through measurements.

2.1 LINK-BUDGET ANALYSIS FOR 28 GHZ BAND

2.1.1 Significance of Link-budget analysis and expected results

Main aim of the current task is the effective design of a beam-steering antenna (e.g. phased array antenna), which will be minimized in size compared with the current scientific research status and commercial state in order to be embedded into a portable terminal (e.g. Laptop PC) to communicate with LEO satellites providing at least 100Mbps and 20 Mbps download and upload (downlink and uplink) data rates (Figure 2-1). Based on the above requirements, some direct limitations are settled such as: low-profile, compact (aim of 10cm x 10cm, see Figure 2-2), medium to high gain average performance (20-35dBi), at least 70deg beam scanning ability, limited input available power (≤1W) due to proximity of human bodies and SAR limitations. Considering these restrictions, the selection of the most appropriate candidate antenna design led to a phased array design concept.

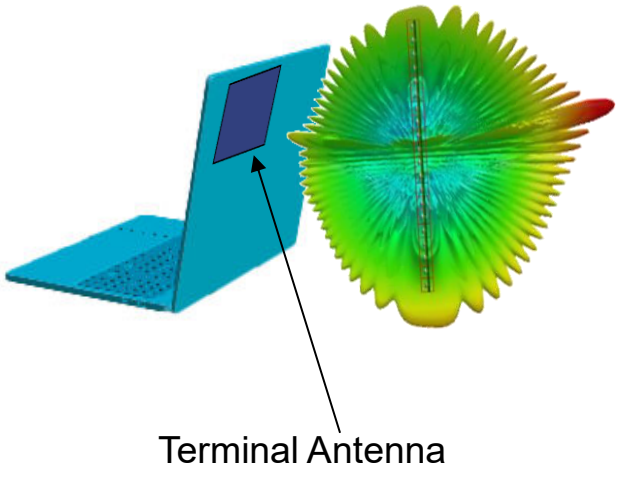

Figure 2-1: Terminal antenna operating concept

According to theory the achievable gain compared with the physical dimensions for squared array geometry are shown in Table 1. The aperture efficiency is assumed to be 60%, which is a normal average for an aperture antenna. A basic KPI such as the gain of the antenna is defined. The aim is to settle for 10cmx10cm with a target maximum Gain of 30.2 dBi.

Table 1 Theoretical Gain vs. dimensions of array antenna

Dimensions (cm x cm)	Gain (dBi)
10x10	30.2
15x15	34.2
20x20	36.4
25x25	38.3

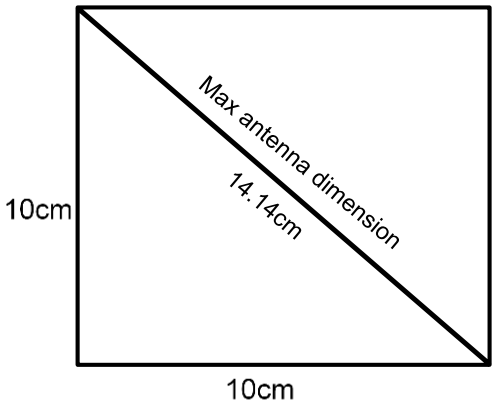

$$Gain\,[dBi] = 10\,log\left(k\left(\frac{\pi D}{\lambda}\right)^2\right)$$

Figure 2-2 Target phased array antenna dimensions

Knowing the above limitations and KPIs of the aim antenna, it is important in terms of communications engineering to validate effective link budget between earth terminal and LEO satellites. So the link budget analysis for system performance evaluation is mandatory. As an effective system requirement, based on literature, the link budget requirements are settled as shown in Table 2. The specific Eb/No value has been found in the literature [3] and it is used for satellite internet supporting 16APSK(3/4) digital modulation.

Table 2 Uplink and Downlink system requirements

direction	bandwidth [MHz]	data-rate [Mbps]	Eb/No [dB]	C/N [dB]
Uplink	100	20	5.5	-1.5
Downlink	200	100	5.5	2.5

In satellite communications engineering the carrier to noise ratio (C/N or CNR) is usually used for link budget calculations and it relates to Eb/No via the following equation. The values presented in Table 2 are derived from these equations.

$$(C/N) = (E_b/N_0)\,(R_b/R_s) \quad (2\text{-}1)$$

where R_s is the channel bandwidth and R_b is the bit rate

$$(C/N)[dB] = (E_b/N_0)\,[dB] + 10\log(R_b)\;[dBHz] - 10\log\,(R_s)\,[dBHz^{-1}] \quad (2\text{-}2)$$

Therefore, it must be noticed that, knowing the required E_b/N_o (depending on the selected digital modulation) could easily estimate the respective C/N.

2.1.2 Link budget theory (Uplink and Downlink)

The geometry of the uplink and downlink are described in Figure 2-3 and Figure 2-4. The equations of the carrier to noise (C/No) are also included in the geometry. The equations will be expanded in the following subsections. The notation U symbolizes the uplink, D the downlink, ES the earth station (or terminal user antenna) and SL the satellite.

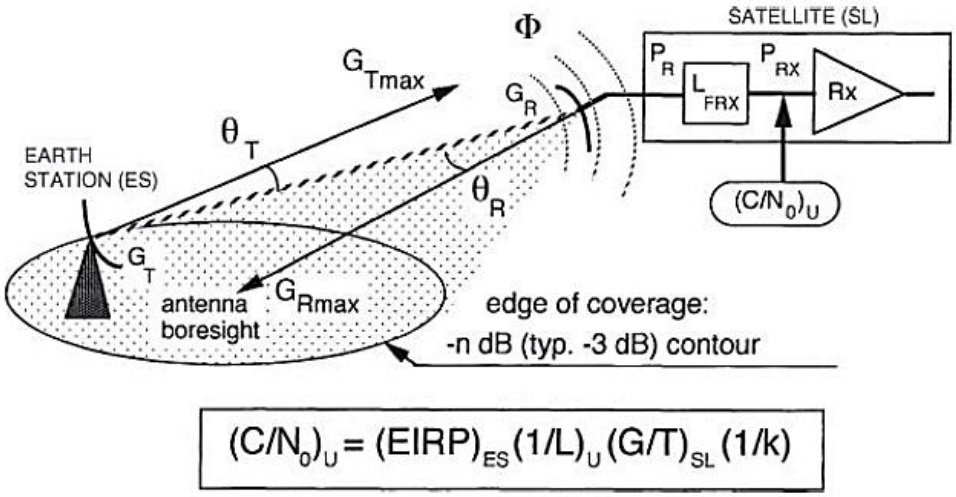

Figure 2-3 Geometry and engineering parameters of uplink

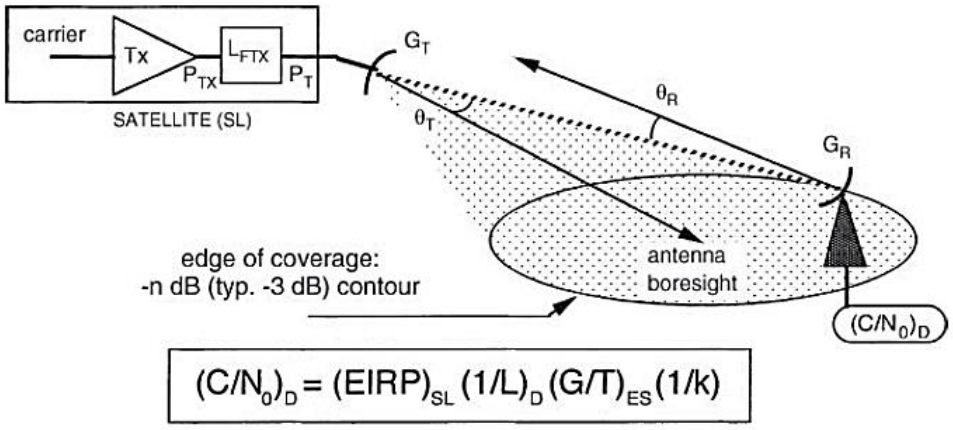

Figure 2-4 Geometry and engineering parameters of downlink

The quality of the link between a transmitter and a receiver can be characterized by the ratio of the carrier power to the noise power spectral density C/No. This is a function of the transmitter EIRP, the receiver figure of merit G/T, and the properties of the transmission medium. In a satellite link, two links must be considered – the uplink, characterized by the ratio $(C/No)_U$; and the downlink, characterized by the ratio $(C/No)_D$. The propagation conditions in the atmosphere affect the uplink and downlink differently; rain reduces the value of the ratio $(C/No)_U$ by decreasing the value of received power C_U, while it reduces the value of $(C/No)_D$ by both reducing the value of received power C_D and increasing the downlink system noise temperature. The differences between two path-links can be described the following equations.

Uplink

$$\Delta(C/N_0)_U = \Delta C_U = (A_{RAIN})_U \quad [dB] \tag{2-3}$$

$$(C/N_0)_{rain} = (C/N_0)_{clear\ sky} - (A_{RAIN}) \ \ [dBHz] \quad (2\text{-}4)$$

Downlink

$$\Delta(C/N_0)_D = \Delta C_D - \Delta(G/T) = (A_{RAIN})_D + \Delta T \ \ \text{[dB]} \quad (2\text{-}5)$$

$$\Delta(G/T) = (G/T)_{clear\ sky} - (G/T)_{rain} \quad (2\text{-}6)$$

$$(C/N_0)_{rain} = (C/N_0)_{clear\ sky} - (A_{RAIN}) - \Delta(G/T) \ \ [dBHz] \quad (2\text{-}7)$$

In simple terms the downlink yields increased noise due to rain on the earth station receiver quality. So, the rain noise degrades the quality factor of the earth station antenna receiver.

Finally, it must be noted that:

$$(C/N) \ [dB] = (C/N_0) \ [dBHz] - 10\log(BW) \ [dBHz^{-1}] \quad (2\text{-}8)$$

This equation fulfils the link budget analysis tool.

2.1.3 Uplink analysis

$$CNR_U[dB] = EIRP_T[dBW] - L_U[dB] + \left(G/T\right)_{SL}[dBK^{-1}] + 228.6\left[\frac{dBW}{HzK}\right] - 10\log(BW)\,[dBHz] \quad (2\text{-}9)$$

The factors of the CNR_U are linked with both the terminal antenna transmitter and the satellite antenna receiver. More specifically the **EIRP** is the effective isotropic radiated power of the terminal transmitter, and it is affected by the power transmitted (PTx), the maximum Gain of terminal antenna (GTmax), the pointing losses (L_T), the transmission line feed and mismatch losses (L_{FTX}) and finally the surface accuracy losses (La) based on fundamental Ruze's equations. Obviously the EIRP describes the characteristics of the Terminal Antenna and Transmitter. The factor $\mathbf{L_U}$ stands for environmental losses such as: free space loss (L_{FS}), the atmospheric losses (L_{atm}) which include the gas attenuation, rain attenuation and scintillation as analytically presented in D3.1. Also, the atmospheric losses include depolarization losses (L_{DEPOL}) due to rain and ice, sandstorm losses (L_{sand}) and the fading losses (L_{fading}) as calculated and simulated in D3.1 representing a general margin of the propagation scenario. The factor $(G/T)_{SL}$ stands for the satellite receiver quality factor which includes a few parameters such as maximum gain of receiver antenna (GR_{max}), losses due to polarization mismatch (L_{POL}), pointing losses (L_R), satellite antenna transmission line losses (L_{FRX}), surface accuracy losses (La), antenna noise temperature due to ground and space (T_A), thermodynamic noise temperature of transmission lines of the satellite receiver (T_F) and finally the active noise temperature of on the receiver's input circuitry (T_{eRx}). The factor **228.6** stands for the Boltzmann constant. The factor $10\log(BW)$ stands for the bandwidth effect.

The scenarios that have been examined so as to validate the parameters of the uplink and to approach the path as more realistically as possible and to define finals terminal antenna KPIs, which will be used for the requirements of the antenna design and as input in the downlink analysis, are:

- **scen.F:** Scenario-F (Fading losses effect): This scenario examines the effect of different values of fading losses as calculated and found in D3.1 from best to worst case scenario. These fading losses values are: 5dB, 10dB, 20dB.

- **scen.B:** *Scenario-B* (Bandwidth effect): The effect of the channel bandwidth on the CNR vs. Gain performance is examined via this model. The values considered in terms of parameter of BW are: 25MHz, 50MHz, 100MHz, 125MHz and 250MHz.

- **scen.I:** *Scenario-I* (Ideal scenario): All losses are minimized so as to find a reference ideal scenario as best performance case. Mainly the atmospheric losses are assumed to be minimal.

- **scen.R:** *Scenario-R* (Realistic scenario): A more realistic losses scenario like an average one.

The link parameters for all scenarios examined are depicted in Table 3. For all the above scenarios elevation angle has been assumed at 90deg as best LOS communication case. Moreover, all above scenarios have been examined for LEO satellite distances of 300-500Km.

Table 3 Uplink parameters

Parameter	Assumed values
GTmax: terminal antenna maximum gain	[20-40dBi] (parameter to be defined)
PTx : power transmitted from terminal	0 dBW *(this refers to 1W which is a safe limitation) (all scenarios)
LFTx: terminal feedline losses	1dB (scen.F, scen.B) 0.1dB (scen.I) 0.5dB (scen.R)
θT: pointing accuracy LT(θT,GTmax): Pointing Loss [0.06-0.6dB]	0.1 deg 0 deg
La : Surface accuracy loss (σ=0.2mm)	0.06 dB (scen.F, B, R) 0 dB (scen.I)
LFS (distance, frequency): distance [300-500Km], freq: 28GHz	170-176dB (scen.F, I, R) 176dB (scen.B)
Latm (rain, gas, sparkle): Atmospheric losses	7.7dB (scen.F, B) 3dB (scen.I) 5dB (scen.R)
LDEPOL: depolarization losses due to rain and ice	1dB: (scen.F, B) 0dB: (scen.I) 0.5dB: (scen.R)
Lsand: sandstorm losses	1dB: (scen.F, B) 0dB: (scen.I) 0.5dB: (scen.R)
(G/T): (Average value)	10dB (all scenarios)
BW: [25, 50, 100, 125, 250 MHz]	100MHz (scen.F, I, R) [25, 50, 100, 125, 250dB] (scen.B)
L_{fading}: Fading Loss	5dB (scen.B, I, R) [5, 10, 20dB] (scen.F)

Scen.F: Scenario-F (Fading losses effect)

The calculation results of this scenario are depicted in Figure 2-5. It can be stated that:

- 20dB fading loss yields very low CNR estimation for all distances examined
- 5dB seems sufficiently improved.
- The target 30dBi gain yields acceptable CNR (>-1.5dB) for L_{fading} 5dB and distances 300Km-450Km.

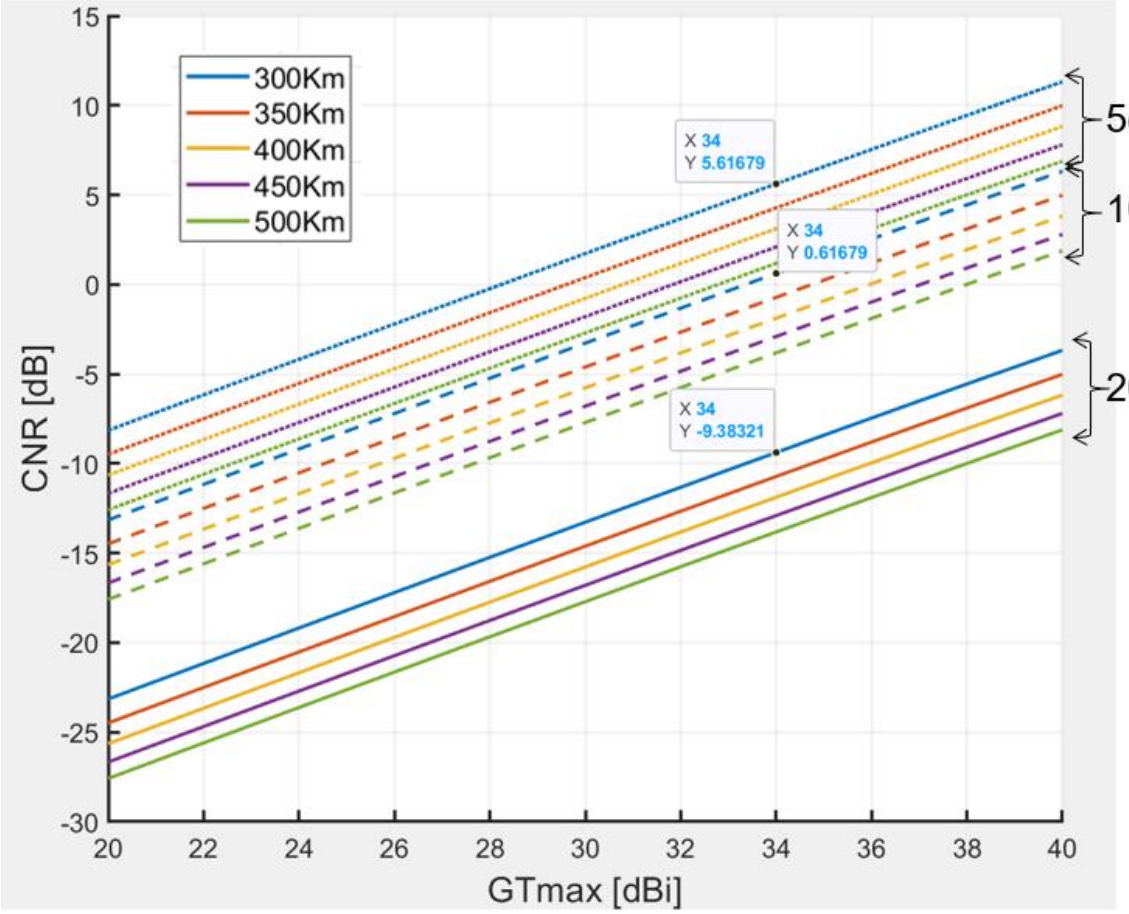

Figure 2-5: Scen F uplink calculations results (CNR vs. Terminal antenna maximum Gain)

Scen.B: Scenario-B (Bandwidth effect)

The calculation results of this scenario are depicted in Figure 2-6. It can be stated that:

- The Bandwidth scenario has been examined for the worst case of distance equal to 500Km
- The increase of the channel BW deteriorates CNR.
- The aim of 30dBi gain can achieve acceptable CNR for channel BW of 25 and 50MHz.

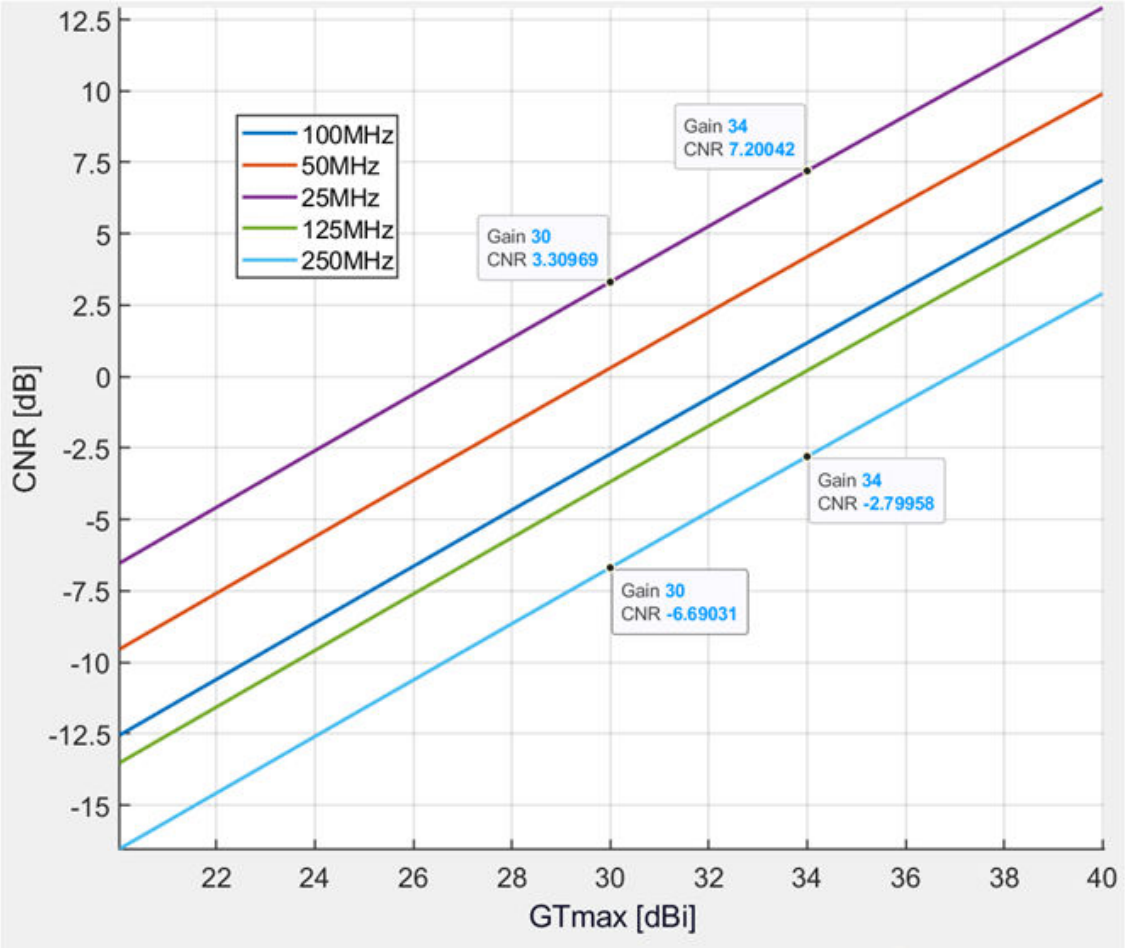

Figure 2-6: Scen B uplink calculations results (CNR vs. Terminal antenna maximum Gain)

scen.I: Scenario-I (Ideal scenario)

- The calculation results of this scenario are depicted in Figure 2-7. It can be stated that:
- The ideal scenario yields very good CNR for all distances at 34 dBi gain and decent CNR for 30dBi gain.
- These curves can be assumed that they represent the upper achievable threshold.

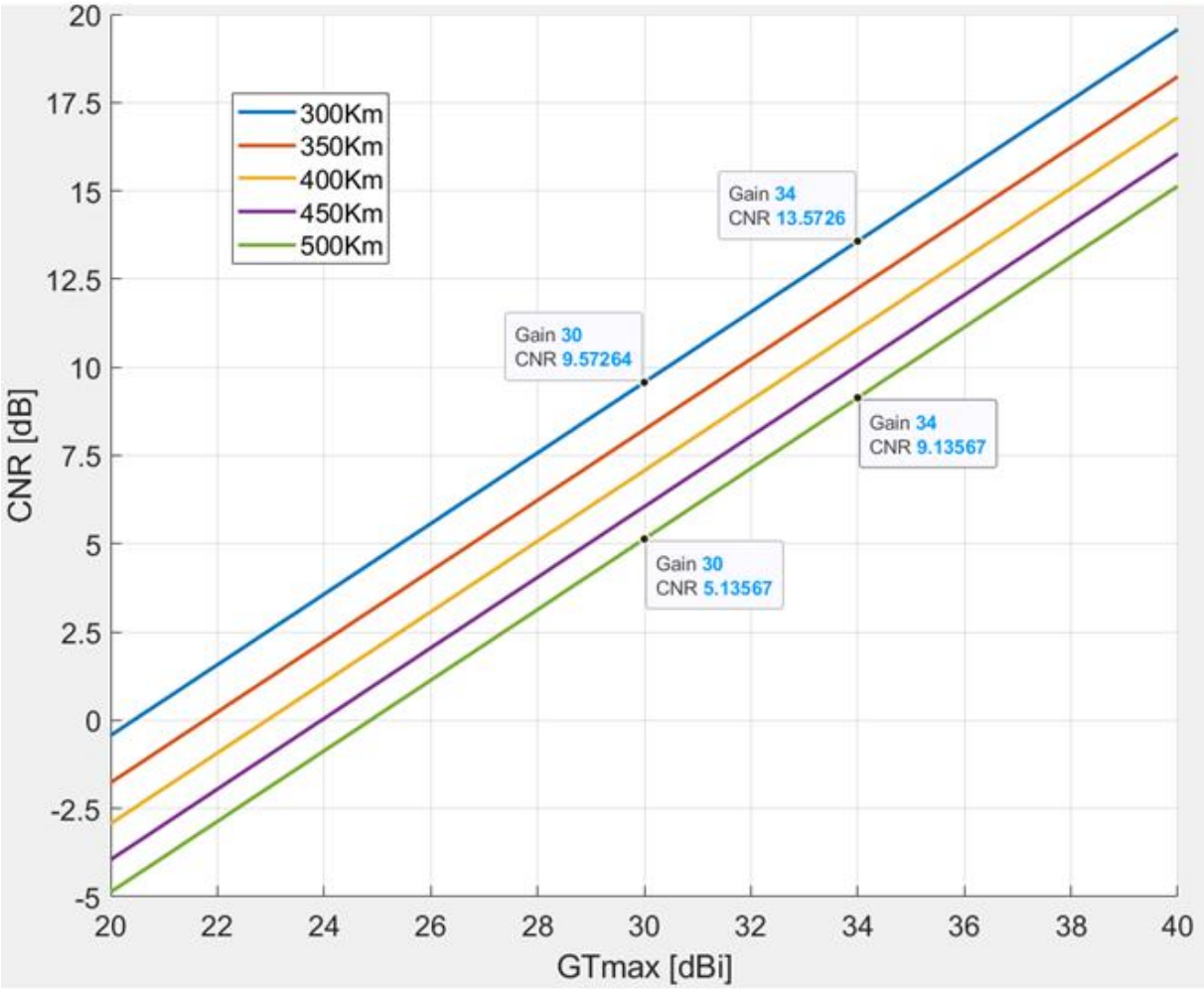

Figure 2-7: Scen I. uplink calculations results (CNR vs. Terminal antenna maximum Gain)

scen.R: Scenario-R (Realistic scenario)

The calculation results of this scenario are depicted in Figure 2-8. It can be stated that:

- The realistic scenario yields very good CNR for Gain above 30dBi for all distances examined
- The realistic scenario yields satisfactory CNR (≥0 dB) for Gain above 30dBi for all distances examined
- For CNR=-1.5dB, Upload bitrate=20Mbps and BW=100MHz the achieved Eb/No=5.5dB is easily targeted with gain of 27dBi and above for all examined distances.

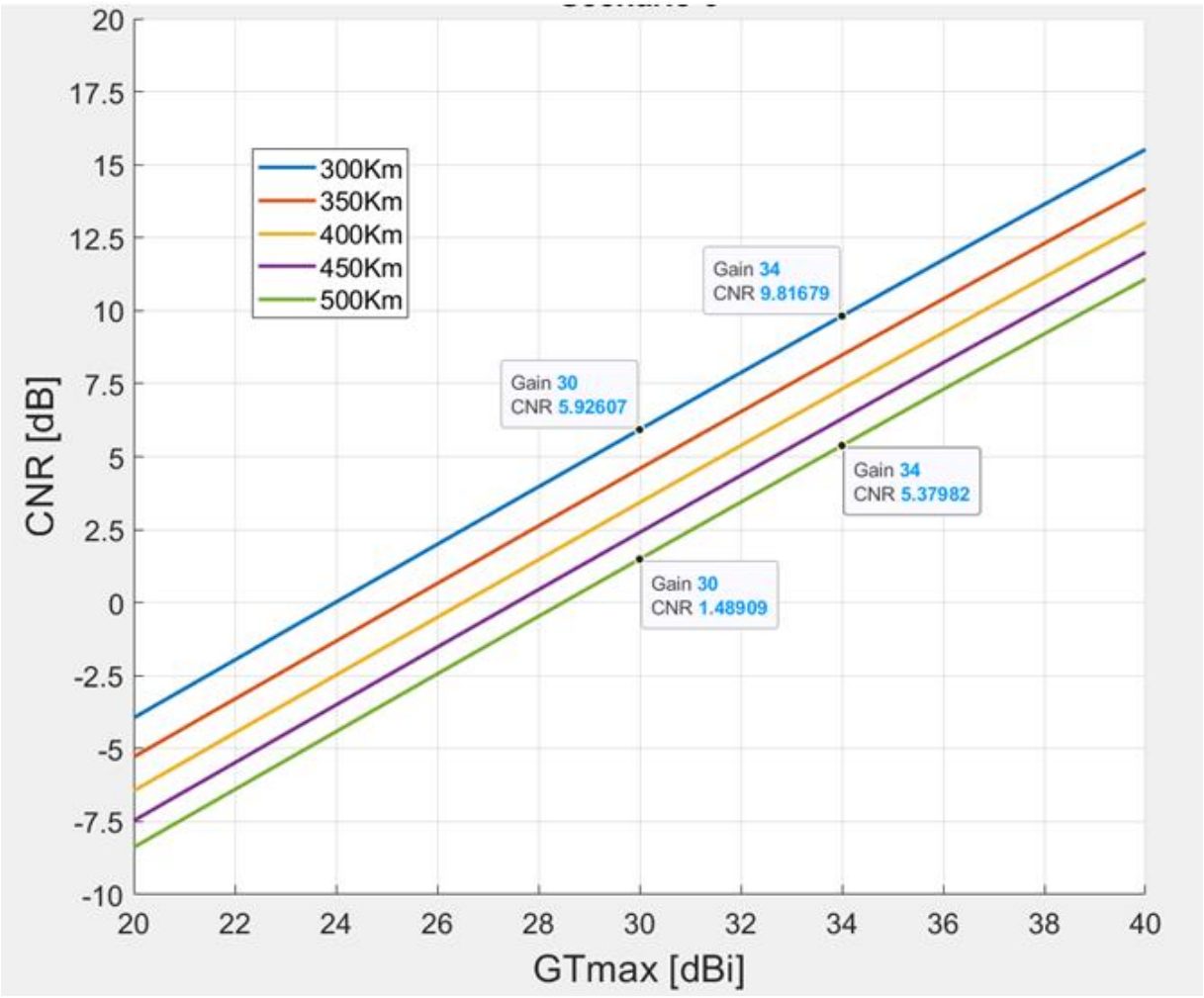

Figure 2-8: Scen R. uplink calculations results (CNR vs. Terminal antenna maximum Gain)

Link budget analysis (elevation angle effect)

The scenarios examined so far assumed elevation angle of 90deg. In real conditions the change of elevation angle from 90deg will vary the terminal to satellite distance. So, it is important to assess the effect onto link budget performance. Generally, it can be stated that the elevation angle affects the losses. The losses mainly increase due to distance increase.

Elevation angle geometry, user distance and its parameters can be seen in Figure 2-9 [4].

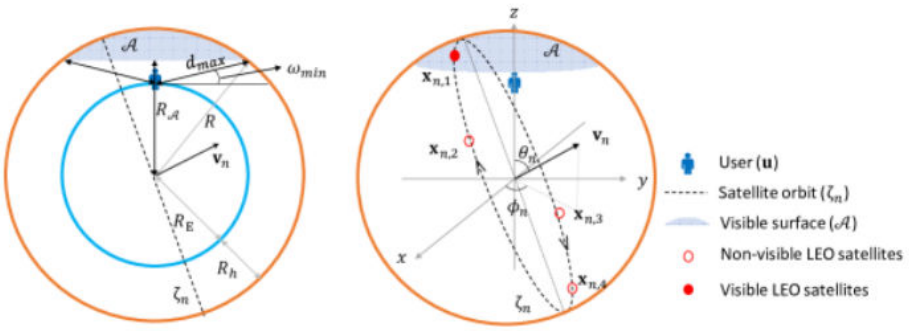

Illustrations of the n-th satellite orbit geometry denoted by ζ_n. The dotted line in the left figure depicts an orthogonal projection view of the orbit ζ_n, and the right one illustrates a three-dimensional view of the satellite orbit ζ_n in terms of relevant parameters, polar angle θ_n and azimuth angle ϕ_n where $M_n = 4$.

Figure 2-9: Geometry of user's distance vs. satellite distance and elevation angle [4]

The definition of the geometric parameters in Figure 2-9 are presented in Table 4.

The visible surface on a sphere with a radius *R* at location *u* of the user is given by:

$$A = \{(x, y, z) \in \mathbb{R}^3 : \{x^2 + y^2 + z^2 = R^2\} \cap \{z > R_A\}\}, \quad (2\text{-}10)$$

where: $R_A = d_{max} sin\omega_{min} + R_E$

and: $d_{max} = -R_E sin\omega_{min} + \sqrt{(R_E sin\omega_{min})^2 + 2R_E R_h + R_h^2}$

Table 4 Definition of geometrical parameters

Symbol	Definition
R_E, R_h, R	Radius of the Earth, altitude of satellites, and radius of satellite orbits
u	Location of the user to measure performance: (0,0,R_E)
ω_{min}	Minimum elevation angle
A	Visible surface on a sphere with a radius R at **u**
R_A	Distance between the center of the Earth and the base of A

d_{max}	Maximum distance between **u** and A
ζ_n, v_n	The *n*-th orbit and its associated unit normal vector
ζ_n	Visible region of ζ_n by the user at **u**
θ_n, ϕ_n	Polar angle and azimuth angle of v_n
Φ_n	All satellites on ζ_n
λ	Density of satellites on each orbit

The results of the geometrical calculations can be seen in Figure 2-10. The distance significantly increases in relation with the elevation angle. The extra propagation losses added due to geometry change can be seen in Figure *2-11* and Figure 2-12. It can be set that down to 50 deg elevation angle the losses are manageable roughly up to 2dB. Below this angle the losses start to significantly deteriorate the system. So, we settle as goal for the antenna beam steering performance a range of 80 deg.

Finally, the change of the elevation angle does not only affect the free space loss, but the atmospheric losses, the gas attenuation, depolarization losses and the thermal noise as well. These extra losses have been already accounted by the fading and the use of worst-case scenario values of the referred losses for the 90deg elevation angle scenario.

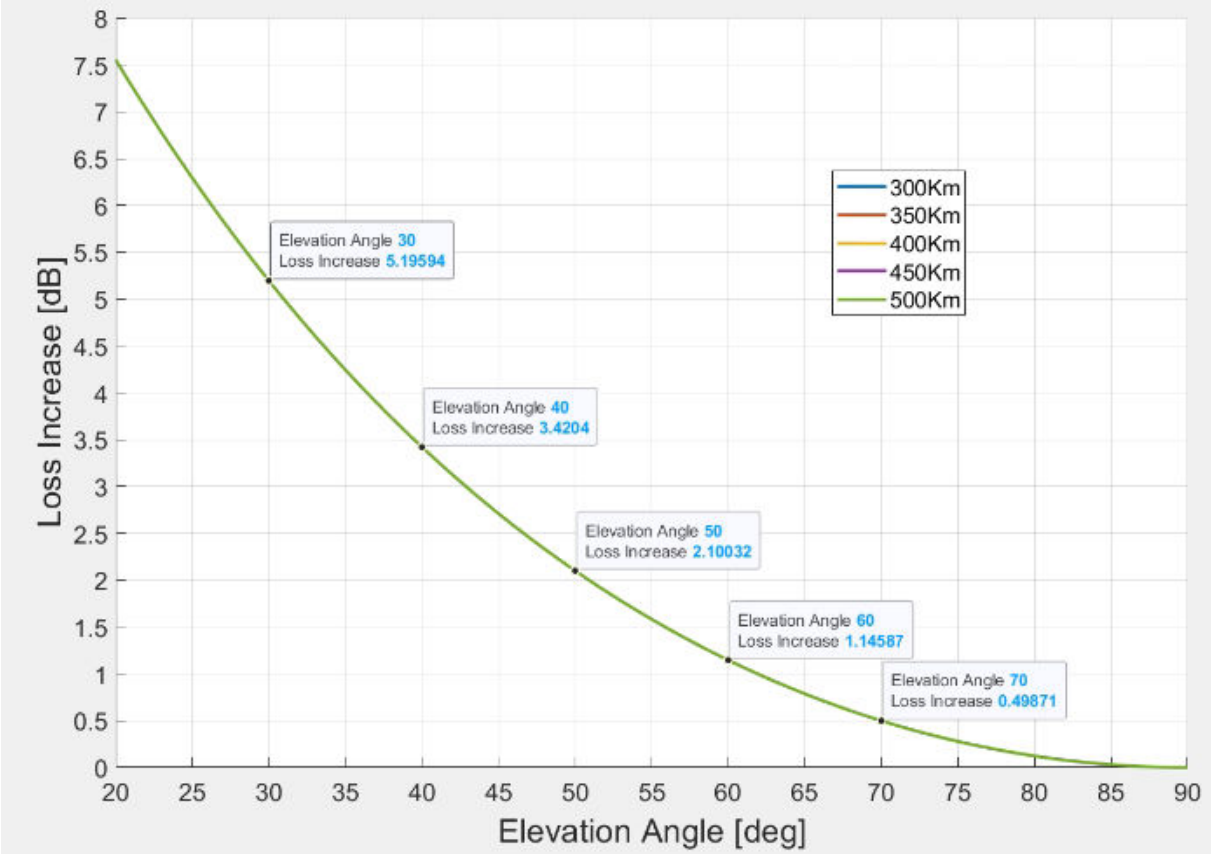

Figure 2-10: Loss increase vs. elevation angles

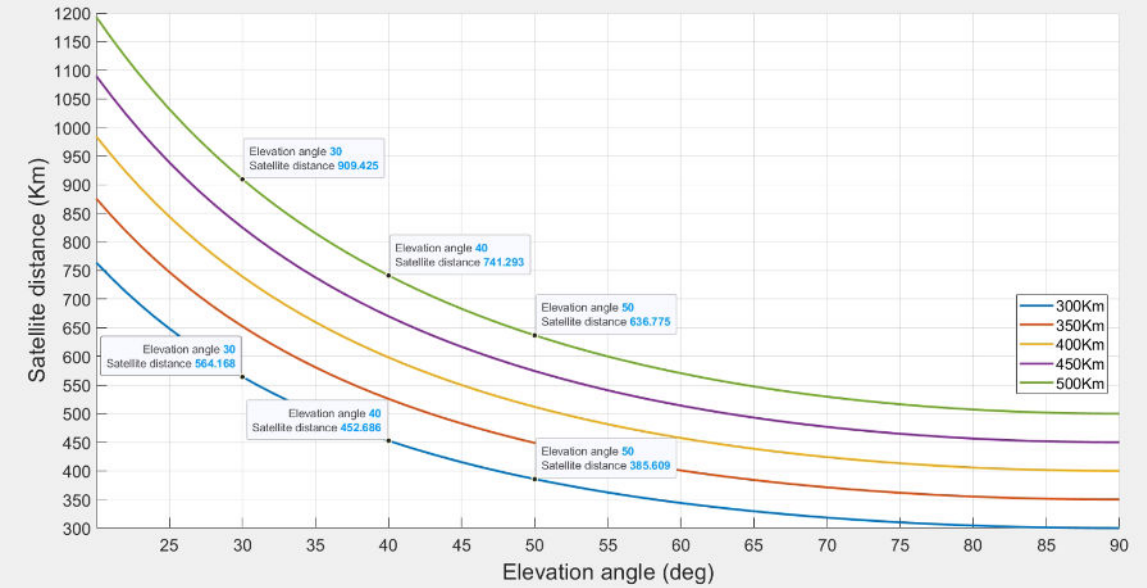

Figure 2-11: *Satellite distance vs. elevation angles*

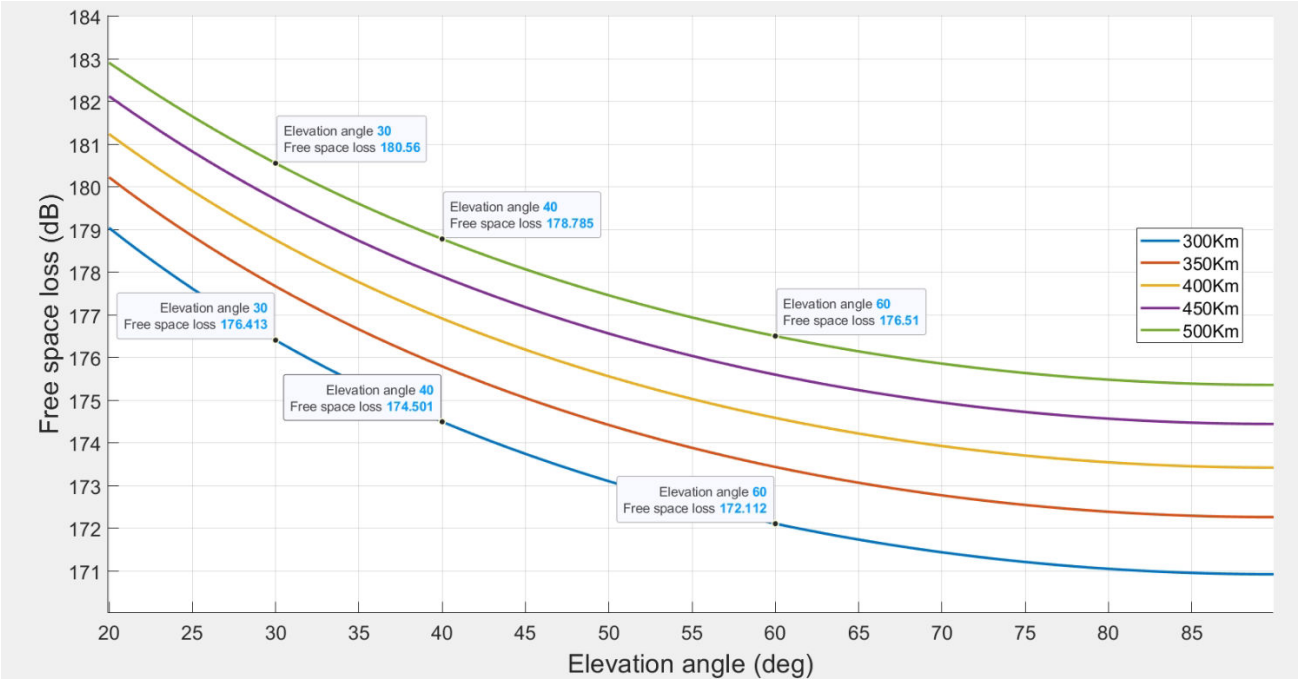

Figure 2-12: Free space losses vs. elevation angles

Concluding, it is noted that the basic terminal antenna KPIs have been defined based on the uplink analysis as follows in Table 5.

Table 5 KPIs of Terminal Antenna

Parameter	Value
Antenna array dimensions	10 cm × 10 cm
Gain	30 dBi
Steering angular range	80°
Power handling	1 W
Pointing accuracy	0.1°
Surface accuracy	0.02 λ
Bandwidth (BW)	≥ 100 MHz
Feed losses	0.5 dB
Polarization	Circular (CP)

2.1.4 Downlink analysis

We have also validated the downlink budget parameters via conducting a proper analysis, using mainly the parameters from realistic scenario conducted in the case of the uplink analysis.

$$CNR_D[dB] = EIRP_{SL}[dBW] - L_D[dB] + \left(G/T\right)_T[dBK^{-1}] + 228.6\left[\frac{dBW}{HzK}\right] - 10\log(BW)\,[dBHz] \quad (2\text{-}11)$$

The factors of the CNR_D are linked with both the terminal antenna receiver and the satellite antenna transmitter. More specifically the EIRP is the effective isotropic radiated power of the satellite transmitter, and it is affected by the power transmitted (PTx), the maximum Gain of satellite antenna (GSLmax), the pointing losses (L_T), the transmission line feed and mismatch losses (L_{FTX}) and finally the surface accuracy losses (La). Obviously the EIRP describes the characteristics of the Satellite Antenna and Transmitter. The factor L_D stands for environmental losses such as free space loss (L_{FS}), the atmospheric losses (L_{atm}) which include the gas attenuation, rain attenuation and scintillation as analytically presented in D3.1 [1]. Also, the atmospheric losses include depolarization losses (L_{DEPOL}) due to rain and ice, sandstorm losses (L_{sand}) and the fading losses (L_{fading}) as calculated and simulated in D3.1 representing a general margin of the propagation scenario. The factor $(G/T)_T$ stands for the terminal receiver quality factor which includes a few parameters such as maximum gain of receiver antenna (GT_{max}), losses due to polarization mismatch (L_{POL}), pointing losses (L_R), terminal antenna transmission line losses (L_{FRX}), surface accuracy losses (La), antenna noise temperature due to ground and space (T_A), thermodynamic noise temperature of transmission lines of the satellite receiver (T_F), the rain extra noise temperature (T_{RAIN}) the active noise temperature of on the receiver's input circuitry (T_{eRx}). The factor **228.6** stands for the Boltzmann constant. The factor $10\log(BW)$ stands for the bandwidth effect.

The scenarios that have been examined to validate the parameters of the downlink and to realistically approach the path are:

- **scen.P:** *Scenario-P* (Transmitted power effect): This scenario examines the effect of different values of transmitted satellite power. These values are: 75W, 80W, 85W, 90W, 95W, 100W, 316W (Maximum ideal case).

- **scen.Q:** Scenario-Q (receiver's Quality factor effect): The effect of the G/T of the terminal antenna on the CNR vs. satellite Gain performance is examined via this model. The values examined in terms of parameter of G/T are: -1dB (REALISTIC); 3dB (AVERAGE); 6.19dB (LITERATURE IDEAL).

- **scen.R:** Scenario-R (Realistic scenario): All link parameters and losses settled to represent realistic scenario.

The link parameters for all scenarios examined are depicted in Table 6. For all the above scenarios, an elevation angle of 90deg has been assumed as best LOS communication case. Finally, all above scenarios have been examined for LEO satellite distances of 300-500Km.

Table 6 Downlink parameters

Parameter	Assumed values
GSLtmax: satellite antenna maximum gain	[20-40dBi] (literature defines it as 39dBi)
PTx : power transmitted from satellite	75W, 80W, 85W, 90W, 95W, 100W, 316W (Maximum ideal case) (scen.P) 75W (scen.Q, R)
LFRx: terminal feedline losses	0.5dB (all scenarios)
θT: pointing accuracy LT(θT,GTmax): Pointing Loss [0.06-0.6dB]	0.1 deg
La : Surface accuracy loss (σ=0.2mm)	0.06 dB (all scenarios)
LFS (distance, frequency): distance [300-500Km], freq: 28GHz	170-176dB (all scenarios)
Latm (rain, gas, sparkle): Atmospheric losses	5dB (all scenarios)
LDEPOL: depolarization losses due to rain and ice	0.5dB: (all scenarios)
Lsand: sandstorm losses	0.5dB: (all scenarios)
(G/T):	-1dB (scen. P, R) -1dB; 3dB; 6.19dB (scen.Q)
BW:	200MHz (all scenarios)
L_{fading}: Fading Loss	5dB (all scenarios)

The respective diagrams representing the calculated results from the above three scenarios (P, Q, R) are shown respectively in Figure 2-13, Figure *2-14*, Figure 2-15.

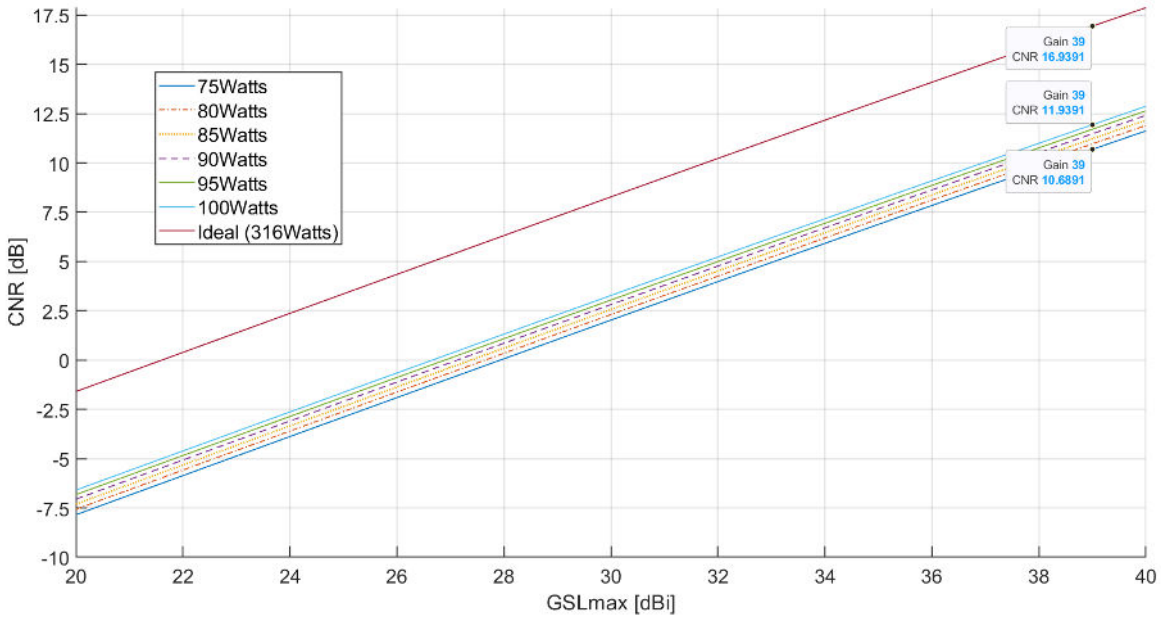

Figure 2-13: Scen P. downlink calculations results (CNR vs. Satellite antenna maximum Gain)

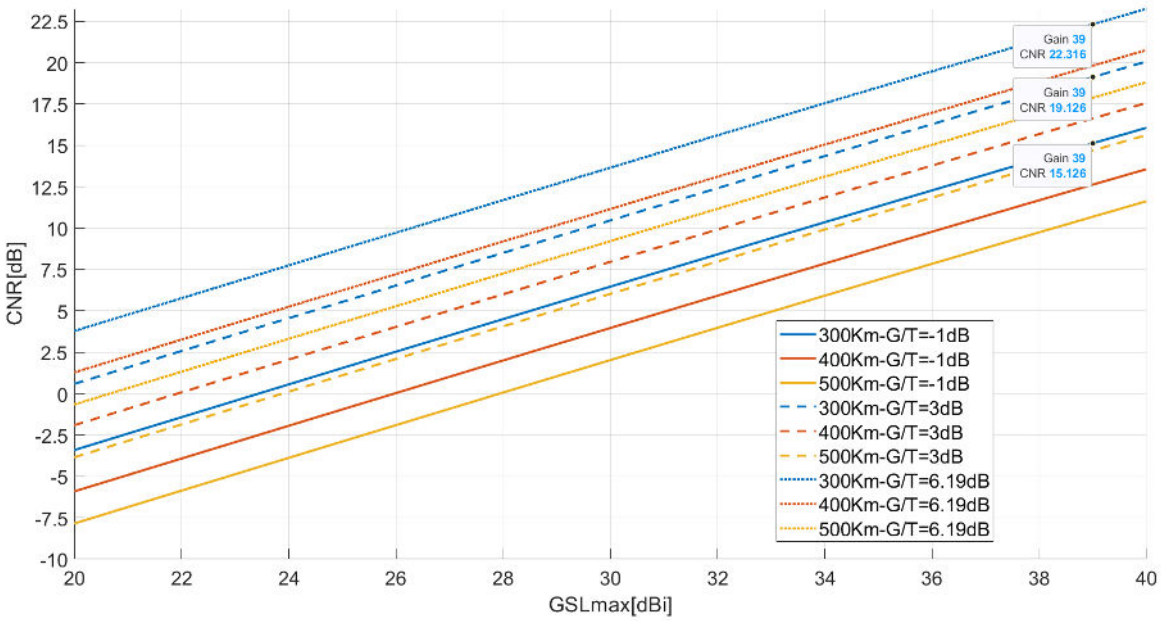

Figure 2-14: Scen Q. downlink calculations results (CNR vs. Satellite antenna maximum Gain)

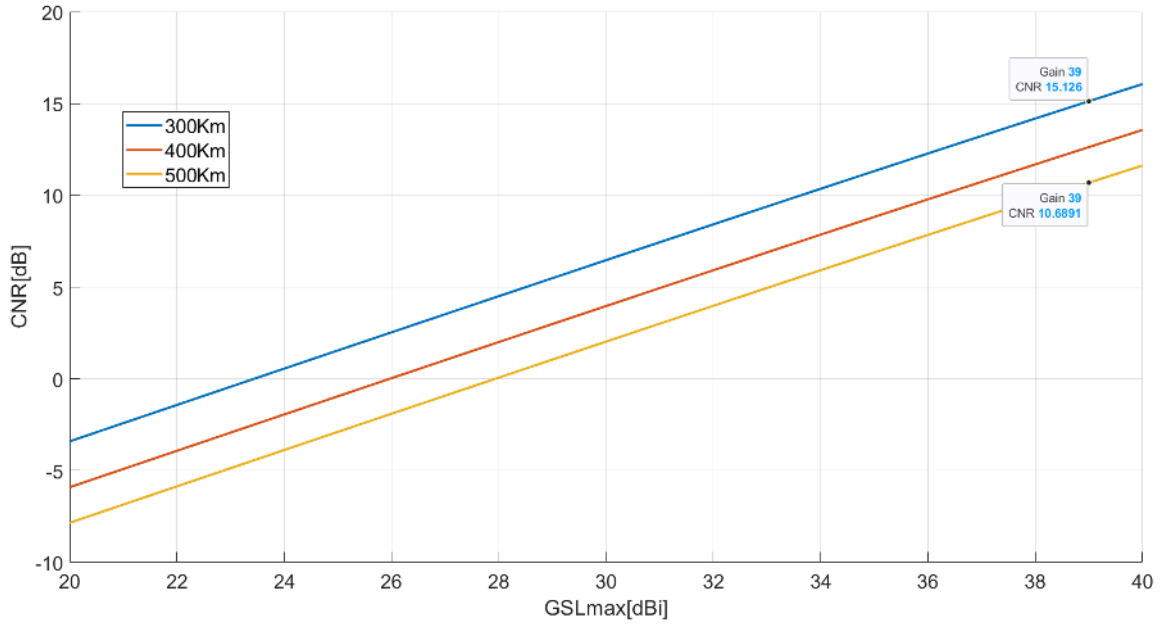

Figure 2-15: Scen R. downlink calculations results (CNR vs. Satellite antenna maximum Gain)

Considering the satellite antenna at 39dBi as indicated in [3] it can be said that the required 2.5dB CNR can be easily achieved. Based on these diagrams the satellite antenna can cover the required CNR by a 32dBi gain for all examined satellite to user distances. Taking into account the losses calculated vs. the change in elevation angle, then 34dBi gain value of the satellite antenna would be adequate to safely meeting the requirements. So, the requirements can be covered by a satellite antenna with 34dBi gain which means that a smaller size satellite antenna is required.

2.2 ANTENNA DESIGN FOR USER TERMINAL

This section describes the simulation results of the phased array antenna design, including single element performance, sub-array characteristics, full-array performance and beam steering capabilities. These results are evaluated against the specified KPI's which are analytically described.

2.2.1 Base line design

The need for limited dimensions of the antenna along with the requirement for high directivity (gain) and beam-steering capability, led us to adopt the phased array antenna as the design concept. Also considering that the system will support time division duplex (TDM) i.e. transmission and reception will use the same frequency band (at 28 GHz) in different time slots, we consider the proposed antenna to be used as a TX/RX antenna.

2.2.2 Antenna requirements

Based on the previous Link Budget analysis, the KPIs of the antenna that is designed are determined. The antenna RF performance requirements are summarized in Table 7. It can be seen that the gain is quite demanding and represents a high gain antenna (HGA). The total antenna BW is at least 2GHz, so as to provide 10 channels for uplink and 5 channels for

downlink. The scanning range across all antenna's radiation planes (phi=0°, 10°, ….45°… 90° etc.) is considered to be 80°, with theta angles to cover the range from -40° to +40°. Polarization is CP, which provides a broadside radiation performance around the planes of the antenna, as described in previous sub-section. The SLL is required to meet the minimum of 15dB which could provide minimum possible interference in terms of satellite link. The axial ratio as an indicative of the circular polarization purity is settled below 2dB. The ideal case would be to achieve 0dB axial ratio, at least in a simulation level.

Table 7. Antenna Requirements

Antenna Parameter	Requirement	Antenna Parameter	Requirement
Center frequency	**28 GHz**	**Return Loss**	**S11< -10dB**
BW	**≥2GHz**	**Sidelobe Level**	**< -15dB**
Gain	**>30dBi**	**X-polar Level**	**< -30dB**
Scan Angular Range	**≥80° (±40°)**	**Axial Ratio**	**< 2dB**
Polarization	**CP (LHCP or RHCP)**		

2.2.3 Phased array antenna design

According to the adopted antenna design concept, the basic structural parts of a phased array antenna are presented in Figure 2-16. The structural parts are divided into three basic layers: a) antenna elements layer, b) feeding network layer and c) the beamforming algorithms ICs. NCSRD contribution to the project concerns the design and analysis through simulation of the first two layers of the antenna structure ("Radiator antenna elements layer" and "Feeding network layer"). At the third layer the beamforming algorithm is the algorithm that is usually implemented using integrated circuits (ICs). The design of the third layer is out of the scope of the project.

The top layer is the main radiator part and the other two layers form together the beamforming network. The top layer includes the phased array antenna, which is formed by the unit cells (or sub-arrays) periodically placed to geometrically form the large array. The middle layer, feeding network will include at least the microstrip line interconnecting the antenna elements with the IC beamforming layer. Depending on the defined periodical structure, single element or specific elements forming a sub-array, can additionally include power divider lines and possible solid state or passive phase shifters. The work conducted by NCSRD examines both cases using a single element or a predefined sub-array (formed by single elements with specific phase rotation between each other).

The design case of single element as a unit cell which forms the large array will include in the feeding network a grounded coplanar waveguide line. The second design case was also examined, where the sub-array is formed by four elements with sequential 90deg phase rotation. The feeding network in that case will additionally include a power divider and phase shifters. The last two parts are formed using SIW (substrate integrated waveguide) and stripline technologies. The bottom layer includes the main power feeding and the beamforming algorithm chip.

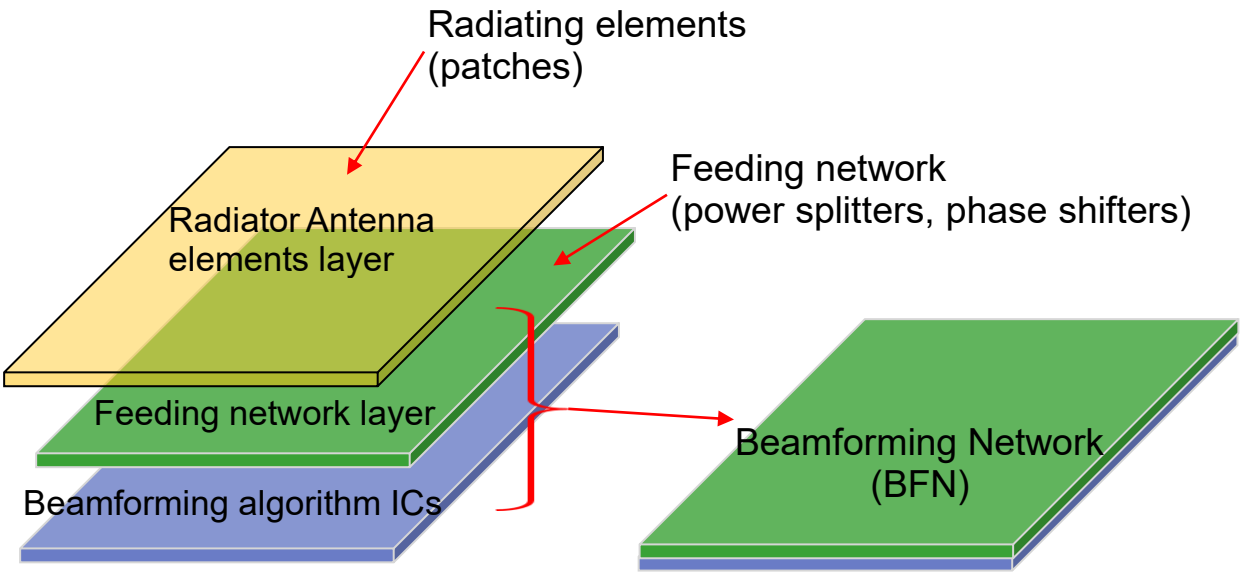

Figure 2-16: Basic structural parts of the antenna phased array

2.2.4 Detailed antenna design

2.2.4.1 Antenna element Radiator

A simple probe-fed microstrip patch antenna topology has been selected for the design of the element radiator. This is a probe feed circular polarized patch antenna operating 28GHz. The initial design of the element is a rectangular patch with truncated corners in order to realize circular polarization. The optimized geometry of the antenna element is presented in Figure 2-17. The top layer of the element is the main radiator truncated patch simulated with copper material, the middle layer is a Rogers substrate with εr=3.51 and tanδ=0.0031. Finally, the bottom layer is a full ground plane simulated with copper. The conductive copper parts are considered to be 35um thick.

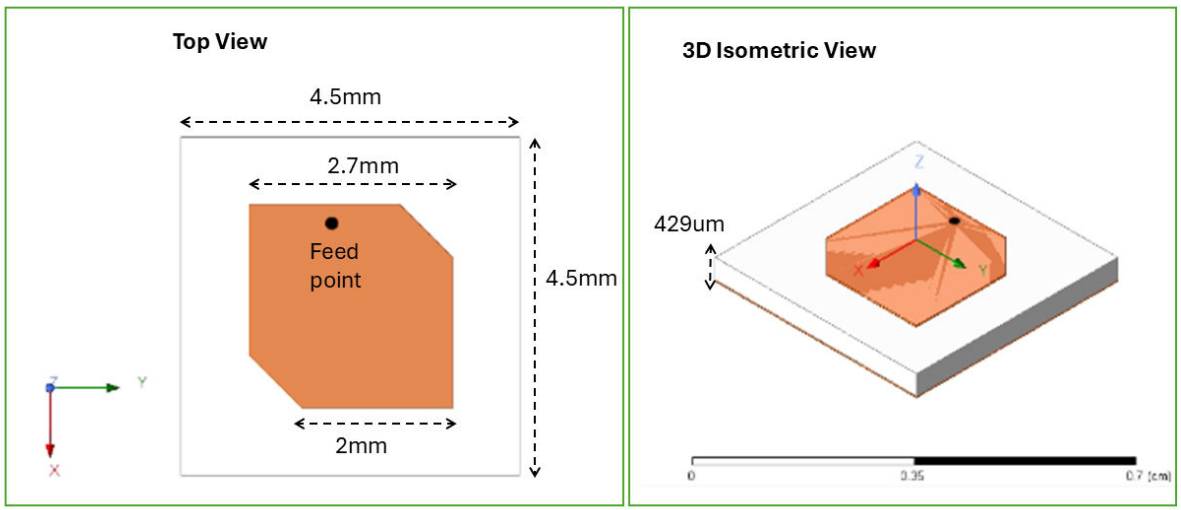

Figure 2-17: Single Antenna element geometry

The results of the RF performance analysis of the antenna element are presented as follows (Figure 2-18 to Figure 2-21).

Reflection Coefficient:

The simulated reflection coefficient (S11) of the single antenna element demonstrates good impedance matching across the target frequency range (200MHz around 28GHz as discussed in previous sub-section where the terminal antenna requirements have been determined). As shown in Figure 2-18 the S11 remains below –10 dB at 28 GHz, fulfilling the impedance matching requirement and ensuring minimal power reflection.

Gain vs. Frequency:

Figure 2-19 illustrates the gain performance of the antenna element over frequency. The element achieves a peak gain at 28 GHz, indicating efficient radiation in alignment with the design target.

Radiation Pattern:

The radiation pattern in Figure 2-20 shows the right-hand circular polarization (RHCP) and left-hand circular polarization (LHCP) components. The dominance of RHCP over LHCP confirms polarization purity, an essential criterion for system performance.

Axial Ratio:

The axial ratio (AR) at 28 GHz is below 2 dB, as shown in Figure 2-21, meeting the design requirement for circular polarization quality and indicating minimal polarization distortion.

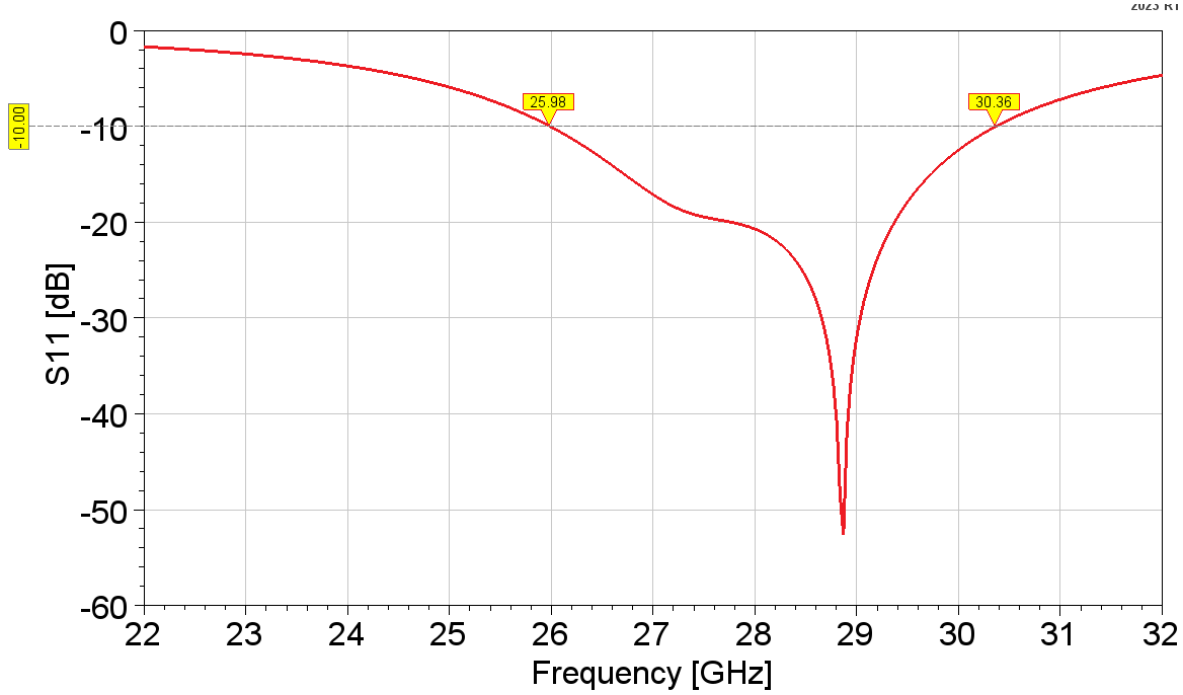

Figure 2-18 Single Antenna Element Reflection coefficient

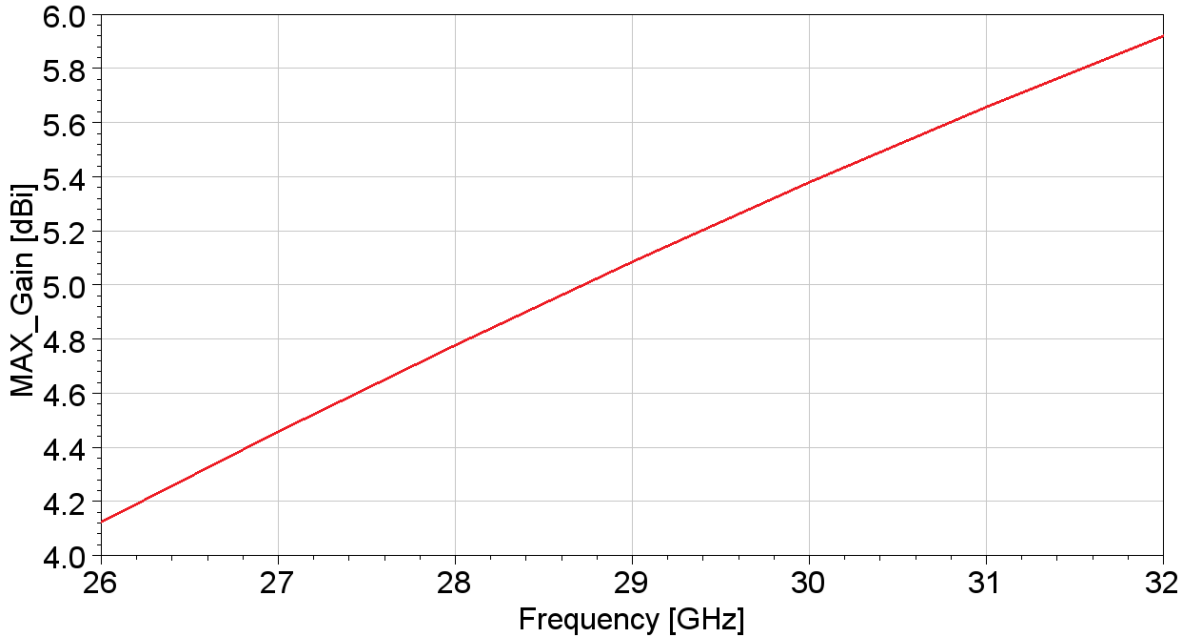

Figure 2-19 Single Antenna Element max Gain per Frequency

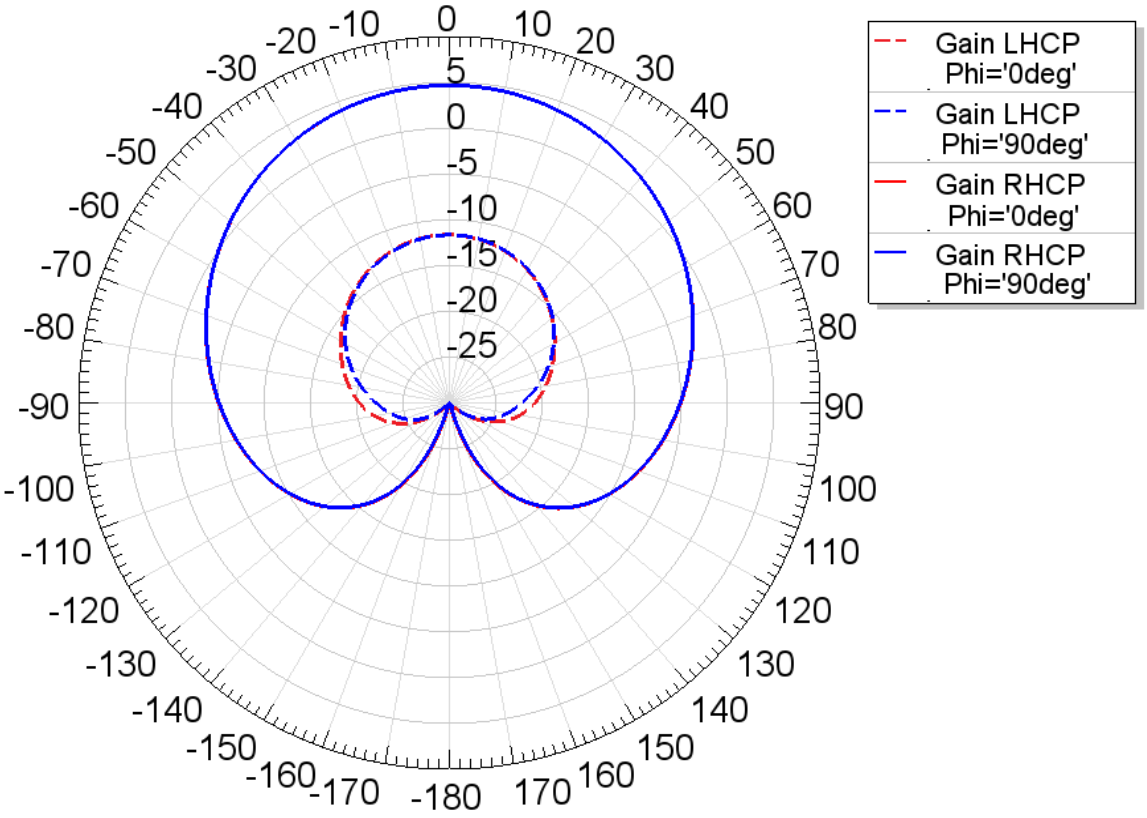

Figure 2-20 Single Antenna Element Radiation Pattern (RHCP and LHCP components) at 28GHz

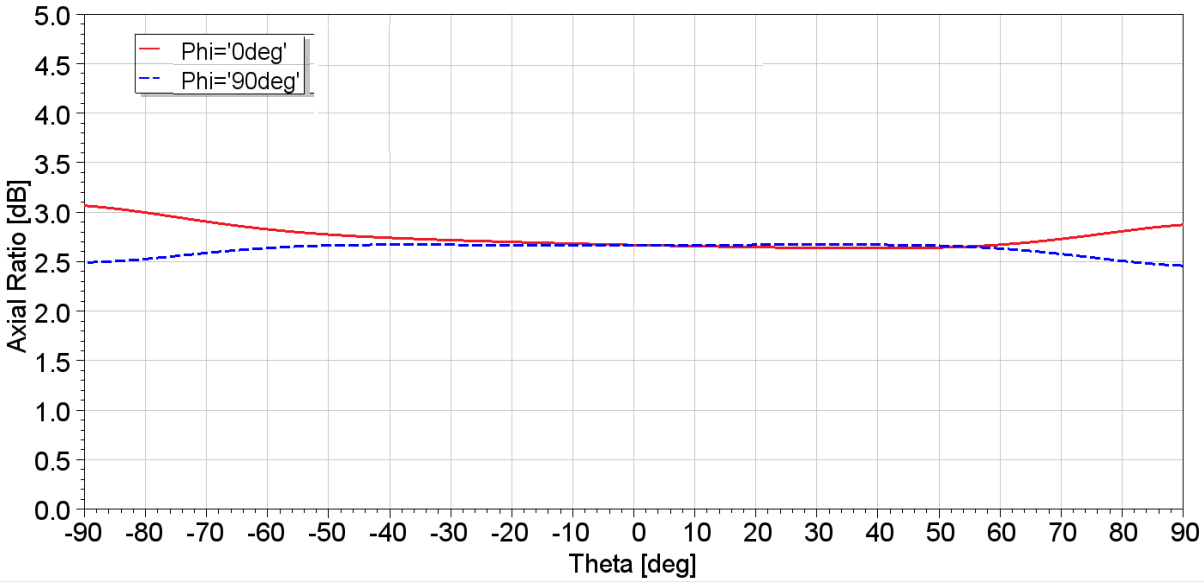

Figure 2-21 Single Antenna Element Axial Ratio at 28GHz

2.2.4.2 Array design

This is the “single element” design scenario. It includes a single periodically repeated element all over the array geometry (Figure 2-22). The main advantage of this array is that the distance between repeated, autonomous phase elements is equal and below λ/2 at 28GHz, meeting the theoretical requirement to reduce grating lobes of the array antenna. A disadvantage of design case is that independent feeding point is required for every element, increasing feeding layer complexity (chip controllers, power splitters, feeding lines etc.). Another disadvantage is the limited CP performance (polarization purity) in the operating frequency bandwidth.

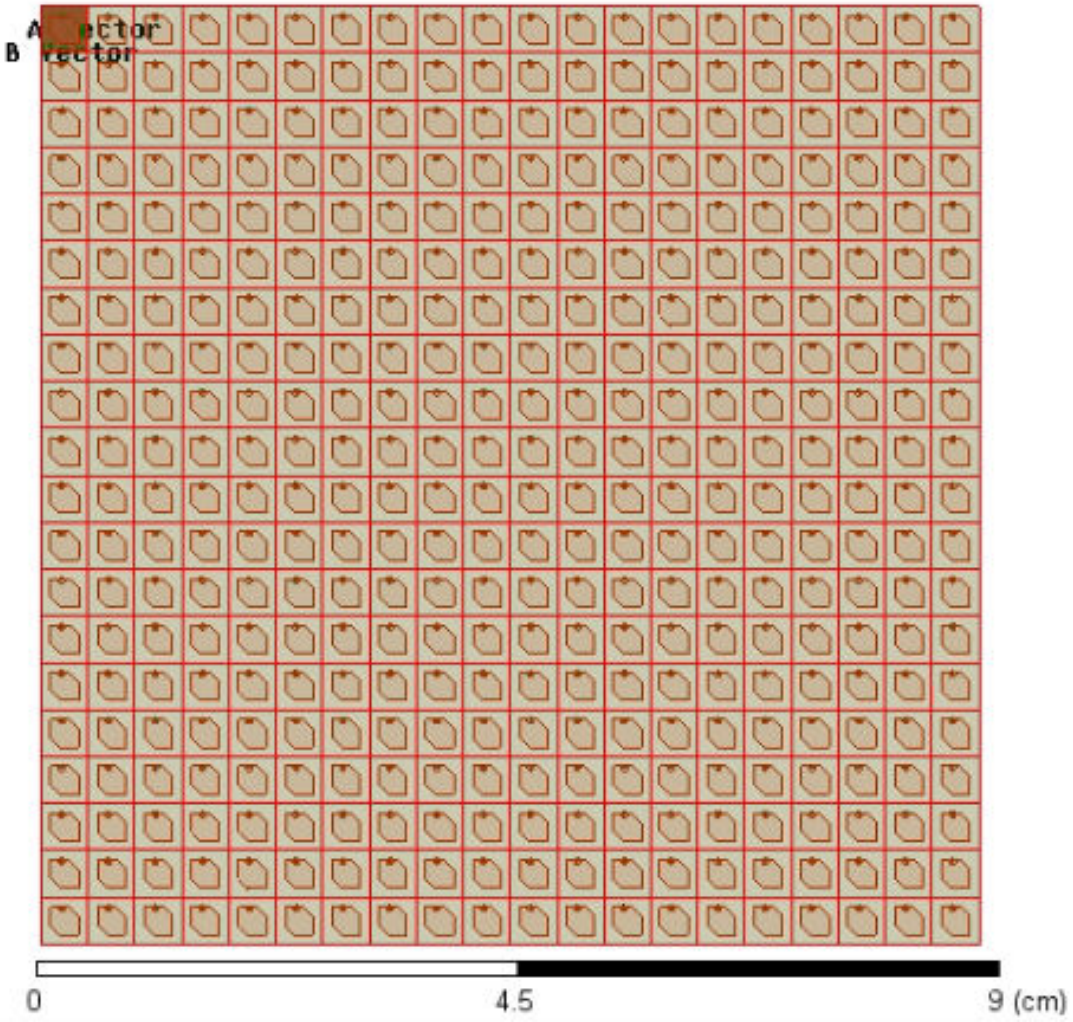

Figure 2-22 Large array 20 X 20 elements (“single element design scenario”)

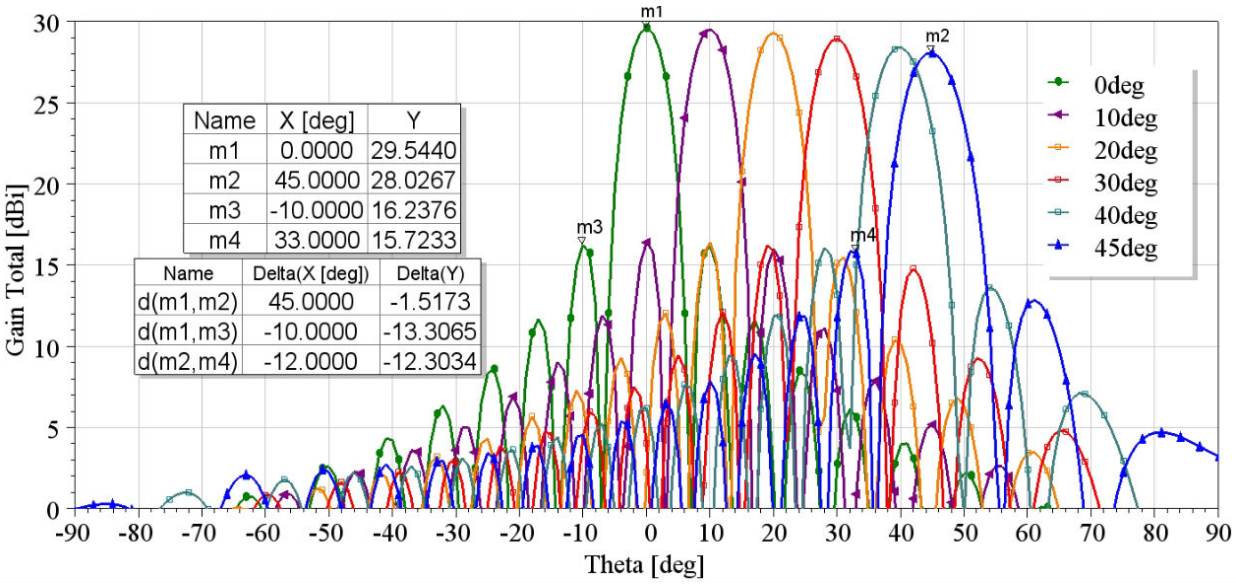

Figure 2-23 Beam steering performance of 20x20 phased array antenna at 28GHz at plane XZ (phi=0deg) with equal element amplitude distribution

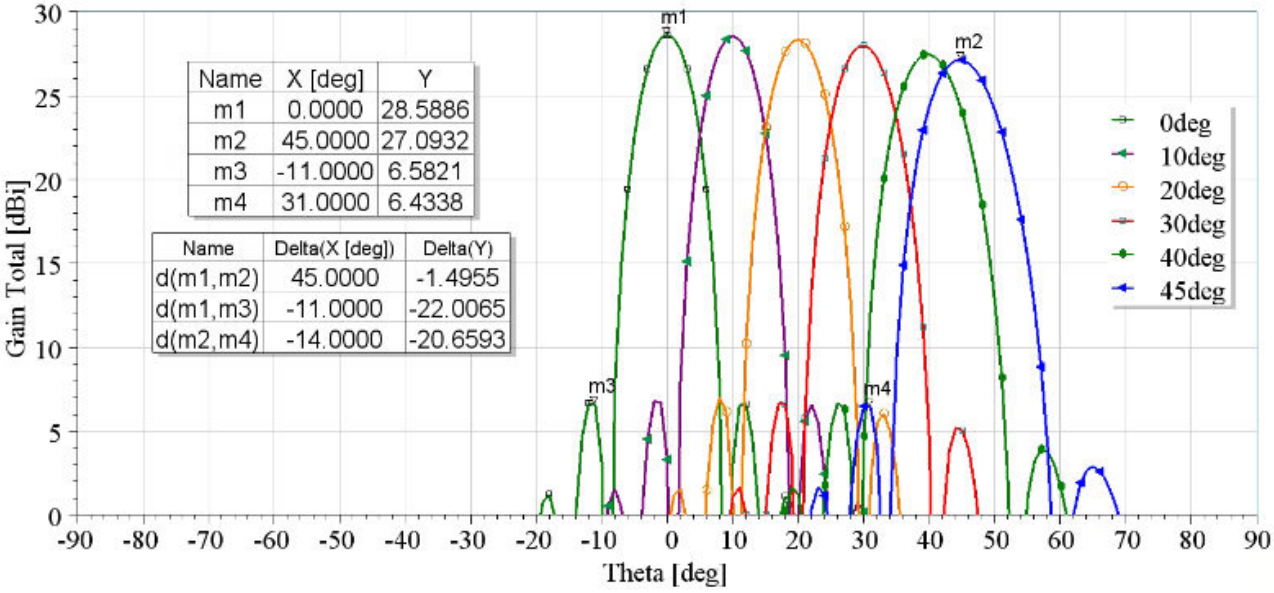

Figure 2-24 Beam steering performance of 20x20 phased array antenna at 28GHz at plane XZ (phi=0deg) with Gaussian element amplitude taper distribution

The beam-steering performance of the large antenna phased array is depicted in Figure 2-23, Figure 2-24. The simulated radiation results are for different element amplitude distributions, for theta steer angles between 0deg-45deg. The Gaussian amplitude distribution yields enhanced performance in terms of side lobes with slightly reduced maximum gain. The scan loss is slightly improved as well and is equal to 1.49dB. The results yielded for the beam steering performance are very good. The axial ratio for the Gaussian amplitude distribution for the examined steered angles are shown in Figure 2-25. The Axial ratio is below 3dB up to 30deg steer angles, yielding circular polarization purity. The beam steer angles of 40deg and 45deg are between 3-6dB, yielding acceptable circular to elliptical polarization performance.

.

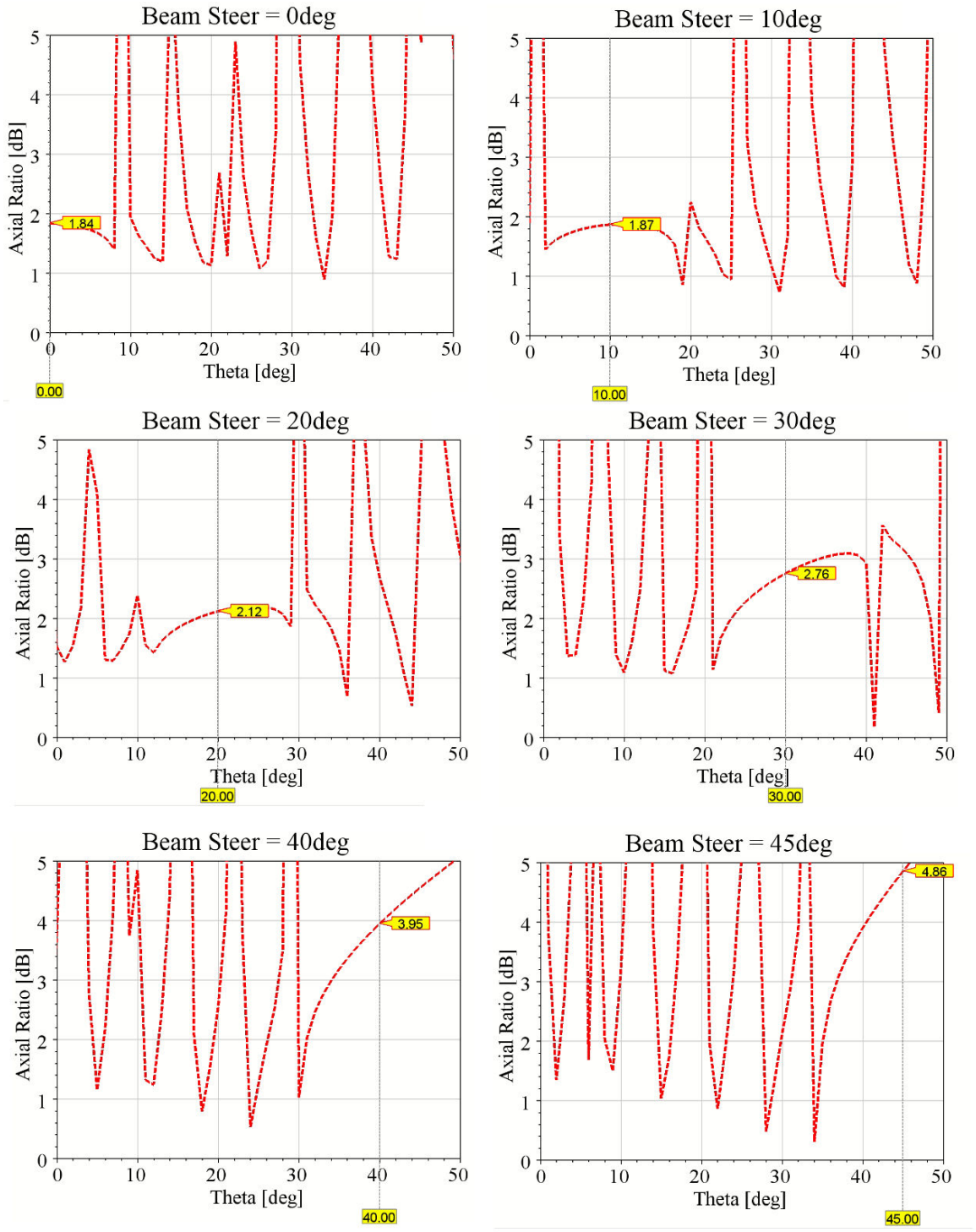

Figure 2-25 Axial ratio performance of 20x20 phased array antenna at 28GHz at plane XZ (phi=0deg) with Gaussian element amplitude taper distribution for examined beam steered angles (0deg, 10deg, 20deg, 30deg, 40deg, 45deg).

2.2.4.3 Case study: 8x8 element array

As a proof of concept, the 8x8 “single element” design concept array is simulated. The array geometry is shown in Figure 2-26. The larger dimension of the array is lower than 4cm, making it quite compact. The required computational resources and analysis time to complete the electromagnetic simulations are match smaller and more manageable than those required for the 20 X 20 design. On the other hand, the conclusions drawn from the simulations can be projected from the 8X8 to the 20X20 array as the basic element is the same. This design although, as expected, has a much lower gain than the corresponding one with the 20X20 elements, presented above, was used to study other performance parameters such as the impedance matching of the antenna, the bandwidth and the characteristics of the polarization regarding the frequency bandwidth and the scanning angular range. However, it should be taken into consideration that the scanning range and performance can be reduced in the case of using less elements by increasing scan loss and side lobe levels.

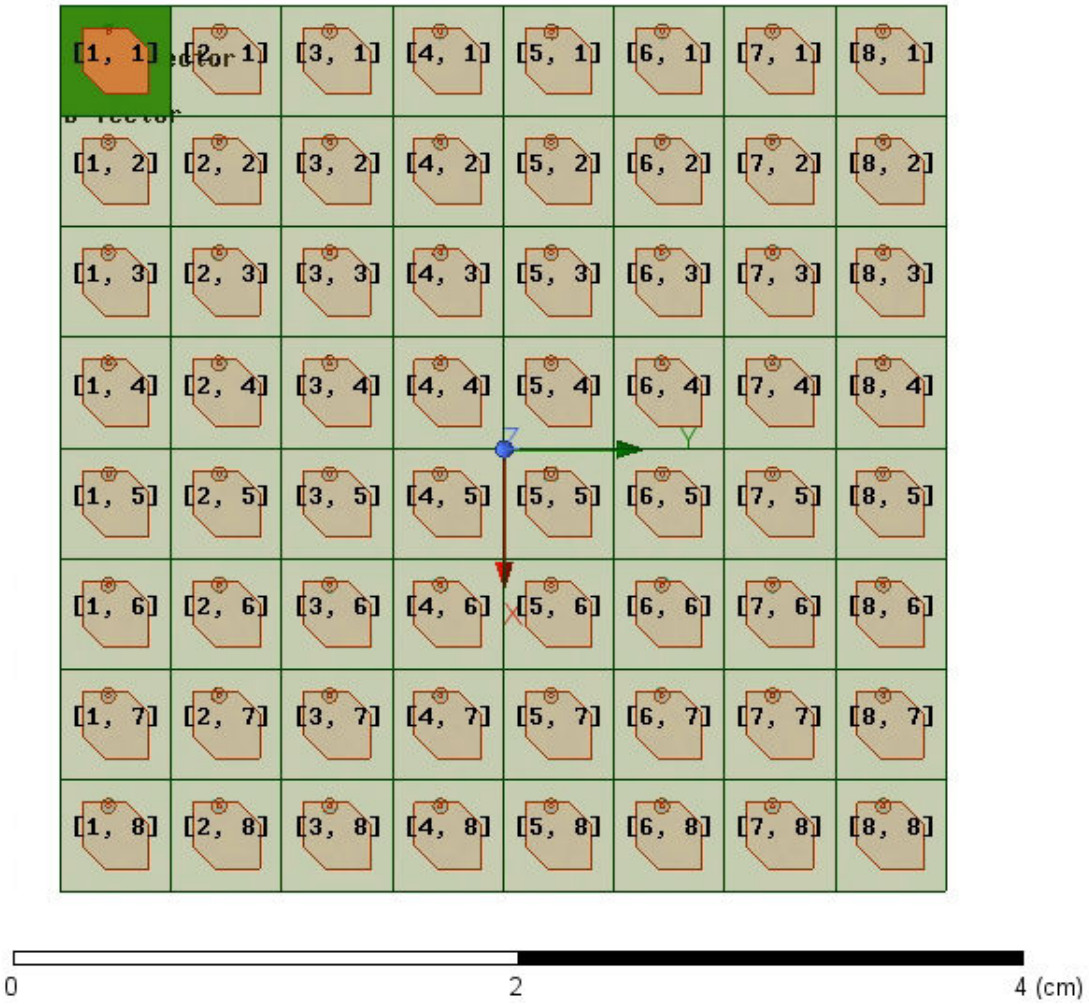

Figure 2-26 Proof of concept array 8 X 8 elements (“single element” design concept)

The results of the RF performance analysis of the 8X8 array are presented in the following (Figure 2-27 to Figure 2-31).

S-Parameter Evaluation:

The simulated S-parameters (Figure 2-27) confirm that the array maintains S11 values below –10 dB, indicating good matching. Mutual coupling (Figure 2-28) among elements is also kept low, supporting effective beamforming capabilities.

Gain and Polarization Performance:

The array achieves high gain and maintains acceptable axial ratio at 28 GHz. This demonstrates the successful upscaling from a single element while retaining polarization quality and gain performance as can be seen in Figure 2-29.

Frequency Response:

The array shows consistent gain performance across frequency, with a peak of 21.55 dBi at 28 GHz. This further validates the radiating structure's suitability for wideband phased array applications.

Beam steering:

The beam steering capability of flat element magnitude taper distribution is shown in, Figure 2-30 for phi=0deg and theta=0deg to 45deg) with scan loss of 1.7dB and acceptable to low SLL without any grating lobe showing up. The co-phased array yields an excellent beam steering ability (Figure 2-31) when the element amplitude taper is simulated as Gaussian where the scan loss is decreased at 1.49 dB and the worst SLL at 45deg theta angle is improved by 7dB compared to the same amplitude distribution. Additionally, from Figure 2-31 it can be noticed and validated the assumption that the less elements yield deteriorated performance compared with the 400 elements in terms of scanning angle range and SLL where it is decreased by 3dB.

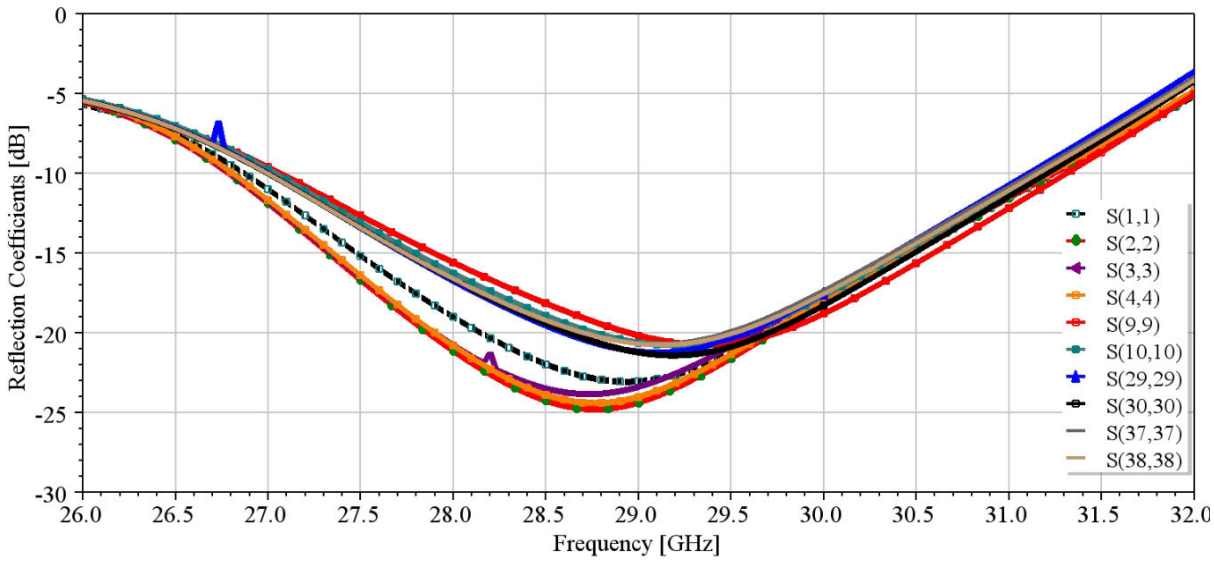

Figure 2-27 Simulated Reflection Coefficient S-parameters of 8x8 single element array

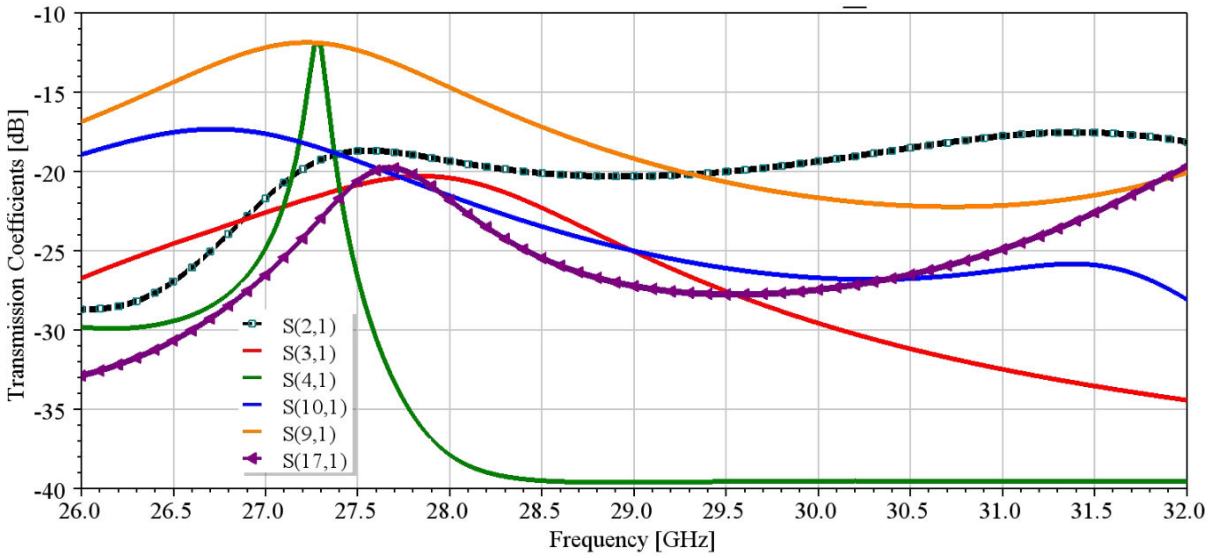

Figure 2-28 Simulated Transmission Coefficient S-parameters of 8x8 single element array

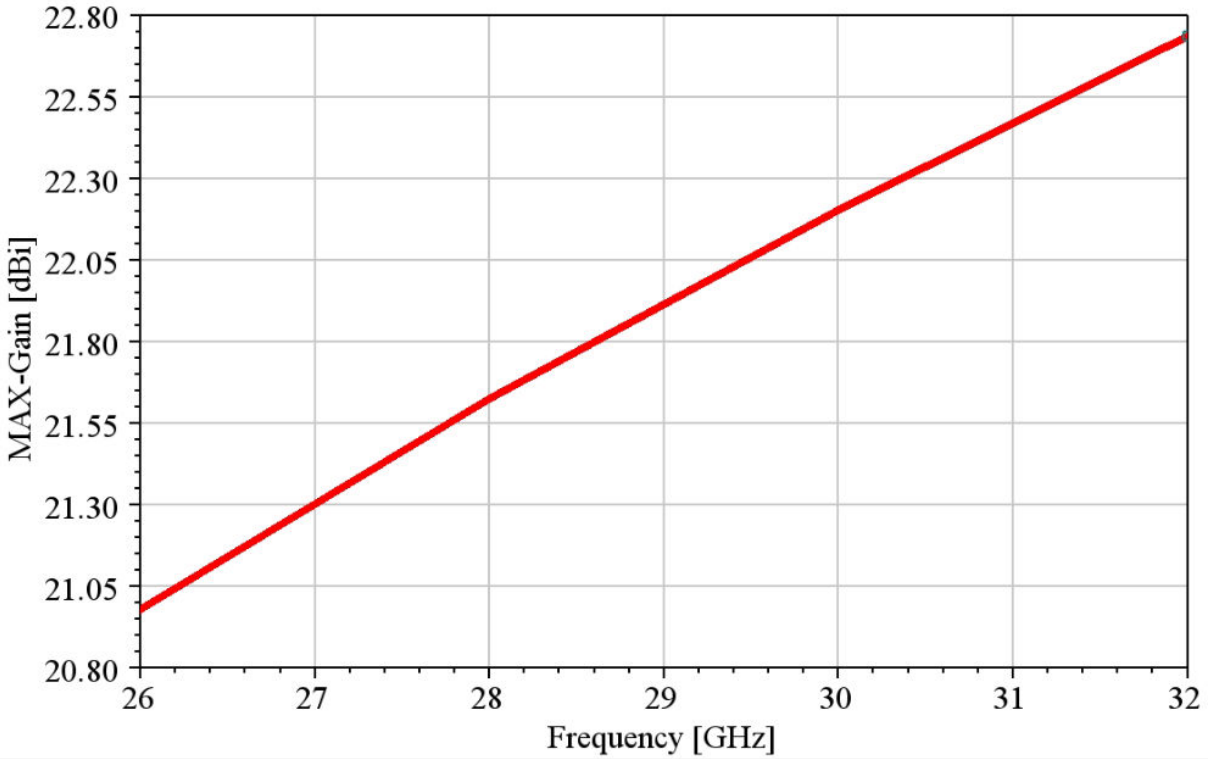

Figure 2-29 Simulated maximum antenna Gain vs. frequency

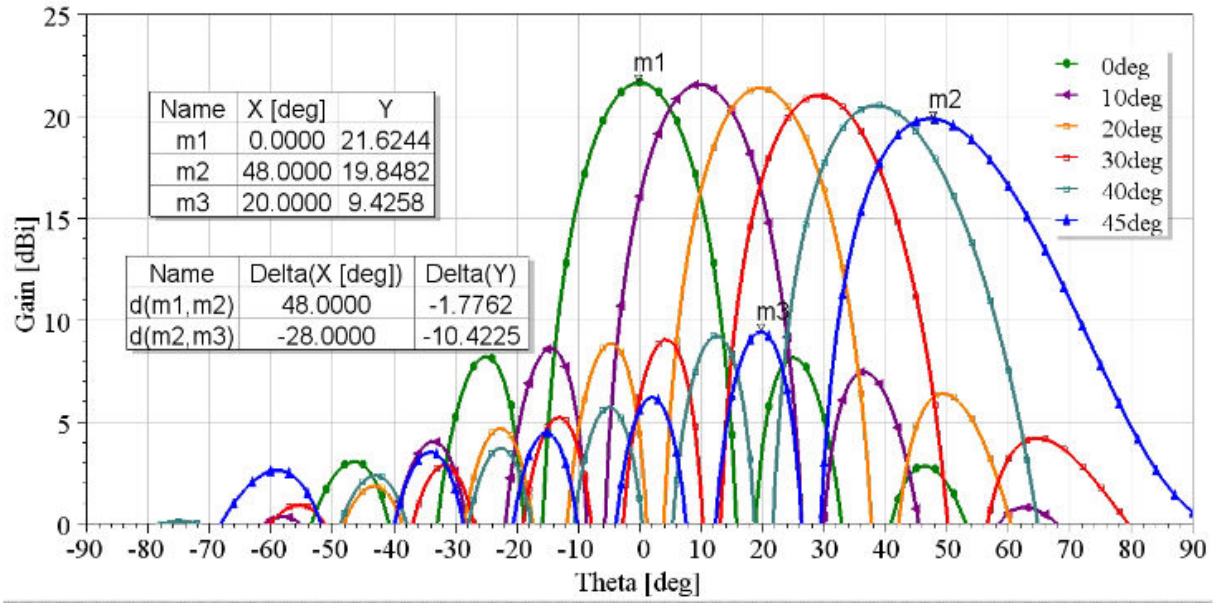

Figure 2-30 Beam steering performance of 8x8 phased array antenna at 28GHz at plane XZ (phi=0deg) with flat element amplitude taper distribution

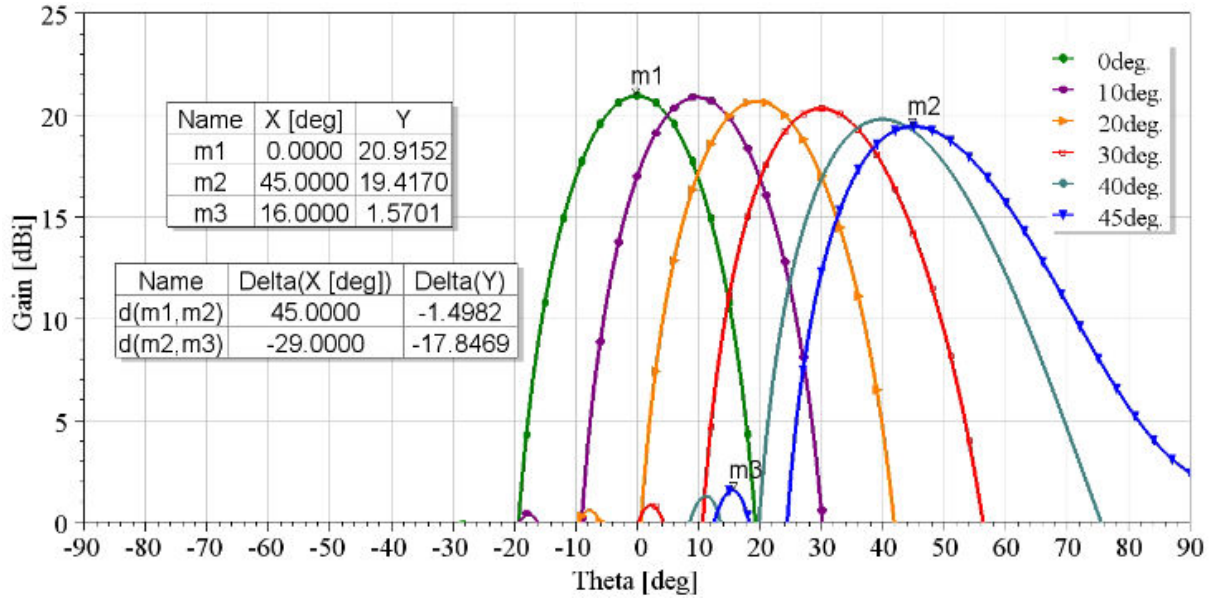

Figure 2-31 Beam steering performance of co-phase 8x8 phased array antenna at 28GHz at plane XZ (phi=0deg) with Gaussian element amplitude taper distribution

2.2.5 Array Antenna design concepts for prototyping

From the previous analysis it can be followed that by utilizing the array element design presented above and developing an array of 20X20 elements, an array antenna that meets the requirements of our application can be successfully designed. Within the framework of the project, we intend to prove the basic performance characteristics of the proposed antenna array through measurements. As already mentioned, this specific design concept, despite its very good RF performance, presents a very high level of complexity in the feeding network even in the downsized version of 8X8 elements. For this reason and with the aim of implementing an antenna experimental prototype (Demo-design) that can be used to prove through measurements the feasibility of implementing a phased array antenna satisfying the ETHER terminal antenna requirements, we have examined two design options: Demo-design concept-1 and concept-2.

The first design concept will basically use the array element presented above, but the array is practically formed by using groups of four such elements (use of 4-elements sub-array).

The second design concept will use the same array element used for the proposed 20X20 array to form an array with match smaller number of elements (i.e. 4X4 elements).

In order to select between the above designs the one that we will use for the antenna prototyping we made sure that the two designs had the same dimensions (same gain) and used the same number of feeding points.

2.2.5.1 Concept-1: Array antenna design based on Sub-array for sequential phase rotation

The initial design had to be modified to use the four-elements sub-array instead of the proposed single element. This design scenario proposes an array to be developed by using a sub-array assembled by four-unit cell patches. The sub-array is composed of 2x2 elements (patches), which are sequentially 90deg-step rotated in terms of both spatial element orientation and phase of element RF-excitation. Sequential rotation has been proved to be a technique that can significantly enhance the AR bandwidth and CP purity, while improving the pattern symmetry of the array. Hence, this sub-array is similar to the element that has been periodically copied to form the large array. Main advantage of this scenario is the polarization purity over the large bandwidth (26-32GHz). Another advantage is the requirement of less feeding points considering the same number of elements, as long as one feeding is required per sub-array (per four elements). A drawback is the significant increased grating lobes in beam steering angles, due to the increment of the distance between the array elements (sub-arrays) which is larger than λ/2.

Sub-array performance

The sub-array consists of multiple single elements arranged to form a radiating unit. Figure *2-32* presents the design layout, which serves as a fundamental building block for full-array construction.

S-Parameter Evaluation:

The simulated S-parameters (Figure 2-33) confirm that the sub-array maintains S11 values below –10 dB, indicating good matching. Mutual coupling among elements is also kept low, supporting effective beamforming capabilities.

Gain and Polarization Performance:

The sub-array achieves high gain and maintains a low axial ratio at 28 GHz, as seen in Figure 2-34. This demonstrates the successful upscaling from a single element while retaining polarization quality and gain performance.

Frequency Response:

The sub-array shows consistent gain performance across frequency band (Figure 2-35), with a center peak at the design frequency of 29 GHz. This further validates the radiating structure's suitability for wideband phased array applications.

Radiation performance:

In Figure 2-36 the radiation patterns of the sub-array antenna yields broadside radiation with medium Gain of 10dBi approximately and effective discrimination between co-polar and cross-polar components validating the CP purity.

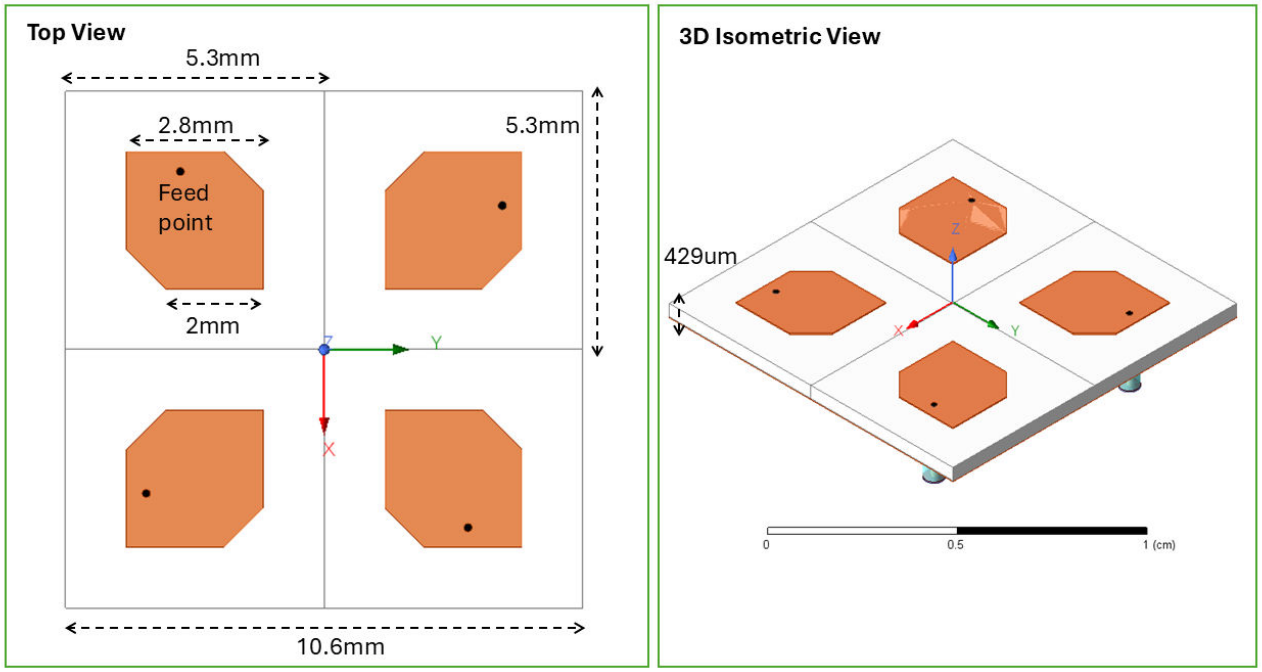

Figure 2-32 Sub-array design geometry

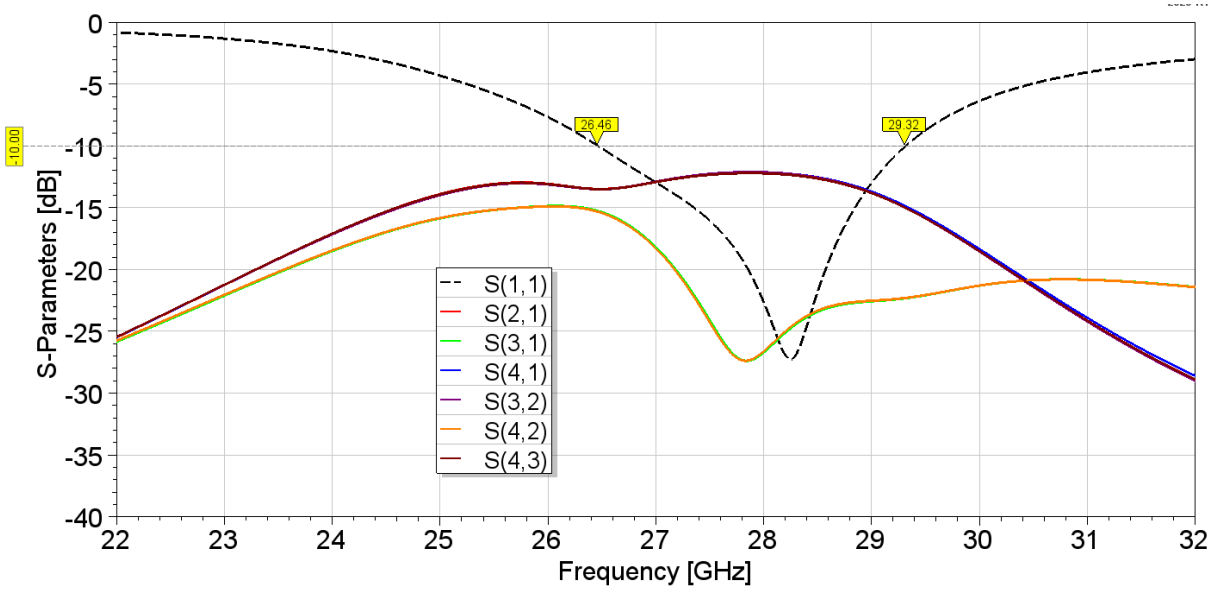

Figure 2-33 Sub-array S-parameters performance

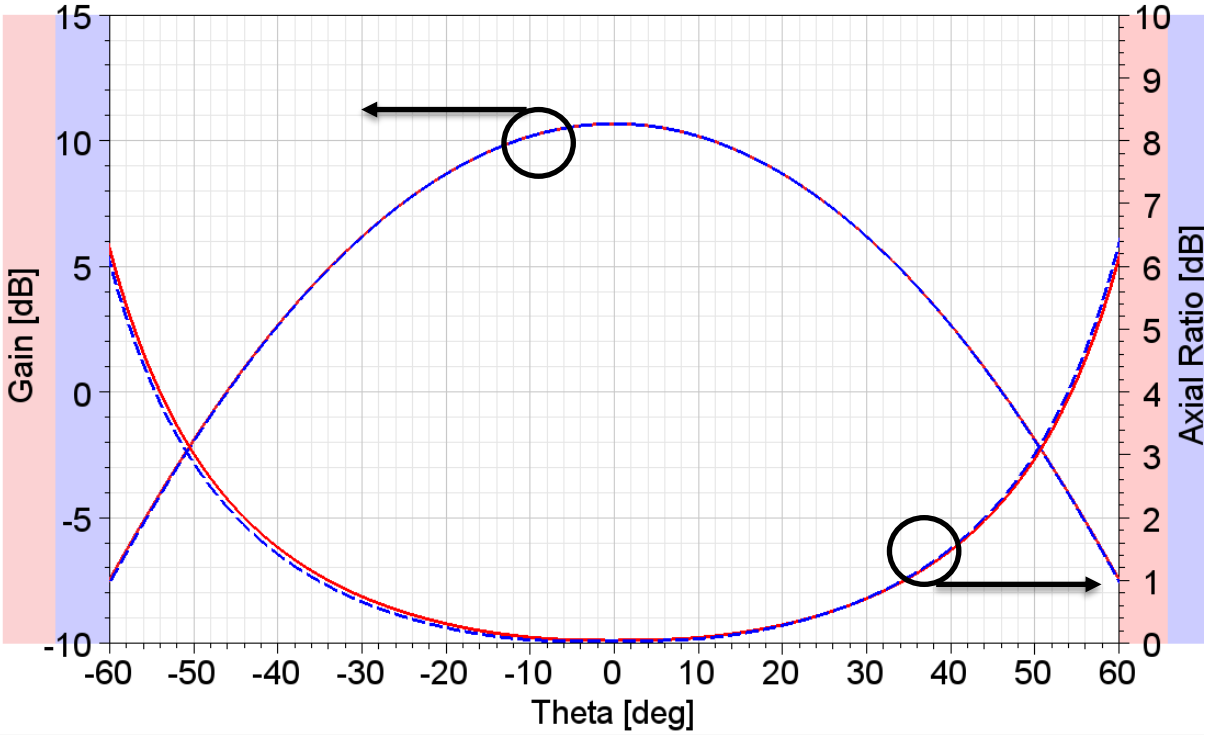

Figure 2-34 Sub-array Gain and Axial Ratio performance at 28GHz (phi=0deg-red, phi=90deg-blue)

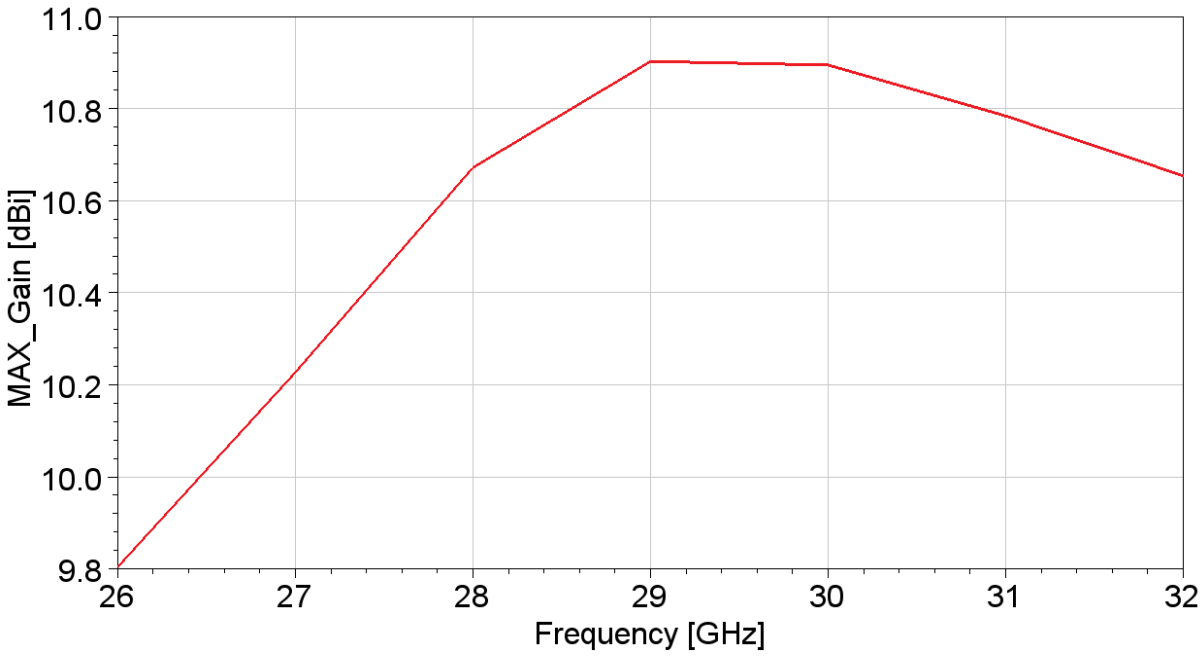

Figure 2-35 Sub-array Antenna Element max Gain per Frequency

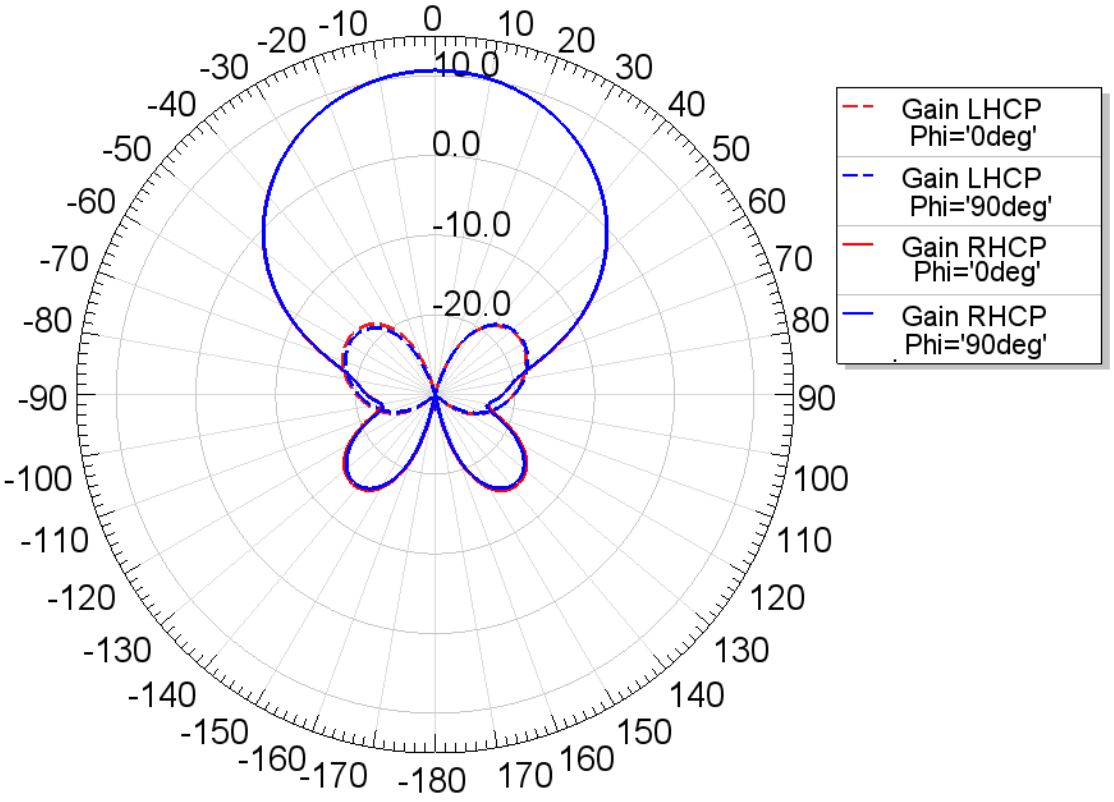

Figure 2-36 Radiation patterns of co and x-polar circular polarization components of sub-array at 28GHz

Sub-array feeding network

The sub-array feeding network can be implemented in multilayer structures using various techniques. Power dividers and phase shifters can be realized using cylindrical conductive posts, SIW (substrate integrated waveguide) delay lines, and stripline configurations to achieve compact and efficient beamforming functionality. After thorough investigation, via simulations and considering physical limitations and fabrication complexity, we have adopted the use of striplines. To implement the desired 90° phase shift in a 2×2 sequentially rotated antenna sub-array, we employ stripline transmission lines with precision-engineered meander paths of varying lengths. This approach provides accurate phase control while ensuring electromagnetic isolation, compactness, and minimal radiation loss in dense RF front-end environments. Stripline technology is chosen over microstrip for its superior shielding characteristics and consistent propagation environment. In a stripline configuration, the signal conductor is sandwiched between two ground planes within a homogeneous dielectric substrate. This symmetric structure offers reduced susceptibility to external interference and suppresses spurious radiation, which is particularly beneficial when routing closely spaced delay lines in phased array architectures. Moreover, the width of striplines, when compared to microstrip lines with the same substrate characteristics, reduce to half, offering significant help to the design of the meander lines.

To achieve the necessary 90° incremental phase shifts across the four elements of the subarray (i.e., 0°, 90°, 180°, and 270°), we implement meandered stripline paths of different electrical lengths. The delay for each path is determined based on the effective dielectric constant ε_{eff} of the stripline and the target operating frequency, f. Given a wavelength $\lambda_g = \frac{c}{f \cdot \sqrt{\varepsilon_{eff}}}$ in the guided medium, a 90° phase shift corresponds to a physical line length difference of $\lambda_g/4$. Accordingly, each arm of the feed network is designed with a progressive multiple of $\lambda_g/4$, implemented through compact meander geometries to conserve substrate area.

The use of meandered stripline paths enables precise phase matching while maintaining a low-profile, planar layout suitable for multilayer integration. By optimizing the spacing and length of each meander line, it is minimized any coupling effect that could degrade the phase accuracy or impedance matching of the feed network. Full-wave electromagnetic simulations (CST Studio Suite) are used to validate the phase performance and power division of each path, ensuring that the sequential feeding mechanism achieves the required circular polarization synthesis in the far-field radiation pattern of the subarray.

Figure 2-37 presents both the top-view and side-view of the designed feeding network. Port #5 serves as the input port and is matched to a 50 Ohm source. The input power is equally split into two branches, each routed through a transmission line with a target characteristic impedance of 25 Ohm, denoted with a length of L_{25}. To ensure proper impedance matching at the junction between the 50 Ohm input line and the two parallel 25 Ohm branches (with present combined impedance of 12.5 Ohm), a quarter wavelength transformer is employed. This transformer is design to be equal to $\lambda_g/4$, which is about $l = 1.384\ mm$ long, and it has width of 0.75mm. At the far end of each L_{25} line, the connection transitions to two parallel 50 Ohm lines. Since the combined parallel impedance of these lines is again 25 Ohm, no additional impedance transformation is required at these junctions. The geometry of all delay lines is illustrated in the Figure below, and the dimensions are given in Table 8.

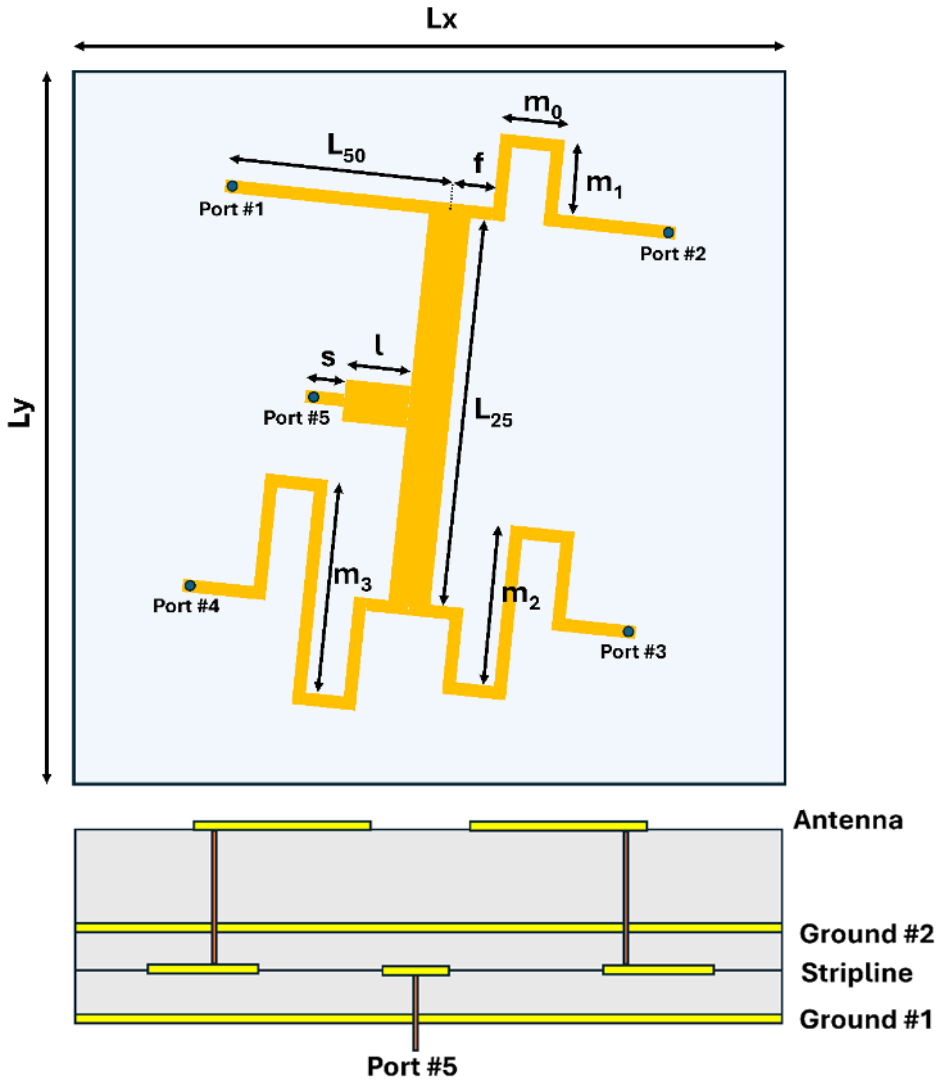

Figure 2-37 Top-view and side-view of the designed feeding network.

From the side view in Figure 2-37, we can see that the stripline is embedded between two ground planes, ground #1 and ground #2, forming a symmetric and shielded transmission structure. Port #5 is positioned on one side of the structure and serves as the input port. On the opposite side, Ports #1 through #4 are coming out from the other side of the structure and are intended for connection to the respective antenna elements in the sub-array.

Table 8 Dimensions of stripline forming the passive sequential phase rotator

Parameter	Value		Parameter	Value
L_x, L_y	10.60 mm		m_1	1.00 mm
L_{25}	6.35 mm		m_2	1.79 mm
L_{50}	6.66 mm		m_3	2.40 mm
m_0	1.00 mm		f, s	0.44 mm

Antenna array design with 20X20 elements

Based on the above-described sub-array element, a 20×20 element array, with overall dimensions of 10.7 cm × 10.7 cm, was also designed to meet the final system specifications. The array achieves a gain of approximately 30 dBi.

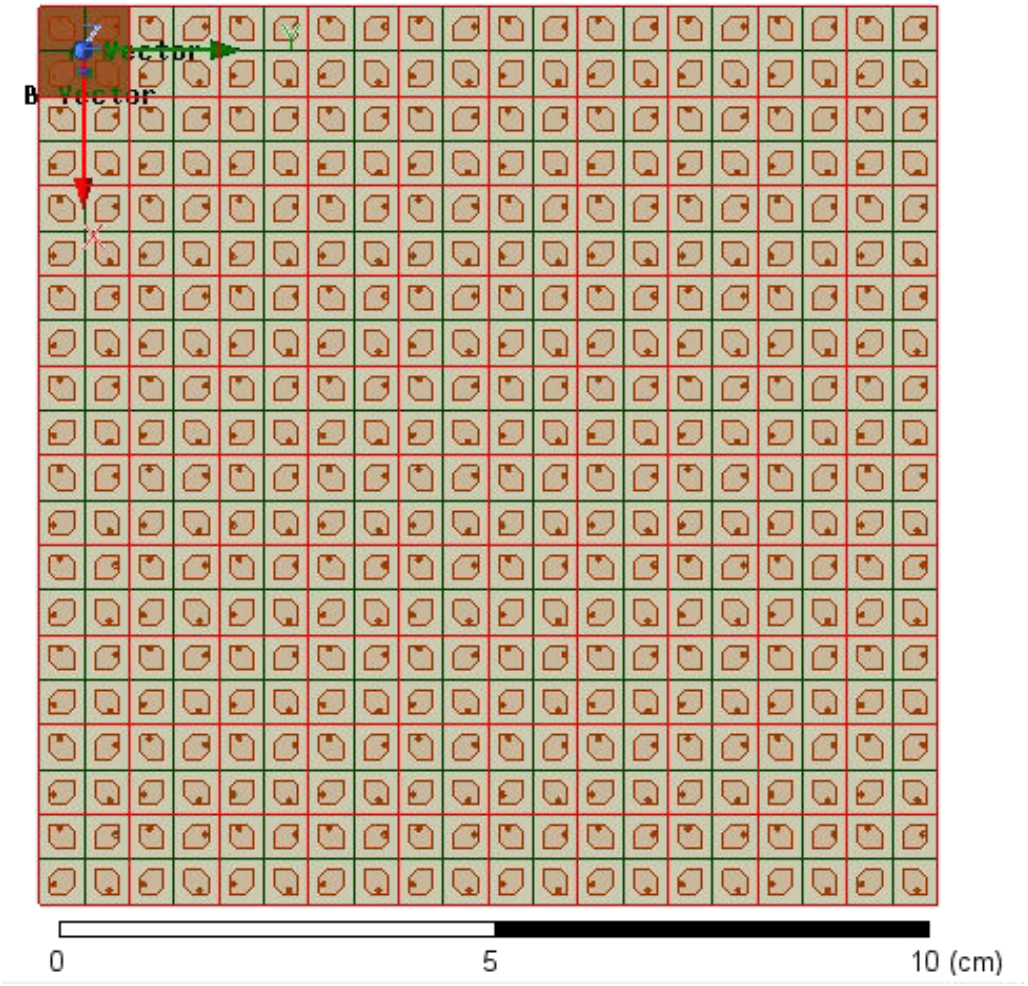

Figure 2-38 20X20 elements array using sub-array design concept

For the analysis of this design concept a downsized 8×8 array with the same sub-array has been used.

Antenna array design with 8X8 elements

An 8×8 element phased array was designed and simulated as a proof-of-concept demonstrator. As shown in Figure 2-39.

Reflection and Transmission Coefficients:

Figure 2-40 and Figure 2-41 present the reflection (Sii) and transmission (Sij) coefficients, forming the S-Parameters table. All diagonal elements remain below –10 dB, indicating effective input matching, while off-diagonal terms remain sufficiently low below -15dB, and confirming minimal mutual coupling between elements.

Gain Performance:

The total gain performance across frequency is presented in Figure 2-42. The array achieves maximum gain near 29 GHz, in line with the expected full-array performance (approx. 30 dBi).

Beam Steering Capabilities:

Figure 2-43 depicts the beam scanning results in the XZ-plane (φ = 0°) at 28 GHz. The element amplitude tapering that has been followed is the Gaussian one as a more effective in terms of providing the lowest possible SLL. Beam steering is effective up to 10deg and barely acceptable at 20deg. Above these angles grating lobe domination is noticed. The non-acceptable steering performance can be seen from the high scan loss of 6dB. To mitigate this specific drawback, the size of the sub-array was reduced by increasing the relative permittivity (ε_r) of the dielectric substrate.

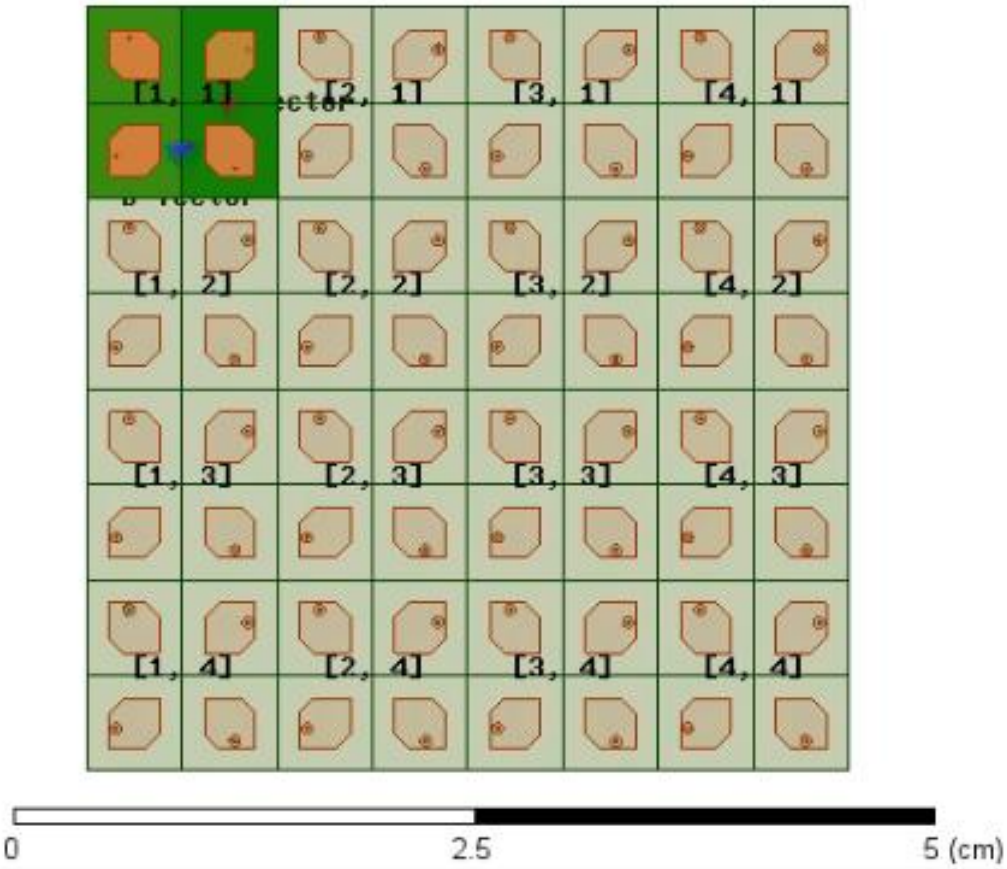

Figure 2-39 8X8 element array formed by the sub-array

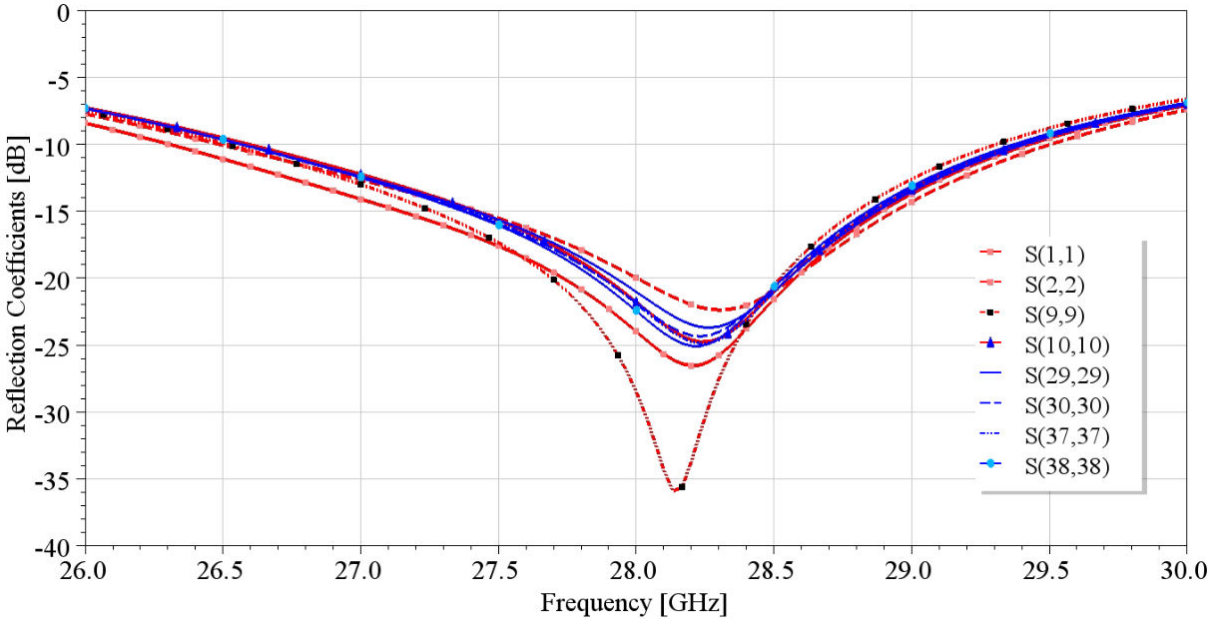

Figure 2-40 Array indicative reflection coefficients S(i,i)

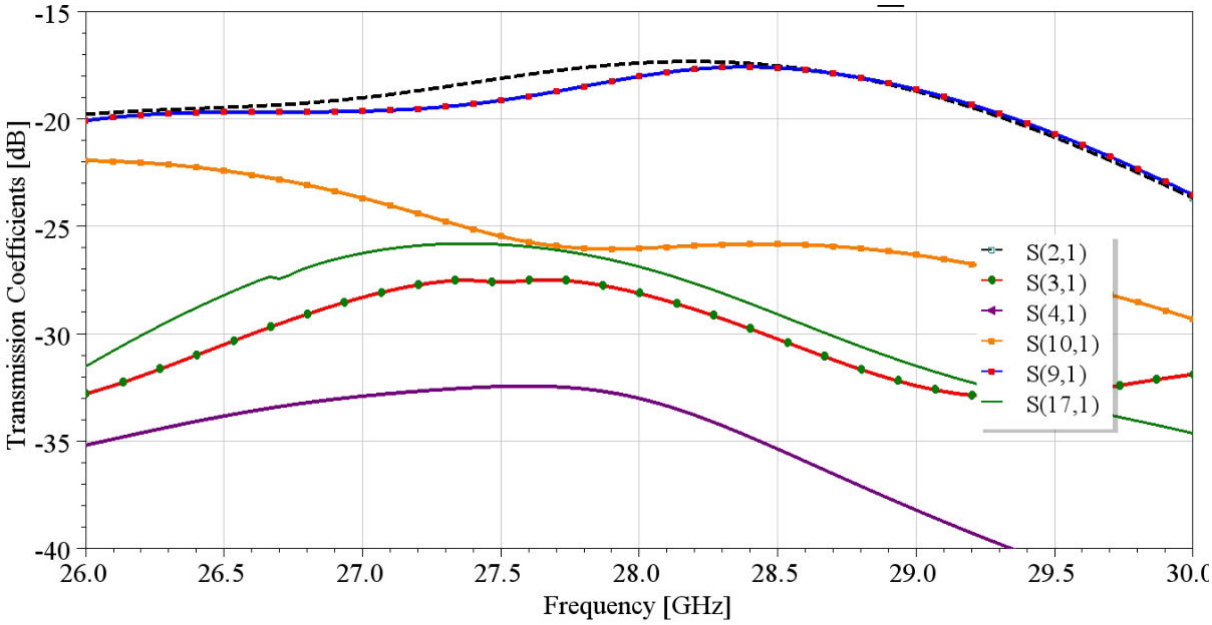

Figure 2-41 Array indicative transmission coefficients S(i,j)

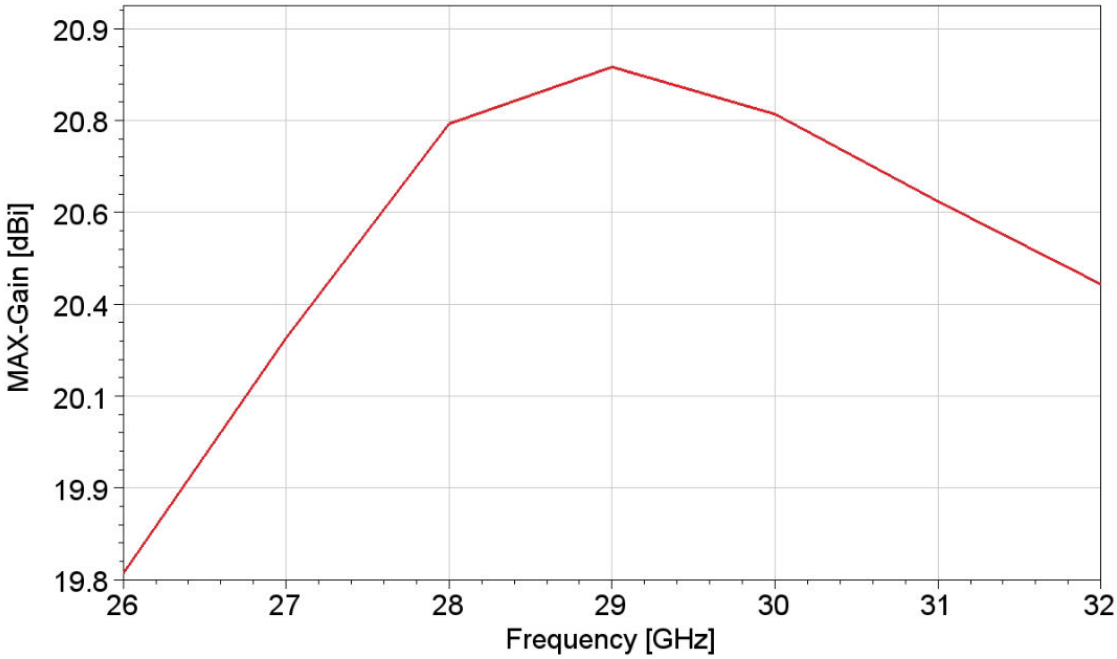

Figure 2-42 Array Antenna total max Gain per Frequency

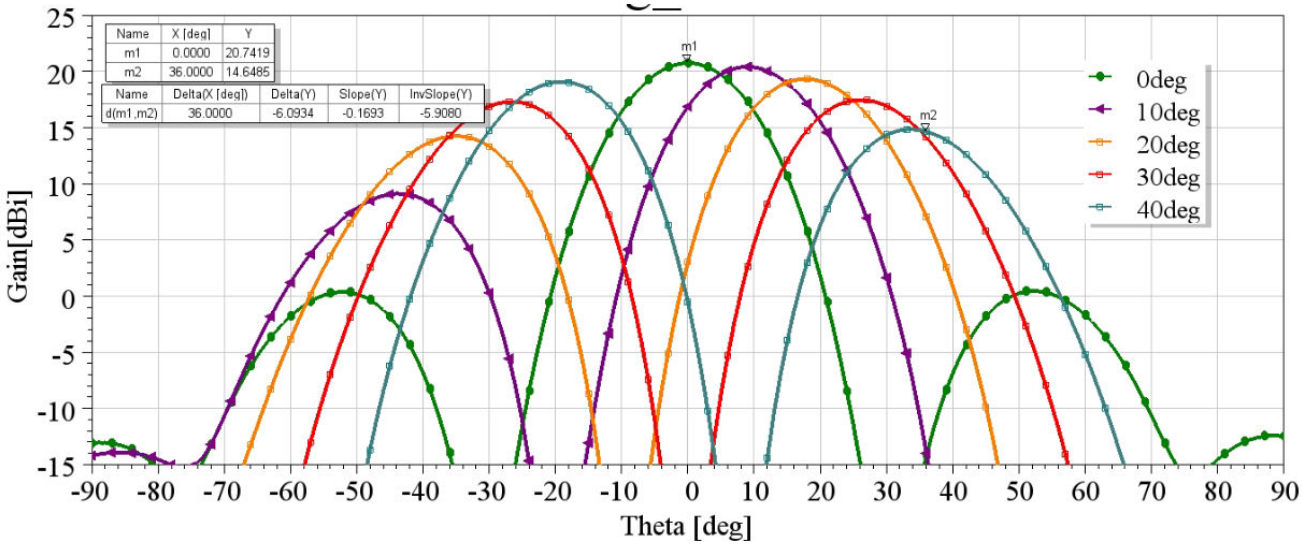

Figure 2-43 Scanning theta angles of array at 28GHz and plane XZ-phi=0°

Reduced size sub-array element

By using a Rogers 3210 substrate with dielectric permittivity (ε_r) equal to 10.2 and appropriately redesign the radiating element, a reduction of almost half the physical size of the sub-array is achieved.

The reduced size sub-array consists of four single elements arranged to form the radiating unit.

Figure 2-44 presents the design layout, which serves as a fundamental building block for full-array construction.

S-Parameter Evaluation:

The simulated S-parameters (Figure 2-45) confirm that the sub-array maintains S11 values below –10 dB, indicating good matching. Mutual coupling among elements is increased as elements came closer, supporting acceptable beamforming capabilities. Still the maximum 6dB mutual coupling is acceptably reduced.

Gain and Polarization Performance:

The sub-array achieves high gain and maintains a low axial ratio at 28 GHz, as seen in Figure 2-46. This demonstrates the successful upscaling from a single element while retaining polarization excellent quality and gain performance.

Frequency Response:

The sub-array shows consistent gain performance across frequency band (Figure 2-47), with a peak gain of 5.8dBi decreased due to physical size limitation, increased dielectric permittivity. This further validates the radiating structure's suitability for wideband phased array applications.

Radiation performance:

In Figure 2-48 the radiation patterns of the sub-array antenna yields broadside radiation with medium gain of 5dBi approximately and effective discrimination between co-polar and cross-polar components confirming the CP purity.

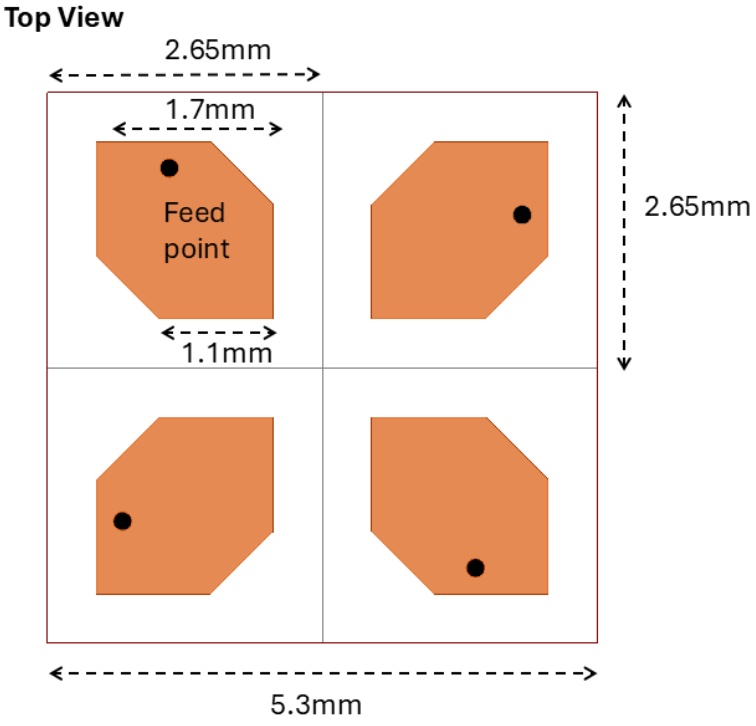

Figure 2-44 Reduced size Sub-array alternative schematic

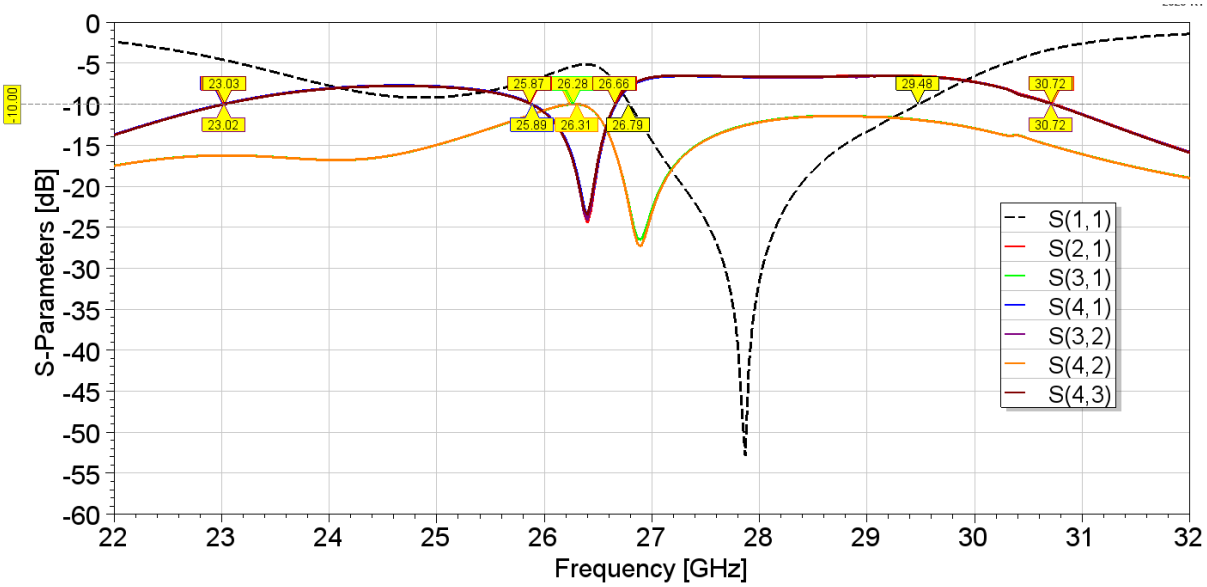

Figure 2-45 S-parameters simulated results of reduced size sub-array

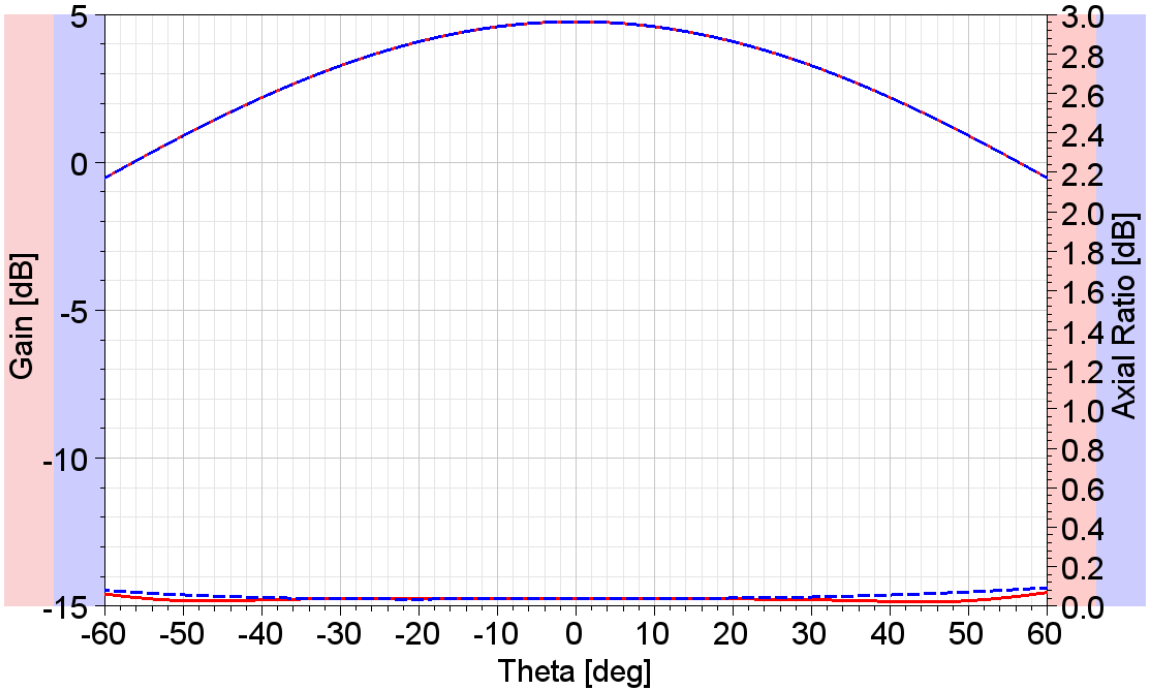

Figure 2-46 Reduced size Sub-array Gain and Axial Ratio performance at 28GHz (phi=0deg-red, phi=90deg-blue)

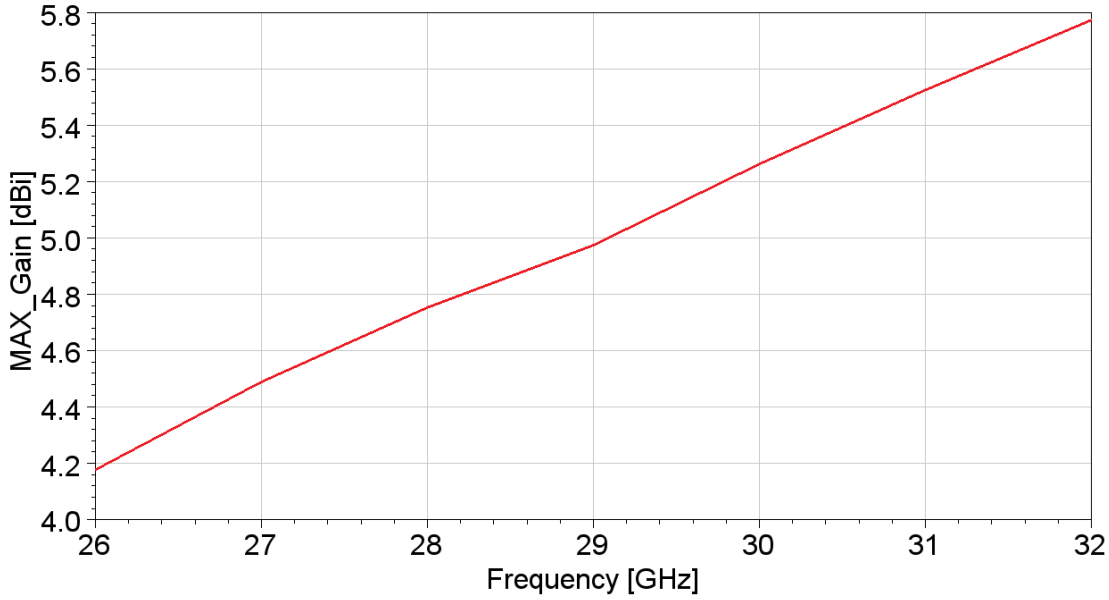

Figure 2-47 Reduced size Sub-array Antenna Element max Gain per Frequency

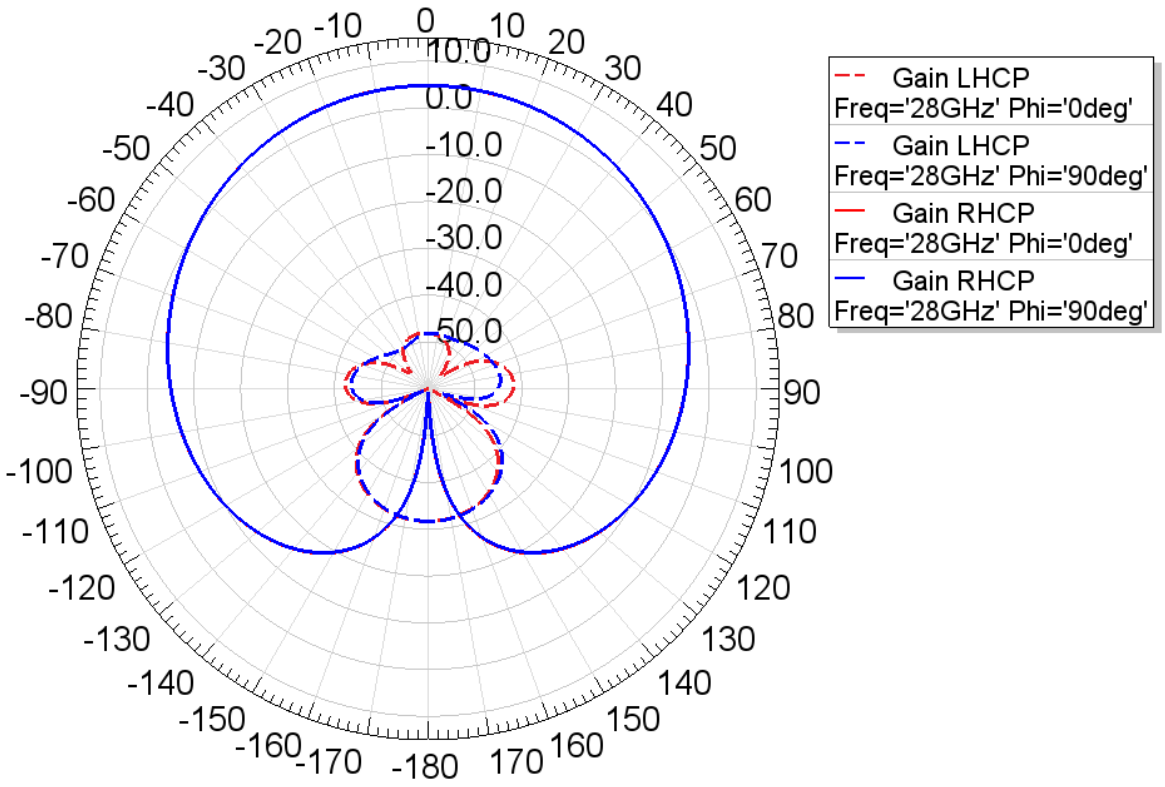

Figure 2-48 Radiation patterns of co and x-polar circular polarization components o reduced sizef sub-array at 28GHz

Antenna array design with 8X8 elements with reduced size sub-array

Based on the reduced size sub-array, it has been developed and analysed by simulation an array of 8X8 elements (Figure 2-49) in which the distances between the sub-arrays have been reduced to approximately λ/2 at 28GHz. This ensures improved grating lobes performance while at the same time making it possible to develop and implement a prototype that can be used to evaluate through measurements the results and conclusions derived from the analysis through simulations of the proposed phased array designs.

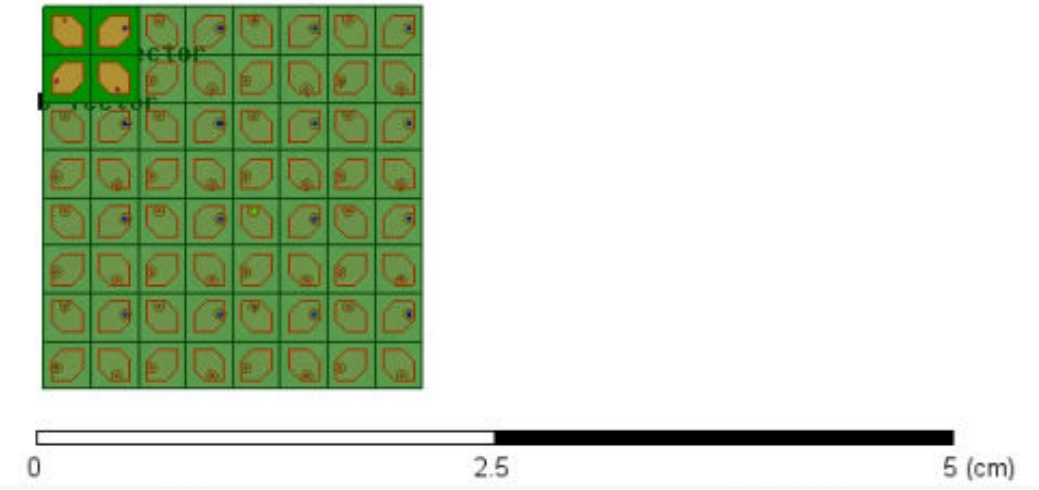

Figure 2-49 8x8 array design with reduced size sub-arrays

The beam steering performance can be seen in Figure *2-50* to Figure 2-52 at 28GHz for 3 main planes (phi=0deg, phi=90deg and phi=45deg). The theta angles that have been examined for the scanning are 0deg up to 40deg. The element amplitude tapering is Gaussian. The scan loss is sufficiently improved from previous 6dB down to 1.8dB. This array performs efficient up to 30deg of scanning and with acceptable performance up to 40deg. Generally, the scanning performance is sufficiently improved and it is summarized in Table 9.

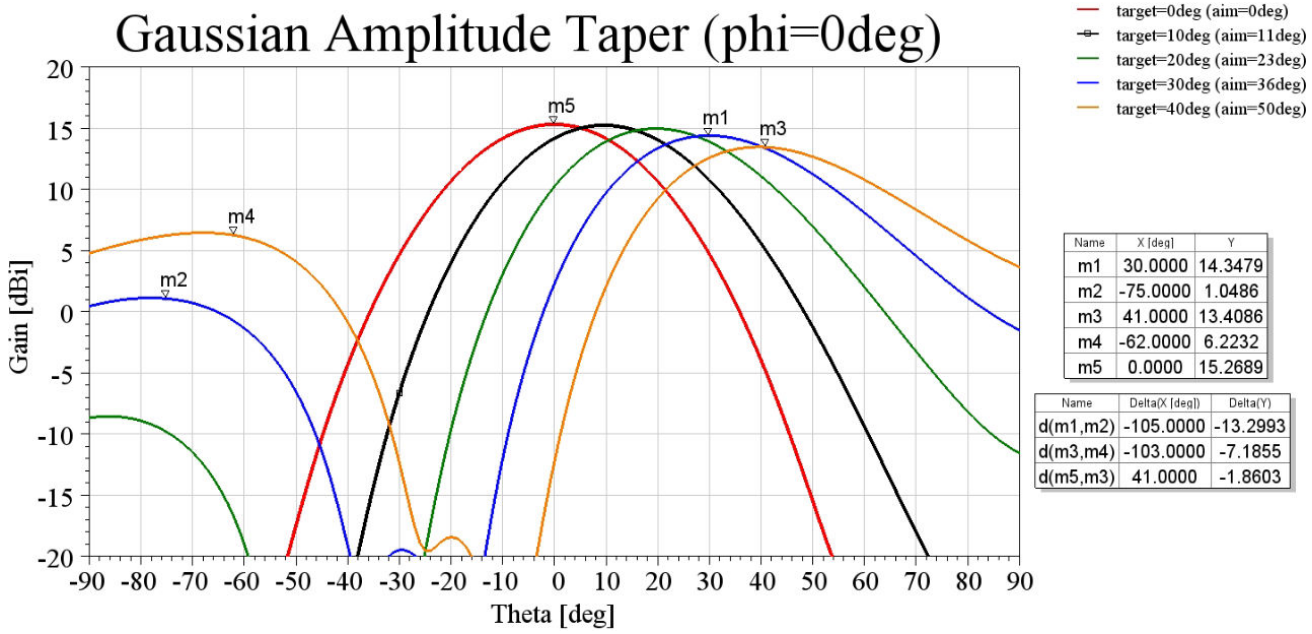

Figure 2-50 Beam steering at 28GHz for plane at phi=0deg

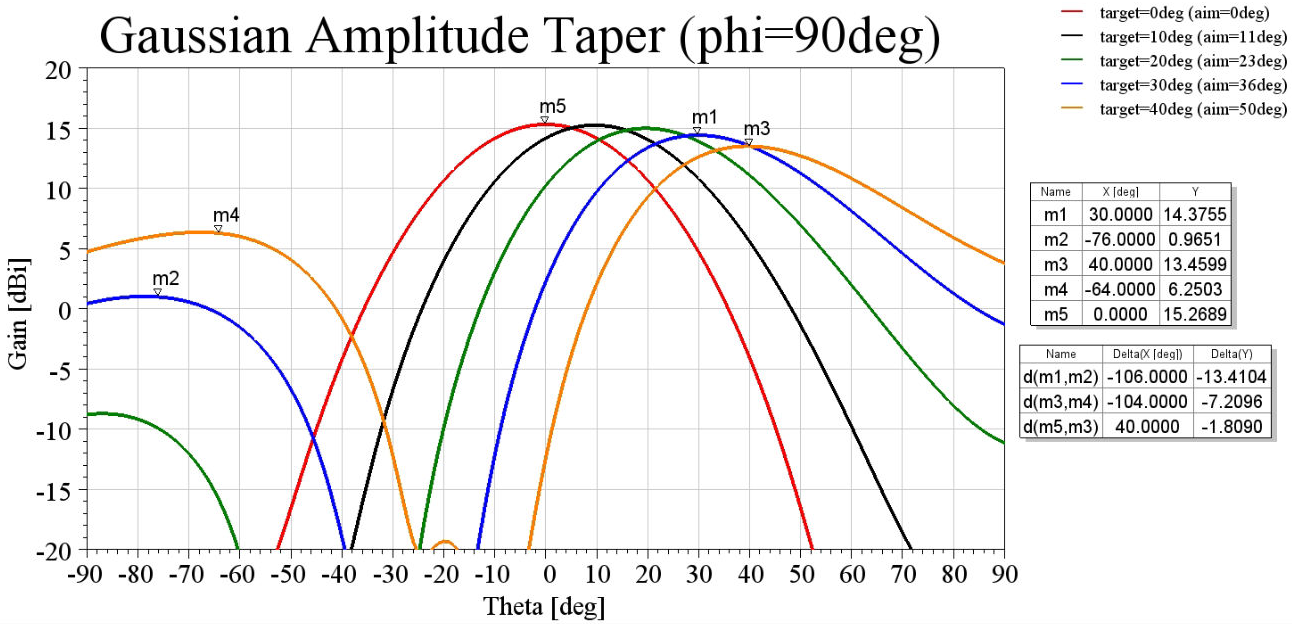

Figure 2-51 Beam steering at 28GHz for plane at phi=90deg

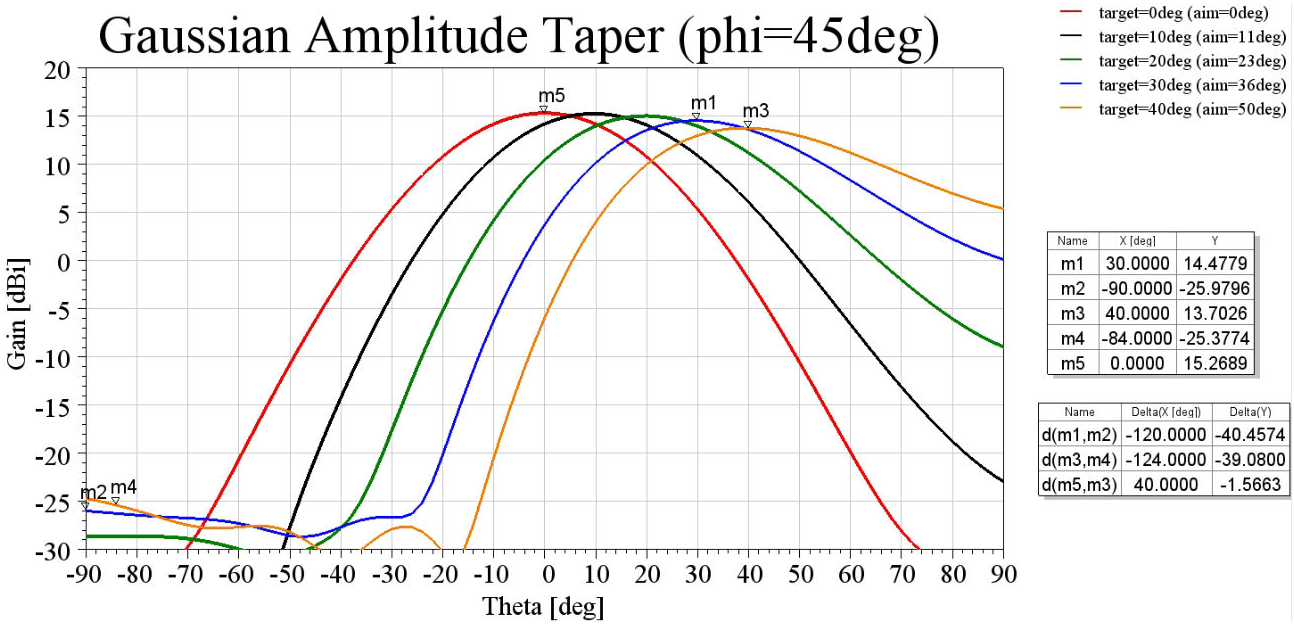

Figure 2-52 Beam steering at 28GHz for plane at phi=45deg

Table 9 Beam steering at 28GHz far field performance parameters

Steer Angle (deg)	Gain (dBi)	SLL (dB)	Scan loss(dB)
0	**15.27**	**31.08**	**1.86**
10	**15.20**	**31.53**	
20	**14.92**	**23.55**	
30	**14.34**	**13.30**	
40	**13.43**	**7.20**	

2.2.5.2 Concept-2: Array antenna design based on single element

In this design, the same array element (Figure 2-22) used for the proposed 20X20 array antenna has been used to form an array with 4X4 elements (Figure *2-53*). The total size of the array is almost the same (18mm x 18mm) as the proposed candidate of Concept-1 design (21.2mm x 21.2mm) (Figure 2-49). Both the arrays have 16 feeding points, the deference is that the Concept-1 array has 4 times larger number of elements than the Concept-2 one (64 vs 16).

The RF performance analysis simulation results regarding beam steering and polarization are presented in Figure 2-54 and Figure 2-55. Comparing the corresponding results of design Concep-1 (Figure *2-50*, Figure 2-51, and Figure 2-52) it is obvious that the Concept-2 array

performance regarding the grading lobes is better than Concept-1 array design. On the other hand, the first design presents better performance regarding the circular polarization.

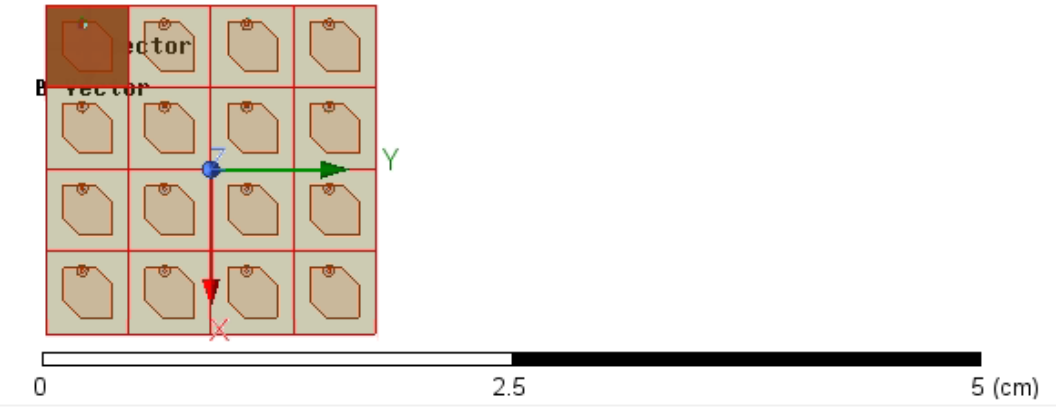

Figure 2-53 4 X 4 array elements (co-phased elements) geometry

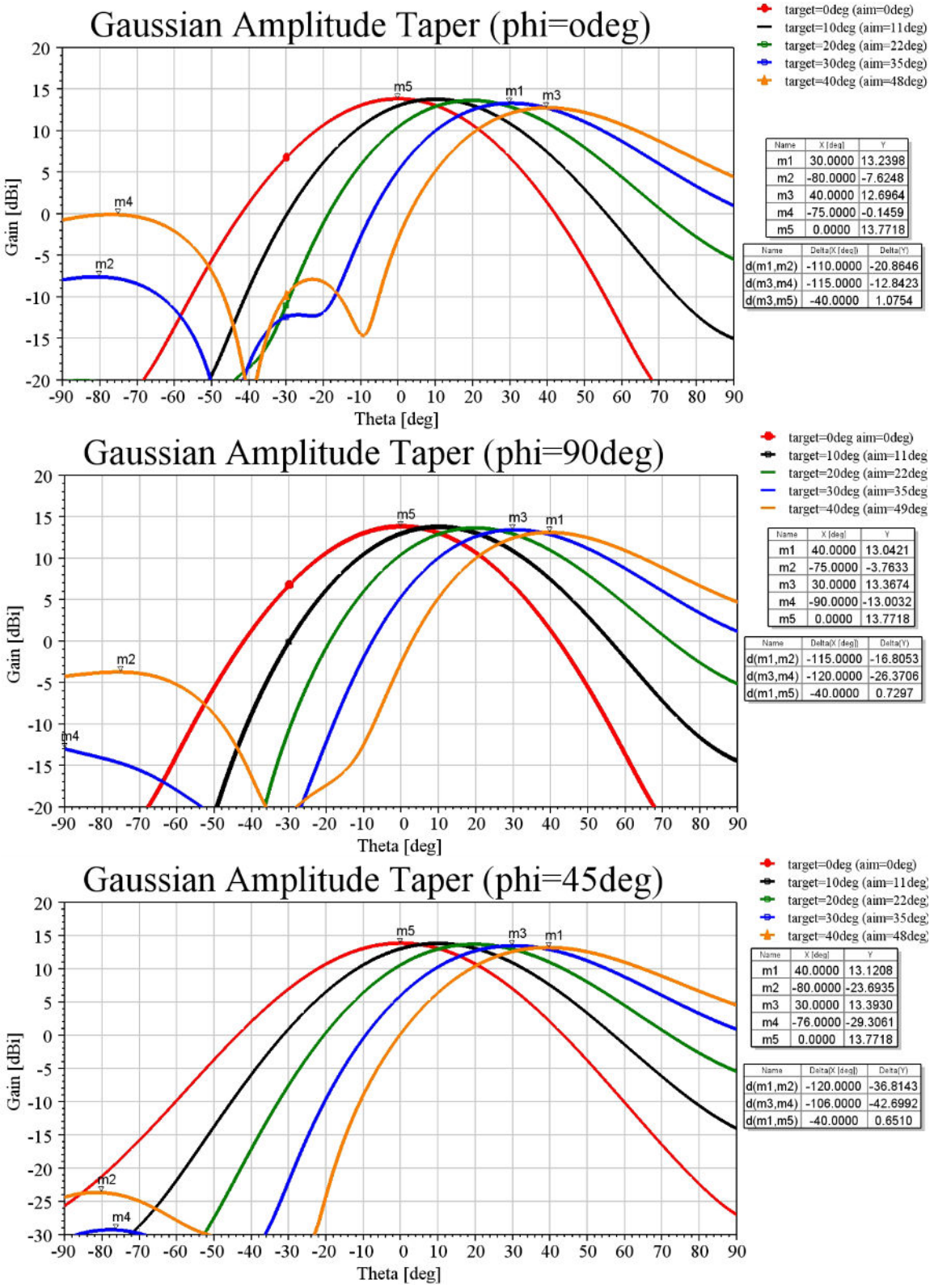

Figure 2-54 Beam steering at 28GHz for plane at phi=0deg, 90deg and 45deg

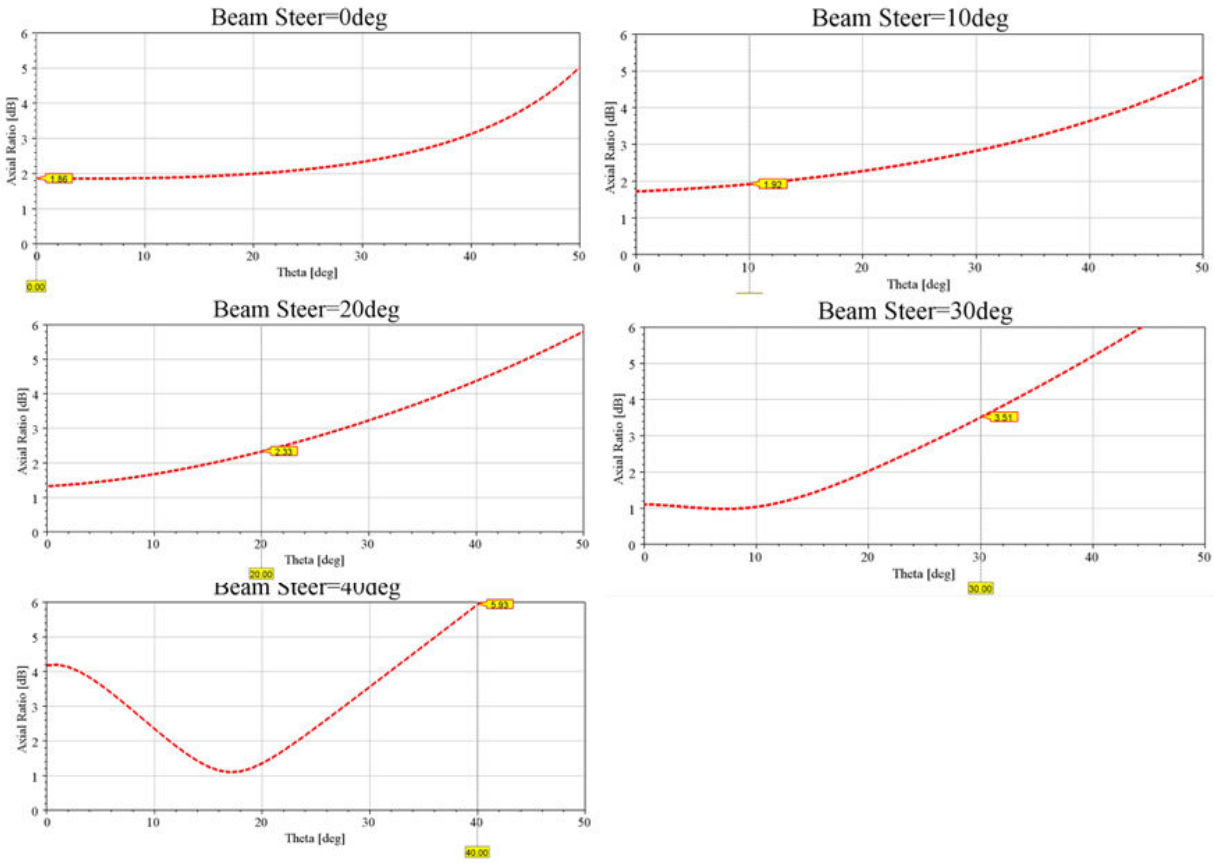

Figure 2-55 Axial ratio performance of 4x4 phased array antenna at 28GHz at plane XZ (phi=0deg) with Gaussian element amplitude taper distribution for examined beam steered angles (0deg, 10deg, 20deg, 30deg, 40deg, 45deg).

Table 10 Trade-off parameters for Concepts 1 and 2

Concept	Gain/Losses	CP Polarization	BW	Beam Steer	No. of elements	Prototyping Complexity
1	Very Good	Excellent	Excellent	Very Good	1600	High
2	Excellent	Acceptable	Very Good	Excellent	400	Fair

In order to select which concept to qualify for demonstration fabrication we have created a trade-off Table (Table 10) for both concepts comparing the following parameters: Gain/Losses; Circular Polarization; Operational bandwidth (Impedance matching); Beam steer performance; Required number of elements (to achieve the 30dBi) and Complexity of prototyping of each concept.

To summarize, after detailed investigation, two options were studied in depth to select the more appropriate one for prototyping. Concept-1 refers to an 8X8 antenna array based on sub-array and Concept-2 refers to a 4X4 antenna array based on single element. The 8X8 antenna array yields more losses than 4X4 antenna array due to higher dielectric losses and consequently the latter yields higher Gain. In terms of circular polarization and bandwidth, 8X8 antenna array is superior due to the use of sequential phase rotation technique. However, beam steering capability of 4X4 array is better than 8X8 array due to lower element distance which meets the theoretical criterion of being lower than $\lambda/2$. Moreover, the required number of elements to be used to achieve the required 10cmx10cm 2D array dimensions are significantly less when the design is based on single element, due to larger size of its elements (lower ε_r of the substrate). Finally, the prototyping complexity of sub-array design is higher than the single element one, mainly due to the use of an extra layer (power divider and passive phase shifters).

Concluding, based on the above data, the 4X4 antenna array is qualified for fabrication and demo measurement setup. The selection is mainly based on superior beam steering performance and lower complexity of prototyping.

3 DISTRIBUTED BEAMFORMING FOR LEO SWARMS AND UNIFIED WAVEFORM DESIGN

Introduction

The 1st part of this chapter focuses on distrbuted beamforming from swarms of small LEO satellites. This is a current research trend that originates from the need to reduce the size of the satellites so to reduce the manufacturing and launching costs. Hence, instead of deploying large antenna arrays in monolithic large satellites, current early-stage efforts focus on the study of creating large virtual arrays from a swarm of small LEO satellites for coherently transmitting to ground users. In D3.1 we focused our study on the impact of phase synchronization errors for the single-user case. Towards this, a closed-form solution for the distribution of the corresponding main-lobe gain has been provided. D3.2 extends such an analysis to the case of multiple users that need to be concurrently facilitated by spatial multiplexing. In particular, a problem is formulated for finding the optimal precoding vector for maximizing the average sum rate under SINR requirements for each user. The problem takes into account the phase synchronization errors among the satellites, so it aims to provide a solution that is robust against such errors.

The 2nd part of this chapter focuses on the Orthogonal Time Frequency Space (OTFS) modulation. As presented in D3.1, this is a recently introduced modulation type that comes as an alternative to OFDM to combat severe Doppler shifts in scenarios with high mobility. Hence, it is very relevant to satellite communications due to the very high velocity with respect to Earth of LEO satellites and the resulting large Doppler shifts that can well exceed the subcarrier spacing for OFDM in standards. In D3.1 results have been presented regarding the comparison of OTFS with OFDM for a single-user communication scenario, facilitated by a LEO satellite. According to the results OTFS largely outperformed its OFDM counterpart. D3.2 compares two versions of OTFS, namely the two-step approach and the single-step Zak transform one, in terms of performance and complexity in a LEO related scenario.

3.1 DISTRIBUTED BEAMFORMING FROM LEO SATELLITE SWARMS FOR MULTIUSER SCENARIOS

Background

A single LEO satellite for multi beam massive MIMO communication is difficult to deploy due to its large size, and high-power requirement. To resolve this issue, the radiating elements/antennas are instead divided into multiple small sized satellites which create a distributed swarm. In addition to reduction in cost, the satellite swarm also offer the advantage of high beamforming gain that could compensate for some of the signal loss which results from the high altitude of the satellite. satellite miniaturization and distributed satellite systems (DSS) have gained popularity [5], [6].

DSS are a collection of satellites each carrying one or more antennas to cooperatively perform beamforming. This helps distribute the power and resources across multiple smaller satellites, which are easier to manage than one large satellite. In pursuit of system of satellites that require little intervention from controllers and yield benefits of distributed nodes, satellite swarms have been proposed [7]. Swarms are similar to clusters but with significantly larger number of satellites [8]. The size of the satellites can be small, which makes them easily manageable as well as maneuverable and significantly reduces the required operation cost.

Proper coordination between satellites in a swarm requires synchronization in time, phase and frequency. This calls for inter-satellite communication [9], and ranging techniques to determine

the positions of satellites relative to an already known reference frame. It's essential for beamforming as the satellites positions determines the precoding weights and phase shifts to steer a beam to the desired user/s. Several works have proposed methods for inter-satellite ranging. The most common is the master-slave architecture where a central (master) satellite acts as a reference point and sends signals to the other satellites, which lock in their phases according to the received signal. Highly directive Optical signals can be sent [10], [11], or alternatively, RF signal can be broadcasted, and detected by all satellites simultaneously [12]. A dual-way ranging where a pair of satellites send signal to each other is discussed in [13].

Motivation

Despite the aforementioned works that estimate satellite positions, and achieve synchronization, there will always be unavoidable errors, leading to imperfect synchronization. [14], [15]. The precoding design for the swarm must be robust to minimize the performance loss as a result of this error. It should, at least, maximize the total throughput reasonably well until we encounter an error so high that the beamforming gain through the distributed satellites is overwhelmed by the loss due to the synchronization error, after which we expect the collocated (no synchronization error) antennas to outperform the DSS. A stochastic weighted MMSE (SMMSE) is analyzed in [16], to reformulate a non-convex sum-rate maximization problem into an equivalent convex expression. Although this method is effective, it relies on sample realizations of the random variable and aggregation of instantaneous solutions until convergence. This could take considerable time depending on the size of the parameters (number of satellites, number of users ...), and the type of additional constraints we choose to impose. The authors of [17], [18] devised a method to minimize the total power consumption of satellites under a probabilistic QoS constraint. This method utilizes the Taylor series to approximate a function of complex exponentials to polynomial expressions. The stochastic constraint is decomposed into a set of convex constraints as shown in [19]. The polynomial term is then re-defined into a set of convex expressions. Semidefinite programming (SDP) and gaussian randomization are used to solve the reformulated optimization problem. After considering previous works, it was observed that a low time complexity precoding design that maximizes total throughput and satisfies the QoS constraint is needed.

System model

Spiral satellite configuration is assumed, meaning that the position of satellite s is specified by the following (in polar coordinates).

$r_s = d/\sqrt{\pi} \times \sqrt{s}$, $\Omega_s = 2\pi\tau s$ r_s is distance and Ω_s is angle from the array centre.

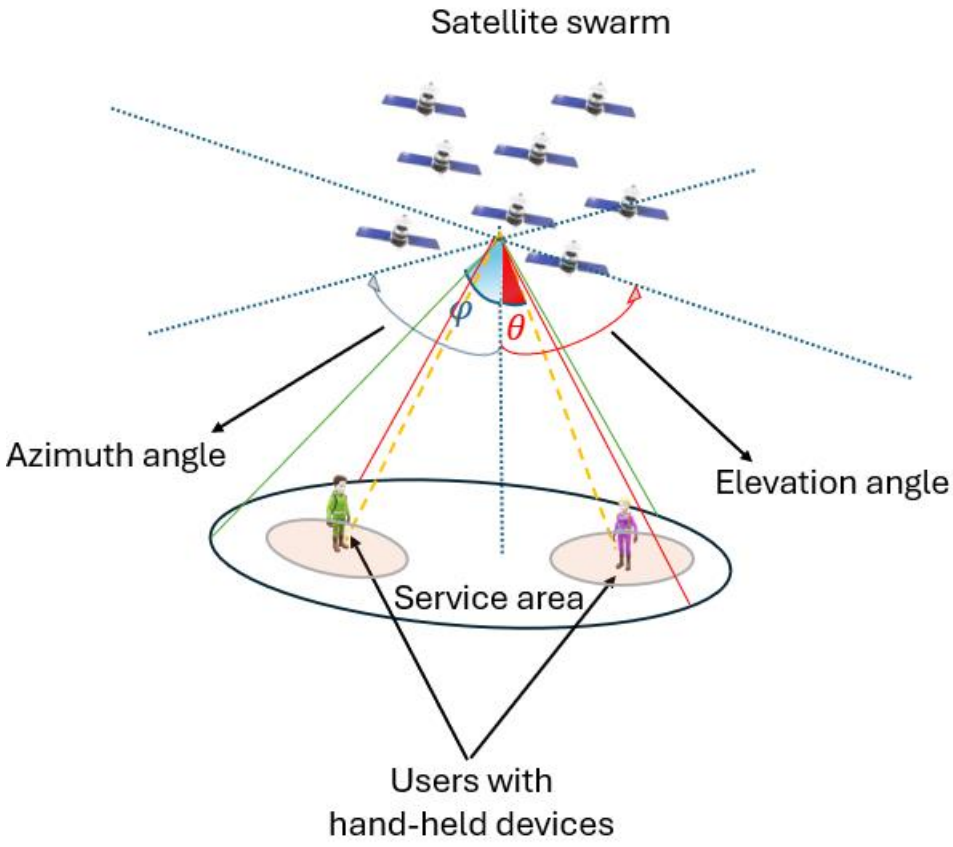

Figure 3-1: Direct to cell connectivity with LEO satellite swarm

The following line-of-sight (LOS) channel model is assumed.

$$\boldsymbol{h}_k = \boldsymbol{a}(\varphi_k, \theta_k) L^{fs}(\theta_k) \tag{3-1}$$

where $\mathbf{h}_k \in \mathbb{C}^{1\times S}$ is the channel from the swarm to user k, $\boldsymbol{a}(\varphi_k, \theta_k) \in \mathbb{C}^{1\times S}$ is the array factor, and $\mathrm{L^{fs}}(\theta_\mathrm{k}) = \frac{\lambda}{4\,\pi\,\mathrm{r_k}}$ is the free space path loss. r_k is the distance from swarm centre to user k.

Thermal noise is modelled as a complex gaussian with zero mean and power of $\kappa\, B\, T$, where κ, B, T are the Boltzmann constant, bandwidth and temperature respectively.

Problem formulation and analysis

The goal is to maximize the expected total sum-rate under the presence of phase errors $\boldsymbol{e} = \left[e^{j\phi_1}, e^{j\phi_2}, \ldots e^{j\phi_S}\right]^H$. Let the erroneous channel be $\boldsymbol{h}'_k = \boldsymbol{h}_k \odot \boldsymbol{e}^H$, then the optimization problem can be written as

$$\max_{\boldsymbol{v}_1,..\boldsymbol{v}_K} \; E_\phi \left[\sum_{k=1}^{K} log\left(1 + \frac{|(\boldsymbol{h}'_k \odot \boldsymbol{e}_k{}^*)\boldsymbol{v}_k|^2}{\sigma_k^2 + \sum_{l\neq k} |(\boldsymbol{h}'_k \odot \boldsymbol{e}_k{}^*)\boldsymbol{v}_l|^2}\right)\right] \tag{3-2}$$

Subject to: $P(\mathrm{SINR_k} > \mu_k) \geq \epsilon_k$

$$\mathbf{m}_s^H \mathbf{V}\mathbf{V}^H \mathbf{m}_s \leq P_s$$

where $\boldsymbol{v}_k$ is the precoding vector for user k, $\mathbf{m}_s$ is a vector with $(\mathbf{m}_s)_s = 1$ and 0 everywhere else, and P_s is the power constraint for satellite s.

According to [18], $: P(\mathrm{SINR_k} > \mu_k) \geq \epsilon_k$ can be decomposed into a set of deterministic constraint as follows.

C1: $\sum_{[j,k]} \boldsymbol{Z}_{i,[j,k]} - 1 + \mathrm{Tr}(\boldsymbol{F_i}) \geq 2\sqrt{-\ln(1-\epsilon_i)}\,(x_i + y_i)$

C2: $\frac{1}{2\sqrt{2}} \|\boldsymbol{G_i}\|_2 \leq x_i$

C3: $v_i \|vec(\boldsymbol{F}_i)\|_2 \leq y_i$ (3-3)

C4: $\boldsymbol{Z_i} = \boldsymbol{X_i} + \boldsymbol{Y_i}$

C5: $\boldsymbol{F_i} = f(\boldsymbol{X}_i), \boldsymbol{G_i} = g(\boldsymbol{Y}_i),$

C6: $\boldsymbol{V}_\mathrm{i} \succcurlyeq 0$

To achieve that the non-convex objective function is reformulated into a convex problem using the stochastic MMSE [16]. After adding the quality of service (QoS) constraint, we define the following optimization problem.

Define $\mathbf{E}_k(\mathbf{V}, \mathbf{H})$ as the following,

$$\mathbf{E}_k(\mathbf{V}, \mathbf{H}) = (1 - (\boldsymbol{e}_k{}^H \times M_k)v_k)(1 - (\boldsymbol{e}_k{}^H \times M_k)v_k)^H + \sum_{j \neq k} (\boldsymbol{e}_k{}^H \times \boldsymbol{M_k})\boldsymbol{v_j}\boldsymbol{v_j}^H(\boldsymbol{e}_k{}^H \times \boldsymbol{M_k})^H$$

$$= 1 - 2Re(e_k \boldsymbol{M_k}\boldsymbol{v_k}) + e_k \boldsymbol{M_k}\boldsymbol{v_k}\mathbf{v}_k{}^H \mathbf{M}_k{}^H e_k + \sum_{j \neq k} e_k \boldsymbol{M_k}\boldsymbol{v_j}\mathbf{v}_j{}^H \mathbf{M}_k{}^H e_k$$

$\mathbf{E} = \mathrm{E}_\phi[\boldsymbol{e}_k \boldsymbol{e}_k{}^H]$ and $\mathbf{R_k} = \mathbf{M}_k{}^H \mathbf{E} \boldsymbol{M_k}$

$$\boldsymbol{\Phi}_k = \mathbf{M}_k{}^H \boldsymbol{e}_k \boldsymbol{e}_k \boldsymbol{M_k}$$

$$E_\phi\left[\sum_{k=1}^{K} \boldsymbol{E_k}(\boldsymbol{V}, \boldsymbol{h_k})\right] = -\sum_{k=1}^{K} \boldsymbol{2Re}\left(E_\phi[\boldsymbol{e}_k{}^H]\boldsymbol{M_k}\boldsymbol{v_k}\right) + \sum_{k=1}^{K}\sum_{j=1}^{K} \boldsymbol{v}_j{}^H \boldsymbol{R}_k{}^H \boldsymbol{v}_j \quad (3\text{-}4)$$

Moreover, since the relationship $\mathbf{P}_\mathrm{k} = \mathbf{v}_\mathrm{k}\mathbf{v}_\mathrm{k}^\mathrm{H}$ cannot be directly imposed, as it would not be a convex constraint, we relax the condition and add a penalty expression into the objective function to ensure that the squared-norm of $\mathbf{v}_\mathrm{k}$ is close to the trace of $\mathbf{P}_\mathrm{k}$. Let β be our scaling coefficient for the penalty.

A convex objective function can be reformulated as follows

$$\min_{V,P,x,y,t} E_{\phi}\left[\sum_{k=1}^{K} \mathbf{E_k}(\boldsymbol{V}, \boldsymbol{h_k}) + \beta t\right] \tag{3-5}$$

$$-Tr(\boldsymbol{P_k})) + \boldsymbol{v_k}^H \boldsymbol{v_k} \leq t$$

$$t \geq 0$$

$$C_1 \; upto \; C_6$$

Simulation results

Table 11: Simulation parameters

Parameter	Value
Number of satellites	50
Number of users	10
Satellite altitude	600 km
Antennas per satellite	1
Number of users	10
Carrier frequency	3 GHz
Bandwidth	30 MHz
Satellite spacing unit (d)	1000λ
Satellite antenna gain	10dB
Service area coverage	$\theta = (-25^0, 25^0)$ $\varphi = (-25^0, 25^0)$

The results for the total sum rate of the optimized precoding design is shown in Figure 3-2 Figure 3-2: Sum rate under an error standard deviation of 20^0.for error standard deviations of 20 degrees. It can be seen that the optimized design outperforms the conventional MRT with and without the probabilistic QoS. For the selected set of parameters, the probabilistic QoS is only satisfied for per satellite power values above 2dBwatt. The empirical probability is analyzed from large enough samples. Figure 3-3 shows that, for the selected set of minimum

SINR and probability thresholds, the constraint is satisfied for transmit power per satellite values above 2dB for 20^0 std of phase error.

Figure 3-4 shows the cumulative distribution function (CDF) comparison for the proposed approach with and without QoS constraint at 2 dBW total transmit power. The approach without QoS sacrifices the SINR of some users in order to maximize the sum rate. Although the case with QoS has a slightly lower total sum rate, it satisfies the SINR constraint.

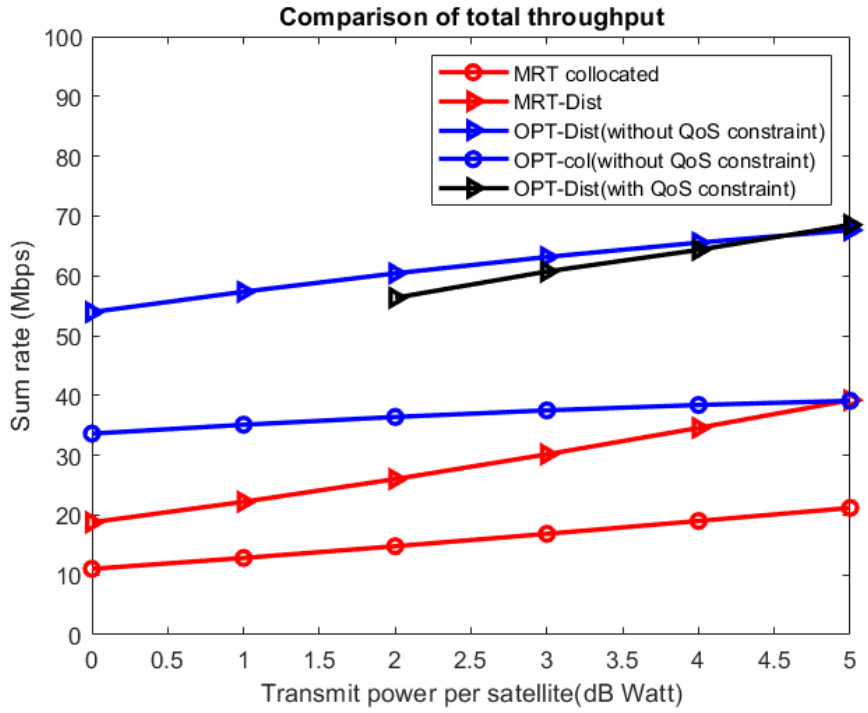

Figure 3-2: Sum rate under an error standard deviation of 20^0.

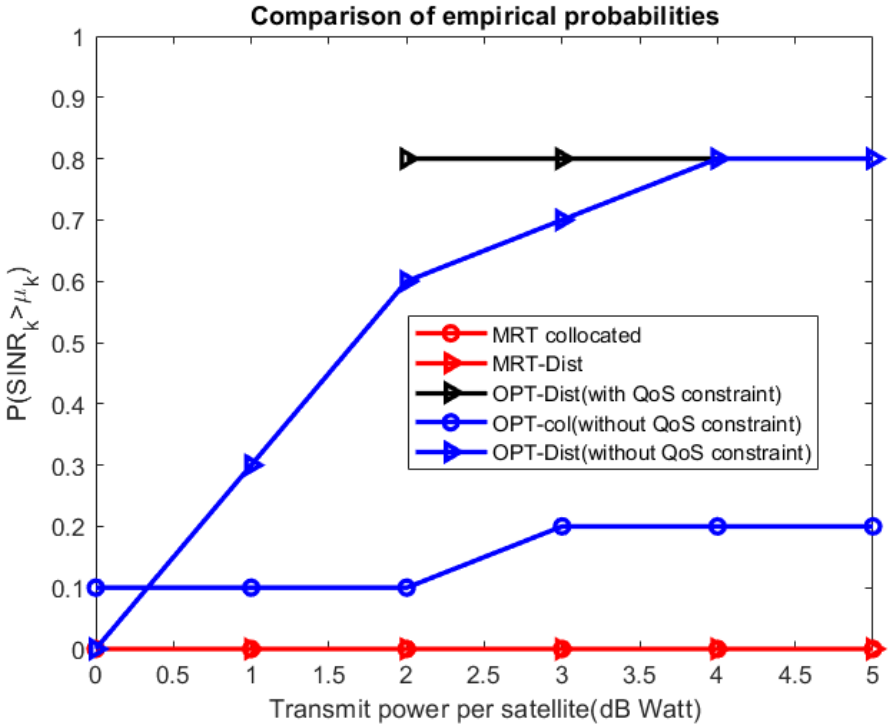

Figure 3-3: Simulated (empirical) values for the probabilistic criteria

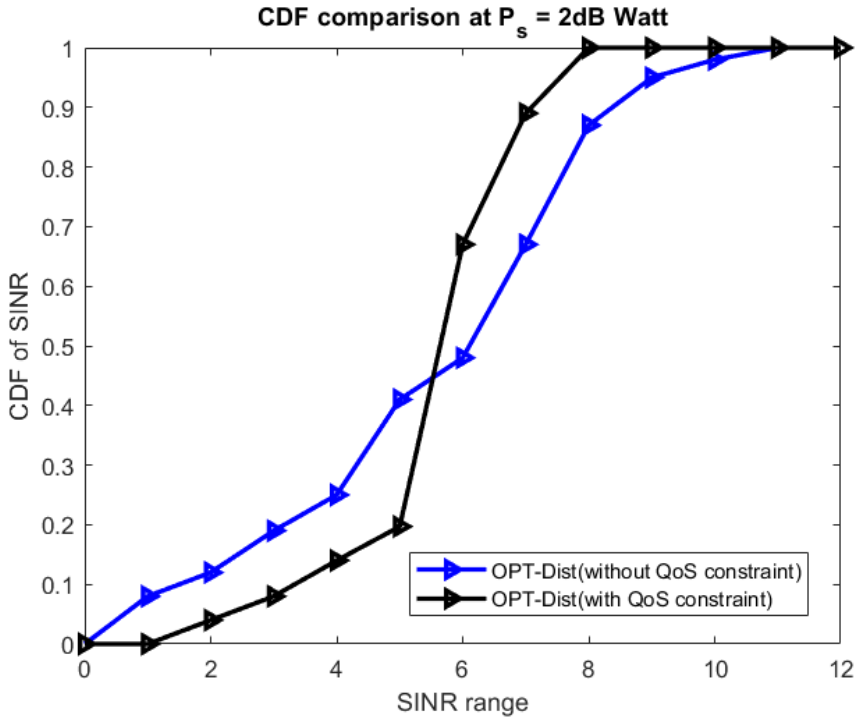

Figure 3-4: CDF comparison at 2dBWatt transmit power

3.2 UNIFIED WAVEFORM DESIGN

The recent interest from industry in providing service to general mobile users from integrated terrestrial and satellite networks necessitated a unified wave form design. Traditional wireless communication waveforms, predominantly Orthogonal Frequency Division Multiplexing (OFDM), have achieved widespread success in terrestrial networks, forming the backbone of 4G, 5G, and Wi-Fi standards. To ensure the network agnostic service to user, OFDM is considered a possible unified waveform for both terrestrial and satellite networks. OFDM's

efficiency in frequency-selective fading channels stems from its ability to divide the available bandwidth into multiple orthogonal subcarriers, allowing parallel data transmission. However, this approach relies heavily on the assumption of quasi-static channels over each symbol duration. This assumption is severely violated in the dynamic LEO satellite environment [20].

3.2.1 Challenges of Doubly Selective Channels in LEO Satellite Systems

LEO satellite communication links are inherently characterized by severe channel impairments that significantly differentiate them from terrestrial wireless environments. The high orbital velocities of LEO satellites, which can reach tens of thousands of kilometres per hour, induce substantial Doppler shifts. These shifts can manifest as frequency variations ranging from several kilohertz (kHz) in the S-band to tens of kHz in the Ka-band, magnitudes that far exceed those typically observed in terrestrial cellular networks. Furthermore, user mobility on the ground can contribute to these already pronounced Doppler effects [21].

In addition to significant Doppler shifts, LEO satellite links are also marked by long propagation delays, a direct consequence of the satellites' altitudes, which typically range from 500 km to 2000 km. The dynamic and time-varying geometry of the satellite-user link, coupled with these delays, leads to considerable delay variations and multipath spread. The confluence of large Doppler shifts (indicating time-varying channels) and extensive multipath propagation (indicating frequency-selective channels) results in what are termed "doubly-selective channels" [20]. These channels are characterized by rapid time-variance, making the acquisition and maintenance of accurate instantaneous Channel State Information (CSI) an extremely challenging task. The fundamental physical characteristic of LEO satellites, their high orbital velocity, is the direct cause of these severe Doppler shifts. These shifts, in turn, lead to rapidly time-varying channels that fundamentally violate the quasi-static assumptions of conventional modulation schemes, thereby degrading their performance. This establishes the LEO environment not merely as a challenging variant of terrestrial channels but as a fundamentally different propagation scenario, necessitating a departure from traditional waveform designs [22].

3.2.2 Overview of Conventional Modulation Schemes and their Limitations

The core design principles of OFDM, particularly its reliance on subcarrier orthogonality in the time-frequency (TF) domain and quasi-static channel assumptions, create a fundamental mismatch with the dynamic and doubly-selective nature of LEO satellite channels. This inherent incompatibility is the root cause of its significant performance degradation. High Doppler shifts in time-varying channels disrupt the crucial orthogonality between OFDM subcarriers, leading to spectral spreading of the transmitted signals. This phenomenon results in overlap and interference between adjacent subcarriers, known as Inter-Carrier Interference (ICI) [23]. To compensate for these rapidly changing channel conditions, OFDM systems in high-mobility scenarios necessitate frequent transmission of pilot symbols and continuous channel estimation. This requirement leads to significant pilot overhead, which consequently reduces the overall spectral efficiency and throughput of the system.

The performance degradation of OFDM is particularly pronounced with increasing mobility. At moderate-to-high mobility levels (e.g., 300–500 km/h), OFDM struggles to track rapid channel

variations, and its performance degrades significantly. In extreme mobility conditions (e.g., 1000–2000 km/h), OFDM experiences severe Doppler effects, leading to poor Bit Error Rate (BER) performance. In such scenarios, increasing the Signal-to-Noise Ratio (SNR) yields diminishing returns, rendering OFDM unsuitable for these conditions. This implies that simply optimizing OFDM parameters or adding complex equalization techniques is insufficient for LEO satellite communications, as the problem stems from a deeper, inherent design limitation [24].

3.2.3 Introduction to Orthogonal Time Frequency Space (OTFS) Modulation

In response to the profound limitations of conventional waveforms like OFDM in high-mobility, doubly-selective channels, Orthogonal Time Frequency Space (OTFS) modulation has emerged as a promising solution for future wireless communication systems, including 6G and Integrated Sensing and Communication (ISAC) applications [25] [20], [26].

The core innovation of OTFS is a strategic shift in the domain of operation from time-frequency to Delay-Doppler (DD). Unlike traditional schemes that operate in the time-frequency (TF) domain, OTFS maps data symbols onto a two-dimensional (2D) DD domain. This is a crucial distinction, as it allows information symbols to have a direct interaction with the DD domain channels, where the physical characteristics of the channel are more effectively represented and managed. This domain transformation effectively "freezes" the rapidly varying, doubly-selective channel into a more stable, sparse, and quasi-static representation for the duration of an OTFS frame. This fundamental re-alignment with the physical channel characteristics is what enables its superior robustness and simplified channel estimation, directly addressing OFDM's main weaknesses.

3.2.3.1 Delay-Doppler Domain Channel Modelling for Doubly Spread Channels

In high-mobility or multipath-rich environments, wireless channels often experience both **time dispersion** (due to multipath delays) and **frequency dispersion** (due to Doppler shifts), resulting in **doubly spread channels**. Traditional time-frequency (TF) domain-based systems, such as OFDM, face significant challenges under these conditions, including inter-symbol interference (ISI), inter-carrier interference (ICI), and rapidly time-varying channel behaviour.

A typical doubly spread channel in the time domain is represented as:

$$h(t,\tau) = \sum_{i=1}^{p} h_i \, \delta(\tau - \tau_i) e^{\{j\, 2\, \pi \nu_i t\}} \tag{3-6}$$

where h_i τ_i and ν_i are the complex gain, delay, and Doppler shift for the i^{th} path.

An alternative and more robust approach is to model the wireless channel in the **Delay-Doppler (DD) domain**. This representation offers the following key advantages:

- **Sparsity**: The DD channel matrix is typically sparse, as only a few delay-Doppler pairs contribute significantly to the channel response.
- **Quasi-Static Representation**: The DD domain channel remains nearly constant over time, enabling more reliable channel estimation and equalization.
- **Improved Robustness**: Systems operating in the DD domain are inherently more resilient to Doppler effects and fast fading, offering better performance in high-mobility scenarios.

The equivalent DD channel representation is

$$h(\tau, \nu) = \sum_{i=1}^{p} h_i \cdot \delta(\nu - \nu_i) \cdot \delta(\tau - \tau_i) \quad (3\text{-}7)$$

This model is particularly suitable for OTFS, which transform the transmitted data symbols into the DD domain before mapping them onto time-frequency resources.

3.2.3.2 Fundamental Principles of OTFS

OTFS is a novel two-dimensional (2D) modulation scheme specifically designed to overcome the limitations of conventional waveforms in highly dynamic and doubly selective channels. Its core innovation lies in operating within the Delay-Doppler (DD) domain.

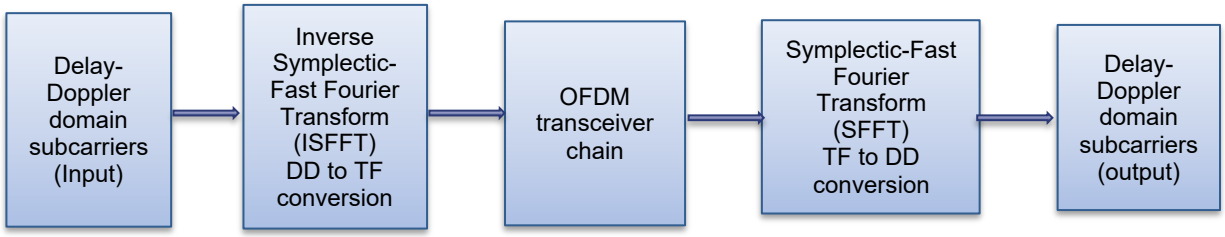

Figure 3-5: OTFS Transceiver block diagram

The first version of OTFS is overlaid on the existing OFDM system as shown in Figure . This system is now referred to as Two-stage-OTFS which is detailed below.

Transmitter Side (DD Domain to Time Domain):

1. **Inverse Symplectic Finite Fourier Transform (ISFFT):** This transform converts the information symbols XDD [l,k] from the Delay-Doppler (DD) domain (with delay index $l \in \{0, \dots, M-1\}$ and Doppler index $k \in \{0, \dots, N-1\}$) to the Time-Frequency (TF) domain symbols $X_{TF}\,[m,n]$ (with subcarrier index $m \in \{0, \dots, M-1\}$ and slot index $n \in \{0, \dots, N-1\}$).

$$X_{\{TF\}[m,n]} = \frac{1}{NM} \sum_{k=0}^{N-1} \sum_{l=0}^{M-1} X_{DD}[l,k]\, e^{j\,2\,\pi\left(\frac{nk}{N} - \frac{ml}{M}\right)} \quad (3\text{-}8)$$

This transformation can also be expressed in terms of standard FFT/IFFT operations for implementation purposes, for example,

$$X_{\{TF\}[m,n]} = M * FFT\left(IFFT(X_{DD}^{T})^{T}\right) \quad (3\text{-}9)$$

2. **Heisenberg Transform (Multicarrier Modulation):** This transform takes the TF domain symbols XTF [m,n] and converts them into a continuous-time transmit signal s(t) suitable for transmission over the wireless channel. This step is analogous to OFDM's multicarrier modulation, realized with an IFFT module followed by a transmit pulse shaping filter.

$$s(t) = \frac{1}{NM}\sum_{\mathrm{n}=0}^{\mathrm{N}-1}\sum_{m=0}^{M-1} \mathrm{X}_{TF}[m,\mathrm{n}]\, g_{tx}(t-nT) e^{\mathrm{j}\,2\,\pi\mathrm{m}\Delta\mathrm{f}(\mathrm{t}-\mathrm{nT})} \quad (3\text{-}10)$$

Where $g_{tx}(t)$ is the transmit pulse shaping filter, T is the slot duration, and Δf is the subcarrier spacing.

Receiver Side (Time Domain to DD Domain):

Assuming doubly dispersive channel with delay–Doppler response $h(\tau, \nu)$. The received signal $r(t)$ is given as

$$r(t) = \iint h(\tau,\nu)\cdot s(t-\tau)\cdot ej2\pi\nu(t-\tau)d\tau d\nu \quad (3\text{-}11)$$

This convolution in **delay–Doppler domain** reflects multipath and Doppler shifts.

1. **Matched Filtering / Receive Gabor Projection**

At the receiver, we project the received signal onto the receive pulse $g_{rx}(t)$ as shown below:

$$Y[m,n] = \int r(t)\cdot g_{rx}^{*}(t-nT)\cdot e^{-j2\pi m\Delta f(t-nT)}dt \quad (3\text{-}12)$$

This gives the **received TF samples** $Y[m,n]$ affected by the channel.

2. **Wigner Transform or Inverse SFFT (ISFFT)**

Then, the **delay–Doppler symbols** $x[k,l]$ are recovered using an **inverse symplectic finite Fourier transform (ISFFT)**:

$$X_{DD}[k,l] = \frac{1}{MN}\sum_{\mathrm{n}=0}^{\mathrm{N}-1}\sum_{m=0}^{M-1} Y[m,n]\cdot e^{-j2\pi(\frac{nk}{N}-\frac{ml}{M})} \quad (3\text{-}13)$$

This is equivalent to a **2D inverse FFT** with a **symplectic twist**:

- Delay corresponds to frequency index m
- Doppler corresponds to time index n

3.2.3.3 Discrete Zak transform based OTFS

The Discrete Zak Transform (DZT)-based OTFS framework implements OTFS modulation directly in the delay–Doppler domain, without embedding into OFDM. This makes the system "OTFS-native," unlike MC-OTFS which overlays OTFS onto OFDM.

3.2.3.4 Transmitter side (DD Domain → Time Domain)

1. **Zak Transform Mapping (DD → Time)**: The discrete Zak transform (DZT) directly maps the delay–Doppler (DD) domain symbols $X\_DD[l,k]$ (with delay index $l \in \{0,\dots,M-1\}$, Doppler index $k \in \{0,\dots,N-1\}$) into a time-domain sequence $s[n]$. The DZT is defined as:

$$s[n] = \left(\frac{1}{\sqrt{MN}}\right) \Sigma_{k=0}^{N-1} \Sigma_{l=0}^{M-1} X_{DD[l,k]} \cdot \exp\left(j\,2\pi \frac{kn}{N}\right) \cdot \delta[n - l \bmod M] \quad (3\text{-}14)$$

   Here, $\delta[\cdot]$ ensures cyclic placement of the DD symbols in the time lattice. Unlike MC-OTFS, this avoids intermediate TF-domain mapping via ISFFT.

2. **Pulse Shaping and Transmission**: The resulting time-domain samples are shaped with a transmit pulse $g\_tx(t)$ and transmitted over the channel:

$$s(t) = \Sigma_{n=0}^{MN-1} s[n] \cdot g_{tx(t-nT_s)} \quad (3\text{-}15)$$

   where T_s is the sampling period. $g\_tx(t)$ can be designed flexibly (not tied to OFDM sinc pulses).

3.2.3.5 Receiver side (Time Domain → DD Domain)

The received signal $r(t)$ is given as

$$r(t) = \iint h(\tau,v) \cdot s(t-\tau) \cdot ej2\pi v(t-\tau) d\tau dv \quad (3\text{-}16)$$

1. **Zak Domain Projection (Time → Zak Transform):**The received signal is projected back into the Zak domain by matched filtering with $g\_rx(t)$:

$$Y[l,k] = \Sigma_{n=0}^{MN-1} r[n] \cdot g_{rx} * (nT_s - lT_s) \cdot \exp\left(-j\,2\pi \frac{kn}{N}\right) \quad (3\text{-}17)$$

   This produces noisy, channel-distorted DD-domain samples $Y[l,k]$.

2. **Equalization in DD Domain (Time → Zak Transform):** Since the channel is a 2D circular convolution in delay–Doppler, equalization is performed directly:

$$\hat{X}_{DD[l,k]} = EQ\{Y[l,k], H[l,k]\} \quad (3\text{-}18)$$

   where $H[l,k]$ is the effective 2D channel response in the DD domain and $EQ\{\cdot\}$ denotes the equalizer (ZF, MMSE, message passing, etc.).

3.2.3.6 Comparison of DZT-OTFS vs Two-stage-OTFS

1. **Complexity:**

- Two-stage-OTFS:
  - Requires both ISFFT/SFFT (2D FFT/IFFT) and OFDM modulation (FFT/IFFT per OFDM symbol).
  - Channel equalization is performed **after OFDM demodulation**, meaning FFT + matched filtering + 2D equalization

- **Advantage:** Lower implementation barrier (reuses OFDM FFT engines).
- **Disadvantage**: Redundant FFT operations and higher computational load.

- DZT-OTFS:
  - Zak transform directly maps DD symbols ↔ time domain.
  - Avoids double FFT chains → only one main transform.
  - Equalization done directly in DD domain (efficient for sparse DD channels).
  - Advantage: Lower asymptotic complexity, no OFDM overhead.

- Overall complexity**:**
  - Two-stage-OTFS≈ O(MN log(MN)) + O(N log N)
  - DZT-OTFS ≈ O(MN log(MN)):
  - **Winner: DZT-OTFS.** DZT-OTFS is more efficient as grid size grows (no redundant FFT stages).

2. Pilot overhead:

- Two-stage-OTFS:
  - Since it inherits OFDM's TF grid, pilots are placed in **time–frequency slots.**
  - Overhead is similar to OFDM but slightly worse due to the need to ensure **channel estimation across Doppler as well as delay**.
  - Structured pilots must span **both time & frequency**, which increases overhead in high-mobility scenarios.

- DZT-OTFS:
  - Pilots placed directly in DD domain.
  - Only a few pilots are needed to probe sparse DD channels (multipath + Doppler are naturally represented).
  - Overhead scales with channel sparsity, not with bandwidth or duration
  - Advantage: Much more pilot efficient in high mobility / wideband channels
- **Winner: DZT-OTFS.** DZT-OTFS is more **pilot efficient** in high mobility / wideband channels

3.2.3.7 Channel estimation and Pilot overhead:

- Two-stage-OTFS:
  - Since MC-OTFS uses the OFDM-style TF grid, pilot placement and estimation strategies (LS, MMSE, DFT-based, etc.) can be reused.
  - To estimate doubly dispersive channels, pilots must span **both frequency and time dimensions**, which increases overhead in high mobility.
  - Since estimation is done in TF domain, mapping back to DD domain causes **error propagation** due to 2D transforms.
  - **Less efficient for sparse channels:** Does not directly exploit DD-domain sparsity of the wireless channel.

- DZT-OTFS:

- **DD-domain pilots:** Pilots placed directly in **delay–Doppler grid**, which naturally matches channel structure.
- **Exploits sparsity:** Wireless channels are often sparse in delay–Doppler → only a few pilots needed for accurate estimation.
- **Lower overhead:** Pilot overhead scales with number of dominant paths, not with grid size.
- **Direct estimation:** No intermediate TF interpolation — estimation is performed where the channel is "sparse and compact."

- Winner: DZT-OTFS as it is much more **pilot efficient** in high mobility / wideband channels. However, DZT-OTFS needs specialized DD domain sparsity-based estimation algorithms which can be computationally heavy.

3.2.4 Performance comparison in LEO satellite scenario

In the following we compare the performance of the following two approaches with respect to precoding:

1. Discrete Zak Transform (DZT)-based OTFS
2. Two-stage OTFS (MC-OTFS)

Simulation setup: Simulation parameters related to OTFS and satellite are listed in **Error! Reference source not found.**.

Table 12: Simulation parameters

Doppler bins	16
Delay bins	48
Carrier frequency	2 GHz (S-band)
Satellite speed	7.11 km/s
Bandwidth	4.5 Mhz
Doppler bandwidth	94.8 KHz
Doppler resolution	5925 Hz
Delay resolution	2.1976e-07 s
Symbol duration	3.5162e-06 s
Frame duration	1.6878e-04 s
Cyclic prefix (τ_{max})	4 (0.25xDoppler bins)

Channel Model

The channel is modeled directly in the **delay–Doppler (DD) domain**, which is the natural representation for OTFS systems. Unlike classical OFDM models (which assume integer-spaced taps in time/frequency), here both **fractional delays** and **fractional Doppler shifts** are explicitly included to capture more realistic propagation effects.

We assume a **multipath channel** with 4 independent paths, corresponding to different reflections and scattering clusters. Each path is characterized by:

- **Delay** ($\boldsymbol{\tau_p}$): The time taken for the signal to reach the receiver. Instead of being limited to integer multiples of the delay bin spacing, delays are drawn from a **continuous range** $\tau_p \in [0, \tau_{max}]$ where τ_{max} is chosen as the length of cyclic prefix
- **Doppler shift** ($\boldsymbol{\nu_p}$): Caused by relative motion between transmitter, receiver, and scatterers. Dopplers are randomly selected within $\nu p \in [-\frac{\nu_{max}}{2}, \frac{\nu_{max}}{2}]$ which ensures that both positive (approaching) and negative (receding) frequency shifts are represented. Here ν_{max} is chosen as 4*doppler resolution
- **Path powers**: The relative strength of each path follows the **3GPP NTN-TDL-B profile**: [0,−1.973,−4.332,−11.914] dB. These are normalized to ensure the total channel power is unity.
- **Fading distribution**: For the line-of-sight (LOS) path, fading is modeled as **Ricean** with K=10, meaning the LOS dominates but is affected by scattered components. Non-LOS paths follow a **Rayleigh distribution**, representing rich scattering.

This setup ensures that each of the 4 paths has a unique fractional delay, fractional Doppler, and fading coefficient.

Bilinear Interpolation: The delay-Doppler domain is represented on a **discrete grid** with delay bins and Doppler bins. However, actual channel taps often **fall between bins**.To accurately project fractional values onto the grid:

1. **Find nearest grid bins** in delay and Doppler. Each fractional value lies between two bins in delay and two bins in Doppler.
2. **Split energy across neighbors** using **bilinear interpolation**:
   - Delay energy is divided proportionally between two adjacent delay bins.
   - Doppler energy is divided proportionally between two adjacent Doppler bins.
   - The result is that each path contributes to up to **4 neighboring bins** instead of being rounded to one.

Precoding: The delay and doppler spread introduced by the channel leads to the interference among the DD subcarriers. Similar to canonical systems, precoding is used for mitigation of inter-carrier interference. For this setup, we assume the availability of perfect CSI and MMSE based precoding is considered for both the schemes.

Performance comparison for integer Doppler and delay channel: In Figure 3-6, the performance as function of mean square error (MSE) as a function of SNR in dB is plotted for DZT-OTFS and Two-stage-OTFS.

In the Two-stage-OTFS, DD symbols are converted into TF symbols and uses underlying OFDM system

- A **single DD impulse** corresponds to a **spread-out pattern in the TF domain**. This is because DD symbols are “localized” in delay and Doppler, but the ISFFT spreads them over multiple subcarriers and time slots in TF. When the channel applies **discrete delays and Dopplers**, the spreading in the TF domain leads to interference across many OFDM subcarriers. At the receiver, the reverse transformations (FFT and SFFT) cannot fully

cancel this spreading because the initial ISFFT combined with channel effects has already "mixed" the signal across time and frequency bins.

DZT-OTFS:

- DZT-OTFS operates directly between the DD domain and the time domain (DD ↔ time) using the Discrete Zak Transform. This avoids the intermediate TF domain spreading. A DD-domain impulse stays more localized after propagation through the channel, and the receiver can effectively cancel the channel effects, leading to better MSE performance.

This direct DD-domain processing allows DZT-OTFS to compensate for channel effects more effectively, resulting in superior MSE performance over Two-stage-OTFS. While both systems improve with increasing SNR, DZT-OTFS consistently outperforms Two-stage OTFS, even at high SNR.

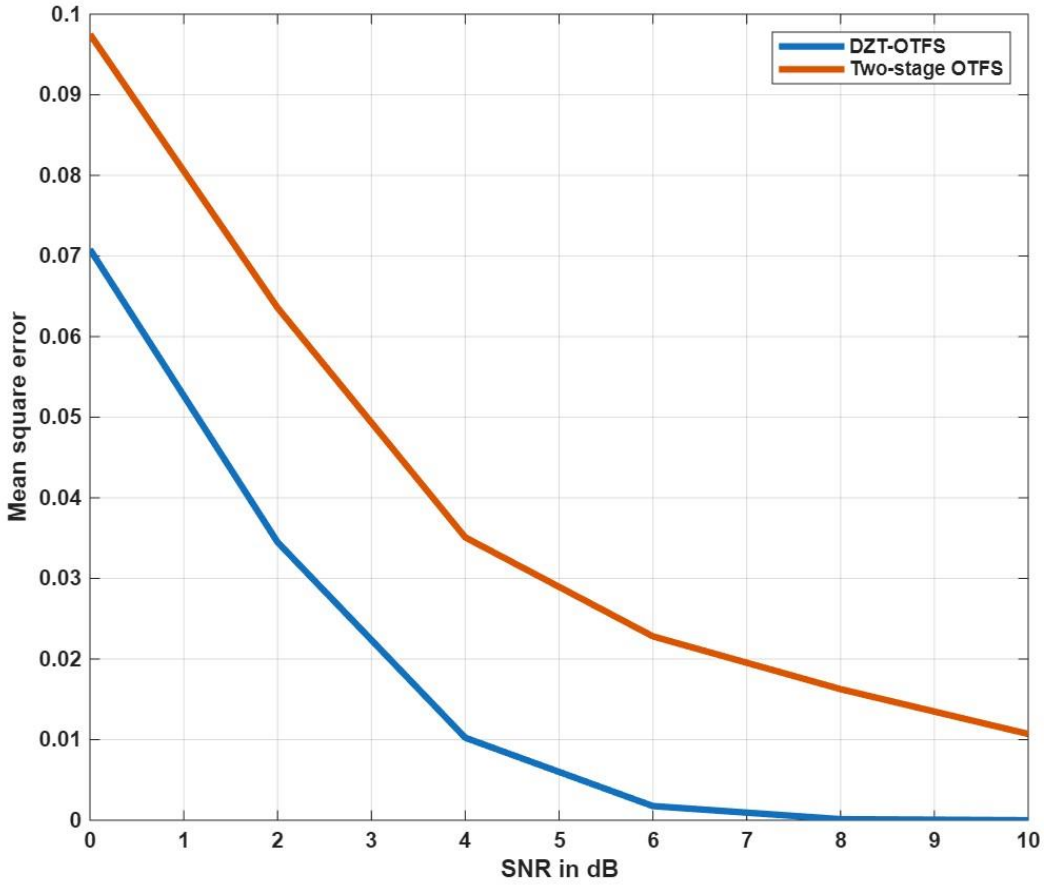

Figure 3-6: Performance comparison in terms of MSE as a function of SNR in dB in integer Doppler and Delay scenario

In Figure 3-7, the performance as function of mean square error (MSE) as a function of SNR in dB is plotted for DZT-OTFS and Two-stage-OTFS for fractional delay and Doppler based channel. While the Two-stage-OTFS gets impacted badly DZT-OTFS still able to recover the symbols even under fractional Delay and Doppler introduced by channel.

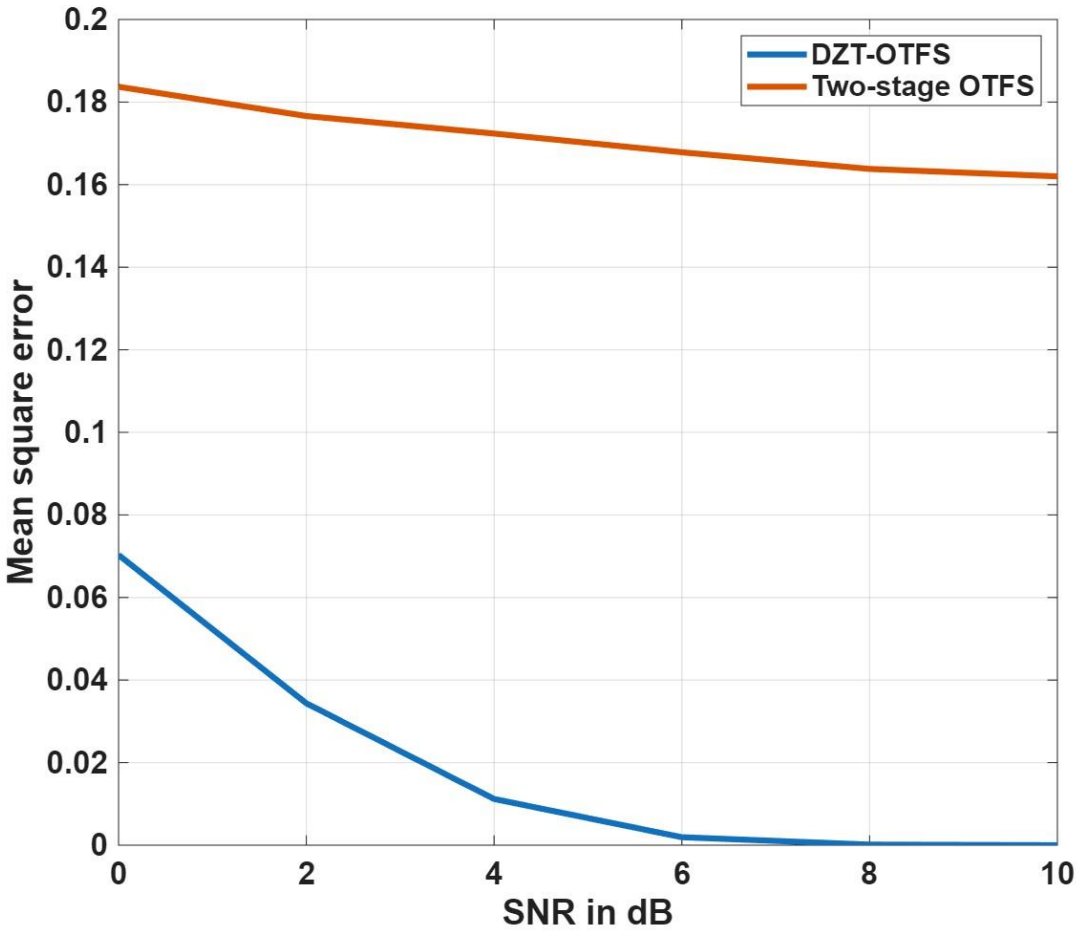

Figure 3-7: Performance comparison in terms of MSE as a function of SNR in dB in fractional Doppler and Delay scenario

Conclusion: By directly operating in Delay-Doppler domain, even under higher Doppler and fractional Doppler scenario, DZT-OTFS achieve better performance than Two-stage-OTFS at a much lower complexity.

4 SOFTWARE-DEFINED PAYLOAD FOR DYNAMIC SPECTRUM MANAGEMENT AND POWER CONTROL IN AERIAL AND SPACE ETHER LAYERS

In this chapter, we first analyse the technical innovations that can be introduced in a LEO satellite payload design towards increasing flexibility in service deployment. The work performed within ETHER includes a real implementation of a flexible payload design using Commercial-Off-the-Shelf (COTS) evaluation boards. The network management aspects of a constellation of satellites configured with flexible payloads is also analysed via the introduction of an orchestration platform encompassing the GS and the payloads. The integrated design is the base for the ETHER Use Case 1, titled “Flexible payload-enabled service provisioning to semantics aware and delay-tolerant IoT applications”, which is described in detail within ETHER deliverable D2.2 [2].

Subsequently in the chapter, by leveraging the flexible payload enabler we present two areas of the unified ETHER network that require effective mitigation of interference. These are: i) Dynamic common spectrum management in concurrent downlink transmissions to ground users of terrestrial gNBs and LEO satellite-based gNBs, and ii) reduction of the interference that LEO satellites can cause to GEO-satellite receivers on ground through effective power control.

4.1 DEVELOPMENT OF ETHER SOFTWARE-BASED FLEXIBLE PAYLOAD FRAMEWORK

4.1.1 Summary from D3.1 document

For a more accurate follow-up and better comprehensive view of the flexible payload development stages in ETHER, it is suggested to review deliverable D3.1 [1], which includes a more detailed view on some of the aspects of the below summary.

Background

Task 3.2 aims to develop a flexible payload architecture for LEO satellite missions, enabling the deployment of software-controlled payloads and reducing costs. The selected approach utilizes a framework composed of hardware COTS (Commercial Off-The-Shelf) electronic components and software modules, allowing for the execution of third-party (operators) software-controlled applications and services.

Until now, payloads were mission-specific [27] [28], and all components (both hardware and software) were designed to perform specific functions being complex to repurpose in future missions. In an attempt to improve reusability between missions, some manufacturers have begun to include features in their developments that allow for a certain degree of flexibility. However, there is still a long way to go, given that the update options they offer are minimal (i.e., the main function is pre-determined) and parameters must be defined before satellite launch. Some commercial and literature solutions are:

- Software-controlled multi-front-ends (using Software-Defined Radio concept) that support different spectrum bands with a single hardware platform [29], [30], [31].
- The use of Digital Signal Processing (DSP) modules with software configurable parameters [32] to change protocol variables, modulation type or transmission bandwidth and power).

- At global level, simulations of the behaviour of dynamic satellite systems within a global TN and NTN network environment to study the operations required by GSs [33], [34].

Motivation and contribution

ETHER's flexible payload architecture goes beyond previous initiatives and provides a rich ecosystem that manages the execution of fully dynamic services, regardless of whether they are software or hardware in nature.

Flexible payloads appear from the need to abstract and decouple satellites from missions at a low cost. In ETHER this is achieved by using standard electronic components (COTS) instead of space-grade solutions which reduces manufacturing and debugging time. On the downside, this type of electronics is less tolerant to failures, especially in space environments where radiation spikes and wide temperature changes can have a very negative impact. This can be mitigated by including backup components and/or tolerating a momentary loss of service (while the satellite is reconditioned in flight).

One of the important features of the ETHER payload design is its independence from the on-board computer (OBC). The base chip is separated from the main platform chip (OBC), as is the current trend in CubeSats, and an FPGA-based system-on-chip (SoC) is chosen as the main payload component. The Figure 4-1 shows a graphic comparative of market available options that could have fit the design. Section 4.1 in D3.1 [1] details the advantages and disadvantages of each and justifies the choice of an FPGA SoC. In summary, this option meets the criteria of flexibility (offering ARM processors and programmable logic), energy efficiency, and performance, while maintaining a reasonable cost.

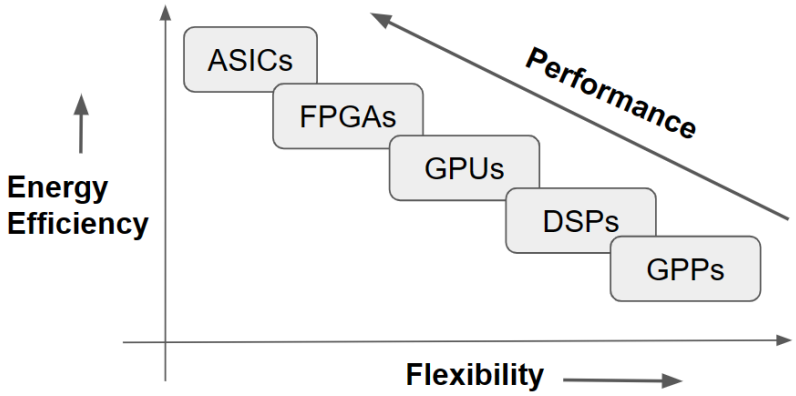

Figure 4-1 Trade-offs to face when selecting a processor architecture for SDR

Architecture and challenges

The flexible payload is a hardware and software-based framework prepared to run over a generic Satellite payload platform via the execution of a custom Linux OS. It adopts the Software-Defined Radio concept by managing the data path between the main system processor and any available Radio Frequency transceiver. To materialise the design, the framework relies on recent FPGA SoC technology, which offers enough resources to deploy an entire payload system in a single Integrated Circuit (IC) combined with a high-speed transceiver.

Given the abundant computational resources currently offered by these platforms, the framework can deploy infrastructure relying in three different levels:

- Level 1: Hardware deployment by programming the available logical resources. The framework has a mechanism to **reprogram in-flight** the empty logic cell areas in-flight to accommodate additional hardware services or replace existing ones.
- Level 2: Software deployment by integrating **containers as a virtualisation mechanism**. Services are deployed inside containers and abstracted from the main OS.
- Level 3: Remote management of the services by using **orchestration** from Ground Station or from other satellites within the constellation via Inter-Satellite Links (ISL).

The general architecture of the flexible payload is shown in Figure 4-2.

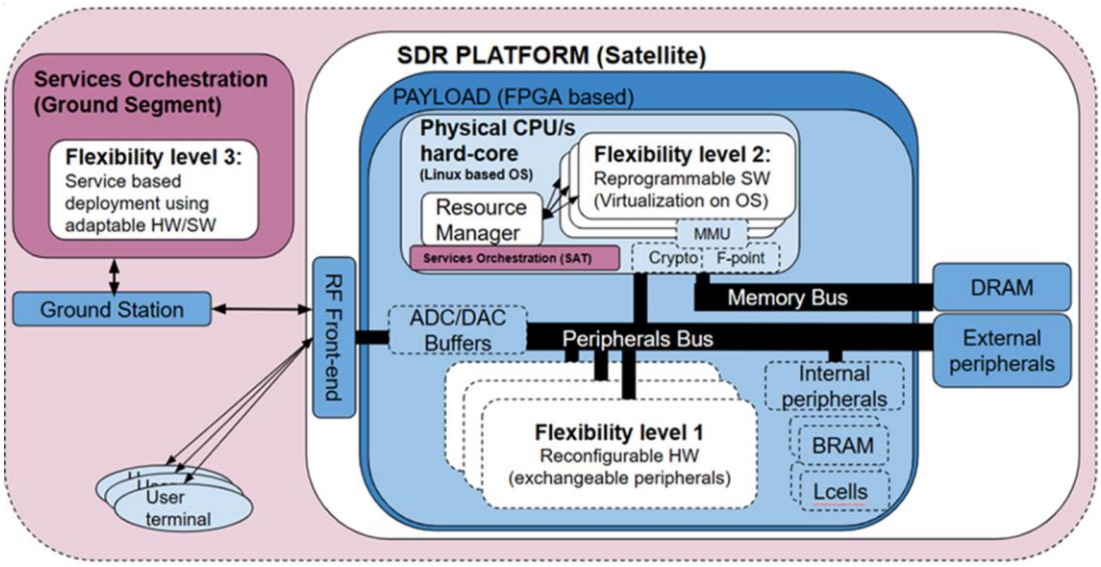

Figure 4-2 General architecture of the flexible payload

The FPGA family selected to demonstrate the framework is the Xilinx Ultrascale+ which has real flight experience as it has been integrated successfully in a wide variety of CubeSats. To act as a complete SDR, the FPGA is connected to an AD936x Analog Devices transceiver offering up to 6 GHz of band coverage and a tuneable channel bandwidth up to 56 MHz. The framework uses a custom Linux OS to control more efficiently the included libraries, using the PODMAN framework to deploy containers and K3s for orchestrate.

Deliverable D3.1 [1] delves into the choice of containers as a virtualization mechanism over other options [35], [36], [37] (virtual machines or even microKernels) and justifies the benefits for this use case in combination with the orchestration. It also presents the network management options to scale and the vision that the framework is easily integrable into the Network Functions Virtualization Infrastructure (NFVI) architecture as a virtualisation layer since high-level applications (software) as well as hardware components are available. This vision matches with the NFV premise of virtualising all physical network resources via available VIM (containers in the ETHER-specific case).

If focus is on resource utilization, up to 6 possible types of operator services appear, listed in Table 13:

Table 13 Service's resource mapping

SERVICE/TASK TYPE	HW MAPPING	SW MAPPING	RECONFIGURABLE
Static service (Executes on PL)	Static logic area	-	No
Static service (Executes on PS)	-	Linux OS space	Yes, using Linux App
Static service (Executes on PS/PL)	Static logic area	Linux OS space	No
Flexible service (Executes on PL)	Dynamic logic area	-	Yes, using FPGA reconfiguration
Flexible service (Executes on PS)	-	Linux OS space or container	Yes, using containers/Linux App
Flexible service (Executes on PL/PS)	Dynamic logic area	Linux OS space or container	Yes, using containers/Linux App and FPGA reconfiguration

Resource sharing is achieved by connecting new services (acquire a peripheral role) to the AXI (Advanced eXtensible Interface) system bus to exchange data via the CPU to other resources. Linux OS can interact with peripherals by mapping them into the system using the Memory Management Unit (MMU). RF transceiver and RAM memory are good examples of peripherals that can be shared.

Work progress

As detailed in D3.1 [1] the workplan for the flexible payload development is divided in different phases. As of the closing date of document D3.1 [1], phases 1 through 6 (except phase 5) were completed. The work already achieved and presented was:

- Selecting a platform (ZCU104) sufficiently representative for testing the entire payload environment at the laboratory level.
- Creating a customized Linux operating system, including libraries for interacting with the transceiver (libiio), the PODMAN virtualization tool, and the K3s orchestrator.
- General system tests (with everything integrated).
- Specific tests of individual peripherals (i.e., RF interface).
- Virtualization tests with containers.
- Orchestration and integration tests with K3s in single node scenario (orchestrating from Ground Station).

The next subsections will focus on the new achievements from D3.1 till current deliverable.

4.1.2 Orchestration extension (multinode and high availability scenario – level 3)

Building upon the single-node architecture validated in the initial phases and detailed in deliverable D3.1 [1], the subsequent work focused on extending the orchestration framework to support multi-node, and high-availability (HA) scenarios. This evolution was necessary to address the scalability and resiliency requirements of a fully operational Non-Terrestrial Network (NTN). The work performed corresponds to the advanced scenarios outlined in the phase 7 to 12, transitioning the framework from a single point of control to a distributed, cooperative system. This legacy system treats each satellite as an isolated node. This single node system lacks inter-satellite communication and resource sharing, limiting the cooperative capabilities that are standard in terrestrial datacentres. To unlock the full potential of a "datacentre in space," it is imperative to evolve beyond this model and develop an architecture that integrates satellites into a cohesive multi-node cluster, capable of sharing resources and executing complex, distributed functionalities [38].

4.1.2.1 Implementation with BATMAN, ISL, and GS Relays

The proposed multi-node architecture, showed in Figure 4-3, addresses these challenges by uniting multiple satellites into a single, hyper-connected cluster. In this model, inter-satellite links (ISLs) serve as the primary communication backbone, enabling direct, low-latency communication between nodes. This is supplemented by a distributed network of ground stations (GS) that function as relay hops, ensuring comprehensive connectivity even when direct ISL paths are unavailable, significantly improving network resilience and data routing efficiency.

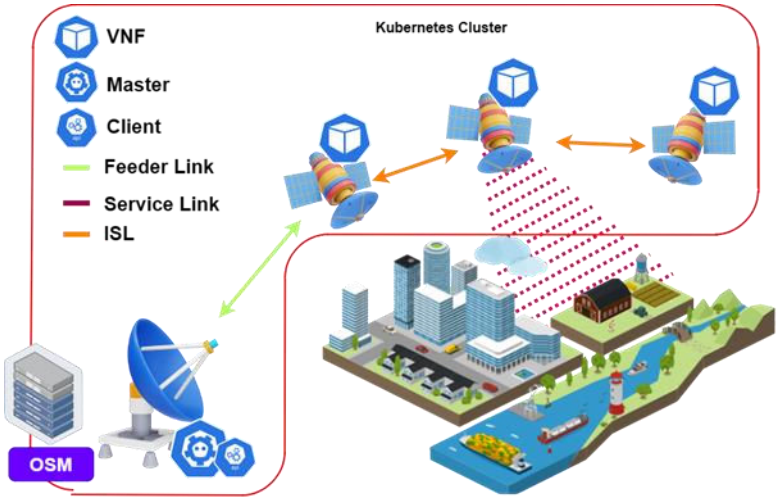

Figure 4-3: Kubernetes Multi-node satellite cluster architecture

ISL integration enables real-time coordination between satellites without dependence on ground station visibility windows. This capability is crucial for maintaining cluster coherence during orbital transitions and enables service handover mechanisms that preserve user connectivity across satellite coverage areas [39].

Managing the network within this highly dynamic environment is challenging, as the orbital mechanics induce a constantly changing network topology, analogous to a mobile ad-hoc network (MANET) [40]. To address this, we have implemented the Better Approach To Mobile Ad-hoc Networking (BATMAN) protocol. BATMAN is a proven routing protocol that excels in

such scenarios, allowing us to leverage a standard and robust technology to manage the mesh network.

BATMAN's proactive routing approach maintains current topology information through periodic originator message (OGM) broadcasts, enabling rapid route convergence when network changes occur. The protocol's distance-vector foundation with transmission quality metrics ensures optimal path selection considering both hop count and link reliability [41]. This protocol, combined with the hyper-connected infrastructure of ISLs and GS relays, creates a resilient and self-organizing mesh network for the cluster as is shown in Figure 4-4.

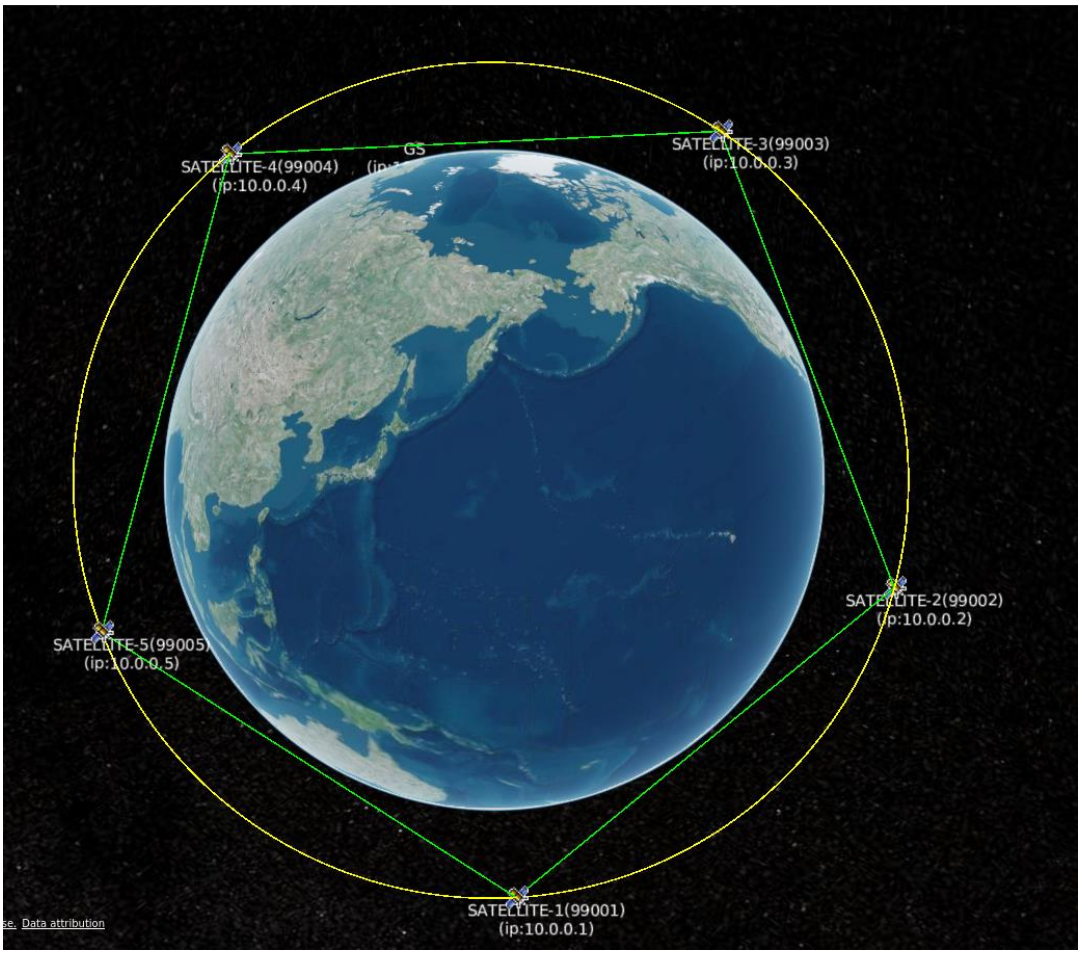

Figure 4-4: Hyper connected satellite network with ISL

4.1.2.2 Multi-Node Service Orchestration and the Service Management Model

Service orchestration is significantly streamlined in the multi-node architecture. Unlike the single-node approach, which requires a manual, time-consuming process to deploy a Network Service (NS) to each satellite via Open Source MANO (OSM) [42], the multi-node cluster allows for distributed deployment. A service deployed from OSM to any single satellite with GS contact can be efficiently propagated across the entire cluster through the BATMAN-managed network.

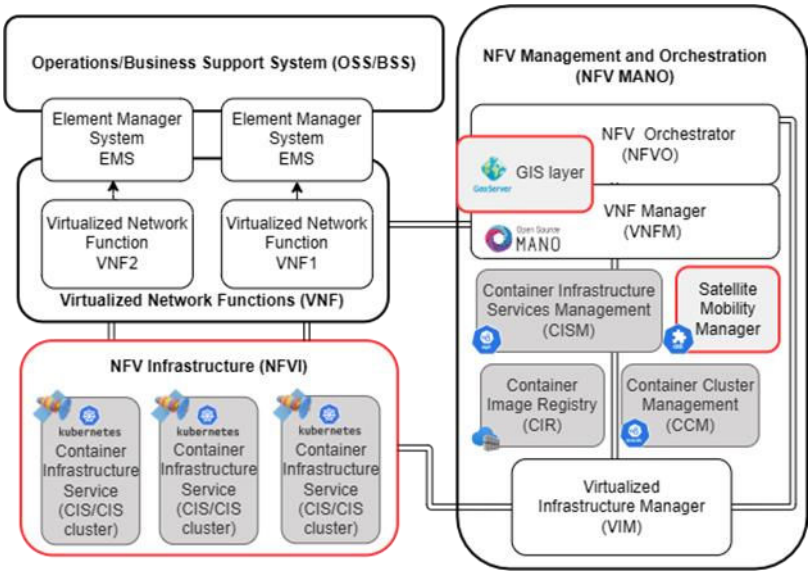

Figure 4-5: ETSI NFV architecture, enhanced for multi-node satellite cluster

To manage service placement within this distributed environment, the Satellite Mobility Manager (SMM), showed in Figure 4-5, has been adapted to use a labelling architecture. From the OSM platform, each satellite node is assigned a unique identifier or label. This allows the orchestrator to intelligently target the appropriate NS to each satellite based on its specific mission, orbital parameters, or real-time resource availability. While the distribution of services is simplified, the service logic must still be tailored for each satellite, as each has a unique orbit and corresponding contact windows for service activation and deactivation.

4.1.2.3 Evolution to a Distributed Control Plane

The initial multi-node implementation relies on a control plane located on a central master node on the ground, accessible via the GS network. While functional, this represents a potential single point of failure. The architecture is designed to evolve into a fully distributed control plane to achieve high availability (HA). The proposed architecture unites multiple satellites into a single, operationally coherent system where each satellite functions as a cluster node governed by a distributed control plane, as is shown in Figure 4-6. Unlike traditional centralized approaches, this architecture employs multiple control plane instances distributed across both ground stations and satellite nodes, ensuring continuous operational capability despite individual node failures.

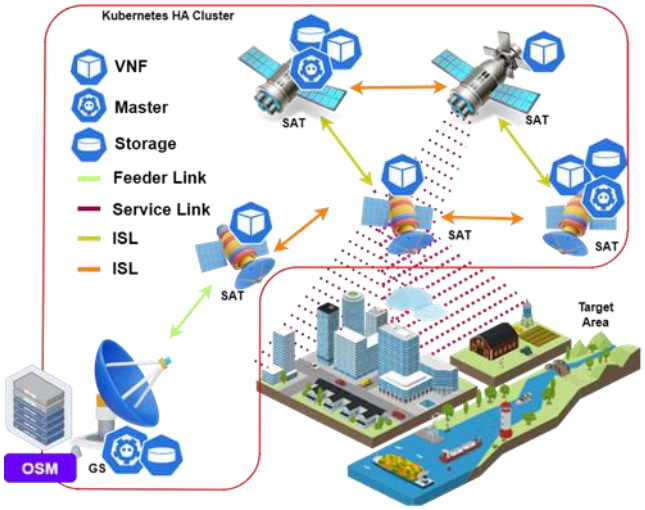

Figure 4-6: Satellite Multi-node architecture with distributed control plane for HA

By creating a multi-master, distributed control plane, the system's resilience is significantly enhanced. In the event of a failure of one master node, another can seamlessly take over cluster management responsibilities, ensuring uninterrupted service orchestration and network operation. This distributed HA configuration transforms the satellite constellation into a truly robust and fault-tolerant computing cluster, mitigating risks and ensuring the continuous availability of mission-critical services. The distributed control plane leverages K3s, a lightweight Kubernetes distribution specifically optimized for resource-constrained environments. K3s provides the necessary orchestration capabilities while maintaining minimal resource overhead, making it suitable for deployment on satellite platforms with limited computational resources. The control plane's distributed nature ensures that cluster operations continue seamlessly even when individual master nodes become unavailable due to orbital mechanics or hardware failures.

4.1.2.4 High Availability Implementation

High availability in the multi-node cluster is achieved through multiple redundancy layers and automated failover mechanisms. The primary HA components include:

- Control Plane Redundancy: Multiple master nodes are distributed across the satellite constellation and ground infrastructure, with each capable of assuming cluster management responsibilities. This eliminates single points of failure inherent in centralized architectures and ensures continuous service availability during planned maintenance or unexpected outages.

- Distributed State Management: Cluster state information is replicated across multiple nodes using consensus algorithms, ensuring data consistency and availability even during network partitions. The etcd distributed key-value store maintains cluster configuration and service state across all control plane nodes.

- Automatic Failover Mechanisms: The cluster continuously monitors node health and automatically redistributes workloads when nodes become unavailable. Service pods are automatically rescheduled to healthy nodes, and traffic routing adjusts dynamically to maintain service continuity.

4.1.3 Flexible Payload extension towards a Dynamic HW architecture

4.1.3.1 Context

Thanks to the diverse integrated resources in a System-On-Chip format, FPGAs offer a good mix of computing solutions, capable of covering almost any type of operation included in common telecommunication services. In FPGAs, these operations can mostly be executed in software (using the ARM processor) or in hardware (using programmable logic). Sometimes, connection to other peripherals such as memory, RF channels, etc. may also be required. These are generally accessible through memory mapping with the CPU or using direct connection to the logic cells.

In the space use case, selecting to which resource a service (or part of it) should be mapped is considered an operator service planning decision. Criteria such as service efficiency (execution speed vs. energy consumption), system load (CPU and RAM available), as well as service deployment according to geographic area can play a key role for achieving the integration into the envisioned Network Functions Virtualization Infrastructure (NFVI) concept.

In this sense, the main objective of the payload designed in ETHER is to provide an environment with a high degree of flexibility to offer operators the ability to run services simultaneously or sequentially, regardless of whether they are software- or hardware-based. It is also important, the option to update or ex-change service functionalities following predefined premises via an automatised procedure.

The mechanisms to deploy software-based services were discussed and tested in D3.1 [1]. The use of containers is preferred over virtual machines or microkernels in software virtualization, given their proven efficiency in embedded systems. The presented framework uses the PODman environment (very similar to the well-known Docker) to control the loading and execution of container images. This task, along with the integration of PODman with K3s (the orchestrator), was completed in D3.1 [1], which primarily focused on the software aspects of the framework.

This section focuses on all the complementary hardware aspects required to complete a full dynamic framework.

4.1.3.2 Motivation

The space industry is undergoing a profound transformation driven by the NewSpace paradigm, which seeks to reduce the traditionally high costs associated with the development, maintenance, and debugging of space infrastructure. This cost reduction and process simplification can be addressed from multiple angles. In deliverables D3.1 [1] and future D4.2, it will be shown how orchestration mechanisms can be employed to intelligently deploy services—provided that appropriate system feedback and status information are available. These services can even be deployed in a distributed manner across satellite nodes, whether within a single constellation or dispersed among different constellations.

A key enabler of service deployment simplification in the NewSpace context is the adoption of Commercial Off-The-Shelf (COTS) electronics. COTS components, widely used and extensively tested by developer communities, are significantly more cost-effective than space-grade components, leading to considerable savings in both mission budgets and development timelines.

Another notable advancement in the NewSpace approach is the application of artificial intelligence to network resource management. This is particularly relevant for Ground Stations, which play a critical role in Low Earth Orbit (LEO) operations by intermittently interacting with

satellites throughout the day. Intelligent systems can help prioritize and manage traffic dynamically, significantly reducing the complexity of network management.

The nature of traffic generated by nanosatellites is highly heterogeneous—varying in bandwidth, latency, frequency, modulation, power, and intermittency—depending heavily on the onboard applications and services. Traditionally, spaceborne services were predefined and fixed for the entire mission duration. Each mission carried a static set of functionalities embedded in hardware and software prior to launch, meaning that replacing a service necessitated launching an entirely new satellite with different electronics and code.

The ETHER project addresses this rigidity by proposing the integration of a reconfigurable electronics layer into the flexible payload framework. As outlined in D3.1 [1], reprogramming or virtualizing software is feasible if the satellite host's CPU is powerful enough to run a Linux operating system and at the top of it virtualization technologies such as containers can operate. However, modifying hardware post-launch is inherently more complex due to the satellite's inaccessibility.

This is where FPGA (Field-Programmable Gate Array) technology becomes a strategic asset. FPGAs consist of reprogrammable circuit logic configured via design files known as bitstreams. These bitstreams effectively define the hardware functionality of an FPGA-based system and may include advanced components such as Look-Up Tables, multipliers, multiplexers, and auxiliary RAM blocks. Modern bitstreams can even instantiate complete computing systems with CPUs, memory, and interfaces—designed entirely through a hardware description language (HDL). In short, a bitstream is the compiled outcome of HDL synthesis and place-and-route processes.

The use of FPGAs in nanosatellite design is not novel—they are flight-proven with respectable performance in space environments. What is innovative in the ETHER proposal is the ability to reconfigure the original HDL-based design (and virtualization), enabling hardware-level reconfiguration. Modern FPGA families support both full and partial reprogramming of their bitstreams. ETHER explores this capability in an extreme-use scenario: in-orbit reconfiguration. The goal is to dynamically deploy or replace hardware-based services during the mission (in-flight), enabling mission objectives to be adapted mid-course and allowing the reuse of satellites that, although fully operational, have been decommissioned after fulfilling their original purposes.

It is important to distinguish between two modes of reconfiguration considered in ETHER: total and partial. Total reconfiguration involves replacing the entire FPGA design, whereas partial reconfiguration targets only specific hardware regions—known as Reprogrammable Partitions (RP)—leaving the static hardware intact. ETHER prioritizes partial reconfiguration, which, while more complex to implement due to the need for synchronization with a system entity (typically the operating system), offers significantly greater flexibility and efficiency by isolating service-specific hardware regions. The outcome of this work will contribute to the definition of a generalized and dynamic architecture for service deployment.

4.1.3.3 General overview of hardware architecture

The mapping of the logical architecture onto the available resources of the FPGA's SoC is illustrated in Figure 4-7. This figure shows how components are allocated on the Processing System (PS) side of the FPGA when they depend on software libraries or require support for standard operating system-level protocols and stacks. All virtualization mechanisms, as well as container orchestration and management, are handled on the PS side.

Conversely, the Programmable Logic (PL) region is dedicated to implementing functions—either static or dynamic—that benefit from hardware execution to enhance performance or achieve acceleration compared to software-based solutions. This includes reconfigurable

partitions (partial bitstreams), the RF chain, and various interface components that serve as glue logic to other peripherals (e.g., Ethernet, high-speed GPIOs, PCIe).

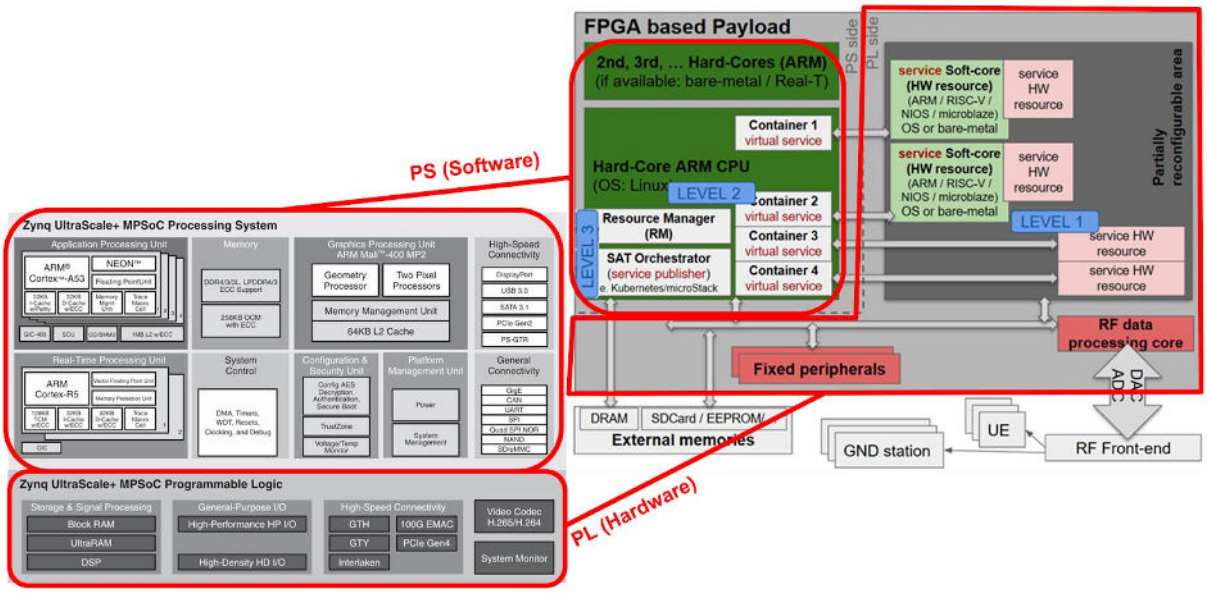

Figure 4-7 Mapping of the logical architecture onto the available resources of the FPGA's SoC

When narrowing the scope to services deployed fully or partially within the FPGA's hardware fabric, Figure 4-8 details the interaction between the architectural components involved in the dynamic reconfiguration workflow of Reconfigurable Partitions (RPs).

- The Processing System (PS) side contains traditional computing elements including a CPU, kernel modules, and memory, all interconnected through a DMA (Direct Memory Access) controller that enables efficient data movement between software and hardware components. The main reconfigurability on this part is provided by the orchestration explained in previous sections, with the addition of the capability to insert custom kernel modules during runtime for low-overhead data transfer operations that interact with the Programmable Logic.

- The Programmable Logic (PL) portion of the FPGA implements the core reconfigurable functionality through dedicated IP blocks designed for high-speed data processing. HDL IP cores can handle different aspects of data flow, depending on whether the data streams are outbound, bidirectional (i.e., full-duplex communication), or inbound. These IP blocks are strategically positioned within reconfigurable areas that can be dynamically modified during runtime without affecting the overall system operation.

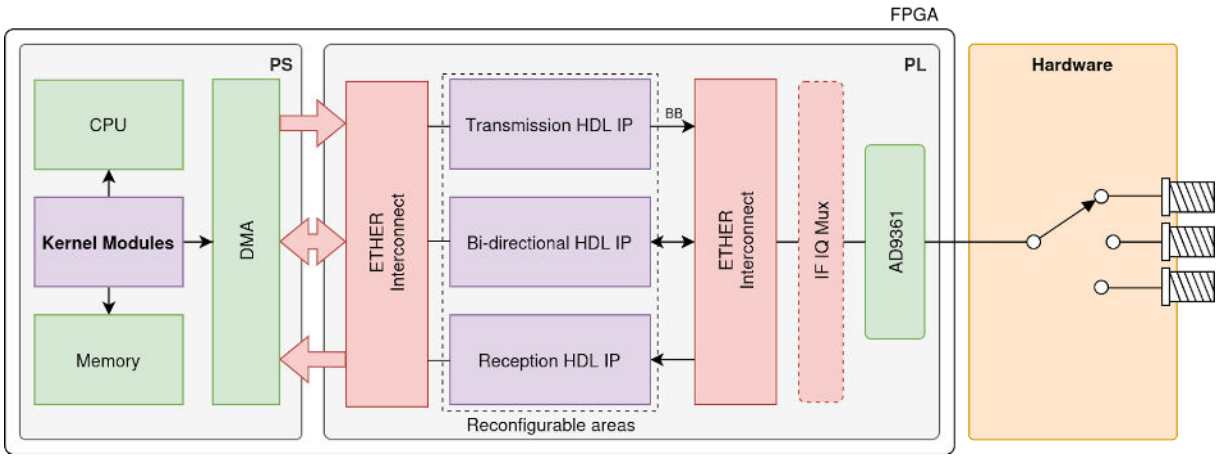

Figure 4-8 Overview of the elements involved in updating Reconfigurable Partitions (RP)

Communication between the PS and PL domains occurs through the so-called ETHER interconnect interfaces that provide high-bandwidth, low-latency data paths. These interconnect boundaries are designed to accommodate the typical interfaces needed by IP cores, such as AXI, AXI-Stream, or IQ (In-Phase and Quadrature) Samples. Due to simplex interface at the input of the transceivers, if the different transmitting IPs can work within the bandwidth provided, they can go through an Intermediate Frequency Multiplexer (IF IQ Mux) that joins the streams at their relative frequency related to the centre one and can direct data flows between the various IP blocks and the transceiver hardware interfaces. The AD9361 component represents the physical layer interface, connecting the FPGA processing capabilities to external RF hardware for real-world signal processing applications.

This architecture enables flexible payload configurations where different processing algorithms can be loaded into reconfigurable areas based on mission requirements, while maintaining consistent interfaces and data flow paths throughout the system. The modular design supports both static baseline functionality and dynamic reconfiguration capabilities essential for adaptive payload operations.

4.1.3.4 Resource sharing mechanisms (local node)

4.1.3.4.1 OS/SW sharing mechanisms

Between low-level hardware and high-level applications lies the kernel and its associated drivers (Figure 4-9), which maintain direct access to the hardware.

The kernel is a critical component of any operating system-based platform. While often associated with Linux systems, it serves as the core of many other architectures that require efficient management of memory and peripherals via a Memory Management Unit (MMU).

The more optimized the kernel functions are—typically implemented in C or C++—the better performance can be extracted from hardware peripherals at higher abstraction layers (user space or application layer). At the kernel level, interaction with hardware peripherals is typically handled through specific drivers or kernel modules. Consequently, the greater the number of supported peripherals, the larger the kernel's disk footprint and memory residency.

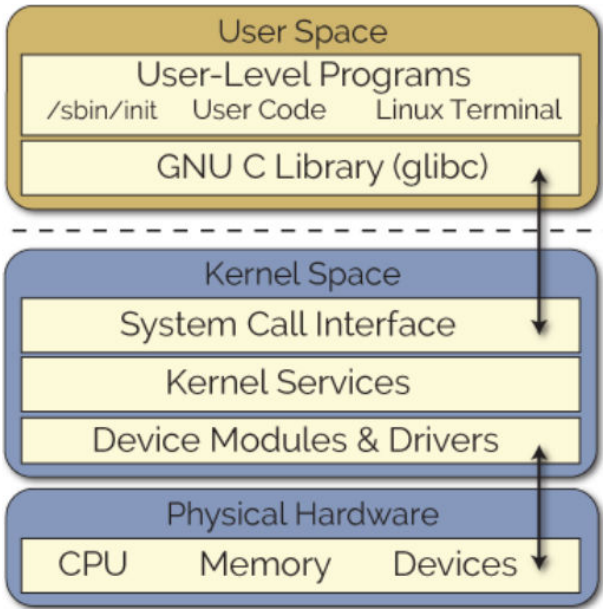

Figure 4-9 Linux abstraction layers (from [43])

The way kernel drivers are implemented plays a key role in enabling optimal sharing of hardware resources across the system. Driver design may involve decisions such as the inclusion of software buffers to adapt input/output rates, function parallelization for concurrent processing, prioritization of execution threads, or support for multiplexed access to the same device by multiple processes. A key point for the reader to understand is that peripheral access performance can vary significantly depending on the specific driver version used for the same hardware device.

In the Flexible Payload Framework, kernel drivers have been utilized to interface with several critical peripherals within the payload. These drivers are mostly developed by the peripheral manufacturers themselves and provide operating system-level access interfaces. The most notable among them include:

- **RF Transceiver:** Analog Devices kernel module ad936x
- **RAM Memory:** Generic Linux module Xilinx/ARM-provided
- **DMA Controller:** Custom i2CAT kernel module optimized to fix issues found in the official module provided by Xilinx
- **Bus Controllers:**
  - AXI: Xilinx/ARM-provided (detailed in D3.1 [1]).
  - I2C: Xilinx/ARM-provided
  - RS232: Xilinx/ARM-provided
- **Memory Management Unit:** Xilinx/ARM-provided (detailed in D3.1 [1]). It is used for peripheral memory mapping.

The DMA module is particularly important for hardware reconfiguration, as it serves as the generic data input/output interface used to feed the partial reconfiguration partitions (RPs). A FIFO-type software buffer has been inserted alongside the DMA to adapt data throughput to variable rates. The reconfigurable service is architecturally situated between two DMAs (input and output), both of which are reset each time the service configuration is changed.

As for the static hardware, in addition to the usual resources (CPU, system bus, AXI peripherals, memory buses, etc.), an RF transceiver has been integrated. Depending on the driver, this transceiver can operate with either one or two transmission channels. Consequently, one of the limitations imposed by the driver is the inability to simultaneously transmit across more than two frequency-band-separated services. This constraint ultimately stems from the hardware chip design itself. Later, we will explore potential solutions to this limitation—particularly in the context of service sharing—which could be considered for future implementations.

4.1.3.4.2 HW sharing mechanisms (to enable HW reconfiguration)

As previously discussed, the flexible payload features a cross-layer architecture, where the key aspect is the use of FPGA technologies to enable the deployment and management of services across different layers—both hardware and software—depending on technical requirements and, primarily, deployment agility. In this context, as has already been briefly outlined, the internal FPGA architecture at the logical level comprises a generic static region including resources that are always available, as they are not exclusively tied to service deployment. The components identified in the ETHER architecture for this static region—which support the mechanisms responsible for managing both hardware and software reconfiguration—are shown highlighted in orange in Figure 4-10.

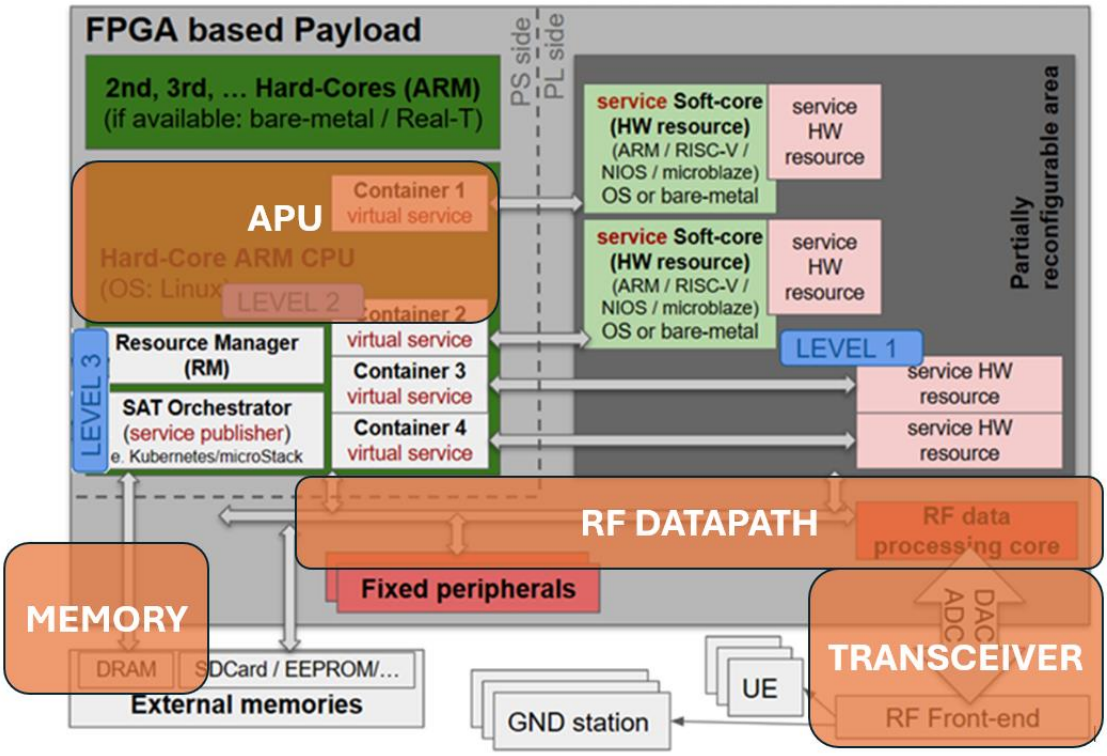

Figure 4-10 Components placement of the static resources used in a RF communication

In addition, this static region is complemented by the so called dynamic region (which include Reconfigurable Partitions), designed to adapt to the specific needs of the services. An illustration of how this division between static and dynamic regions is structured in the FPGA can be found in Figure 4-11.

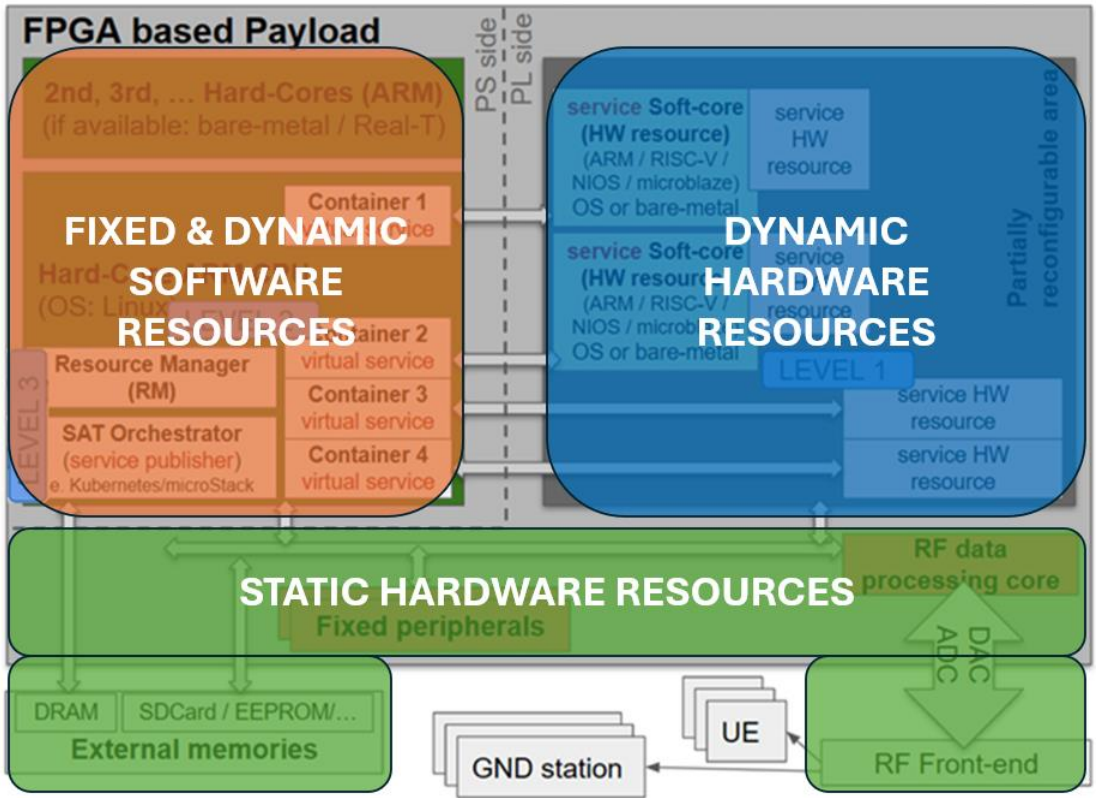

Figure 4-11 Placement of different payload resources & Flexible Payload division

Complementary to the hardware sharing mechanisms that can be achieved through FPGA reconfiguration, it is important to consider external hardware multiplexing that can provide further functionality in parallel to the aforementioned methods. For instance, power multiplexing and switching can be beneficial for powering up and down circuitry in combination with the FPGA reconfiguration, allowing for further instruments to be connected to the system in response to changing priorities. In terms of RF, by implementing switching networks outside the FPGA domain, the system gains the ability to dynamically route RF signals between multiple antennas, frequency bands, and processing chains without consuming valuable FPGA logic resources.

4.1.3.4.3 RF sharing mechanisms options and discussion

Current transceiver configurations in many spaceborne RF payloads operate in simplex mode, where the AD9361 or similar transceivers can only accept a single stream of IQ data at any given time. This limitation creates a significant bottleneck in multi-channel systems, as multiple IP cores generating different communication protocols or data streams must compete for access to the shared RF frontend. In such architectures, IP cores must effectively "take turns" transmitting, requiring complex scheduling and arbitration logic to determine which core has access to the transceiver at any given moment. This time-division approach inherently wastes valuable transmission opportunities and reduces overall system throughput, as only one communication channel can be active while others remain idle regardless of their data requirements or priority levels.

Implementing RF multiplexing through VHDL-based intermediate frequency processing addresses these limitations by creating a highly flexible and resource-efficient architecture for managing multiple simultaneous RF channels. This approach leverages the computational power of the FPGA to perform complex signal processing operations that combine multiple IQ streams before reaching the transceiver, transforming the simplex limitation into a true multi-channel capability.

The fundamental advantage of IF-based multiplexing lies in its ability to aggregate multiple baseband IQ streams from different IP cores into a single composite signal for transmission. This aggregation dramatically reduces the number of required RF chains, as multiple independent communication channels can share a common final RF stage through the AD9361. For spaceborne applications, this translates to significant reductions in power consumption, mass, and volume compared to implementing separate RF chains for each channel. Channels can be dynamically activated, deactivated, or reconfigured through software updates without any hardware modifications. This capability is particularly valuable for missions where communication requirements evolve over time or vary based on orbital position, operational phase, or changing ground station availability. The ability to reprogram channel configurations in-flight enables rapid response to changing mission priorities or emergency scenarios.

4.1.3.5 Service deployment/replacement methods

4.1.3.5.1 SW-based services deployment

The deployment of software services has been discussed throughout deliverable D3.1 [1]. The use of PODMan as a container manager enables the deployment of any service encapsulated within a container image. Although this is a proven mechanism in other domains, virtualization technologies are not commonly employed in space environments. This is primarily due to the additional complexity they introduce in event monitoring, as well as the potential performance degradation compared to running a native application. Nevertheless, advancements in virtualization mechanisms have progressively mitigated these drawbacks.

To summarize, several key requirements must be met for a container to be deployable from the platform using the flexible payload framework:

1. Architecture Compatibility: The container must be compatible with the ARM64v8 architecture, which is native to the platform. While it is technically possible to execute content designed for other architectures through emulation, this approach is strongly discouraged due to the severe performance penalties it incurs.

2. Host Kernel Compatibility: It is essential to ensure that the host kernel includes all necessary modules required by the containerized service. Since the container's guest operating system inevitably relies on the host kernel, missing modules could lead to service malfunction. For instance, the IPTABLES package depends on specific kernel modules to perform network traffic filtering. If these modules are absent, proper filtering cannot be achieved.

3. Container Size: When deploying a service for the first time, the container image may not yet exist on the satellite node. In such cases, the orchestrator will initiate the upload of the image to the target node. Given the use-case scenario in Low Earth Orbit (LEO), where communications are intermittent, larger container images require more ground station passes to be fully downloaded to the satellite. This introduces both a time and data transmission cost. For instance, even a few hundred megabytes might take up to a full week to complete, depending on ground station availability.

4. Resource Management: By default, the RAM and CPU resources available to a container are capped according to pre-defined consensus values. These limits help prevent individual containers from monopolizing system resources, which could otherwise lead to system instability or total host failure. As such, the development of monitoring services - though not initially covered in the ETHER framework- is intrinsically tied to this challenge and represents a critical area for further evolution.

The PODman environment integrates a comprehensive set of commands for container lifecycle management, including construction, creation, loading, and unloading of containers. Among its most relevant command categories are:

- **Repository-related** commands:
  - pull: Retrieve an image from a remote registry
  - push: Upload an image to a registry
  - images: List locally stored container images
  - ps: Display a list of running or stopped containers
  - load: Import an image from a TAR archive or standard input
  - save: Export one or more images into a TAR archive (streamed to standard output by default)
  - rmi: Remove one or more images from the local repository
- **Image management** commands:
  - run: Instantiate and launch a new container based on a given image
  - exec: Execute a command within a running container
  - build: Construct a container image from a Dockerfile
- **Status monitoring** commands:
  - logs: Retrieve container log outputs
  - stats: Display real-time resource usage statistics for one or more containers
- **Internal PODman** commands:
  - version: Display version information of the container runtime
  - info: Provide system-level metadata and status
- **Container state control** commands:
  - start: Initiate one or more previously stopped containers
  - restart: Restart container execution
  - pause: Suspend all processes within one or more containers
  - stop: Terminate container processes while retaining memory allocation
  - rm: Permanently remove one or more containers from the system

Typically, PODman can be configured to maintain a local image repository on the satellite node (Figure 4-12). While online registries could be leveraged, the preference within the mission context is to use onboard repositories to maintain strict control over network traffic and data flow. These repositories serve as the source of deployable service containers.

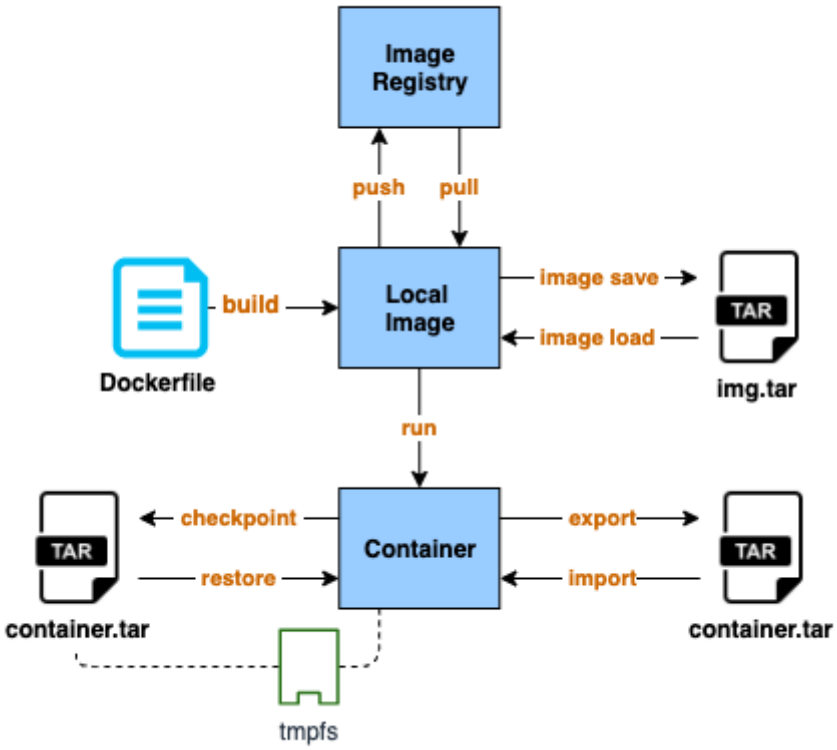

Figure 4-12 PODman image creation flow (From [44])

Each container can exist in one of several states: start (running), pause (execution temporarily suspended), stop (terminated but still occupying system memory), or rm (fully removed from the system). When supervised by the K3s orchestrator, PODman can transition containers between these states as required by the operational context.

Additionally, PODman exposes diagnostic and performance data—such as logs and real-time metrics—which can be made available to higher orchestration layers via integration with K3s, thereby enabling informed decision-making and autonomous service management.

Additional auxiliary tools can complement the typical container deployment workflow in environments such as PODMan (or its counterpart, Docker). Notably, podman-compose stands out as a tool that facilitates the description of image build and runtime configurations through simplified YAML files.

This tool enables the orchestration of multi-container applications and the declarative definition of services, volumes, and networking, thereby streamlining the deployment process. A typical Docker/PODMan execution flow, as envisioned for use within the ETHER framework, is illustrated in Figure 4-13.

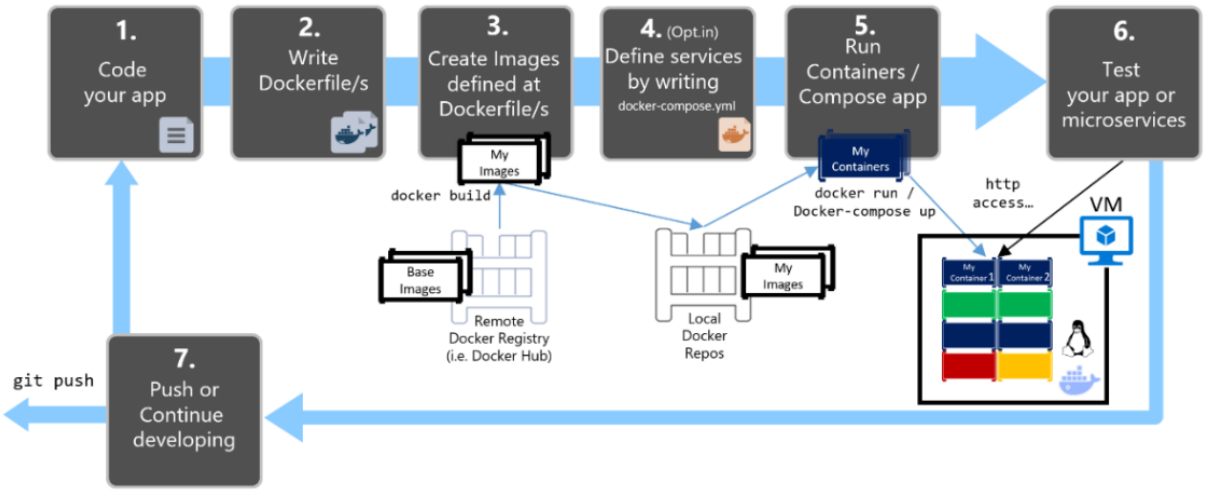

Figure 4-13 PODMan/Docker development workflow (From [45])

4.1.3.5.2 HW-based services deployment

Similarly to software-based services, PODMan can also be utilized to deploy hardware services. This essentially involves replacing the existing bitstream that configures the reprogrammable logic with a new bitstream representing the desired hardware configuration. While PODMan does not natively support hardware bitstream deployment, certain adjustments can be made to the container structure to enable this functionality. In any case, all the command structures and operational states described for software deployment remain fully applicable to hardware services with slight modifications that are detailed in the below points:

- **Bitstream Generation:** The bitstream must be generated using the specific FPGA vendor's toolchain. At a minimum, a full (base) bitstream is required to define the static region of the FPGA, including the empty Reconfigurable Partitions (RPs). Additionally, one or more partial bitstreams (services) must be generated for each specific hardware service, as determined by the architecture outlined at the beginning of the section.

- **Container Image Composition:** When building the container image (step 3 in Figure 4-13) for a hardware service, the following files must be included in the Dockerfile:
  - **Device drivers** required to interact with specific hardware peripherals (if applicable to the service).
  - **Partial bitstream file**, representing the hardware logic of the service.
  - **Reconfiguration utility** compatible with Linux. Within the ETHER framework, we use FPGAUtil due to its ease of use and integration with Xilinx's FPGA Manager framework (as detailed in D3.1 [1], section 4.1.4.4.2).
  - **Software code**, if the service is hybrid in nature and includes both software and hardware components.

- **DMA Safety Check**: Prior to deploying a new container image that reprograms the FPGA, it is critical to ensure that existing DMA channels are not disrupted. It is therefore recommended to unload the DMA driver from the host OS beforehand (step 5 in Figure 4-13).

- **Bitstream Loading and Service Execution**: Upon launching the container with PODMan, the first instruction executed should invoke FPGAUtil to load the new bitstream into the FPGA (step 6 in Figure 4-13). After reprogramming, the DMA kernel modules must be reloaded, followed by the execution of any complementary software code (if present).

Finally, the remaining secondary processes included in the container image can be launched.

4.1.3.6 Performed tests

To test the dynamic hardware reconfiguration on a real SoC, an HDL-based hardware design has been developed, following the architectural principles outlined in above sections. The design is partitioned into two distinct regions: a **static region**, which is always present and operational, and a **dynamic region**, intended for partial reconfiguration. The full implemented Vivado design is illustrated in Figure 4-14:

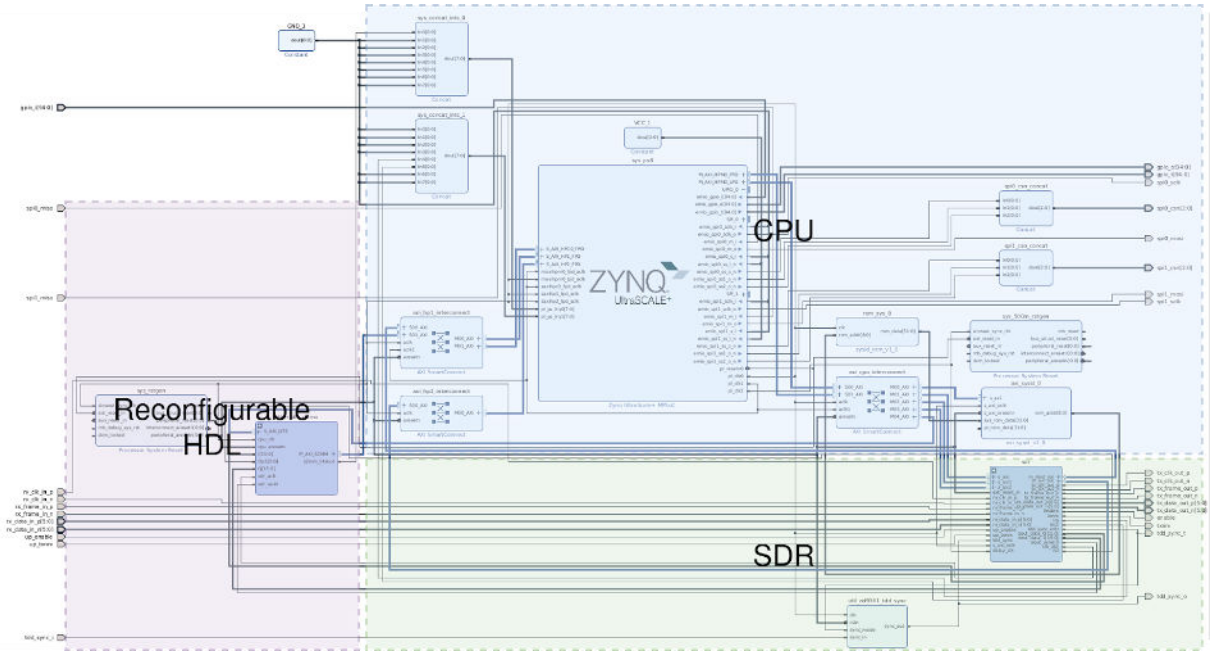

Figure 4-14 Vivado HDL design used for testing Flexible Payload framework

1. **Static Region:** This section comprises all fixed system modules, including:
   - **ZYNQ Processing System**: configured with CPU settings.
   - **SDR Subsystem**: integrating the AD936x transceiver and its corresponding interfaces.
   - **ether_dfx_demo**: which includes:
   - An integrated logic analyser (ILA) instance (*ila_0*) for debugging.
   - A generic DMA controller (*ether_dma*) used to extract data from the Reconfigurable Partition (RP).
   - The interface modules connecting to the RP (*ether_DFX*).
   - **AXI Interfaces and peripheral connections**: supporting communication with secondary system components.
2. **Dynamic Region (ether_dfx_demo)**: This region contains all the HDL IP blocks corresponding to services subject to dynamic reconfiguration. As a test case, a Fast Fourier Transform (FFT) service has been implemented (see Figure 4-15). This service will later serve as the foundation for an RF interference scanner in ETHER Demo1 (WP5). Key IP modules instantiated within the RP for the FFT service include are:

- **IQ Formatting** (*concat_iq_fft*): acquires and reformats IQ input signals to match the FFT input specifications.
- **FIFO Buffer** (*fifo_generator*): manages data flow and ensures proper timing alignment with the FFT core.
- **FFT Core** (*fft*): implements the Fast Fourier Transform algorithm.
- **CORDIC** (*cordic_abs*): computes the magnitude of the FFT output using a CORDIC algorithm.
- **FFT Accumulator** (*fft_accum*): averages up to 8 FFT samples to enhance signal stability and reduce noise.

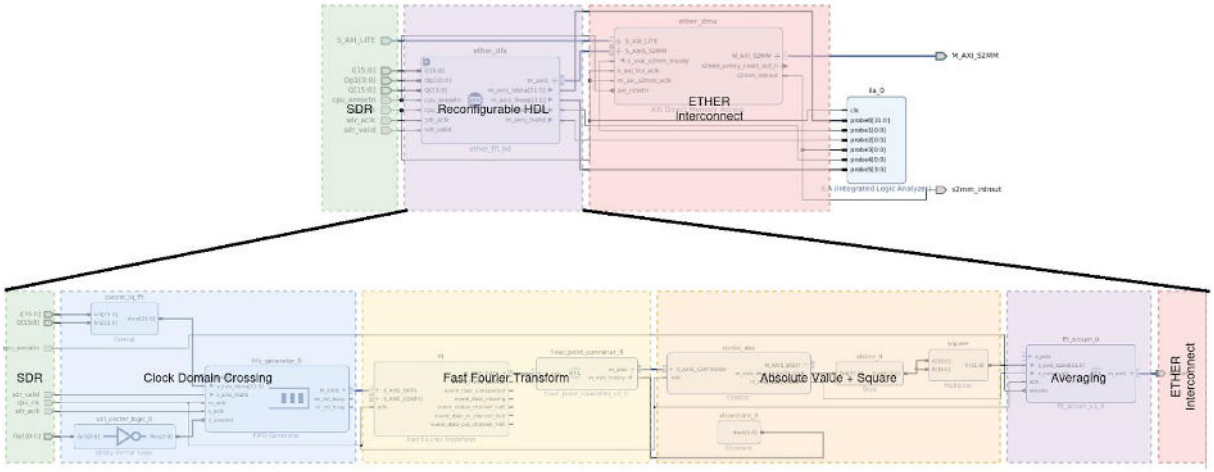

Figure 4-15 Dynamic Reconfigurable partition content for FFT example service (ether_dfx_demo)

Regarding the scope of the test, to simplify and focus the experiment exclusively on the dynamic reconfiguration aspects, the design of elements for multiplexing intermediate frequency (IF) IQ signals has not been considered, nor has a transmission DMA been included. This is because the FFT example selected for the current use case (RF interference) only requires signal reception, without the need to transmit data. These developments will probably be carried out in the future, outside the scope of the ETHER project. The final implemented scheme for the test is illustrated in Figure 4-16. Non-grey parts correspond to final ETHER architecture design:

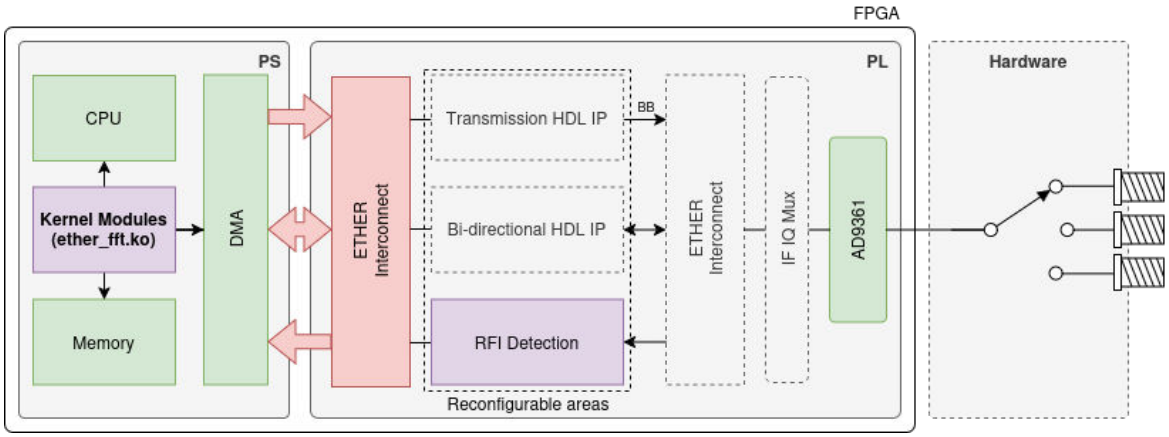

Figure 4-16 Elements involved in update Reconfigurable Partitions (RP) in ETHER payload test

Once synthesis and place-and-route are completed in Vivado, the HDL design is fitted onto the ZCU104 SoC FPGA layout, as depicted in Figure 4-17.

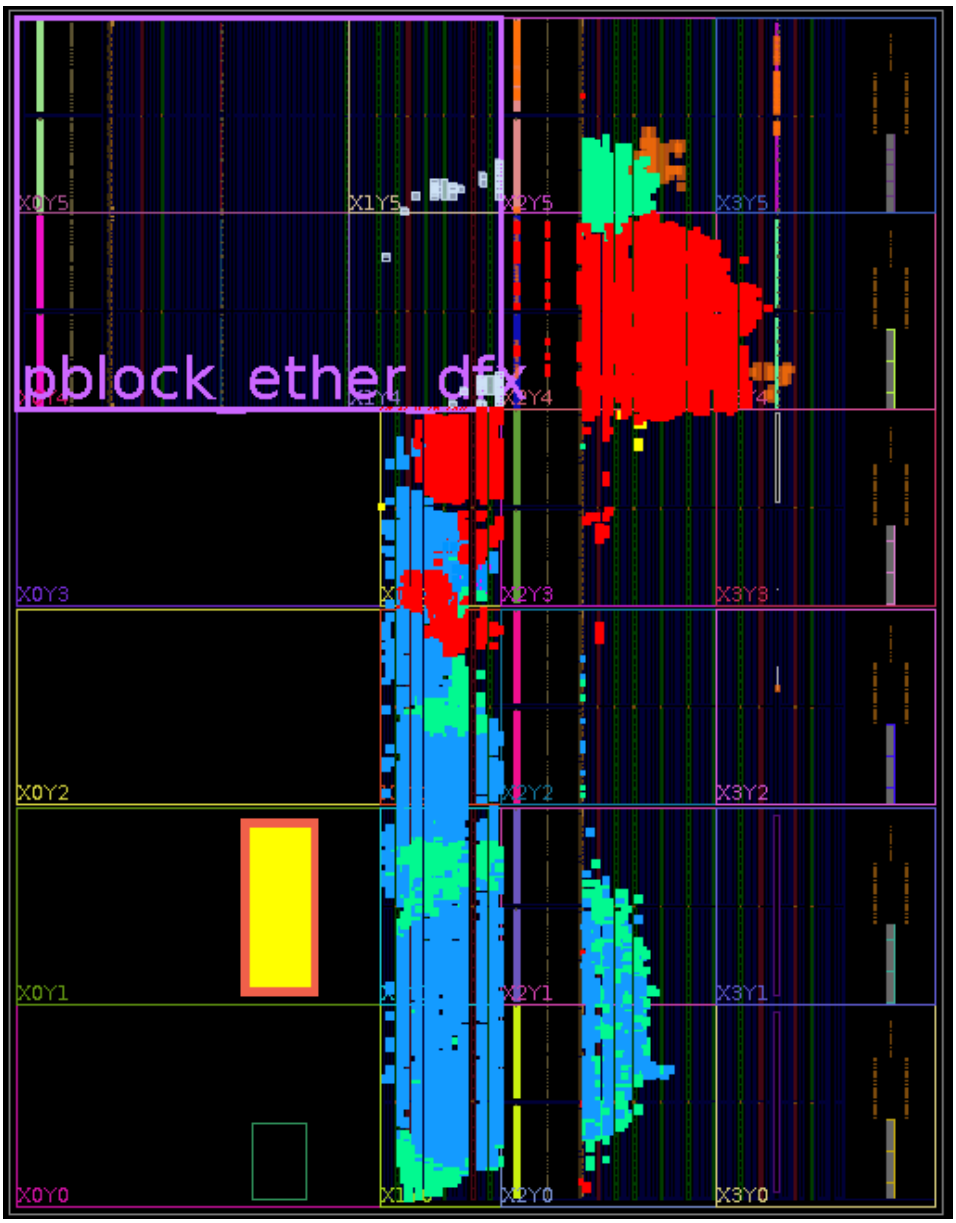

Figure 4-17 Zcu104 layout with the static HDL mapped

Colours in Figure 4-17 represent the below IP modules (Figure 4-18):

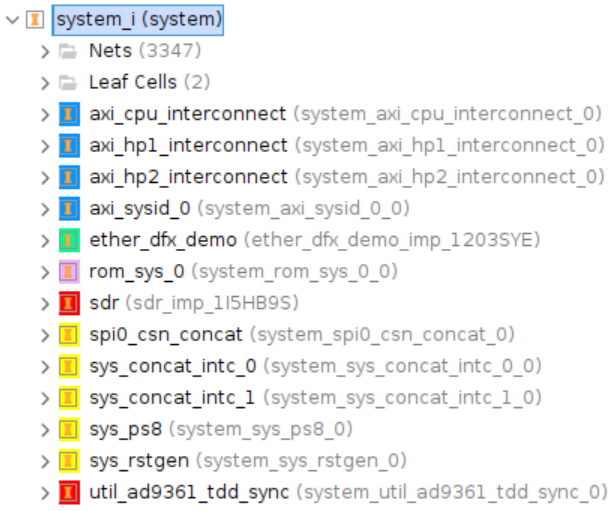

Figure 4-18 Available IP modules for the static region

For the dynamic region, the **top-left section of the FPGA layout** was selected. Two clock regions within this area were reserved to define the Reconfigurable Partition (RP), as shown in Figure 4-17 (*pblock_ether_dfx* area*)*. The FFT example (Figure 4-15) was synthesized and routed to generate the reconfigurable layout (Figure 4-19) and bitstream for the dynamic region. The bitstream will be subsequently loaded using the FPGAUtil tool.

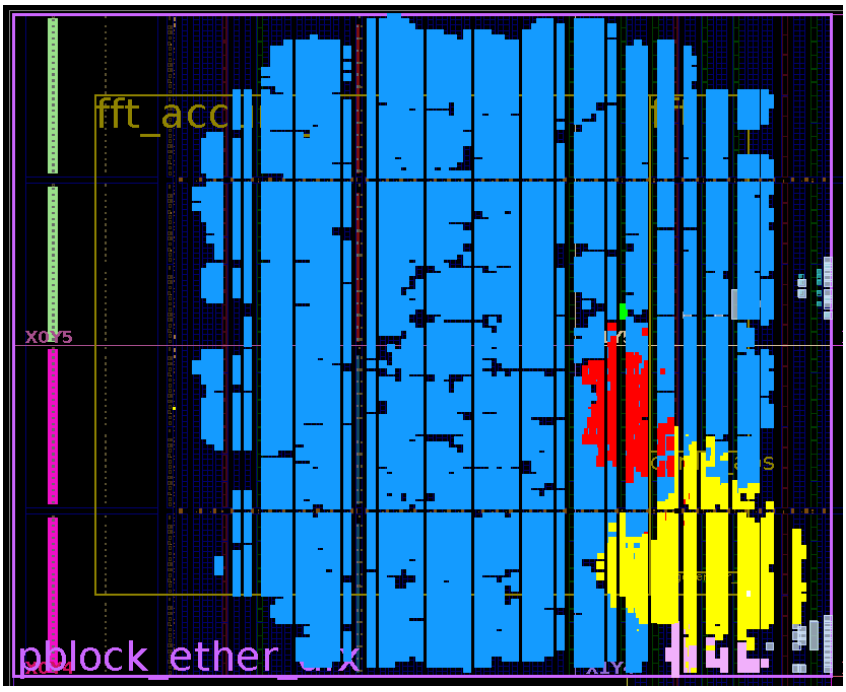

Figure 4-19 Reconfigurable partition layout content when deploying FFT example

Colours in Figure Figure 4-19 represent the below IP modules for the FFT example (Figure 4-20):

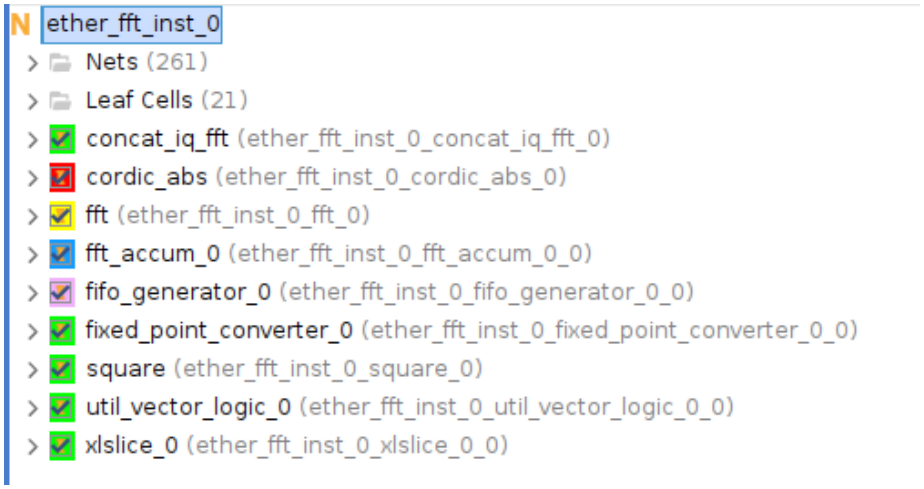

Figure 4-20 Available IP modules for the dynamic region

To validate hardware reconfiguration, a second service (**dummy service**) was developed for the dynamic region, implementing a simple counter instead of a full FFT processing chain. The expected test result is that upon reconfiguring the FFT bitstream with the dummy bitstream, the DMA transmits counter values instead of the IQ data originally provided by the FFT.

The basic steps to run the test are:

1. To start the test, a standard Linux OS boot is executed using the custom Linux OS created with Yocto [46]. The FPGA configuration used for this boot is the static bitstream region.
2. After boot, DMA driver needs to be enabled. The driver offers a mechanism to acquire FFT output data via DMA from hardware FFT module to OS Linux memory system (Figure 4-21).

```
root@zcu104-zynqmp-fmcomms4:~# insmod dma_test.ko
[  814.080527] DMA buffer allocated: virt=0000000031a96c56, phys=8db6000, size=4096
[  814.088241] DMA test device initialized with major number 240
[  814.094196] DMA controller base address: 0xa0000000, virtual: 00000000d749054a
[  814.101505] DMA interrupt number: 50
[  814.105133] DMA Register Dump:
[  814.108218] S2MM_DMACR   (0x30): 0x00011002
[  814.112416] S2MM_DMASR   (0x34): 0x00000000
[  814.116625] S2MM_CURDESC (0x38): 0x00000000
[  814.120818] S2MM_TAILDESC(0x40): 0x00000000
[  814.125028] S2MM_DA      (0x48): 0x00000000
[  814.129220] S2MM_LENGTH  (0x58): 0x00000000
[  814.133453] Initial DMA status: 0x00000000
[  814.137562] Post-reset DMA status: 0x00000000
[  814.141946] DMA control register after init: 0x00011002
[  814.147179] DMA controller initialized
[  814.150959] DMA Register Dump:
[  814.154027] S2MM_DMACR   (0x30): 0x00011002
[  814.158238] S2MM_DMASR   (0x34): 0x00000000
[  814.162429] S2MM_CURDESC (0x38): 0x00000000
[  814.166640] S2MM_TAILDESC(0x40): 0x00000000
[  814.170830] S2MM_DA      (0x48): 0x00000000
[  814.175042] S2MM_LENGTH  (0x58): 0x00000000
[  814.179234] DMA status before start: 0x00000000
[  814.183793] DMA control register after start: 0x00011003
[  814.189128] DMA length register after start: 0x00000000
[  814.194381] DMA transfer started
[  814.197618] DMA Register Dump:
[  814.200699] S2MM_DMACR   (0x30): 0x00011003
[  814.204892] S2MM_DMASR   (0x34): 0x00000000
[  814.209102] S2MM_CURDESC (0x38): 0x00000000
[  814.213294] S2MM_TAILDESC(0x40): 0x00000000
[  814.217505] S2MM_DA      (0x48): 0x00000000
[  814.221696] S2MM_LENGTH  (0x58): 0x00000000
[  814.225906] DMA test module loaded successfully
```

Figure 4-21 DMA kernel module activation to collect FFT data from hardware

3. Once the Linux OS is booted and DMA driver charged, the FFT bitstream is loaded via FPGAUtil using the **partial bitstream** flag (-f Partial). Within milliseconds (Figure 4-22), the new design is active. The ILA oscilloscope confirms this by displaying the expected FFT pattern (Figure 4-23, Figure 4-24).

```
root@zcu104-zynqmp-fmcomms4:~# fpgautil -b system_top_fft.bit -f Partial
[  660.052528] fpga_manager fpga0: writing system_top_fft.bit to Xilinx ZynqMP FPGA Manager
Time taken to load BIN is 46.000000 Milli Seconds
BIN FILE loaded through FPGA manager successfully
```

Figure 4-22 FPGAUtil commands and times to reprogram Full or Partial FPGA layout bitstream for fft

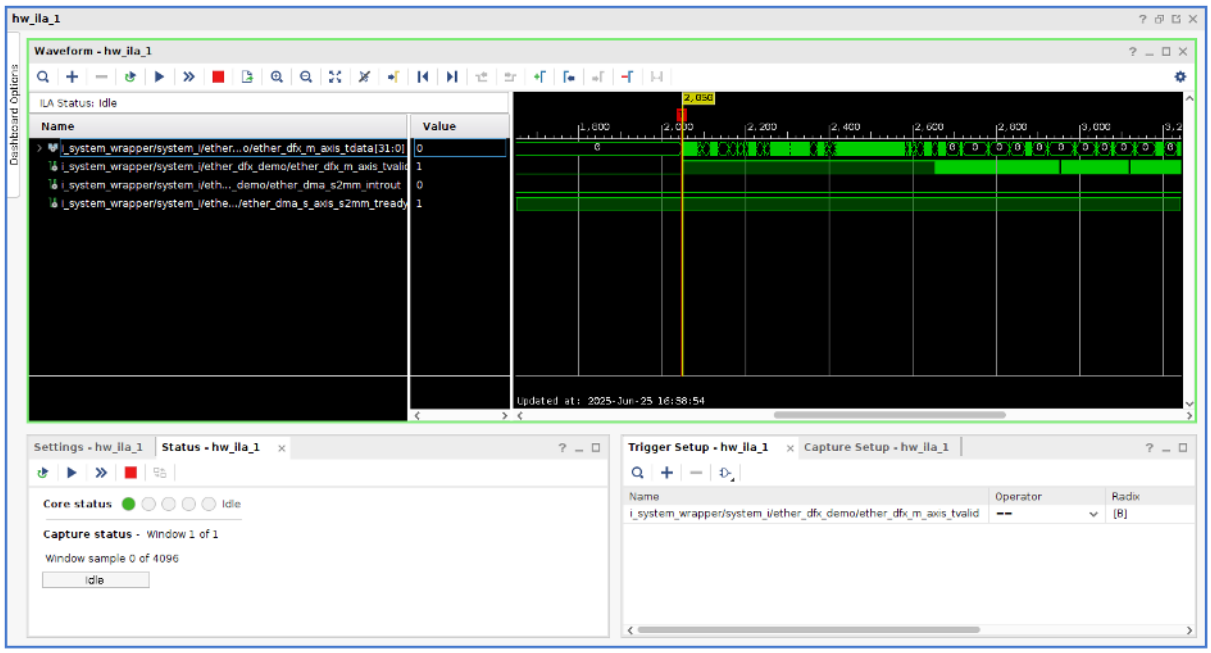

Figure 4-23 ILA oscilloscope IQ data extracted from FFT

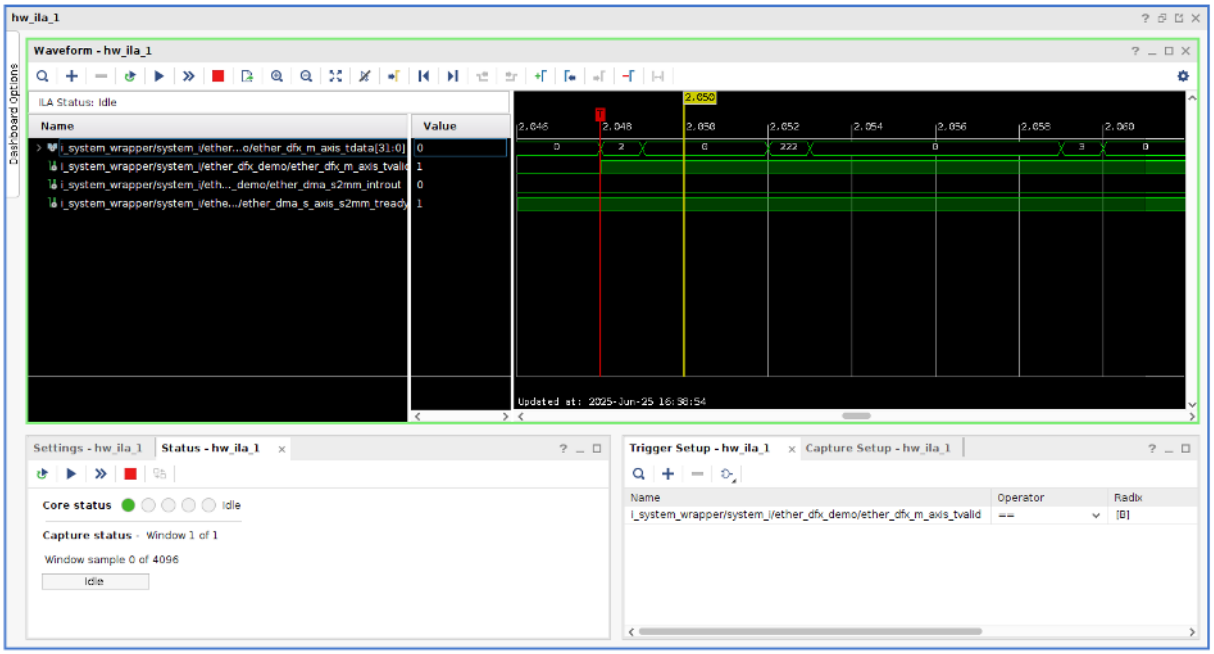

Figure 4-24 ILA Oscilloscope IQ data extracted from FFT (zoom)

4. Subsequently, the FFT bitstream is replaced with the counter bitstream (fft2 is the dummy service) using FPGAUtil (Figure 4-25), and a new pattern is captured via ILA (Figure 4-26, Figure 4-27).

```
root@zcu104-zynqmp-fmcomms4:~# fpgautil -b pblock_fft2_partial.bin -f Partial
[  600.535961] fpga_manager fpga0: writing pblock_fft2_partial.bin to Xilinx ZynqMP FPGA Manager
Time taken to load BIN is 20.000000 Milli Seconds
BIN FILE loaded through FPGA manager successfully
```

Figure 4-25 FPGAUtil commands and times to reprogram Partially FPGA layout bitstream for fft2

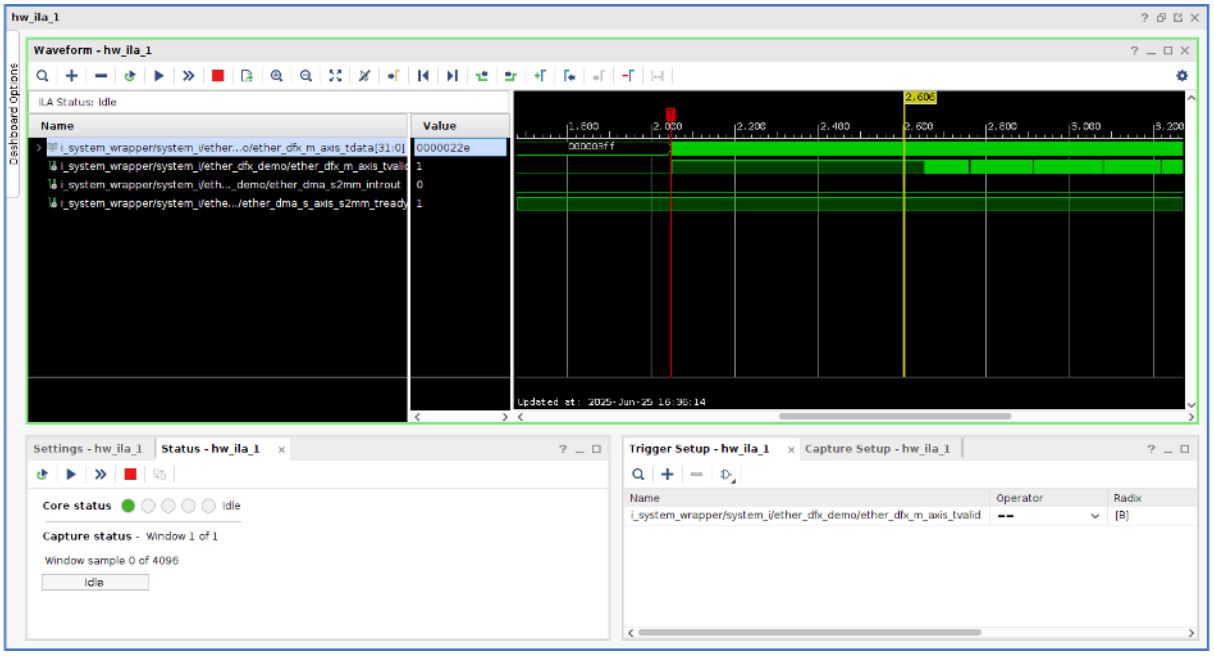

Figure 4-26 ILA oscilloscope fake IQ data (counter) extracted from FFT2 (dummy counter module)

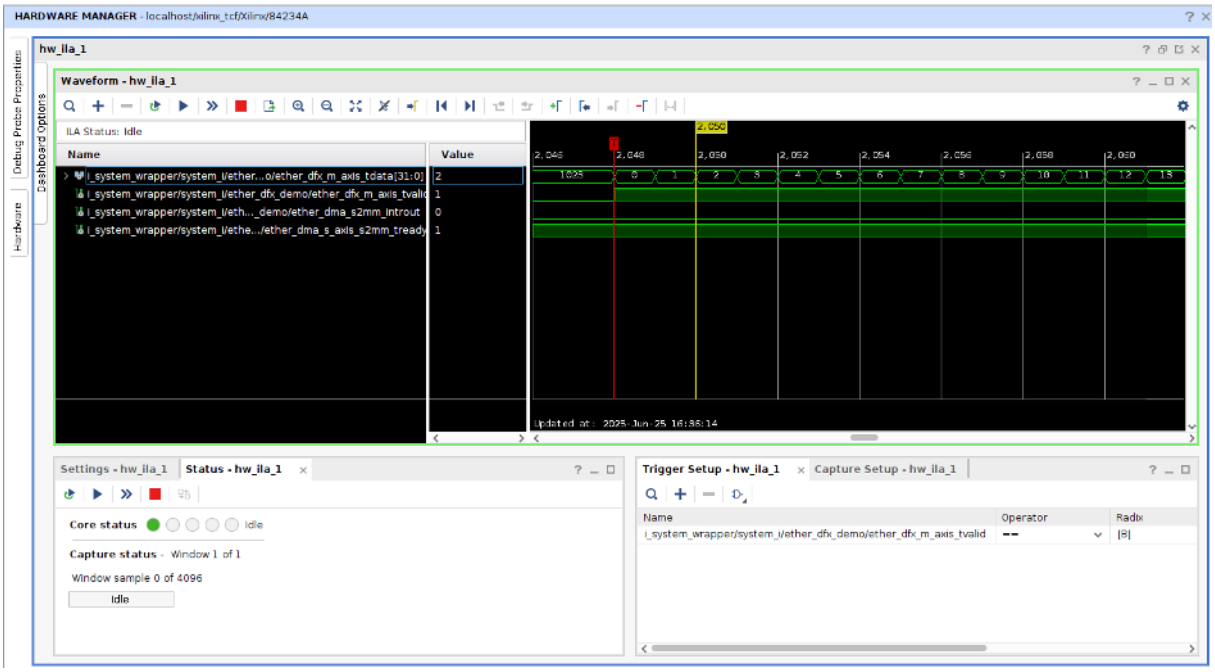

Figure 4-27 ILA oscilloscope fake IQ data extracted from FFT2 (dummy counter module) (zoom)

Results: The expected counter signal pattern is correctly observed, demonstrating that partial reconfiguration was successfully executed. This validates the functional integrity of the dynamic reconfiguration framework at **level 1**.

4.1.4 Final development results summary

The design phase of the flexible payload framework under Task T3.2 has been successfully completed. As a final achievement, the integration and validation of multiple mechanisms enabling flexible service deployment have been demonstrated.

The software foundation of the framework consists of a customized operating system that incorporates:

- A lightweight container orchestrator (K3s),
- Container-based virtualization tools,
- RF signal processing libraries, among other components.

This entire software and hardware stack has been successfully ported and deployed on a real hardware platform, the ZCU104 evaluation board, which, when combined with an AD936x transceiver, provides a fully functional test environment implementing the Software Defined Radio (SDR) concept.

Regarding dynamic hardware reconfiguration, an HDL-based architecture has been validated, allowing the exchange of IP modules representative of real satellite services. In Xilinx environment this is known as Dynamic Function eXchange (DFX). This architecture supports the replacement of hardware functions at runtime, demonstrating the capability of the system to adapt its hardware resources dynamically and efficiently.

4.2 DYNAMIC RESOURCE MANAGEMENT AND POWER CONTROL TECHNIQUES IN AERIAL AND SPACE ETHER LAYERS

Previous work reported in D3.1 entailed the definition and utilization of the Equivalent Power Flux Density (EPFD) as the main metric introduced by ITU-R's Article 22 to quantitatively determine the maximum amount of allowable interference created by non-Geostationary satellites to Geostationary ones. Specifically, a LEO/GEO coexistence scenario (with both satellite types operating in the same frequency band) within an "underlay" cognitive radio setting was studied, with the GEOs and LEOs acting as the primary and secondary users, respectively, and a power control algorithm for LEOs was proposed to satisfy a subset of the ITU-R constraints. However, no numerical evaluation of the proposed algorithm was provided.

In D3.2, the previous work of D3.1 has been expanded to allow for the complete set of ITU-R constraints to be handled, a unique aspect of which is their "soft" nature, i.e., the fact that they can be violated but only for a certain amount of time (equivalently, with a given probability). A concrete optimization problem has been formulated for the optimal LEO power control and a heuristic solution technique has been proposed relying on an "EPFD satisfiability" algorithmic module, which computes the EPFD for actual satellite orbits (instead of only the "worst case scenario" typically studied in the literature) while guaranteeing ITU-R compliance by properly turning-off LEO satellites (causing excessive GEO interference) only as needed. D3.2 also contains a complete Matlab-based numerical evaluation study of the above algorithmic suite, using actual satellite orbit data from publicly available TLE files, showcasing its versatility and wide applicability.

Regarding dynamic resource management, in D3.1 the joint resource management and interference cancellation is addressed through precoding: A precoder with non-zero power indicates the assignment of resource (spectrum band) and not assigned otherwise. Then the joint problem is formulated for the network throughput maximization under the per base station

(BS) and per satellite total power constraints. Further this problem is transformed into a weighted minimum mean square (WMMSE) which results in parallel optimization per user. The earlier version includes high level description of WMMSE algorithm. In addition, results were presented for this algorithm.

In D3.2, detailed description of WMMSE algorithm is provided. Further, the results of this solution are compared against two benchmarks: Uncoordinated and uncoordinated-disjoint solutions.

4.2.1 Dynamic resource management

4.2.1.1 Problem formulation

Let B, W, and $L = \frac{W}{B}$ be the smallest unit of bandwidth, the total available bandwidth, and the total number of bandwidth units available for allocation, respectively. The bandwidth units assigned to a user at a satellite or at any terrestrial cell must be consecutive; this is a critical constraint arising from practical considerations. All the BS are connected to central unit by backhaul. High-capacity backhaul that is capable of handling the coordination between the BS and satellite is assumed.

Towards modelling the received signal at the users terminals, it is assumed that the channel does not vary across the spectrum under allocation. Hence, the channels and the corresponding precoding vectors contain only indices of a user not of a band. Now, let $\widetilde{\mathbf{H}}^{\boldsymbol{l}}{}_{i}$ and $\mathbf{H}_{ij}^{l}$ denote the downlink channel of user i from satellite and cell j respectively, and let $\boldsymbol{n}_i^l$ be the noise at user i on band l. Furthermore $\mathbf{W}_i^l \in \mathbb{C}^{N_s \times N_{UE}}$ is the precoding vector of user i from satellite and $\mathbf{V}_{ij}^l \in \mathbb{C}^{N_t \times N_{UE}}$ the precoding vector of user i from cell j, and $\boldsymbol{x}_i^l$ be the data symbol vector of user i on band l with $\mathbb{E}\{\boldsymbol{x}_i^{l^*}\boldsymbol{x}_j^l\} = \mathbf{I}$.

With the defined notation, the signal received at user i from the satellite in band l, $\boldsymbol{y}_i^l$, is given by:

$$\boldsymbol{y}_i^l = \boldsymbol{H}_i{}^H \boldsymbol{W}_i^l \boldsymbol{x}_i^l + \sum_{k\neq i}^{N_u} \boldsymbol{H}_i^H \boldsymbol{W}_k^l \boldsymbol{x}_k^l + \sum_{j=1}^{N_c}\sum_{k\neq i}^{N_u} \boldsymbol{H}_{ij}{}^H \boldsymbol{V}_{kj}^l \boldsymbol{z}_{kj}^l + \boldsymbol{n}_i^l, \forall\, i,l \quad (4\text{-}1)$$

The rate of satellite user i on band l is given by:

$$\tilde{R}_i^l = logdet\,(\boldsymbol{I} + \boldsymbol{A}_{ii}^l \boldsymbol{A}_{ii}^{l^H}\,(\sigma_i^2 \boldsymbol{I} + \sum_{k\neq i}^{N_u} \boldsymbol{A}_{ik}^l \boldsymbol{A}_{ik}^{l^H} + \sum_{j=1}^{N_c}\sum_{k\neq i}^{N_u} \boldsymbol{B}_{jk,i}^l \boldsymbol{B}_{jk,i}^{l^H})^{-1}) \quad (4\text{-}2)$$

where $\boldsymbol{A}_{ik}^l = \mathbf{H}_i{}^H \boldsymbol{W}_k^l$; $\boldsymbol{B}_{jk,i}^l = \mathbf{H}_{ij}{}^H \boldsymbol{V}_{kj}^l, \forall\, i,j,k,l$

Similarly, the received signal at user i in cell j in band l, $\boldsymbol{y}_{ij}^l$, is:

$$\boldsymbol{y}_{ij}^l = \mathbf{H}_{ij,i}{}^H \boldsymbol{V}_{ij}^l \boldsymbol{z}_{ij}^l + \sum_{k\neq i}^{N_u} \mathbf{H}_{ij,i}{}^H \boldsymbol{V}_{ik}^l \boldsymbol{z}_{ik}^l + \sum_{j\neq i}^{N_c}\sum_{k=1}^{N_u} \mathbf{H}_{ij,j}{}^H \boldsymbol{V}_{kj}^l \boldsymbol{z}_{kj}^l + \sum_{k=1}^{N_u} \widetilde{\mathbf{H}}_{ij}{}^H \boldsymbol{W}_k^l \boldsymbol{x}_k^l + \boldsymbol{n}_{ij}^l, \forall\, i,l \quad (4\text{-}3)$$

The rate of cellular user i of cell j on band l is given by:

$$R_{ij}^{l} = logdet\left(\boldsymbol{I} + \boldsymbol{C}_{ii}^{l}\boldsymbol{C}_{ii}^{l^H}\left(\sigma_i^2\boldsymbol{I} + \sum_{k\neq i}^{N_u}\boldsymbol{C}_{ik}^{l}\boldsymbol{C}_{ik}^{l^H} + \sum_{j=1}^{N_c}\sum_{k\neq i}^{N_u}\boldsymbol{D}_{jk,i}^{l}\boldsymbol{D}_{jk,i}^{l^H}\right)^{-1}\right) \quad (4\text{-}4)$$

where $\boldsymbol{D}_{ij,k}^{l} = \widetilde{\mathbf{H}}_{ij}{}^{H}\boldsymbol{W}_{\boldsymbol{k}}^{\boldsymbol{l}}$; $\boldsymbol{C}_{ij,mn}^{l} = \mathbf{H}_{ij,n}{}^{H}\boldsymbol{V}_{\boldsymbol{mn}}^{\boldsymbol{l}}, \forall\, i,j,k,l.$

4.2.1.2 WMMSE algorithm

The Weighted Minimum Mean Square Error (WMMSE) algorithm for the weighted sum-rate maximization problem within a coordinated satellite and cellular network is presented below. The algorithm aims to maximize the overall system capacity by iteratively optimizing receiver filters, weighting factors, and precoding matrices.

Step 1: Define Mean Square Error (MSE) for Each User

The core of the WMMSE algorithm lies in minimizing the MSE, which quantifies the difference between the estimated signal and the actual transmitted signal for each user.

The estimated signals, $\hat{\boldsymbol{x}}_i^l$ and $\hat{\boldsymbol{x}}_{ij}^l$, are obtained by applying a receiver filter $\boldsymbol{U}_i^l$ and $\boldsymbol{U}_{ij}^l$ to the received signals at satellite users and cellular users respectively:

$$\begin{aligned}\hat{\boldsymbol{x}}_i^l &= \boldsymbol{U}_i^{l^H}\boldsymbol{y}_i^l \\ \hat{\boldsymbol{x}}_{ij}^l &= \boldsymbol{U}_{ij}^{l^H}\boldsymbol{y}_{ij}^l\end{aligned} \quad (4\text{-}5)$$

The Mean Square Error (MSE) for satellite user i on band l, denoted as E_i^l, is given by

$$\mathrm{E}_{\mathrm{i}}^{\mathrm{l}} = (\mathbf{U}_{\mathrm{i}}^{\mathrm{l}^{\mathrm{H}}}\mathbf{y}_{\mathrm{i}}^{\mathrm{l}} - \mathbf{x}_{\mathrm{i}}^{\mathrm{l}})\,(\mathbf{U}_{\mathrm{i}}^{\mathrm{l}^{\mathrm{H}}}\mathbf{y}_{\mathrm{i}}^{\mathrm{l}} - \mathbf{x}_{\mathrm{i}}^{\mathrm{l}})^{\mathrm{H}} = \left(\mathbf{I} - \mathbf{U}_{\mathrm{i}}^{\mathrm{l}^{\mathrm{H}}}\boldsymbol{H}_i{}^{H}\mathbf{W}_i^{\mathbf{l}}\right)\left(\mathbf{I} - \mathbf{U}_{\mathrm{i}}^{\mathrm{l}^{\mathrm{H}}}\boldsymbol{H}_i{}^{H}\boldsymbol{W}_{\boldsymbol{i}}^{\boldsymbol{l}}\right)^{H} + \mathbf{U}_{\mathrm{i}}^{\mathrm{l}^{\mathrm{H}}}\left(\sum_{k\neq i}^{N_u}\boldsymbol{H}_i{}^{H}\mathbf{W}_k^{l}\boldsymbol{W}_{\boldsymbol{k}}^{\boldsymbol{l}}\boldsymbol{H}_i + \sum_{j=1}^{N_c}\sum_{k=1}^{N_u}\mathbf{H}_{ij}{}^{H}\mathbf{V}_{jk}^{l}\boldsymbol{V}_{\boldsymbol{kj}}^{\boldsymbol{l}^{\boldsymbol{H}}}\mathbf{H}_{ij} + \sigma_i^2\mathbf{I}\right)\mathbf{U}_{\mathrm{i}}^{\mathrm{l}} \quad (4\text{-}6)$$

Similarly, the MSE for cellular user i in cell j, denoted as E_{ij}^l, is given by

$$\mathrm{E}_{\mathrm{ij}}^{\mathrm{l}} = (\mathbf{U}_{\mathrm{i}}^{\mathrm{l}^{\mathrm{H}}}\boldsymbol{y}_{ij}^{l} - \boldsymbol{z}_{ij}^{l})\,(\mathbf{U}_{\mathrm{i}}^{\mathrm{l}^{\mathrm{H}}}\boldsymbol{y}_{ij}^{l} - \boldsymbol{z}_{ij}^{l})^{\mathrm{H}} = \left(\mathbf{I} - \mathbf{U}_{\mathrm{ij}}^{\mathrm{l}^{\mathrm{H}}}\mathbf{H}_{ij,i}{}^{H}\mathbf{V}_{ij}\boldsymbol{Q}_{\boldsymbol{ij}}^{\boldsymbol{l}}\right)\left(\mathbf{I} - \mathbf{U}_{\mathrm{ij}}^{\mathrm{l}^{\mathrm{H}}}\mathbf{H}_{ij,i}{}^{H}\mathbf{V}_{ij}\boldsymbol{Q}_{\boldsymbol{ij}}^{\boldsymbol{l}}\right)^{H} + \mathbf{U}_{\mathrm{ij}}^{\mathrm{l}^{\mathrm{H}}}\left(\sum_{k\neq i}^{N_u}\mathbf{H}_{ij,i}{}^{H}\mathbf{V}_{kj}\boldsymbol{Q}_{ik}^{\boldsymbol{l}} + \sum_{j\neq i}^{N_c}\sum_{k=1}^{N_u}\mathbf{H}_{ij,j}{}^{H}\mathbf{V}_{jk}\boldsymbol{Q}_{\boldsymbol{kj}}^{\boldsymbol{l}} + \sum_{k=1}^{N_u}\widetilde{\mathbf{H}}_{ij}{}^{H}\mathbf{W}_k\boldsymbol{P}_{\boldsymbol{k}}^{\boldsymbol{l}} + \sigma_i^2\mathbf{I}\right)\mathbf{U}_{\mathrm{ij}}^{\mathrm{l}^{\mathrm{H}}} \quad (4\text{-}7)$$

The sum-throughput maximization can be equivalently formulated as follows

$$P_2: \max_{\boldsymbol{W},\boldsymbol{V},\boldsymbol{P},\boldsymbol{Q}} \sum_{l=1}^{L}\sum_{i=1}^{N_c}\sum_{j=1}^{N_u} B\eta_{ij}\left(Tr\{M_{ij}^{l}E_{ij}^{l}\} - logdet\{M_{ij}^{l}\}\right) + \sum_{l=1}^{L}\sum_{i=1}^{N_u} B\tilde{\eta}_{i}\left(Tr\{M_{i}^{l}E_{i}^{l}\} - logdet\{M_{i}^{l}\}\right) \quad (4\text{-}8)$$

$$C_1: \sum_{i=1}^{N_u}\sum_{l=1}^{L} \mathrm{Tr}\{\mathbf{W}_i^l\,\mathbf{W}_i^{l\mathrm{H}}\} \le P_{tot};$$

$$C_2: \sum_{i=1}^{N_u}\sum_{l=1}^{L} \mathrm{Tr}\{\mathbf{V}_{\mathrm{ij}}^l\mathbf{V}_{\mathrm{ij}}^{l\mathrm{H}}\} \le P_{tot}, \forall\, j$$

where $\mathbf{M}_{\mathrm{i}}^{\mathrm{l}}$ and $\mathbf{M}_{\mathrm{ij}}^{\mathrm{l}}$ are slack weight matrices corresponding to satellite and cellular users. The problem P_2 is typically referred to as a WMMSE problem.

Step 2: Iterative Updates

The WMMSE algorithm is iterative, meaning it refines the parameters (receivers, weights, and precoding matrices) in a repetitive manner until a convergence criterion is met. Each iteration consists of the following sub-steps:

(a) Update Receivers combiners

The receiver filters are updated to minimize the MSE for a given set of precoding matrices and weights. These updates typically involve a closed-form solution derived from the Karush-Kuhn-Tucker (KKT) conditions. This means that the receive combiners $\boldsymbol{U}_i^l$ and $\boldsymbol{U}_{ij}^l$ are simply obtained by setting the first derivative of objective of P_2 to zero. This results in closed form updates given by,

$$\mathbf{U}_{\mathrm{i}}^{l} = \left(\sum_{k=1}^{N_u} \boldsymbol{H}_i{}^{H}\mathbf{W}_k^l\mathbf{W}_k^{l^H}\,\mathbf{H}_i + \sum_{j=1}^{N_c}\sum_{k=1}^{N_u} \mathbf{H}_{ij}{}^{H}\mathbf{V}_{jk}^l\mathbf{V}_{jk}^{l^H}\mathbf{H}_{ij} + \sigma_i^2\mathbf{I}\right)^{-1} \boldsymbol{H}_i{}^{H}\mathbf{W}_i \quad (4\text{-}9)$$

$$\mathbf{U}_{\mathrm{ji}}^{l} = \left(\sum_{k\neq i}^{N_u} \mathbf{H}_{ij,i}{}^{H}\mathbf{V}_{kj}^l\boldsymbol{V}_{ik}^{\boldsymbol{l}\boldsymbol{H}}\mathbf{H}_{ij,i} + \sum_{j\neq i}^{N_c}\sum_{k=1}^{N_u} \mathbf{H}_{ij,j}{}^{H}\mathbf{V}_{jk}^l\boldsymbol{V}_{kj}^{\boldsymbol{l}}\,\mathbf{H}_{ij,j} + \sum_{k=1}^{N_u} \widetilde{\mathbf{H}}_{ij}{}^{H}\mathbf{W}_k^l\boldsymbol{W}_{\boldsymbol{k}}^{\boldsymbol{l}}\,\widetilde{\mathbf{H}}_{ij} + \sigma_i^2\mathbf{I}\right)^{-1}\mathbf{H}_{ij,i}{}^{H}\mathbf{V}_{kj}^l$$

(b) Update Weights (w)

After updating the receivers, the WMMSE weights are updated based on the current MSE values. This step aims to give higher weights to users with better signal quality, which indirectly prioritizes their sum-rate contribution.

$$\boldsymbol{M}_{\mathrm{i}}^{l} = \left(\boldsymbol{E}_{i}^{l}\right)^{-1}; \boldsymbol{M}_{\mathrm{ij}}^{l} = \left(\boldsymbol{E}_{ij}^{l}\right)^{-1} \tag{4-10}$$

(c) Update Precoding Matrices ($\boldsymbol{W}, \boldsymbol{V}$)

The precoding matrices are optimized to maximize the weighted sum-rate, subject to various constraints. This step is crucial for managing interference and optimizing resource allocation. The problem P_2 is transformed into unconstrained form with the help of Lagrange variables λ_j and $\hat{\lambda}$ corresponding to cellular and satellite users respectively as

$$\begin{aligned} \mathrm{P}_3\colon \max_{\mathbf{W},\mathbf{V},\mathbf{P},\mathbf{Q}} & \sum_{\mathrm{l}=1}^{\mathrm{L}}\sum_{\mathrm{i}=1}^{\mathrm{N_c}}\sum_{\mathrm{j}=1}^{\mathrm{N_u}} \mathrm{B}\eta_{\mathrm{ij}}\left(\mathrm{Tr}\{\mathrm{M}_{\mathrm{ij}}^{\mathrm{l}}\mathrm{E}_{\mathrm{ij}}^{\mathrm{l}}\} - \mathrm{logdet}\{\mathrm{M}_{\mathrm{ij}}^{\mathrm{l}}\}\right) \\ & + \sum_{\mathrm{l}=1}^{\mathrm{L}}\sum_{\mathrm{i}=1}^{\mathrm{N_u}} \mathrm{B}\tilde{\eta}_{\mathrm{i}}\left(\mathrm{Tr}\{\mathrm{M}_{\mathrm{i}}^{\mathrm{l}}\mathrm{E}_{\mathrm{i}}^{\mathrm{l}}\} - \mathrm{logdet}\{\mathrm{M}_{\mathrm{i}}^{\mathrm{l}}\}\right) + \hat{\lambda}\left(\sum_{\mathrm{i}=1}^{\mathrm{N_u}}\sum_{\mathrm{l}=1}^{\mathrm{L}} \mathrm{Tr}\{\mathbf{W}_{\mathrm{i}}^{\mathrm{l}}\,\mathbf{W}_{\mathrm{i}}^{\mathrm{l}^{\mathrm{H}}}\}\right. \\ & \left. - \mathrm{P_{tot}}\right) + \lambda_{\mathrm{j}}\left(\sum_{\mathrm{i}=1}^{\mathrm{N_u}}\sum_{\mathrm{l}=1}^{\mathrm{L}} \mathrm{Tr}\{\mathbf{V}_{\mathrm{ij}}^{\mathrm{l}}\mathbf{V}_{\mathrm{ij}}^{\mathrm{l}^{\mathrm{H}}}\} - \mathrm{P_{tot}}\right) \end{aligned} \tag{4-11}$$

Simply the setting the first derivation of P_3 w.r.t $\mathbf{V}_{ij}^{l}$ and $\mathbf{W}_{i}^{l}$ give the following closed form expressions

$$\begin{aligned} \boldsymbol{w}_{\mathrm{i}}^{l} &= \left(\sum_{k=1}^{N_u} \mathbf{H}_{\boldsymbol{k}}^{\boldsymbol{l}\,H}\mathbf{U}_{k}^{l}\mathbf{M}_{k}^{l}\mathbf{U}_{k}^{l^{H}}\mathbf{H}_{k}^{l} + \sum_{J=1}^{N_c}\sum_{k=1}^{N_u} \widetilde{\mathbf{H}}^{\boldsymbol{l}}{}_{\iota J}{}^{H}\widehat{\mathbf{U}_{Jk}^{l}}\mathbf{M}_{Jk}^{l}\mathbf{U}_{Jk}^{l^{H}}\widetilde{\mathbf{H}}^{\boldsymbol{l}}{}_{\iota J} + \hat{\lambda}\,\mathbf{I}\right)^{-1}\mathbf{H}_{i}^{l^{H}}\boldsymbol{U}_{i}^{l}\boldsymbol{M}_{i}^{l} \\ \boldsymbol{v}_{ij}^{l} &= \left(\sum_{j=1}^{N_c}\sum_{k=1}^{N_u}\mathbf{H}_{ij,j}^{l}{}^{H}\mathbf{U}_{jk}^{l}\mathbf{M}_{jk}^{l}\mathbf{U}_{jk}^{l^{H}}\mathbf{H}_{ij,j}^{l} + \sum_{k=1}^{N_u}\mathbf{H}_{ik}{}^{H}\mathbf{U}_{k}^{l}\mathbf{M}_{k}^{l}\mathbf{U}_{k}^{l^{H}}\mathbf{H}_{ik} + \right. \\ & \left.\lambda_j\mathbf{I}\right)^{-1}\mathbf{H}_{ij,i}{}^{H}\boldsymbol{U}_{ij}^{l}\boldsymbol{M}_{ij}^{l} \end{aligned} \tag{4-12}$$

- Optimal values of Lagrange variables λ_j and $\hat{\lambda}$ are found through bisection search adhering the power constraints.

Algorithm Summary

The WMMSE algorithm can be summarized as an iterative process that converges to a locally optimal solution for the weighted sum-rate maximization problem:

1. **Initialize** precoding matrices (W, V, P, Q).
2. **Repeat** until convergence (e.g., when the change in the objective function or parameters falls below a threshold):
    1. **Update MMSE receivers** $\boldsymbol{U}_{i}^{l}$ and $\boldsymbol{U}_{ij}^{l}$ using the derived closed-form expressions.
    2. **Update MSE weights** $\boldsymbol{M}_{\mathrm{i}}^{l}$ and $\boldsymbol{M}_{\mathrm{ij}}^{l}$ based on the current receiver filters and channel conditions.

3. **Update precoders** $\mathbf{V}_{ij}^{l}$ and $\mathbf{W}_{i}^{l}$ by solving an optimization problem that satisfies the power and unit-norm constraints.

This iterative process effectively decouples the complex sum-rate maximization problem into smaller, more manageable subproblems, which are then solved sequentially until a stable solution is reached.

4.2.1.3 Simulation results

In this section, the results of the proposed WMMSE algorithm, which is referred to as "Coordinated", is compared against the following benchmarks:

- **Uncoordinated:** In this allocation, both TN and NTN occupy the whole available spectrum and allocate resources without considering the cross interference to each other. This is an interesting benchmark as in reality coordination among satellite and terrestrial BSs is unrealistic due to the distances. Both TN and NTN employ the WMMSE algorithm individually (without considering the cross interference) to maximize its own sum-throughput. Finally at the end with obtained precoders of the individual networks, a total sum-throughput of total TN-NTN network is calculated considering the cross interference.

- **Uncoordinated-Orthogonal allocation:** It is similar to "uncoordinated" scheme in terms of coordination but TN and NTN use orthogonal spectral resources. The existing networks follow this kind of allocation, and comparison with this allocation sheds a light on potential improvements. In this set of simulations, we consider 50-50% allocation, meaning that first half (50%) of spectrum is dedicated for TN and the rest is for NTN. Similarly to the above schemes, WMMSE algorithm is employed to maximize the sum-throughput of the networks individually. Finally, the total sum-throughput of the joint TN-NTN network is calculated which is simply the sum of throughputs of both networks.

Network layout: The layout of the TN-NTN used for simulations is shown in Figure 4-28. Satellite network contains a single beam with a radius of 1000 meters and TN consists of 20 cells each with a radius of 200m. Each cell has an overlapping region of 0.2% with one or more of the neighbouring cells. These details are summarized in Table 14.

Table 14: Integrated TN-NTN coverage layout

Parameter	Value
Number of cells	20
Number of satellite beams	1
Satellite coverage radius	1000 m
Cell coverage radius	200 m
Overlapping of neighbouring cells	20%
Cellular and satellite user distribution	Uniform distribution

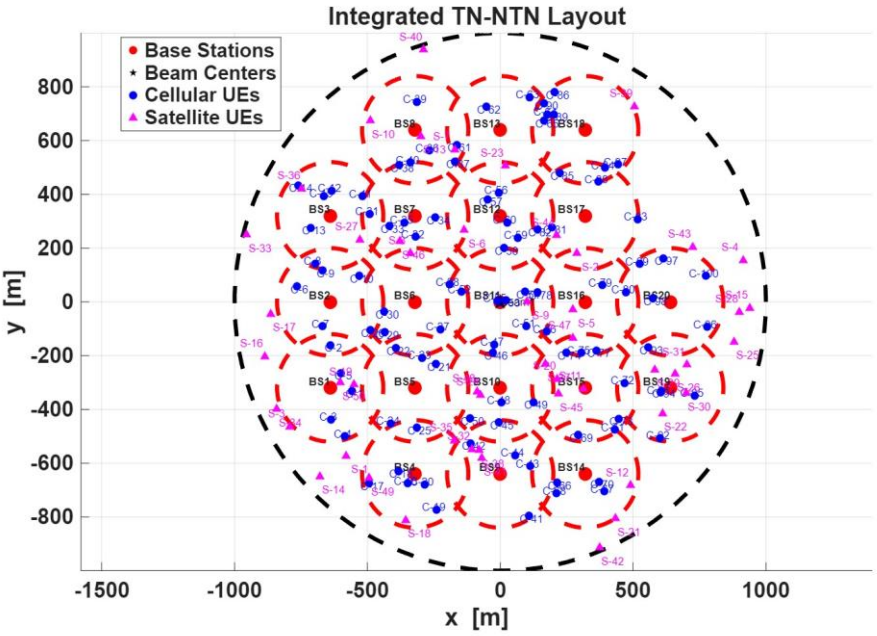

Figure 4-28 TN-NTN layout

Simulation setup: The parameters that are fixed for the simulations are summarized in Table 15

Table 15: Simulation parameters that are fixed

Parameter	Value
Number of cells	20
Number of users per cell	5
Number of transmit antennas per BS	64
Number of receive antennas per cellular UE	2
Number of transmit antennas at Satellite	64
Number of receive antennas at satellite UE	2
Total transmit power per BS	10 dBW
Cellular channels	Rayleigh fading with pathloss and shadowing included
Satellite channels	Rician fading (Rician factor 7dB) with pathloss and shadowing included

In Figure 4-29, the performance of the proposed WMMSE scheme (Cooperated) is compared against the benchmarks. Sum-throughput is plotted as a function of satellite transmit power in dB varying from 10 to 20 dB in steps of 2. This comparison is interesting as we want to evaluate

the impact of the cross interference of the networks. A couple of interesting observations are revealed in Figure 4-29.

- **Performance decline of Uncoordinated-joint scheme with power**: The available satellite power is utilized to boost the signal to the satellite users which inadvertently causes stronger interference to cellular users. This stronger interference leads to poorer sum-throughput in an uncoordinated network which is manifested in the performance decline of "Uncoordinated-joint" as shown in Figure 4-29.

- **Spectrum reuse vs Orthogonal usage:** An interesting observation is revealed in Figure 4-29. Lower transmit power regime is essentially the lower interference regime. In this regime, full spectrum reuse achieves better performance than uncooperated-orthogonal spectral allocation scheme. However, in the high interference regime, which is on the far-right side, reveals the superiority of uncooperated-orthogonal spectral allocation scheme.

- **Superior performance of coordinated allocation:** Coordinated allocation schemes simply outperforms both schemes in terms of sum-throughput performance in both lower and higher interference regimes. This is because "Coordinated" schemes intelligently and adequately decide by design when to reuse the spectrum and when to orthogonally allocate at user level instead of network level. This performance improvement come at the expense of increased complexity of WMMSE algorithm. In other words, availability of all the channels information, and coordination among TN and NTN networks (which are separated in hundreds of kilometres in space) is a prerequisite for achieving this performance.

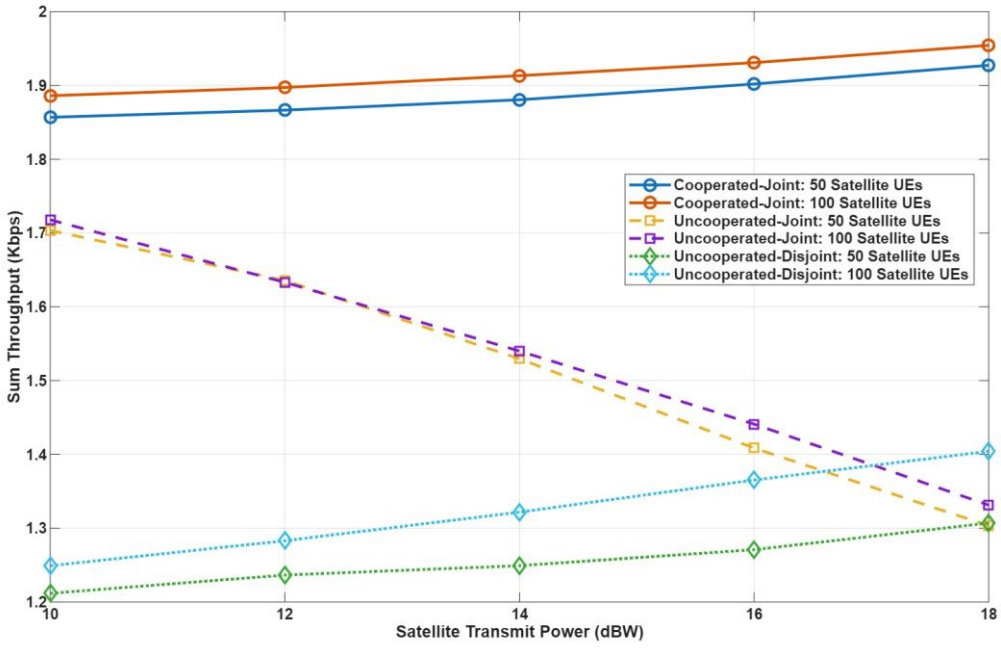

Figure 4-29 Performance of different resource allocation schemes.

Key Findings

- **Best Performance**: The *Cooperated-Joint* scenario consistently achieves the highest throughput across all power levels and UE densities due to coordinated scheduling and interference management.

- **Power Trade-Off in Uncoordinated Modes**:

  - In the *Uncooperated-Joint* case, increasing satellite power leads to **increased interference**, especially at high UE loads, causing throughput to **decline** with power.
  - The *Uncooperated-Disjoint* scenario benefits modestly from higher power since interference between TN and NTN domains is minimized.

- **Complexity and feasibility:**

  - Coordinated strategies require global channel information of all the users and coordination among the BS and satellite which are separated in hundreds of kilometres thus the question of feasibility arises strongly. Although statistical and prediction based historical CSI schemes can employed to obtain the imperfect CSI, WMMSE still require an exchange among satellite and BS to converge. Further, consideration of WMMSE design of all the users in the joint network led to increase in dimensionality of the problems hence the complexity of algorithm.

Conclusion

Joint TN-NTN cooperation significantly enhances throughput and system scalability. Coordinated strategies involve global knowledge of all the users in the integrated network and also communication exchange among the TN-NTN which are separated in large distances. This leads to difficulties in deploying the solution in its current form. By simply understanding the performance gaps, and complexity and feasibility trade-offs better algorithms can be designed to the ambitions of the designer. Along these directions, several efforts are ongoing:

- Prediction of global CSI at the local nodes based on historical, statistical and user distribution. This is an active area of research and prediction accuracies of the schemes are far from the reality.

- Fully distributed WMMSE: Several efforts have been made to reduce the number of iterations, limit the exchanges among the nodes but the pursuit for fully distributed WMMSE without much compromise for the gains is still on-going.

4.2.2 Power control in heterogeneous satellite networks

4.2.2.1 System model

We briefly summarize the LEO-to-GEO interference model described in D3.1 [1], which is motivated by the regulations imposed by the International Communication Union Radio sector (ITU-R) in Article 22 [47] . The EPFD metric is defined in [47] at the receiver of the LEO satellite to GEO-Earth-Station link, and applies to both Downlink (i.e., LEO satellite to GEO-Earth-Station) and Uplink (i.e., LEO-Earth-Station to GEO satellite). For economy of space, subsequent numerical results are presented only for the Downlink case; however, the approach carries verbatim over to the Uplink as well. The Downlink EPFD at the GEO-Earth-station is expressed (in dBW/m^2) as:

$$EPFD(\sigma) = 10\log\left[\sum_{i=1}^{N_a} P_i \frac{G_t(\theta_i)}{4\pi d_i^2}\frac{G_r(\varphi_i)}{G_{r,max}}\right] \quad (4\text{-}13)$$

where:

- σ is the location of the GEO-Earth-Station receiver.
- N_a is the number of LEO transmitters that are visible to the GEO-Earth-Station receiver.
- d_i is the distance between the LEO satellite and the GEO-Earth-Station.
- P_i is the ith LEO satellite's transmitter power (in linear, not dBm, scale) in the specified reference bandwidth of [47].
- θ_i and φ_i are the off-axis angles between the boresight direction and the GEO-Earth-Station receiver or LEO satellite transmitter directions, respectively, as shown in Figure 4-30 below.
- $G_t(\cdot)$ and $G_r(\cdot)$ are the antenna gains (in linear, not dB, scale) of the LEO satellite and GEO-Earth-Station receiver, respectively, as a function of angle. Depending on the employed frequency bands, [47] dictates that specific reference radiation pattern from ITU-R S.1428-1 [48] are employed, for the purposes of this calculation.
- $G_{r,max}$ is the maximum gain (in linear, not dB, scale) of the GEO-Earth Station link receiver.

Since EPFD is a sum of individual contributions from the LEOs, we can identify the term $P_i \frac{G_t(\theta_i)}{4\pi d_i^2}\frac{G_r(\varphi_i)}{G_{r,max}}$ as the EPFD caused by LEO satellite i and denote it as $EPFD_i(\sigma)$ so that Eq. 4-1 can be written as $EPFD(\sigma) = 10\log[\sum_{i=1}^{N_a} EPFD_i(\sigma)]$. We further note that computation of EPFD in Eq. 4-1, for given values of P_i, is essentially a geometrical problem in terms of the relative positions and angles of Figure 4-30, which requires knowledge of the positions of LEO satellites and GEO-Earth-Stations but no additional channel state information.

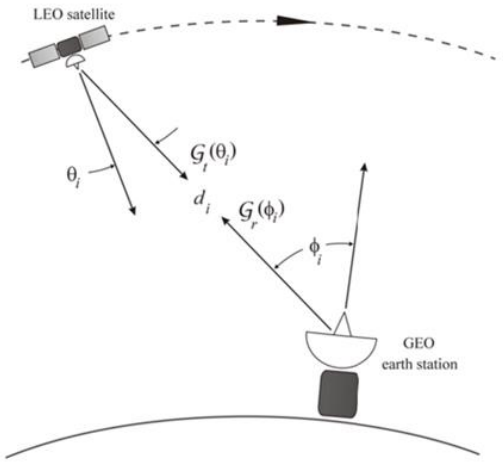

Figure 4-30 Geometry of angles for LEO satellite and GEO Earth station [49].

ITU-R imposes different EPFD "soft" regulatory upper bounds, depending on the employed frequency band, and the percentage of time wherein these bounds are allowed to be violated (hence, their "soft" nature), essentially providing a reference cumulative distribution function (CDF) for the EPFD. These bounds are provided in Tables 22-1A to 22-1E of [47], with some additional bounds being enforced in certain geographical latitudes and further "operational limits" being applicable when GEO-Earth-station antenna gains exceed certain thresholds. For concreteness, we hereafter consider the 19.7-20.2 GHz band as the operating band of the LEO satellites, along with a 40 kHz reference bandwidth and a 70 cm GEO-Earth-station

reference antenna diameter, for which [47] provides the bounds shown in Table 16 below, without any additional operational limits.

Table 16: Downlink EPFD limits for LEO transmission in the 19.7-20.2 GHz band with a 70 cm GEO-Earth-Station reference antenna (taken from Table 22-1C of [47]).

Downlink EPFD level (dBW/m^2)	Percentage of time that EPFD level can be exceeded
-187.4	100%
-182	28.571%
-172	2.857%
-154	0.017%

As the ITU-R bounds are applicable ***at all possible locations*** of the GEO-Earth-Stations ***regardless of the actual existence*** of a GEO-Earth-Station therein, we employ the "underlay" Cognitive Radio model, where secondary (LEO) users transmit concurrently with primary (GEO) users in the same spectrum (i.e., 19.7-20.2 GHz), albeit with proper transmission power control so as to cause acceptable disturbance to the primary transmissions from GEO satellites. The disturbance is deemed acceptable as long as the limits of Table 16are satisfied. In case any of these limits is violated, the following mitigation measure is applied: a subset of LEO satellites considered to be the primary contributor to the excessive EPFD is determined and these satellites either turn off their transmitters or have their transmission power properly reduced **for a certain amount of time** so that the EPFD limits are no longer violated.

As described in [1], most of the excessive EPFD is caused during the "in-line" events, where the LEO satellite is directly above the GEO-Earth-Station and aligned with the GEO satellite to GEO-Earth-Station direction. Due to the deterministic nature of satellite orbits, these events can be predicted in advance and the above mitigation measure can be activated as soon as the offending LEOs enter the "restriction/exclusion zones" of the GEO links [50] and for as long as they remain within these zones. However, optimally determining the angular extent of the exclusion zone to avoid unnecessarily turning off the LEOs is a challenging problem. In the following, we present a LEO power control algorithm and an associated optimization problem, wherein the identification of the specific LEOs to turn off and the amount of time to do so will naturally arise, based on data analysis, and will be provided as the output of the algorithm.

4.2.2.2 Problem formulation and proposed algorithm

Given the orbits of LEOs, obtained through publicly available TLE data files from [51], and the reference antenna patterns in [48] as inputs, and using a discrete grid on the Earth's surface for the N_{GS} GEO-Earth-Stations where the ITU-R EPFD bounds will be checked, we employ MATLAB's Satellite Communication toolbox [52] to simulate the satellite's orbital motion and acquire "snapshots" of the satellites' positions every T_s seconds. Since the maximum value of the LEO transmission power P_i depends on the actual payload's communication hardware, we can, without loss of generality, assume that each class c of LEO satellites (i.e., Cubesats, mini-satellites, full-blown LEOs etc.) is characterized by a parameter P_c^{max}, which captures **only the communication hardware capabilities and not the EPFD-constrained** maximum transmission power.

Let $\mathcal{C}$ be the set of LEO satellite classes, $\mathcal{N}$ the set of all LEOs and $\mathcal{G}$ the set of all GEO-Earth-Stations (GS) considered. Denoting with $\mathcal{T}$ the set of time instants where the satellite

snapshots are obtained and with $c(i)$ the class of LEO satellite i, we first formulate the following **EPFD satisfiability problem** for given values of $(P_c: c \in \mathcal{C})$

$$\begin{gathered} \max 1 \\ s.t.\ P_{i,t} = P_{c(i)} a_{i,t}, \qquad \forall i \in \mathcal{N}, , \\ \text{Table 8 EPFD limits are satisfied for all GS in } \mathcal{G}, \\ \sum_{t \in \mathcal{T}} a_{i,t} \geq T_s(1-\delta), \forall i \in \mathcal{N} \end{gathered} \tag{4-14}$$

where the control variable $a_{i,t}$ is a Boolean variable indicating whether the transmitter of LEO satellite i is active at snapshot t, and $P_{i,t}$ is the actual transmission power employed by satellite i at snashop t. The last constraint in (*4-14*) is imposed to ensure that the LEO satellites are active for a significant amount of time (controlled by the parameter δ) during their mission, to allow for proper LEO coverage and service provision. Without the last constraint, trivial solutions such as globally setting $a_{i,t} = 0$, would be feasible for (*4-14*) but would offer no meaningful insights to the network operator and would essentially be "operationally unacceptable". Hence, the last constraint is crucial to properly guard against aggressively turning off the LEO satellites to satisfy the EPFD limits.

Despite the linear dependence of EPFD (in linear scale) on transmission power $P_{i,t}$, the "soft" EPFD limits introduce some complexities, since these limits can be violated in a "statistical" sense. Although it is possible to convert (*4-14*) into a bona fide Linear Program (LP), this conversion entails the introduction of additional auxiliary variables and the increase of the search space, which significantly increases the computational time, while also introducing major scaling artifacts due to the very low EPFD values (in linear scale) leading to roundoff errors affecting the "quality" of the LP solution. To this end, we propose a heuristic algorithm to solve (*4-14*), as described in pseudocode form below:

Input: orbital information for LEOs (i.e., T_s snapshots), grid of points (i.e., GEO-Earth Stations) N_{GS} on Earth surface to test EPFD bound compliance, parameter δ for satellite turn off control, and transmission powers $(P_c: c \in \mathcal{C})$ for each class of LEO satellites

Output: Pass/Fail depending on whether there exists feasible solution to (*4-14*) or not

1. allocate transmission power $P_{c(i)}$ at each LEO link transmitter, according to its hardware class
2. **foreach** $(t = 1,2,\cdots,T_s)$
3. **foreach** (GS $g = 1,2,\cdots,N_{GS}$)
4. compute $N_v^{t,g}$ as the number of visible LEO link transmitters visible from GS g at snapshot t
5. compute the downlink $EPFD_{t,g,i}$ caused by satellite $i = 1,\dots,N_v^{t,g}$ to GS g via Eq. 4-15 at snapshot t and compute the overall EPFD as $EPFD_{t,g} = \sum_{i=1}^{N_a} EPFD_{t,g,i}$ (where $N_a = N_{vi}^{st,g}$).
6. sort $EPFD_{t,g,i}$ in decreasing order (for fixed t, g)
7. set $a_{i,t} = 1$ for all i, t
8. **end for**

9. **end for**
10. check EPFD limits violation; if they are satisfied, there is no need to turn off any further satellites, return **Pass**
11. otherwise,
12. determine the set of snapshots and GS where $EPFD_{t,g}$ violates Table 16 limits, i.e., compute set $\mathcal{V} = \{(t,g): EPFD_{t,g} \text{ violates Table 8 limits}\}$
13. **foreach** $(t,g) \in \mathcal{V}$
14. find the first (i.e., earliest) i in $EPFD_{t,g,i}$ (this has already been sorted in step 6) such that $a_{i,t} = 1$. Denote this with $\bar{\imath}$ and set $a_{\bar{\imath},t} = 0$, $EPFD_{t,g,i} = 0$
15. test if it still holds $\sum_{t \in \mathcal{T}} a_{\bar{\imath},t} \geq T_s(1-\delta)$. If not, return **Fail**
16. **end for**
17. **goto** step 10

It is easy to confirm that the above algorithm runs in polynomial time, since steps 1-10 can be executed in $O(N_{GS}T_sN_{LEO})$ time while each execution of steps 12-16 also runs in $O(N_{GS}T_sN_{LEO})$ time and there can be at most N_{LEO} executions of steps 12-16 (depending on the specific data structures used to store and sort the $EPFD_{t,g,i}$ values, some of the steps can be executed faster).

Having an efficient heuristic algorithm for solving the EPFD satisfiability problem in Eq. 4-2, we now formulate the main problem of interest, i.e., finding the highest possible LEO transmission powers that still result in an EPFD-compliant solution, which can be described as

$$\begin{gathered} \max \min_{c \in \mathcal{C}} P_c, \\ s.t. P_c \leq P_c^{max}, \quad \forall c \in \mathcal{C} \\ P_c \text{ satisfies Eq. 4-2.} \end{gathered} \tag{4-16}$$

The problem in Eq.4-3 is non-linear wrt. P_c and can be solved with any global optimization or meta-heuristic technique. In the following, we employ a simple shooting-like method, where we arbitrarily select initial starting values for P_c and, as long as they satisfy Eq. 4-2, we keep increasing these values until we reach a threshold where Eq. 4-2 is no longer satisfied. This is illustrated in a detailed numerical example in the following Section.

4.2.2.3 Numerical results

We discretize the Earth's surface along the latitude $(-90°, 90°)$ and longitude $(-180°, 180°)$ by a step of $DLat$ and $DLon$, respectively, and place GEO-Earth-Stations at the respective grid points. We consider two different pairs of values, namely $(DLat, DLon) = (10°, 10°)$ and $(DLat, DLon) = (10°, 5°)$, resulting in 614 and 1262 GEO-Earth-Stations (hereafter referred to as GS), respectively. We consider 4 different LEO constellations of size 200, 400, 800, 1600, respectively, and compute their positions and relative angles from each GS, as well as the Downlink EPFD at the GS, for a period of 24 hours (specifically, in the time interval from June 25, 2025, 00:01:00 UTC to June 26, 2025, 00:01:00 UTC), which is sufficiently long to capture multiple revolutions of the LEOs around the Earth. We discretize this time interval in steps of 2 minutes, resulting in a total of 721 "snapshots". We assume that all LEO satellites belong to a single class with $P_c^{max} = 20$ W (i.e., 13 dBW), the value being selected in accordance with

the literature as a typical power level. We also select $\delta = 0.05$, which corresponds to a maximum 5% percentage of cumulative time (i.e., not necessarily contiguous) over which any LEO satellite can be turned off during its mission time.

To determine whether the selected latitude/longitude resolution of the GEO-Earth-Stations allows for the collection of grid points to accurately represent the Earth's surface, we compare in Figure 4-31 the maximum EPFD, over all GS, caused by a 200 LEO constellation. The boxplots for the two different GS grids are almost identical, with less than 5 dBW/m^2 difference in their Q3 points, indicating that the GS grid corresponding to the $(DLat, DLon) = (10°, 10°)$ configuration is already sufficiently fine so that any further refinement will have minimal impact. For this reason, all subsequent results will be provided for this GS grid only, i.e., considering 614 GSs only.

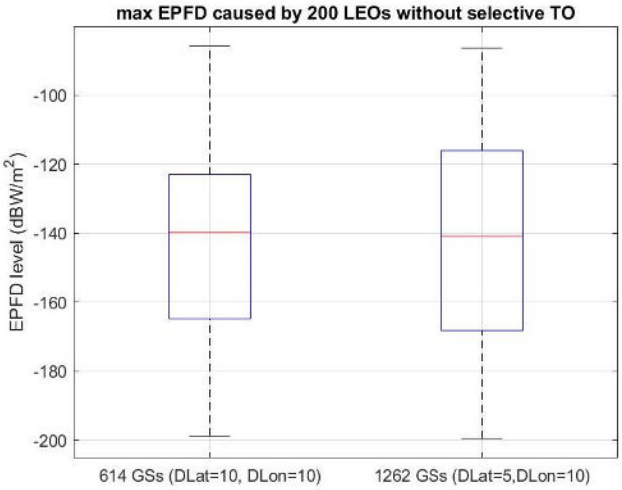

Figure 4-31 Boxplot of the maximum EPFD caused by a 200 LEO constellation on different GS grids

As mentioned in the previous Section, the EPFD must be calculated at each of the 614 GSs over the 24 hour period (i.e., 721 time snapshots), and the collection of these EPFD values must then be checked against the soft limits of Table 16An indicative EPFD curve vs. time is provided in Figure 4-32 for the GS with id 493 (selected arbitrarily), located at (50°N, 60°E), for all 4 different LEO constellations, without any LEO satellite being turned off at any instant during the 24 hour period. For visual convenience, we have selected to only show the stems of the EPFD values above -200 dBW/m^2 (i.e., any vertical lines without a stem correspond to EPFD values below -200 dBW/m^2, which is well below the ITU-R limits) and also indicate with a filled red stem all time instances where the EPFD value at the given GS exceed the highest threshold of -154 dBW/m^2 provided in Table 16. Some interesting observations can be immediately drawn from Figure 4-32:

- as the constellation size increases, the number of time instances where EPFD may exceed the ITU-R limits also increases (recall the additive nature of EPFD in 4-1). However, a plateau effect appears (most evident by comparing the EPFD variations from 200 to 400 LEOs again the variations from 800 to 1600 LEOs), where, once a sufficient number of satellites have been added to create a "canopy" over the Earth, adding more satellites in the same orbits is no longer possible and a different orbit must be selected, possibly at higher altitudes leading to a less significant EPFD increase.
- the level at which the EPFD limits are violated suggests the type of corrective action to be taken. For example, at time snapshot 55, all 4 LEO constellations exhibit an EPFD level of -116 dBW/m^2, which indicates an inline event (as this EPFD level does not

change between 200 LEOs and 1600 LEOs). Compared to the ITU-R threshold of -154 dBW/m^2, the violation is too high to be compensated by globally scaling down the power of all satellites by an amount of -116-(-154)= 38 dB. Instead, it is better to turn off the offending satellite for an amount of time that will decrease the EPFD to the required levels.

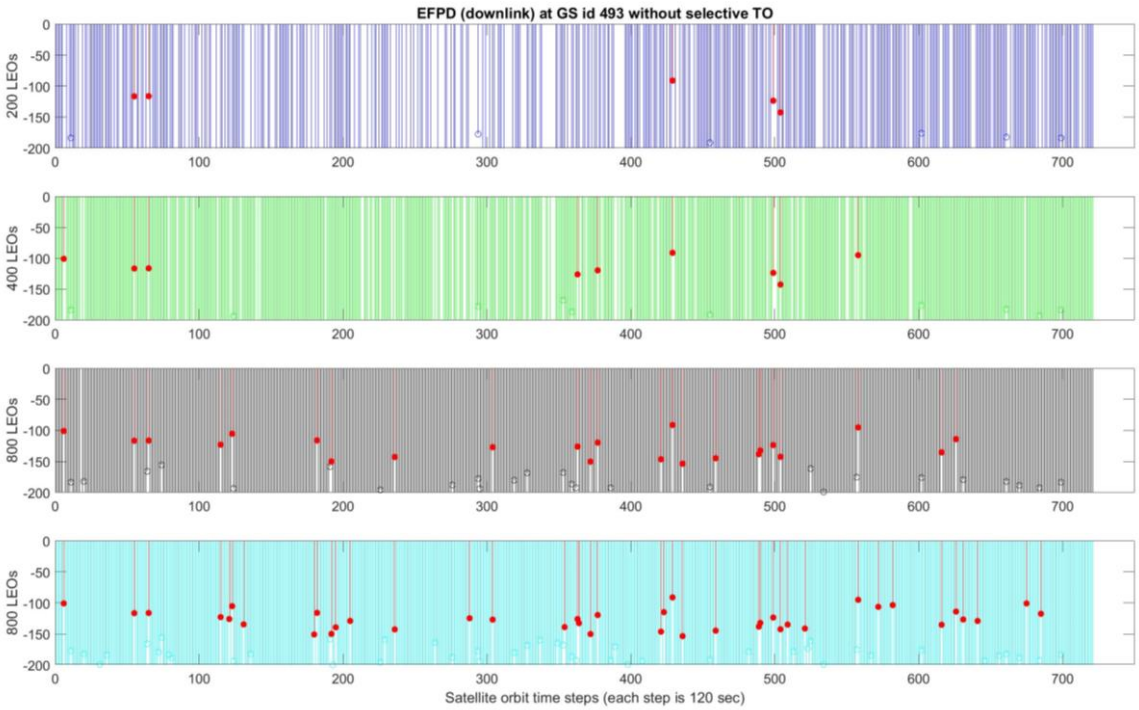

Figure 4-32 EPFD vs time at GS 493 for the 4 different LEO constellations.

Since in the current setup the LEO constellation does not satisfy the EPFD limits, we next examine the effect of selectively turning off (TO) some LEOs during the periods of time where they cause excessive EPFD. To this end, we apply steps 12-16 of our heuristic EPFD satisfiability algorithm and turn off all LEOs whose **individual** $EPFD_i$ **exceeds** the ITU-R limits. Performing this selective TO action yields the new EPFD results for GS 493 shown in Figure 4-33, where the green ovals indicate that high EPFD values violating ITU-R limits without TO drop significantly and satisfy the ITU-R limits once TO is applied. For example, turning off the satellites whose $EPFD_i$ values violate the ITU-R limits at snapshot 55 results in the EPFD at GS 493 dropping from -116 dBW/m^2 to below -200 dBW/m^2 for the 200 LEO constellation! Similar trends are observed for the other LEO constellations (the green ovals only appear on the top plots of Figure 4-33 to avoid obscuring the denser plots in the bottom part).

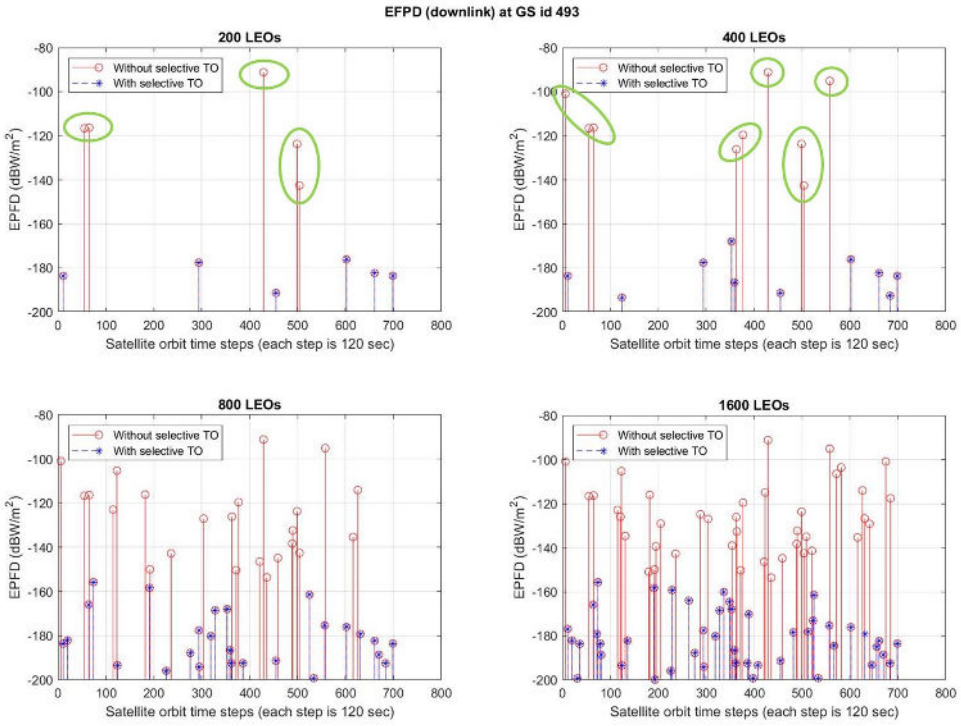

Figure 4-33 EPFD vs time at GS 493 for the 4 different LEO constellations with selective turnoff of LEOs.

The same data in Figure 4-33 can be used to produce the more informative plot in Figure 4-34, which distinctively shows the beneficial effect of selective TO towards bringing the EPFD lower (in a probabilistic sense) than the vertical dotted line corresponding to the strictest ITU-R limit of -154 dBW/m^2.

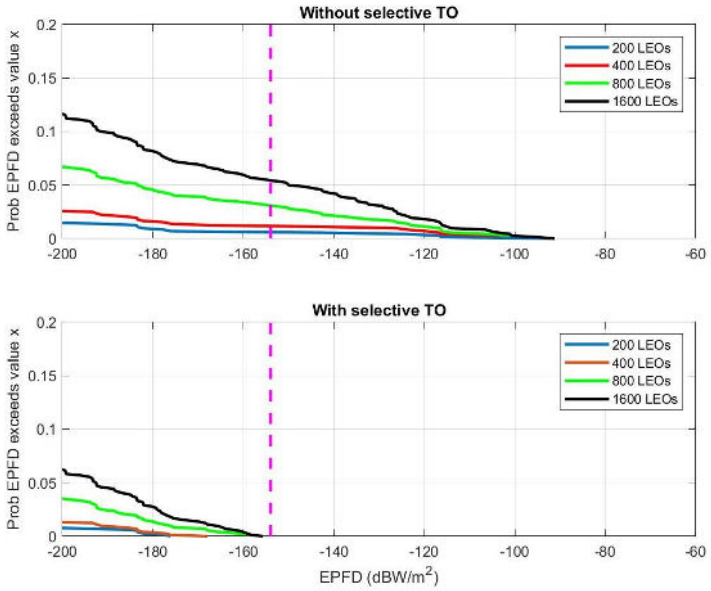

Figure 4-34 Probability that EPFD at GS 493 exceeds given levels

Since the numerical results have focused thus far on a specific (albeit, arbitrary) GS, it is important to determine the statistical properties of the EPFD **over all GSs**, so that we can

conclusively decide whether the EPFD satisfiability problem is feasible or not for the specified solution. This is performed in Figure 4-35, which provides the probability (in absolute value, not as a percentage) that the EPFD of any of the 614 GSs exceeds the specified ITU-R limits (with and without TO). Out of the 4 probability values provided in Table 16, the values 100% and 28.571% (for -187 and -182 dBW/m^2, respectively) are out of the range of Figure 4-35and always satisfied, so that we focus our attention on the remaining probability values of 2.857% and 0.017% (for -172 and -154 dBW/m^2, respectively). Hence, the horizontal dotted line in Figure 4-35 should only be compared to the bars corresponding to the -172 dBW/m^2 level to determine compliance with ITU-R.

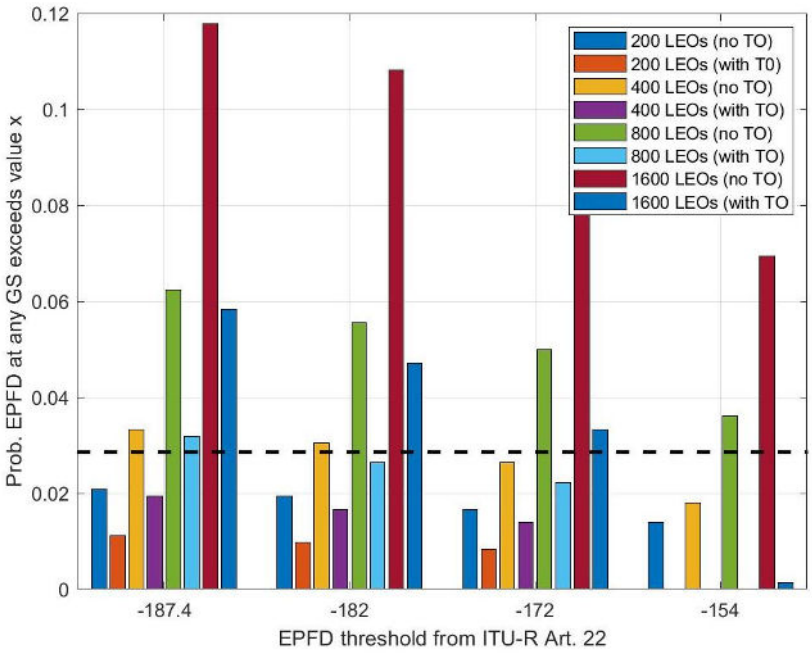

*Figure 4-35 Probability that EPFD at **any** GS will exceed the specified ITU-R limits*

An examination of Figure 4-35 confirms that, **by enabling selective TO** for a maximum LEO transmission power of 20W (equivalently, 13 dBW), **we can indeed satisfy the ITU-R limits for the 200, 400, 800 LEO constellation but not for the 1600 LEO constellation**. In the latter case, the 1600 LEO constellation exceeds the -154 dBW/m^2 level with probability 0.14% instead of the required 0.017%. Although this may appear as a huge discrepancy, careful data analysis reveals that the -154 dBW/m^2 level is violated at a single instance, specifically for GS id 272 at snapshot 1, where the EPFD level is -151.5614 dBW/m^2. Hence, we can satisfy the ITU-R limits even for the 1600 LEO constellation either by decreasing transmission power by 3 dB, or by turning off the LEO satellite causing the highest EPFD at GS 272 and snapshot 1.

Finally, we determine the amount of time for which the LEOs should be selectively turned off and verify that it is within the allowed operating regime specified by parameter $\delta = 0.05$. This is shown in the boxplots of Figure 4-36, which indicates that most LEO satellites are turned off for a maximum amount of 20 minutes during the entire 24 hour duration, with a few outliers reaching up to 40 minutes of deactivation. Even for these outliers, the maximum percentage of time that they are turned off during their mission corresponds to 40/(24*60)= 2.78%, which lies well within the 5% limit. Hence, we conclude that, with the turnoff schedule indicated in Figure 4-37 (where each blue dot corresponds to a snapshot where the respective satellite is turned off) and a maximum transmission power of 20W, full ITU-R compliance is achieved wrt. EPFD while also satisfying the LEO service parameters.

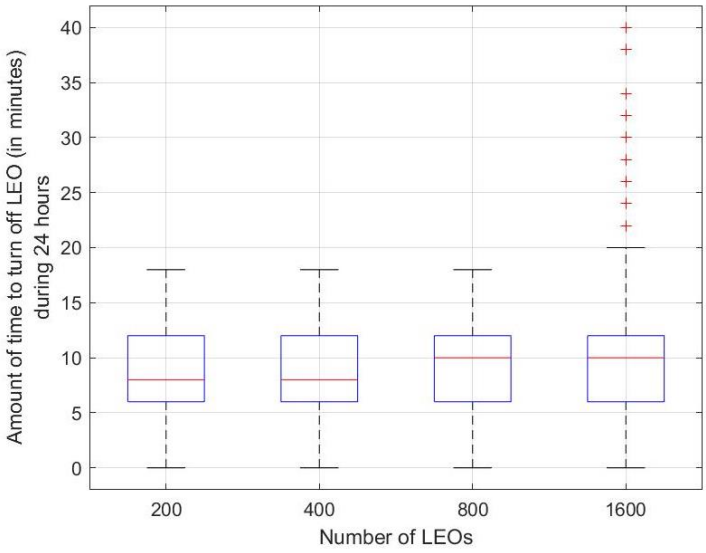

Figure 4-36 Distribution of the amount of time that LEOs should be turned off to satisfy the ITU-R EPFD limits.

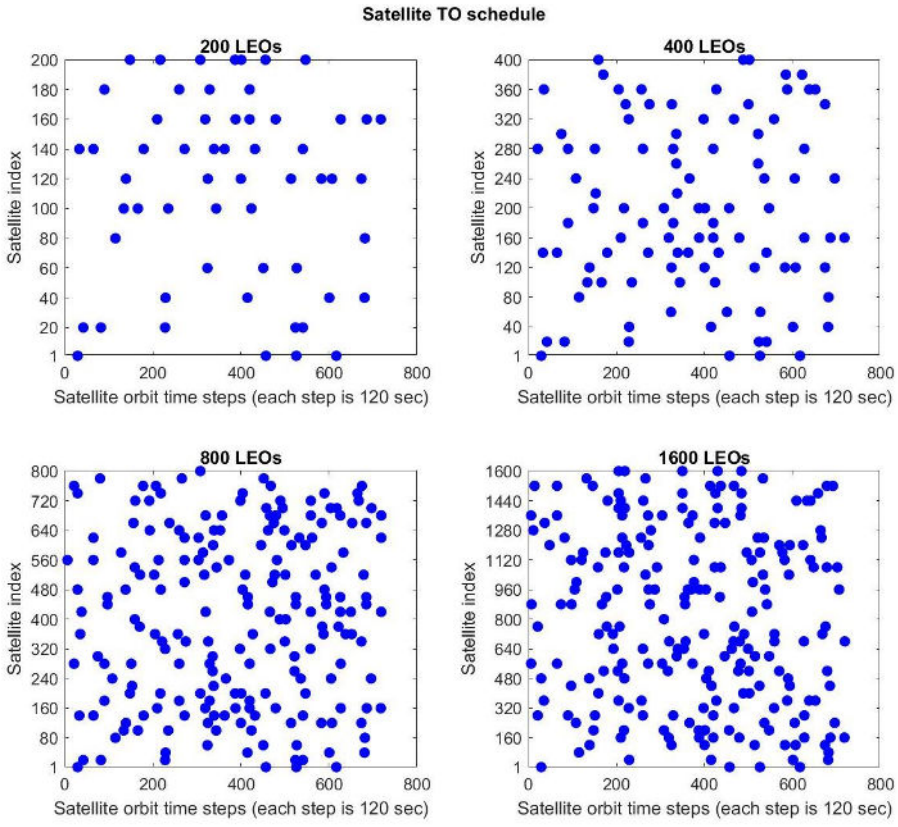

Figure 4-37 LEO transmitter turn off schedule yielding an ITU-R compliant EPFD solution.

In case the above analysis indicated that the maximum transmission power of 13 dBW resulted in a turn off percentage exceeding 5%, the analysis would be repeated for a lower transmission power, say 12 dBW, essentially following the shooting-like approach for solving Eq.4-17. Thankfully, due to the linear dependence of EPFD on the transmission power, this analysis need only be performed as a post-processing stage on the computed EPFD values and does

not require re-computation of the satellites' relative positions and angles. Since the LEO transmission power of 13 dBW is ITU-R compliant under the satellite turn off schedule of Figure 4-37, we increase the transmission power to 14 dBW and check whether this is still ITU-R compliant. Figure 4-38 indicates that this is not the case, as the -154 dBW/m^2 limit is exceeded with probability 0.55% instead of the required 0.017%. Hence, a new turn off schedule must be derived and checked against the 5% turn off threshold. It turns out that such a new turn off schedule exists and also satisfies the 5% threshold so that a LEO transmission power of 14 dBW is also ITU-R compliant. The above procedure continues until the maximum ITU-R compliant LEO transmission power is determined.

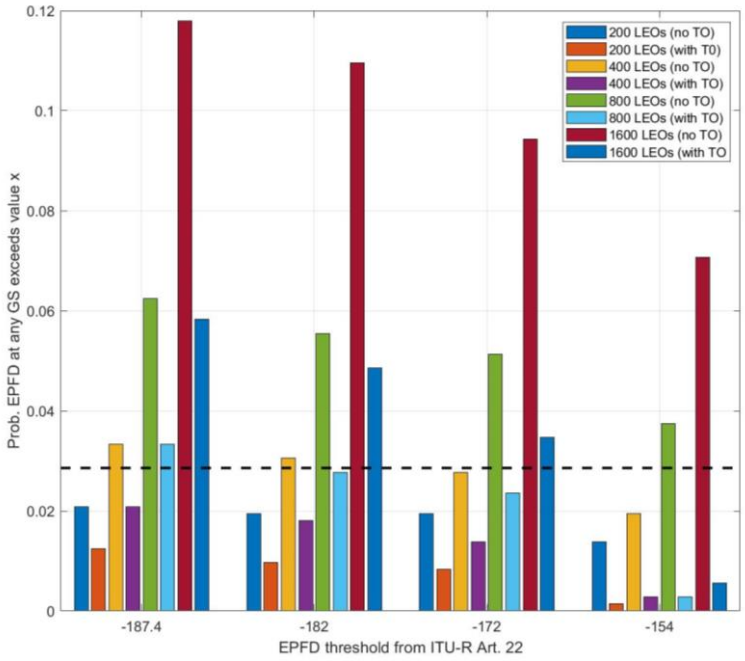

*Figure 4-38 Probability that EPFD at **any** GS will exceed the specified ITU-R limits for a maximum LEO transmission power of 14 dBW under the turn off schedule of Figure 4-37.*

In conclusion, the presented heuristic algorithm for EPFD satisfiability and the associated optimization problem offer an efficient computational toolset that allows the ITU-R EPFD limits to be verified for any LEO constellation, once a sufficient amount of data is collected for the satellite snapshots and the relative positions and angles at each snapshot, while the solution of Eq. 4-18 can then be effected as a post processing stage. The LEO satellite turn off schedule arises naturally within this procedure without the need to compute "worst-case" geometries or employ external "black-box" tools. Furthermore, the overall methodology is general enough to account for arbitrary LEO orbits and ITU-R limits in different frequency bands, thus providing a powerful tool to the satellite operator during the network provisioning stage.

5 DATA ANALYTICS AND SEMANTICS-AWARE CACHING FOR HIGH ENERGY EFFICIENCY

Introduction

ETHER employs semantics-aware information handling combined with edge computing and caching to achieve high energy efficiency. By leveraging the Version Age of Information (VAoI) as a semantic metric, this approach enables the transmission of only essential updates, thereby preserving the conveyed information while significantly reducing data transmissions and energy consumption. VAoI extends the traditional Age of Information (AoI) by incorporating both timeliness and content changes, thus supporting context-aware decision-making. In Deliverable D3.1, we introduced semantics-aware communication schemes by reviewing key semantic metrics and proposing an information-handling framework for a status update system that transmits data from an energy-harvesting (EH) sensor to a unidirectional ring gossiping network. In the present deliverable, we extend this work to real low Earth orbit (LEO) satellite networks with two distinct topologies. We develop explicit stochastic models for VAoI in the destination satellite network and optimize the average VAoI over both finite and infinite time horizons.

Specifically, we employ a semantics-aware approach to handling information from an energy-constrained IoT device to a network of interconnected LEO satellites with two distinct topologies: ring and star. We analyse the VAoI at LEO nodes and optimize its network-wide average by adopting a transmission policy at the device, subject to energy constraints in an EH scenario, where the effective energy use for delivering timely and informative data is targeted. This work has been published in [53]

5.1 SYSTEM MODEL

We consider a system model in which a remote EH IoT device measures and transmits status updates from an information source to a network of $(N+1)$ LEO satellites. During a visibility window, the IoT device connects to a satellite, referred to as the Connected Satellite (CS), and transmits updates according to an *update policy* while adhering to the constraints imposed by the harvested energy stored in the device's battery. The update policy, denoted by π, decides whether the device transmits a fresh update to the CS, thereby consuming energy, or remains idle to conserve energy for future use. This decision, or action, is made sequentially in each time slot along a slotted time axis.

Energy Harvesting: The device harvests energy from ambient sources and stores it in a battery with capacity B. The energy harvesting process follows a Bernoulli distribution with an arrival probability of β, which is commonly used as a general stochastic model. Each transmission to the CS consumes one energy unit and occupies one time slot.

LEO Network Topologies: We consider two topologies for the LEO network: a ring topology and a star topology (as depicted in Figure). In the ring configuration, enabled by permanent Inter-Satellite Links (ISLs), updates received at the CS are disseminated in both directions along a bidirectional ring topology. Nodes are indexed by the set $\mathcal{N}_{\mathcal{R}} = \left\{-\frac{N}{2}, -\frac{N}{2}+1, \cdots, \frac{N}{2}-1, \frac{N}{2}\right\}$, where N is an even integer. Each node forwards the updates to its neighbors, thereby continuing the propagation throughout the network. We assume that transmissions between neighboring satellites via ISLs are deterministic, occurring error-free and at regular intervals. In the star configuration, the CS multicasts status updates to N neighboring satellite nodes, each one hop away via unreliable ISLs with success probabilities $\rho_n, \in \mathcal{N}_{\mathcal{S}} \setminus \{0\}$ where $\mathcal{N}_{\mathcal{S}} = \{0,1,2,\cdots,N\}$. This multicast occurs in every time slot. In both topologies, each transmission

occurs in one time slot, and each node retains only the most recent data update, discarding any previous ones.

VAoI as the Semantic Metric: The ultimate objective is to develop an update policy that optimizes network performance by delivering timely and informative data while efficiently managing energy, using VAoI as the semantic performance metric. VAoI measures both the timeliness and relevance of information in status update systems, reflecting the number of versions the receiver lags behind the source as new content or versions are generated [54]. By assigning version numbers to new content at the source, the VAoI at a destination node D can be defined as: $\Delta(t) = V\_S(t) - V\_D(t)$, where $V_S(t)$ is the version stored at the source, and $V_D(t)$ denotes the version stored at node D at time t. We assume that a new version at the source is generated with probability p_g in each time slot, following a Bernoulli distribution.

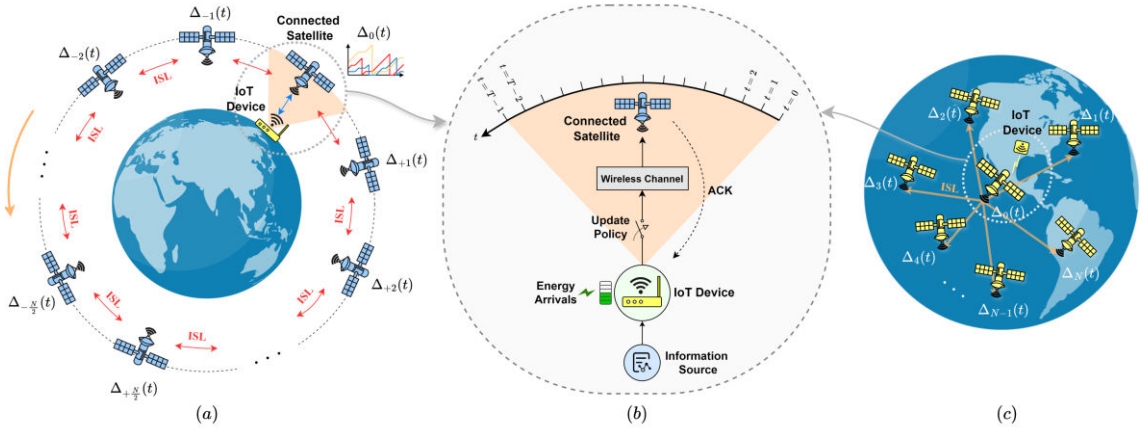

Figure 5-1: Status updates from an IoT device to an (N+1)-satellite LEO network: (a) ring, (c) star topology. (b) shows the direct link from the device to the CS.

5.2 VERSION AGE OF INFORMATION WITHIN THE SATELLITE NETWORK

Our objective is to model the average VAoI in the satellite network and optimize it by deriving an optimal update policy. Considering a time horizon T, the time-average VAoI of the n-th satellite and the average VAoI across the entire network, for a given update policy π, are defined as follows:

$$\overline{\Delta}^{\pi}_{n,T} = \frac{1}{\mathrm{T}} \sum_{\mathrm{t}=0}^{\mathrm{T}-1} E[\, \Delta^{\pi}_{n}(t)\,] \tag{5-1}$$

$$\overline{\Delta}^{\pi}_{T} = \frac{1}{N+1} \sum_{n \in \mathcal{N}} \overline{\Delta}^{\pi}_{n,T} \tag{5-2}$$

where $\Delta^{\pi}_{n}(t)$ denotes the VAoI at the n-th satellite at time t under the policy π, and $\mathcal{N}$ is either $\mathcal{N}_{\mathcal{R}}$ or $\mathcal{N}_{\mathcal{S}}$.

It can be shown [53] that the average VAoI of the network is given by:

Ring topology: $\overline{\Delta}_T^{\pi} = \frac{\mathrm{N(N+2)}}{4(\mathrm{N+1})}\mathrm{p_g} + \mathrm{E}\left[\frac{1}{\mathrm{T'}}\sum_{\mathrm{t=0}}^{\mathrm{T'-1}}\Delta_0^{\pi}(t)\right]$

Star topology: $\overline{\Delta}_T^{\pi} = \frac{p_g\sum_{n=1}^{N}\frac{1}{\rho_n}}{N+1} + E\left[\frac{1}{T}\sum_{t=0}^{T-1}\Delta_0^{\pi}(t)\right]$

where $\Delta_0(t)$ denotes the VAoI at the Connected Satellite and $T' = T - \frac{N}{2}$. The optimization of the average VAoI in both networks is formulated as follows:

$$\overline{\Delta}_T^{*} = \min_{\pi\in\Pi}\overline{\Delta}_T^{\pi}$$

Ring topology: $\overline{\Delta}_T^{*} = \frac{N(N+2)}{4(N+1)}p_g + \min_{\pi\in\Pi} E\left[\frac{1}{T'}\sum_{t=0}^{T'-1}\Delta_0^{\pi}(t)\right]$

Star topology: $\overline{\Delta}_T^{*} = \frac{p_g\sum_{n=1}^{N}\frac{1}{\rho_n}}{N+1} + + \min_{\pi\in\Pi} E\left[\frac{1}{T}\sum_{t=0}^{T-1}\Delta_0^{\pi}(t)\right]$

where a standard finite-horizon average cost Markov Decision Process (MDP) problem is obtained for both topologies:

$$\mathcal{P}_1: \overline{\Delta}_0^{*} = \min_{\pi\in\Pi}\frac{1}{\mathcal{T}}E\left[\sum_{t=0}^{\mathcal{T}-1}\Delta_0^{\pi}(t) \mid s(0)\right] \quad (5\text{-}3)$$

where $s(0)$ is the initial system state, Π the set of feasible policies, and $\mathcal{T}$ the MDP time horizon, equal to T' for the ring topology and T for the star topology. The problem models a status update system where an EH IoT device monitors a source and transmits updates to the CS node over an error-prone wireless channel, as illustrated in Figure b. Each update succeeds with probability p_s. The update policy π is a sequence of actions $a(t)$, where $a(t) = 1$ denotes a transmission at time t, and $a(t) = 0$ indicates idling to conserve energy. The optimal policy π^* minimizes the average VAoI in $\mathcal{P}_1$ and can be computed using dynamic programming. The solution to this finite-horizon MDP depends on $\mathcal{T}$, the initial state $s(0)$, and time t, making it non-stationary. However, for sufficiently large $\mathcal{T}$, $\mathcal{P}_1$ can be approximated by an infinite-horizon average cost MDP, $\mathcal{P}_2$, yielding a stationary policy independent of the initial state—more suitable for analyzing the optimal policy's behavior.

$$\mathcal{P}_2: \overline{\Delta}_0^{*} = \min_{\pi\in\Pi}\lim_{\mathcal{T}\to\infty}\frac{1}{\mathcal{T}}E\left[\sum_{t=0}^{\mathcal{T}-1}\Delta_0^{\pi}(t) \mid s(0)\right] \quad (5\text{-}4)$$

5.3 NUMERICAL RESULTS

The optimal policy for $\mathcal{P}_1$ is derived using backward dynamic programming and for $\mathcal{P}_2$ using the Relative Value Iteration Algorithm (RVIA). We compare the performance of the optimal policies with two baselines: the Greedy policy, which transmits an update whenever energy arrives and the battery is not empty, and the Randomized Stationary (RS) policy, which transmits with probability α each time slot, provided the battery is not empty. All simulations utilize fixed parameters, as summarized in Table 17. Expected values are averaged over 4000 Monte Carlo iterations.

Table 17 Simulation parameters

Simulation parameters	Value
p_g	0.3
p_s	0.5
$\{\rho_n\}_{n=1}^{N}$	0.7
B	20
Δ_{max}	30

The Structure of the Optimal Policy:

Figure 5-2 shows the optimal policy for $\mathcal{P}_2$ with an energy arrival probability $\beta = 0.1$. Red circles denote idle actions ($a = 0$), and blue asterisks indicate updates ($a = 1$). This policy follows a threshold-based structure: for each battery state b, the device remains idle until the VAoI at the CS exceeds a certain threshold, which triggers updates. This reflects a key aspect of semantics-aware communication: *conserving energy for later usage when it is most needed*. In energy-scarce settings, this prevents early battery depletion at low VAoI, avoiding long update gaps. Delaying depletion until VAoI is reasonably high mitigates excessive growth.

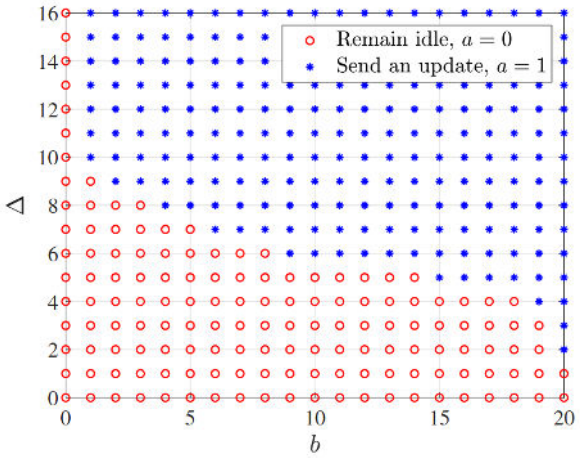

Figure 5-2: The structure of the optimal policy for the problem $\mathcal{P}_2$

The Impact of Energy Arrival Probability (β):

Figure 5-3 shows the average VAoI for both topologies versus energy arrival probability β, under optimal, Greedy, and RS policies, for $\alpha = 0.1, 0.2$, and 0.3. A large horizon $T = 3000$ is used, where finite- and infinite-horizon policies yield similar results, with the latter slightly better. As seen, the average VAoI differs between the ring and star topologies by a constant offset, reflected in the separate left and right y-axes. As β increases, average VAoI decreases, with the optimal policies performing best using optimal update thresholds. The performance gap between optimal and Greedy narrows with higher energy availability, approaching the *always update* policy. However, this gap widens under low β, making optimal actions crucial for a fresher, more informative system.

In this simulation, the RS policy performs worse than the Greedy policy. Notably, the Greedy policy is a special case of the RS policy with $\alpha = 1$, so increasing α causes RS to converge toward Greedy, as shown in the figure. When the energy arrival probability is high, energy is more often available. The Greedy policy uses all available energy, while the RS policy with $\alpha < 1$ sometimes skips updates, allowing energy to accumulate. As a result, Greedy yields more updates and RS fewer, leading to a worse average VAoI for RS. In contrast, when the energy arrival probability is low, both policies deplete the battery in a similar manner-Greedy by transmitting at the first opportunity and RS at a random slot-resulting in the same number of updates and similar performance.

Remark: An important result is that to maintain a target average VAoI—such as 8 for the ring topology or 3.5 for the star—the optimal policy requires an energy arrival rate of 0.1, half that of the Greedy policy (0.2). This shows that ***a semantics-aware update policy can significantly reduce the energy consumption by*** $\mathbf{50\%}$. The reduction stems from fewer updates, leading to less satellite dissemination, significantly improving energy efficiency and extending system lifetime.

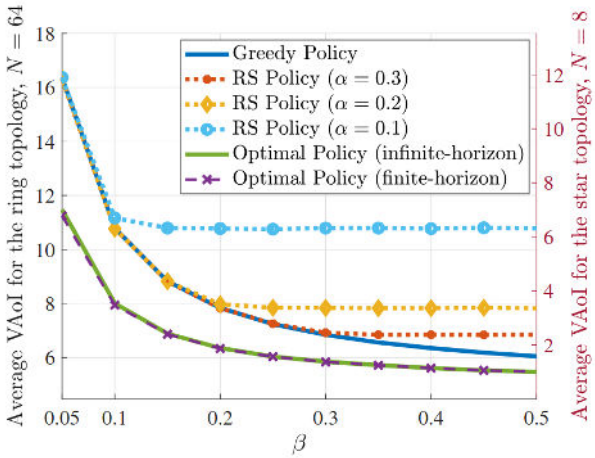

Figure 5-3: Average VAoI vs. β; same curves with different y-axes (ring: left, star: right)

6 HORIZONTAL AND VERTICAL HANDOVER POLICIES ACROSS ETHER LAYERS

Introduction

The previous deliverable D3.1 established the foundational work for horizontal handovers in LEO-based Store & Forward networks, presenting the initial design, implementation, and laboratory validation of the UE Context Proxy. While D3.1 successfully demonstrated the basic proof-of-concept for transferring UE contexts between satellites, it also identified key limitations such as outdated contexts causing communication failures. Building upon these foundations, D3.2 presents enhancements including advanced features for selective context updates and, most notably, the successful demonstration of the technology at IEEE INFOCOM 2025, showcasing its evolution from laboratory proof-of-concept to a practical solution validated under realistic satellite constellation constraints.

Regarding the Vertical HOs in the previous Deliverable (D3.1) we showed the initial implementation of our simulator framework, made precisely to simulate the ETHER environment. Specifically we had presented the Omnet++ based simulator in its first working version, capable of simulating complex satellite networks, including Terrestrial and Non-Terrestrial entities, with the use of several simulation libraries, such as INET (general networking protocols), Simu5G (the Omnet++ 5G simulation library), and of course OS3, a library that can produce the satellite mobility patterns, albeit being inactive at the time of working on D3.1 and had to be updated to be functional again. In D3.2, we present the progress we had with the simulator platform, and specifically, the introduction of a realistic Satellite wireless channel model that is taking place through the use of a Matlab wrapper class, plus the first working version of the PETA algorithm, a vertical HO algorithm that performs the HOs, not on the basis of SINR measurements, but on the basis of energy efficiency.

6.1 HORIZONTAL HANDOVERS IN LEO-BASED S&F NETWORKS

6.1.1 Background and motivation

The increasing demand for ubiquitous IoT connectivity has driven significant interest in satellite-based NB-IoT services within 3GPP's Non-Terrestrial Networks framework. 3GPP Release 19 introduces S&F satellite operation for delay-tolerant communication services, relying on regenerative payload architectures with core network functions onboard satellites. This represents a significant evolution from earlier releases that assumed continuous end-to-end connectivity requiring large constellations and extensive ground infrastructure or limited coverage due to lack of concurrent service and feeder link availability. While Release 19 provides the foundation for S&F operations through regenerative satellite payloads, the standards do not specify how horizontal handovers should be realized in sparse constellation scenarios, where satellites cannot maintain continuous communication links with ground infrastructure or with each other. However, the autonomous operation of satellites in absence of feeder link connectivity requires the presence of UE context information on the satellites. Furthermore, UEs in delay-tolerant applications may need to communicate with multiple satellites within a constellation to maintain sufficient service levels that cannot be achieved with a single satellite.

6.1.2 Challenges and goals

Key challenges:

1. **S&F-based UE Context Proxying**: The first major challenge involves developing a S&F-based proxying element capable of disseminating UE contexts generated at one

satellite during network registration procedures to other satellites in the constellation. This UE context, containing UE identifiers, state information, security keys, session information and subscription data, needs to be extracted from the source satellite's AMF/MME, packaged, and transmitted to the ground segment during the next feeder link availability window. The ground-based counterpart then distributes this context to other satellites as their feeder links become available, with each receiving satellite's proxying element interacting with the onboard core network component to integrate the newly received UE context for future signalling connections with the given UE.

2. **Multi-satellite Operation Validation**: The second challenge involves validating that UE context transfer mechanisms work effectively in realistic scenarios that replicate the constraints of sparse LEO constellations, including discontinuous feeder link availability, satellite visibility windows, and varying network conditions.

Primary Goals:

- **Design and validate a S&F proxying element** capable of extracting and inserting UE contexts in satellite-based core network elements (AMF or MME) and interfacing with ground-based counterpart proxying elements to enable seamless multi-satellite service provision.

- **Demonstrate proof-of-concept operation** of UE context transfer between satellites in a laboratory testbed environment, identifying key technical challenges and limitations of basic context dissemination approaches in sparse constellation scenarios.

6.1.3 Results achieved

During the execution of T3.4, the following results were achieved in relation to the challenges and goals described above.

6.1.3.1 S&F UE Context proxying element

The need for a S&F proxying element to enable NB-IoT service provision via sparse LEO constellations featuring discontinuous FLs was envisioned by Kellermann et al. [55]. Its first practical implementation as the *UE Context Proxy* was undertaken during the ETHER project, as it was reported earlier in D3.1 [1].

The initial implementation of the UE Context Proxy reported in D3.1 already included the planned main features and allowed us to fetch a UE context data structure from a given satellite, download it to the ground, and disseminate it within the constellation by updating it to other satellites. Development on the proxy continued after D3.1, by performing bug fixing, adding minor features for ease of operation, and porting it to version v1.9 of the Magma core network software (on which the Context Proxy integrates), which was branched[1] in early 2025 and had its first release[2] v1.9.0 on May 16th 2025.

6.1.3.2 S&F UE Context Proxy validation and demonstration

The validation of the UE Context Proxy in a laboratory environment was reported in D3.1 [1] and shown in a video demonstration [56]. That work was leveraged and demonstrated later by

[1] https://github.com/magma/magma/compare/master...v1.9

[2] https://github.com/magma/magma/releases/tag/v1.9.0

i2CAT and SIoT in May 2025 at the IEEE International Conference on Computer Communications (INFOCOM 2025) in a demo session[3], as summarized in the following.

The INFOCOM 2025 demo presented a testbed with a novel implementation of a UE Context Proxy demonstrating asynchronous UE context dissemination in NTN, focusing on 3GPP-compliant S&F architectures for a novel testbed implementation for sparse LEO constellations. The primary objective was to validate mechanisms for disseminating UE contexts across MMEs/AMFs in multi-satellite and multi-user NB-IoT service environments, enabling seamless handovers between satellites despite the inherent challenges of discontinuous and non-concurrent FL operations.

The demonstration consisted of a testbed implementing a practical in-lab UE context dissemination across satellites through a central, ground-based proxy. By accurately modelling satellite visibility and contact windows, the testbed replicated real-world constraints, demonstrating its relevance for global IoT connectivity. It showcased the attachment/registration of a UE to one satellite, the retrieval of its context during FL availability from the ground, and the subsequent transfer of the context to another satellite. The process allowed the UE to seamlessly resume service with another satellite, reducing latency and enhancing user experience. The results confirmed the practicality of this approach, aligning with ongoing 3GPP Release 19 standardization efforts [57].

Figure 6-1 illustrates the system architecture and testbed hardware, including UEs, satellites, and ground segment operations designed to emulate realistic NTN services. The testbed emulated two satellites, each equipped with an onboard MME/AMF (Magma core network) and a commercial Amarisoft gNB[4]. A UE Context Proxy on each satellite handled S&F functions, including UE context extraction, injection, and updates. A central Control Proxy on ground retrieved and disseminated UE contexts during FL windows, enabling seamless handovers between satellites and ensuring continuity of service across the constellation.

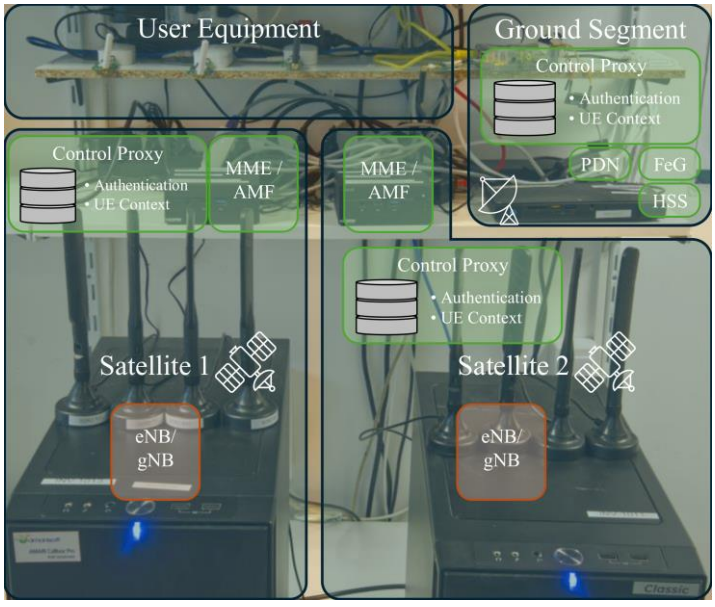

Figure 6-1 Testbed Equipment - Hardware and core components.

The testbed could simulate larger constellations by running multiple satellite core instances in parallel. Reloading the Amarisoft gNB software with different configurations allowed the

[3] https://infocom2025.ieee-infocom.org/program/postersdemos

[4] https://www.amarisoft.com/test-and-measurement/device-testing/device-products

testbed to model varying satellite behaviours, including different orbital parameters, signal strengths, and network conditions. An essential feature of the system was its ability to update specific parts of a UE context on a satellite. For instance, the NAS count, which changes with each interaction between a satellite and a UE and necessitates continuous updates, could be updated disseminated without need for sending the whole UE context.

Figure 6-2 illustrates the demonstration workflow, starting with the attachment of a UE to Satellite 1, where its context was established at the onboard MME and stored in the database. During Satellite 1's FL availability, the ground proxy retrieved the UE context and stored it in a central database. Once the FL of another satellite became available, the ground proxy transferred the context to that satellite, where it was injected into the local MME/AMF through the connected database. The constellation simulation mimicked real-world constraints by determining satellite visibility windows and dynamically adjusting SL and FL connectivity. Disruptions were reproduced through traffic interruptions and signal power variations, ensuring realistic validation of the asynchronous dissemination mechanism.

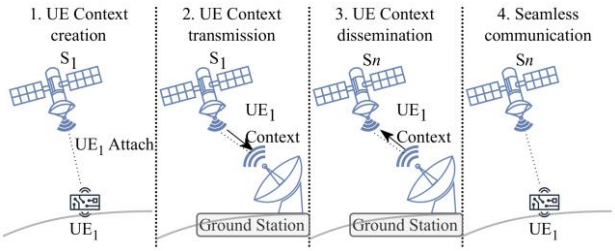

Figure 6-2 UE lifecycle with context dissemination steps.

6.2 VERTICAL HANDOVERS ACROSS ETHER LAYERS

Vertical handover in 5G networks refers to the mobility management process whereby a user equipment (UE) switches between access nodes of different network types or technologies. In the context of 5G Non-Terrestrial Networks (NTNs), vertical handover becomes a key enabler of seamless connectivity between terrestrial gNodeBs (gNBs) and satellite-based gNBs. The integration of satellite segments into the 5G system, standardized in 3GPP Releases 17 and 18 [58], aims to ensure ubiquitous coverage, especially in remote, maritime, or underserved areas. However, achieving seamless mobility across these heterogeneous domains presents significant architectural and procedural challenges. In terrestrial networks, horizontal handovers typically occur between adjacent gNBs via the Xn interface, utilizing the Radio Resource Control (RRC) and Non-Access Stratum (NAS) procedures defined in 3GPP TS 38.331 and TS 24.301. In contrast, vertical handovers between terrestrial and satellite access nodes involve substantial differences in link characteristics, including high latency (up to 500 ms in GEO systems), intermittent visibility, and large Doppler shifts [59]. These factors necessitate enhancements in mobility decision algorithms, particularly in the handover trigger conditions and link adaptation mechanisms. The satellite gNB may be either a transparent payload (relay function) or a regenerative satellite (gNB onboard the satellite). In both scenarios, handover decisions must consider satellite pass predictions, beam coverage dynamics, and earth station gateway availability [60]. For example, a terrestrial-to-satellite handover may be triggered when the UE moves out of terrestrial coverage or the satellite link offers better signal-to-noise ratio or reduced outage probability. Efficient vertical handover in NTNs also requires cross-layer coordination, especially in the RAN and core network segments. Multi-access edge computing (MEC) and AI-assisted mobility prediction are being investigated to support proactive handover decisions and reduce service interruption [61]. Furthermore, inter-system signaling support is essential to harmonize context transfer, QoS continuity, and session preservation. The ongoing research aims to develop robust handover

frameworks that incorporate location-awareness, satellite trajectory knowledge, and adaptive timing advance schemes. The coordination between terrestrial and satellite domains under a unified 5G core remains an open area of standardization and innovation, critical to ensuring service continuity in integrated space-terrestrial 5G deployments.

6.2.1 Results achieved this period

During this period we have greatly enhanced our TN-NTN simulation platform based on Omnet++. As a reminder, there are two popular discrete-event simulators (DESs) platforms, i.e., NS3 [62] and Omnet++ [63]. However, both platforms lacked proper support for simulating satellite networks: NS3 has a functioning satellite library but only supports GEO satellites [64], while Omnet++ had an old non-functioning library named OS3 that however supported all LEO, MEO and GEO mobilities [65]. After an evaluation of both pros and cons, we concluded that Omnet++ was the best platform to adopt and we set to properly update the Omnet++ satellite library and publish it as open source back to the community. Once this strong foundation is laid, our goal was to develop novel vertical HO solutions with focus on continuous connectivity and energy efficiency. So far, we have completed the following steps:

1. We have re-written the Omnet++ satellite library, termed OS3, to make it functional again in the latest Omnet++ versions,

2. We have also added crucial functionality that allows it to co-exist with the other Omnet++ critical libraries and carry out complex simulations (i.e., simulations that combine 5G and satellite environments). These critical libraries include INET, as the most important Omnet++ library that includes implementation of the most common protocol stacks, and Simu5G, which is Omnet++'s 5G library.

3. We have tested that all mobility models and protocol stacks are functioning with OS3. We have revised the simulation library to be able to get and update the positions of satellites using both Two-Line-Element (TLE) files or by setting the average Keplerian parameters (such as altitude, eccentricity, inclination etc.), so as to allow the simulation of any constellation not bounded by a TLE file.

4. One of the things missing from the OS3 library is a suitable channel model for the LEO-to-ground communication. To this end we implemented a satellite channel modelling through the use of Matlab libraries. This implementation essentially provides us with a realistic channel model that can provide us with detailed SINR calculations using Matlab's superior models that include Free Space Path Loss, elevation angle, and atmospheric attenuations (rain, fog, cloud, scintillation etc.).

5. We have created a flight mobility mode for the UE which allow us to simulate such type of aviation scenarios. This mobility module allows the simulated UE to follow a normal airplane mobility pattern that includes lift off, cruising and landing.

6. We have integrated TN and NTN nodes in the same experiment, thus allowing vertical handovers of the UE between the TN gNB and the NTN satellite gNB through the use of the Xn interface.

6.2.1.1 SINR NTN experiment

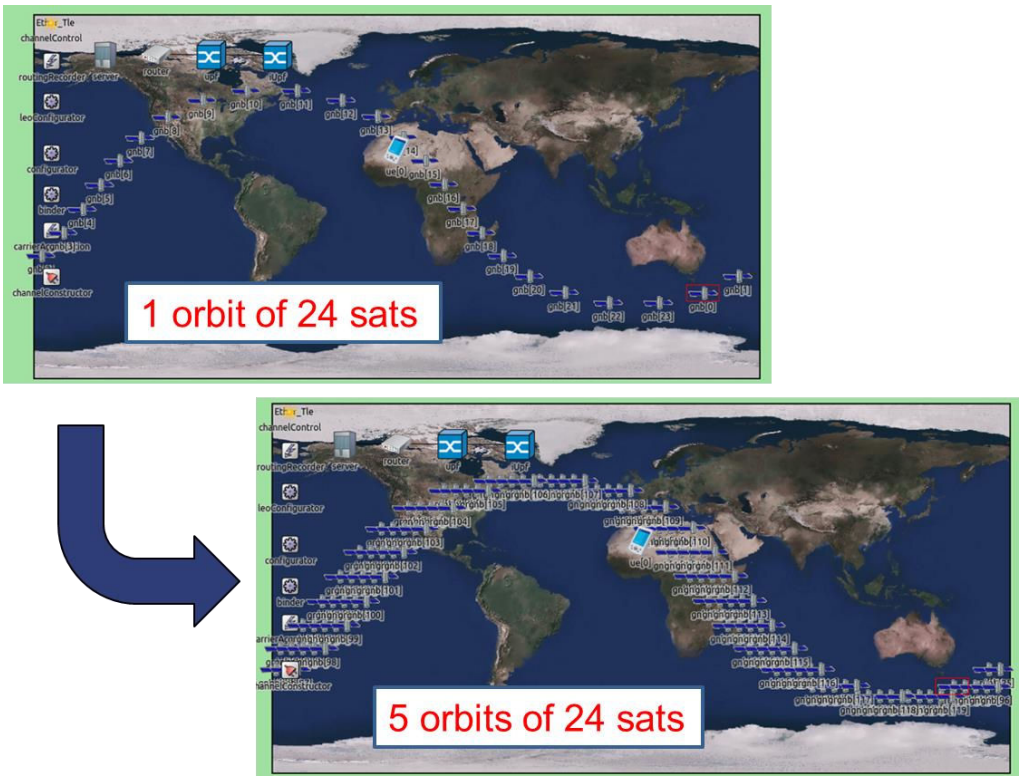

Figure 6-3: Several gNB LEO satellites orbit the earth and provide 5G service coverage to one UE located in the ground near the centre of the map; the simulation starts with only one orbit, consisting of 24 satellites, while more orbits, each of them with 24 satellites, are progressively added to increase the service coverage time.

In this first simulation setup, and in order to test the newly introduced Matlab-based channel model, we consider the setup depicted Figure 6-3. In this setup, we consider a 5G NR UE that is immobile on the ground while several LEO satellites orbit above it. For the satellite orbits, we have considered the positions of the Starlink satellites where each orbital plane consists of 24 satellites. In this setup, we start with one orbital plane and keep adding more orbits so that the UE maintains connectivity for longer periods of time. This experiment is a repetition of a similar experiment presented in D3.1, only this time we use the more realistic satellite channel model.

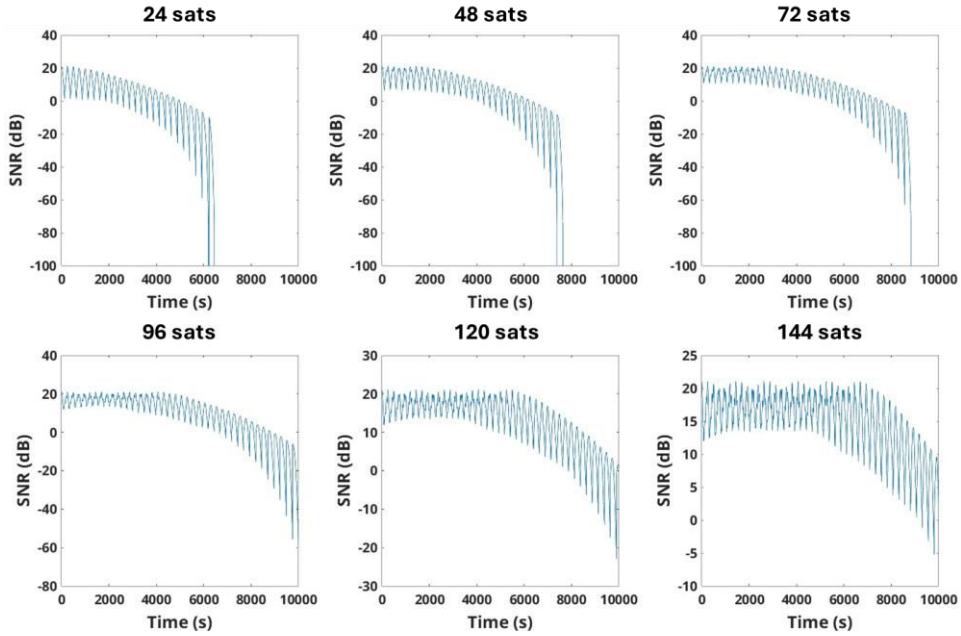

Figure 6-4: SINR vs. simulation time results for 24, 48, 72, 96, 120 and 144 satellites modules.

Figure 6-4 contains the SINR results as they are measured in the uplink direction vs. the simulation time. As observed, the SINR curves fluctuate with every handover, going up and down as satellites come in and out of range while the UE performs handovers. It must be noted here that the handover criterion is the SINR itself, i.e., when the candidate satellite has a higher SINR, then the HO is performed. From the top row of the graph, where we have relatively few satellites, we observe that, as expected, after a certain point in time the satellites move out of range of the mobile phone and the SINR values plunge. As more and more satellites are added into the simulation setup, the UE maintains high SINR values for longer periods. We also observe that the SINR fluctuations coincide with the handovers that are presented in Figure 6-5, depicting the new serving cell (i.e., LEO satellite) ID each time a HO is performed.

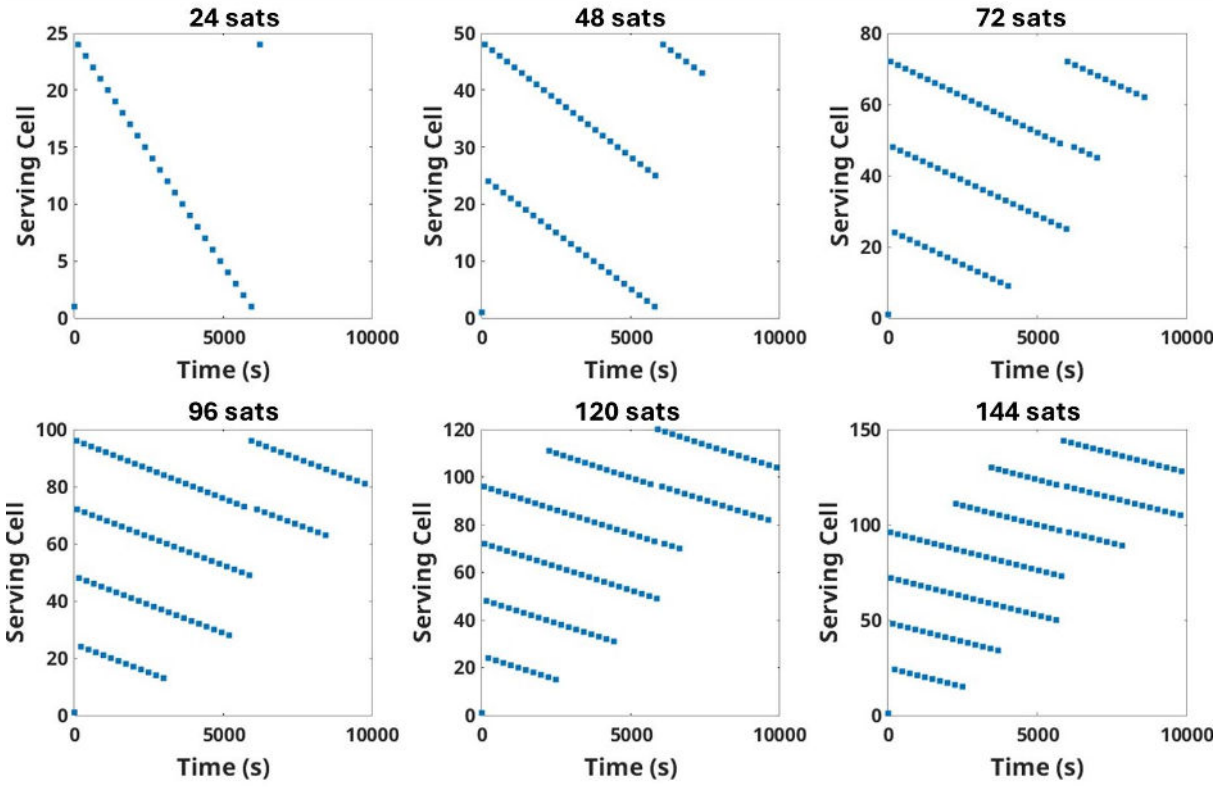

Figure 6-5: Serving cell ID vs. simulation time results for 24, 48, 72, 96, 120 and 144 satellites modules.

6.2.1.2 Consolidated TN-NTN experiment

The second test we have conducted in the updated Omnet++ simulator, is a test that carries out a Vertical HO between a Terrestrial gNB and a Non-Terrestrial gNB. This tests allows us to concurrently test the functionality of items 4-6 from the previous list, i.e. the new realistic Matlab-leveraging channel model, the flight mobility movement pattern, and the and the vertical HO capabilities. This test involves the following entities and scenario. A UE is on very close proximity to a terrestrial gNB and is boarding a plane. Then the plane takes off and follows a specified trajectory. The specific trajectory of this experiment is to fly westwards for the whole duration of the experiment which in this case is 1000 seconds. The area is serviced by a series of LEO satellites that follow the Starlink positions and trajectories. As the UE takes off on the plane, the distance between it and the TN gNB continuously grows in all directions (i.e. horizontally and vertically as the plane ascents) until it reaches a point where the SINR from the signal of the TN gNB is lower than the SINR received from the satellite (NTN) gNB. In this way, a Vertical HO is triggered (of the type Xn) and the UE connects to the NTN gNB. As the UE continues to fly westwards and the LEO satellites keep on moving on their trajectories, the UE starts losing signal from the current satellite, and to this end engages in a Horizontal HO with the next satellite in the same orbit. The measured SINR of the UE in this scenario is depicted in the following figure.

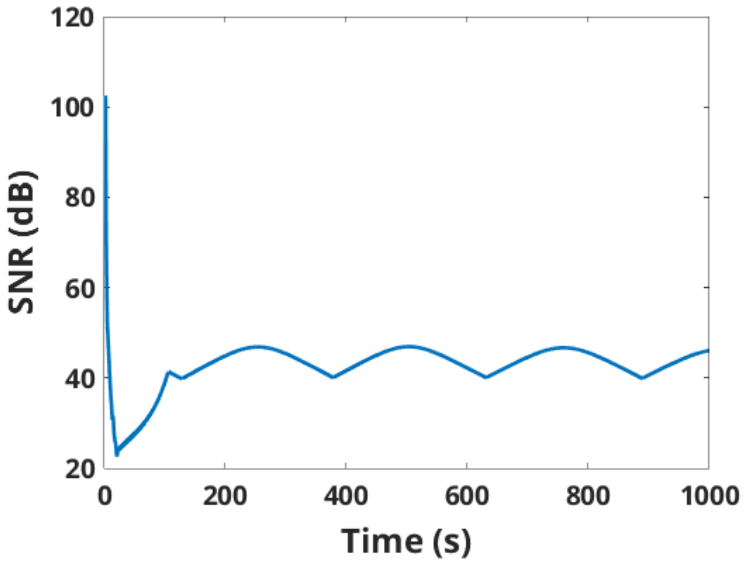

Figure 6-6 Measured SINR at the UE vs. time.

In Figure 6-6 we display the SINR measured at the UE, always with the serving cell, vs. the simulation time. The curvature of the SINR follows a series of changes, depending on which cell (TN or NTN) serves the UE. As described in the previous paragraph the UE is initially connected to a TN gNB that is located very close to it. To this end, in the left side of the graph we notice very high SINR values, that however decrease rapidly as the UE starts flying. As a side note we should mention here that the channel model for the terrestrial connection implemented in Simu5G library is the 3GPP TR 38.901. This channel model implements path loss, LOS probability, and shadowing according to the following specifications:, "Study on channel model for frequencies from 0.5 to 100 GHz", v16.1.0, December 2019. At around 20 seconds the SINR has dropped so much so the SINR from the satellite exceeds the corresponding value of the TN gNB and therefore the UE performs a Vertical HO to the NTN gNB. Following the vertical HO, the SINR grows quadratically until second 112, where the curvature changes again. From second 112 and onwards we notice the curvature of the SINR oscillates, by decreasing and decreasing in a periodic fashion. This periodicity, depicts the Horizontal HOs that take place from satellite to satellite within the same orbit, i.e. as each satellite approaches the UE, the SINR increases until the satellite reaches the maximum elevation angle. Afterwards the satellite decreases in the horizon, a fact that causes the decrement of the SINR respectively. However, the next satellite in orbit comes into view, with continuously increasing elevation angle. As the next satellite comes closer to the UE, a point is reached where the SINR of the next satellite surpasses the SINR of the current serving cell. Since in this experiment the SINR is the main criterion for a HO, and since hysteresis is set to zero, when the aforementioned shift in SINR happens, the UE performs a horizontal HO. The valleys in the curvature signify the HO times, and denote the start of the next period of the SINR curve, where we see the familiar pattern of going up and down, as the satellite moves closer at the beginning and further away later after reaching its maximum elevation angle. The periodicity of the curvature is around 250 seconds, i.e. for ~125 seconds the current satellite moves closer to the UE (due to its orbit trajectory), and for ~125 seconds the current satellite moves further away from the UE.

In the area between seconds 20 and 112 we observer the following paradox. If we take into account the periodicity of the SINR, we can derive that the distance between the UE and the serving NTN gNB increases as the satellite moves lower into the horizon, during this specific time period. However, we also observe that in the same time period the SINR increases in a quadratic fashion as it was mentioned before. In order to explain this paradox, we analyse the

derived SINR results to its constituents, i.e. the Free Space Path Loss (FSPL) and the Atmospheric Losses and we contrast them against the SINR and distance metrics.

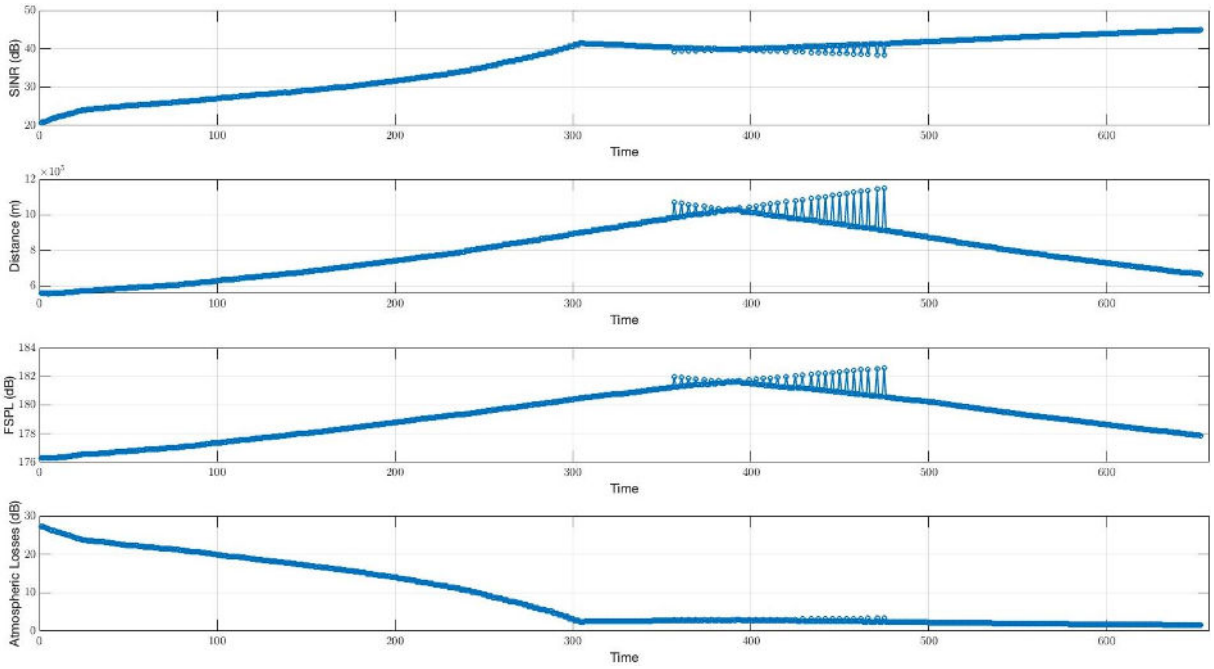

Figure 6-7 SINR and Distance to Serving Cell vs. SINR constituents.

Figure 6-7 displays the SINR, distance (of UE from serving cell), FSPL and Atmospheric Losses vs. simulation time for a similar experiment that is comprised only by NTN gNBs. In this experiment the Horizontal HO takes place around second 400. By evaluating the top two graphs of the figure we can derive that, in the SINR grows in a quadratic fashion until around second 300, then it decreases until the Horizontal HO takes place (around ~400 seconds), where we see it increases again in a similar fashion to the previous experiment. By observing the distance curve, we see that indeed the distance increases together with the SINR. In order to explain the concurrent increase in distance and SINR, we have broken down the SINR into the FSPL (3rd graph from the top) and Atmospheric Losses (4th graph from the top). As we can see, the FSPL indeed increases linearly with the distance gaining in total around 4 dBs (which would increase the SINR normally) but the Atmospheric Losses decrease quadratically around 30 dBs, therefore creating the biggest impact and thus dominating the total SINR measurements. The reason the Atmospheric Losses are decreasing this rapidly is that the UE is on a plane taking off, therefore ascending in height for the first 300 seconds. As the airplane ascents, the air becomes less dense and therefore the air volume between the UE and the NTN gNB decreases rapidly, affecting the atmospheric losses at a great extend.

6.2.1.3 Consolidated TN-NTN experiment – Hysteresis test

In this section we present an experiment designed to test the impact of the hysteresis factor on the SINR measurements. In wireless networks, the hysteresis factor in the handover procedure is used to prevent frequent and unnecessary handovers, especially when the signal strength between neighboring base stations fluctuates rapidly. It introduces a threshold margin such that a handover is only triggered when a neighboring cell's signal is not just slightly better, but exceeds the serving cell's signal by a defined offset. This avoids the so-called "ping-pong" effect, where the UE rapidly switches back and forth between cells due to small and transient signal variations. In the Simu5G library, the hysteresis factor is applied during the evaluation of handover conditions inside the UE's physical layer logic, typically within the `handoverHandler()` method of the `LtePhyUe` class. The decision is based on the following code comparison:


```
if (rssi > candidateMasterRSSI + hysteresis)
```

This means that a handover is triggered only if the Received Signal Strength Indicator (RSSI) of a neighboring cell exceeds that of the current (master) cell by at least the hysteresis value. The hysteresis parameter is defined in the configuration files and can be tuned to control the aggressiveness of the handover mechanism. In Omnet++ a factor of 1/5th will allow handover only when the new RSSI is greater than the current RSSI by 20%.

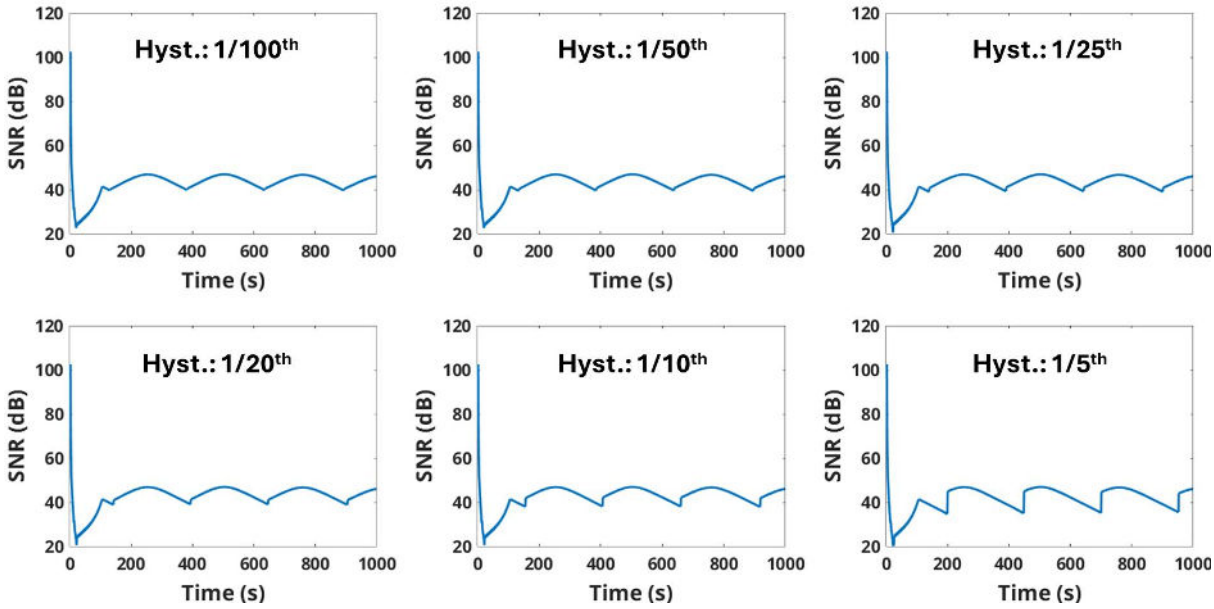

Figure 6-8 SINR vs Simulation time for various Hysteresis factors.

Figure 6-8 displays the SINR performance of the same consolidated TN-NTN experiment of Figure 6-6 for various Hysteresis factors. The Hysteresis factors range for very small values (1/100th) and up to 1/5th. By means of Figure 6-8, we can clearly observe that SINR transitions due to the Handovers taking place become increasingly discontinuous as the hysteresis factor increases, since the candidate SINR has to surpass the current SINR by a specific factor, making the curves discontinuous.

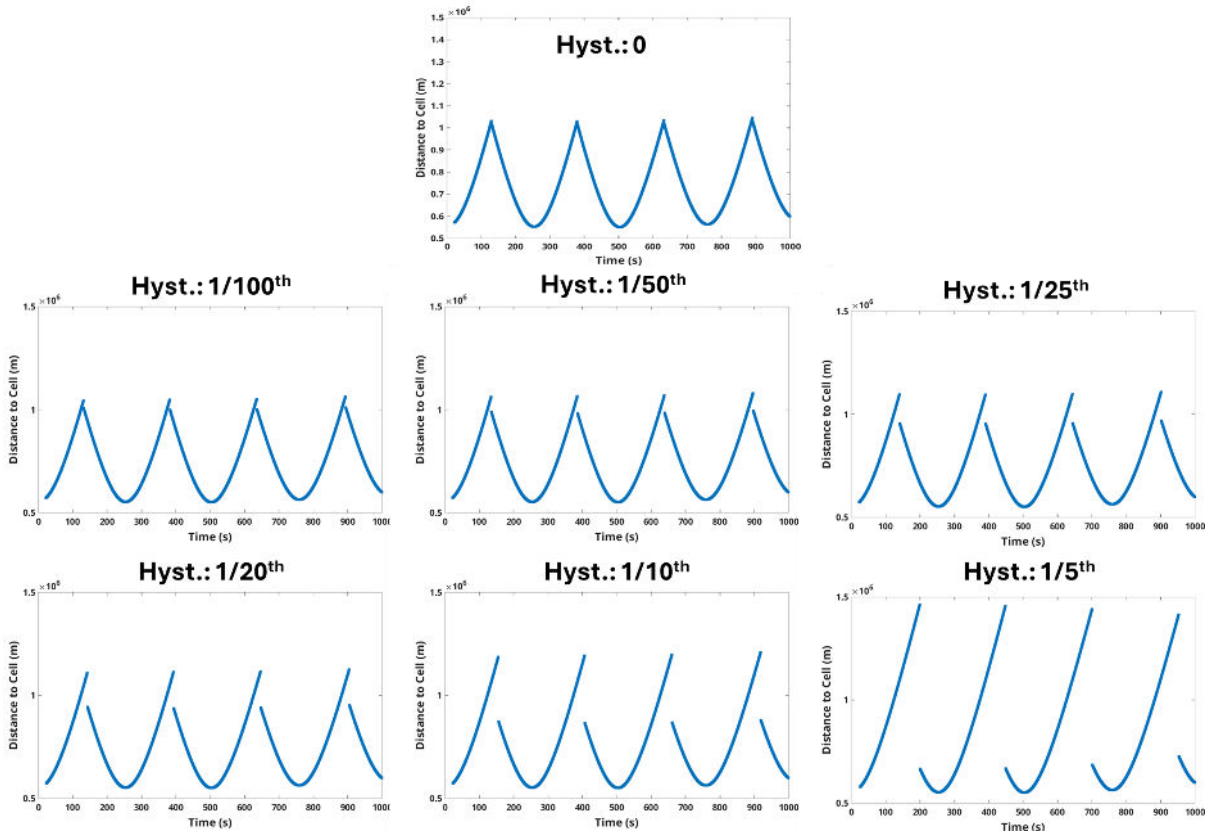

Figure 6-9 Distance of UE to Serving Cell vs. simulation time.

In order to support the findings of Figure 6-8, we also present Figure 6-9 that depicts the distance between the UE and the serving cell vs. the simulation time for the various Hysteresis factors presented previously. As can be seen, when Hysteresis factor is set to zero, the distance curve is continuous, as the HO takes place when the candidate Master Cell is marginally higher than the current SINR, which also translates to marginally lower distance with the next cell. However, as the Hysteresis factor increases, we notice that with each handover, there is a discontinuous "jump" of the observed values to lower distances. As it is expected, the higher the hysteresis factor, the longer the "jump" of these values, since the hysteresis delays the handover until such time that the SINR is X% higher than the current SINR, which causes the candidate serving cell to come closer to the UE. Also it is observed that, the higher the hysteresis, the longer time does the UE stay connected to the current serving cell, that causes in turn the distance metric to skyrocket, as for instance can be seen in the bottom right corner of Figure 6-9.

6.2.1.4 Vertical Handovers – Energy efficiency driven HOs

One of the targets of this task is the implementation of a Vertical HO mechanism that performs the handovers, not based on the measured SINR, but on the total energy efficiency of the system, i.e. the main target is to choose the data paths that reduce the overall energy consumption of the system. In order to visualize a use case where this functionality could produce energy savings, we produce the following scenario:

In a semi-urban/rural network topology, late at night there are only a few active UEs attached to a terrestrial gNB that are actively transmitting/receiving data. The area in question is being covered in terms of service by a series of LEO satellites (similar to the Starlink service). Since, only a few UEs are connected to the TN gNB, and given that the gNBs usually have a very high energy consumption (Huawei data notes a 64T64R AAU can draw about 1–2 kW, BBU

another ~1 kW, and multi-band sites can exceed 10 kW, or even 20 kW+ at higher complexity sites [66]), it would be beneficial to the carrier to offload the UEs traffic to the satellite network, that consumes no power as it gets its energy from the solar panels. To this end, and if the Vertical HO does not interrupt any ongoing services, say by not fulfilling any outstanding SINR or delay demands, the TN gNB triggers the HOs and offloads the remaining UEs to the satellite network. Finally, the TN gNB shuts down, therefore producing energy savings for the operator.

To this end we have implemented a function that triggers a handover (HO) based on energy efficiency considerations. The decision is made by comparing the energy savings from switching off or stop serving the UE from the serving cell with the energy cost of activating or serving the UE from the target cell. We also apply hysteresis to prevent unnecessary handovers. In parallel, the targeted cell should have acceptable SINR (above a threshold), while also satisfying the UE's delay requirement, if any.

In order to implement this mechanism, we have created an algorithm that is similar in nature to the PETA algorithm, that has been presented in WP4 of ETHER. In this specific mechanism, we essentially insert all network nodes and links available to the system in a graph. The weights of the graph links is the power consumption of this specific path of the data link. When the algorithm is triggered, we employ the Dijkstra algorithm to short the available paths in terms of power consumption, and if a path is chosen that is different than the current one, a handover is triggered. Of course, the handover is enabled if and only if the candidate master cell provides adequate SINR (above a predetermined threshold) and if the new data path does not violate any delay constraints.

To showcase the operation of the power-efficient HO algorithm, we have created a simple setup where the a UE is located within the range of two gNBs and receiving the pilot signals from both of them, however the gNB is certainly closer to one of the gNBs and receives a stronger signal from them. In this experiment we have set that the further away gNB, consumes zero power, in order to simulate the fact that the NTN gNBs do not get their energy from terrestrial power sources, but rather (free) from the sun. The following figure depicts the SINR graph of the UE.

In the depicted experiment, the Vertical HO algorithm is triggered to commence in second 5 of the simulator run. From what can be observed, the handover takes place when target Power Consumption (PC) is lower than current PC plus a hysteresis factor to avoid Ping Pong effects, i.e. single UE traffic handed over to cell further away, which causes SINR to drop (but to acceptable levels) lowering the system's overall power consumption.

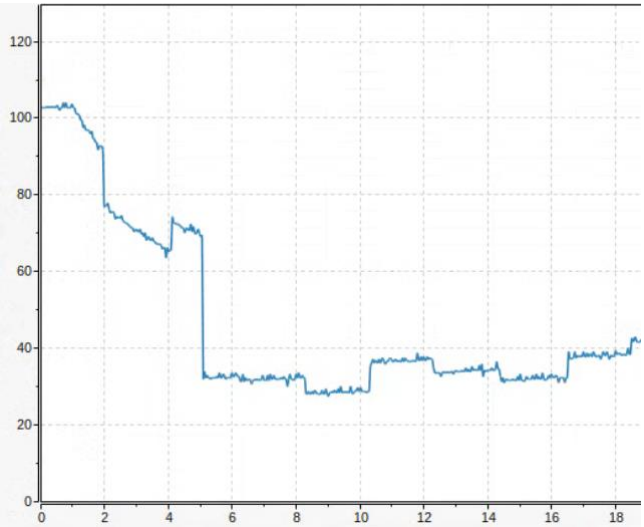

Figure 6-10 Energy Efficient Vertical HO algoritm operation example. The allgorithm is triggered in second 5 of the simulator.

7 CONCLUSIONS

This deliverable captures the work performed in WP3 in the period from M22 to M32, on key technological enablers for the seamless and energy efficient ETHER Network Operation, and it is the final report of the WP. The performed work has evolved in four directions, namely i) user terminal antenna design for direct access between LEO satellites and ground users, ii) dynamic resource management leveraging the development of flexible payload framework, iii) application of semantics-aware communication schemes, iv) development of horizontal and vertical handover policies.

In **Chapter 2**, the final design of the user terminal antenna reflects a trade-off among RF performance specifications, physical size limitations, and practical implementation constraints. The designed antenna comprises a 20×20 element phased array, where each element is a microstrip patch antenna optimized for array performance. The size of the antenna is roughly 10×10 cm, with gain of around 30 dBi operating at 28 GHz and bandwidth larger than 2GHz. It is circularly polarized and the scanning range across all antenna's radiation planes is around 80° (-40° to +40°) preserving the required characteristics of the designed antenna. The full implementation of the antenna requires a multilayer structure with a complex feeding network including the beamforming layer, making the required time and implementation cost unrealistic in the framework of ETHER. Thus, a downsized 4×4 version of the proposed antenna has been adopted for prototyping. The dimensions of the antenna prototype are roughly 2×2 cm demonstrating a medium gain directional antenna (of gain around 14 dBi) with very good beam-steering capabilities, suitable for handheld terminals. The antenna prototype is currently under implementation.

In **Chapter 3**, aiming at tackling severe signal attenuation and multipath fading in LEO-to-user direct access channels**,** a robust to phase errors distributed precoding problem has been investigated for simultaneously transmitting information to multiple users on Earth from a swarm of collaborative LEO satellites. The problem targets to maximize the average sum rate of the users under a stochastic SINR constraint per user. The problem is NP-hard and thus non-convex. To solve it, the objective function is reformulated into a convex problem using the stochastic MMSE approach. Results reveal that the proposed approach achieves significant sum rate gains with respect to the state-of-the-art MRT approach.

Regarding OTFS, two version of OTFS have been compared with respect to each other in A LEO-satellite communication scenario, namely the much lower complexity discrete Zak-transform based and the two-stage one. Their comparison in terms of MSE vs. SNR reveals that apart from a much lower complexity, the discrete Zak-transform OTFS version also results to a much better performance than its conventional two-stage counterpart.

In **Chapter 4**, the ETHER concept on TNT integration is based on software defined flexible payload architecture. A flexible payload framework has been designed, integrating an orchestrator (K3s), software virtualization mechanisms (PODman containers), and partial bitstream reconfiguration of services via a customized Linux operating system. The framework has been tested on an FPGA platform representative of real payload hardware based on the Xilinx UltraScale+ family. Within WP5, Demo1 of the ETHER project will execute demonstrative applications on the framework to validate its functionality.

Furthermore, given the capability of software-based flexible payload, joint dynamic spectrum allocation is investigated. A detailed description of the WMMSE algorithm is provided, which has been introduced in D3.1 for the coordinated resource allocation in a scenario where terrestrial and LEO satellite users are using the same resources. The results of this solution are compared against two benchmarks: Uncoordinated and uncoordinated-disjoint solutions. In the former benchmark there is no coordination for allocating the resources to terrestrial and satellite users. In the latter benchmark, disjoint resources are user for the terrestrial and

satellite users. Results reveal that the proposed coordinated resource allocation approach results in notable sum rate gains with respect to the benchmark approaches.

Subsequently, a concrete optimization problem has also been formulated for the optimal LEO power control in a GEO/LEO coexistence transmission scenario, subject to the statistical nature of the EPFD ITU-R constraints, by computing the EPFD values for actual satellite orbits (instead of only the “worst case scenario”) while guaranteeing ITU-R compliance by properly turning-off LEO satellites (causing excessive GEO interference) only as needed. A heuristic solution technique has been proposed relying on an “EPFD satisfiability” algorithmic module and a complete Matlab-based numerical evaluation study has been performed, showcasing the flexibility of the proposed algorithm.

In **Chapter 5**, ETHER leverages on data analytics and semantics-aware caching for high energy efficiency. Towards that goal, we optimized the Version Age of Information (VAoI) to ensure the timely transmission of informative updates from a ground-based IoT device to a network of interconnected LEO satellites. Within this network, updates are disseminated among nodes arranged in a ring or star topology. Optimizing the VAoI across the LEO network, the proposed policy reduces the transmission of stale and irrelevant updates, thereby enhancing energy efficiency.

Finally, **in Chapter 6** horizontal and vertical handovers techniques are integrant building blocks of the integrated terrestrial and non-terrestrial networks. The horizontal handover work successfully addressed a critical challenge in sparse LEO constellation operations by developing and validating a practical UE Context Proxy solution for seamless multi-satellite IoT connectivity. The implementation, built upon the Magma core network framework, demonstrated the feasibility of asynchronous UE context dissemination across satellites with discontinuous feeder links. Laboratory validation proved the system's capability to extract UE contexts from satellite-based MME/AMF instances, transfer them via ground-based proxies during feeder link availability windows, and inject them into target satellites to enable seamless service continuation. The solution supports advanced features such as selective context updates for dynamic parameters and accurately replicates real-world NTN constraints. This work establishes a foundation for 3GPP Release 19 Store & Forward operations and demonstrates that sparse LEO constellations can provide reliable IoT connectivity without requiring extensive ground infrastructure or continuous satellite to ground links. Regarding vertical handovers, the ETHER TN-NTN simulation platform was significantly advanced by fully rewriting and extending the Omnet++ satellite library (OS3), enabling seamless integration with INET and Simu5G for complex terrestrial–non-terrestrial simulations. Realistic satellite channel models were introduced leveraging Matlab, mobility patterns for aviation scenarios, and support for vertical handovers (VHO) between terrestrial and satellite gNBs. Extensive experiments validated SINR-based handovers, hysteresis effects, and realistic orbital behaviors. Furthermore, an energy-efficiency-driven VHO mechanism was implemented, allowing dynamic offloading of traffic from power-intensive terrestrial gNBs to energy-neutral satellites. These achievements establish a robust foundation for future research in continuous connectivity and sustainable NTN solutions.

8 BIBLIOGRAPHY

[1] ETHER_project, “D3.1: Initial report on key technological enablers for the seamless and energy efficient ETHER network operation,” September 2024.

[2] ETHER Project, “D2.2: Use cases and KPIs/KVIs,” December 2023. [Online]. Available: https://www.ether-project.eu/wp-content/uploads/sites/100/2024/04/ETHER_Deliverable_D2.2_V1.0-clean.pdf. [Accessed November 2024].

[3] G. Amendola, D. Cavallo, T. Chaloun and N. Defrance, “Low-Earth Orbit User Segment in the Ku and Ka-Band: An Overview of Antennas and RF Front-End Technologies,” *IEEE Microwave Magazine,* vol. 24, no. 2, pp. 32-48, Feb 2023.

[4] J. Lee, S. Noh, S. Jeong and N. Lee, Coverage Analysis of LEO Satellite Downlink Networks: Orbit Geometry Dependent Approach, arXiv, 2022.

[5] Savazzi, P. a. Vizziello and Anna, “Carrier synchronization in distributed MIMO satellite links,” *IEEE International Conference on Wireless for Space and Extreme Environments (WiSEE),* pp. 1-6, 2015.

[6] U. B. Madhow, D. S. D. R. and R. & Mudumbai, “Distributed massive MIMO: Algorithms, architectures and concept systems,” *Information Theory and Applications Workshop (ITA),* pp. 1-7, 2014.

[7] C. J. Verhoeven, M. J. Bentum, G. L. E. Monna, J. Rotteveel and J. & Guo, “On the origin of satellite swarms,” *Acta Astronautica,* pp. 1392-1395, 2011.

[8] L. M. Marrero, “Architectures and synchronization techniques for distributed satellite systems: A survey,” *IEEE access,* pp. 45375-45409, 2022.

[9] R. Radhakrishnan, W. W. Edmonson, F. Afghah, R. M. Rodriguez-Osorio, F. Pinto and a. S. C. Burleigh, “Survey of inter-satellite communication for small satellite systems: Physical layer to network layer view,” *IEEE Communications Surveys \& Tutorials,* pp. 2442-2473, 2016.

[10] D. Bykhovsky, D. Kedar and S. Arnon, “Fiber-Ring Delay Line for High-Resolution Intersatellite Ranging,” *IEEE Photonics Technology Letters,* pp. 673-676, 2015.

[11] Y. Tian, J. Zhong, X. Lin, H. Yang and D. Kang, “Inter-Satellite Integrated Laser Communication/Ranging Link with Feedback-Homodyne Detection and Fractional Symbol Ranging,” *IEEE International Conference on Space Optical Systems and Applications (ICSOS),* pp. 1-5, 2019.

[12] J. L. MacArthur and A. S. Posner, “Satellite-to-Satellite Range-Rate Measurement,” *IEEE Transactions on Geoscience and Remote Sensing,* pp. 517-523, 1985.

[13] J. Kim and B. D. Tapley, “Simulation of dual one-way ranging measurements,” *Journal of spacecraft and rockets,* pp. 419-425, 2003.

[14] P. Sundaramoorthy, E. Gill and C. Verhoeven, “Enhancing ground communication of distributed space systems,” *Acta Astronautica,* pp. 15-23, 2013.

[15] M. Younis, R. Metzig and G. Krieger, “Performance prediction of a phase synchronization link for bistatic SAR,” *IEEE Geoscience and Remote Sensing Letters,* pp. 429--433, 2006.

[16] M. Razaviyayn and M. S. Boroujeni and Z. -Q. Luo, “"A stochastic weighted MMSE approach to sum rate maximization for a MIMO interference channel,"," *IEEE 14th Workshop on Signal Processing Advances in Wireless Communications (SPAWC), Darmstadt, Germany, 20,* 2013.

[17] M.-C. Yue, S. X. Wu and A. M.-C. So, “A robust design for MISO physical-layer multicasting over line-of-sight channels,” *IEEE Signal Processing Letters,* pp. 939-943, 2016.

[18] X. Zhang, J. Wang, C. Jiang and Y. R. a. L. H. C. Yan, “"Robust Beamforming for Multibeam Satellite Communication in the Face of Phase Perturbations,"," *in IEEE Transactions on Vehicular Technology, vol. 68, no. 3, pp. 3043-3047, doi: 10.1109/,* March 2019.

[19] K.-Y. Wang, A. M.-C. So, T.-H. Chang, W.-K. Ma and C.-Y. Chi, “Outage constrained robust transmit optimization for multiuser MISO downlinks: Tractable approximations by conic optimization,” *IEEE Transactions on Signal Processing,* pp. 5690-5705, 2014.

[20] S. Jia, Z. Li, J. Hu and Z. Tie, "OTFS Enabled LEO Satellite Communications: A Promising Solution to Severe Doppler Effects," pp. 203-209, 2024.

[21] I. Ali, N. Al-Dhahir and J. Hershey, “Doppler characterization for LEO satellites,” *IEEE Transactions on Communications,* 1998.

[22] L. Yu, C. Ming, P. Cunhua, G. Tantao, Y. Jinhong and W. Jiangzhou, “OTFS Versus OFDM: Which is Superior in Multiuser LEO Satellite Communications,” *IEEE Journal on Selected Areas in Communications,* pp. 139-155, 2025.

[23] H. Zhu and J. Wang, “Chunk-Based Resource Allocation in OFDMA Systems—Part II: Joint Chunk, Power and Bit Allocation,” *IEEE Transactions on Communications,* 2012.

[24] Y. Zuo, M. Yue, M. Zhang, S. Li, S. Ni and X. Yuan, “OFDM-Based Massive Connectivity for LEO Satellite Internet of Things,” *IEEE Transactions on Wireless Communications,* 2023.

[25] R. Hadani, S. Rakib, M. Tsatsanis, A. Monk, A. Goldsmith, A. Molisch and R. Calderbank, "Orthogonal Time Frequency Space Modulation," *2017 IEEE Wireless Communications and Networking Conference (WCNC),* 2017.

[26] S. K. Mohammed, R. Hadani, A. Chockalingam and R. Calderbank, "OTFS—Predictability in the Delay-Doppler Domain and Its Value to Communication and Radar Sensing," *IEEE BITS the Information Theory Magazine,* 2023.

[27] G. Thomas, S. Laws, S. Rose, S. Stirland, S. Amos and P. Jung, "Airbus flexible payload perspective," in *39th International Communications Satellite Systems Conference (ICSSC 2022)*, 2022.

[28] Elena Godino; Luis Escolar; Pablo Honold; Enrique Fraga, "Flexible Payload Operations of Satellite Communication Systems," in *2018 SpaceOps Conference*, Marseille, France, 2018.

[29] Muñoz-Martín, Joan Francesc; Capon, Lara; Ruíz-de-Azúa, Joan Adrià; Camps, Adriano, "The Flexible Microwave Payload-2: A SDR-Based GNSS-Reflectometer and L-Band Radiometer for CubeSats," *IEEE Journal of Selected Topics in Applied Earth Observations and Remote Sensing,* vol. 13, pp. 1298-1311, 2020.

[30] Y. Lu, D. Wang and S. Zhu, "Design of an embedded multi-antenna satellite data acquisition system based on ARM-Linux," in *Chinese Control And Decision Conference (CCDC)*, Shenyang, China, 2018.

[31] European Space Agency, "Flexible RF/IF Down-Converter For Flexible Payload," 2016. [Online]. Available: https://connectivity.esa.int/projects/flexible-rfif-downconverter-flexible-payload. [Accessed November 2024].

[32] Thales, "ARAMIS Flexible Payload," March 2022. [Online]. Available: https://www.thalesgroup.com/en/worldwide-market-specific-solutions/microwave-imaging-sub-systems/news/aramis-flexible-payload. [Accessed November 2024].

[33] ATRIA Project, "AI-based control for the next generation of flexible satellite payloads," 2022. [Online]. Available: https://www.atria-h2020.eu/. [Accessed November 2024].

[34] F. Vidal, H. Legay, G. Goussetis, M. G. Vigueras, S. Tubau and J.-D. Gayrard, "A methodology to benchmark flexible payload architectures in a megaconstellation use case," *International Journal of Satellite Communications and Networking,* vol. 39, no. 1, pp. 29-46, January/February 2021.

[35] V. Montilla, J. Ferrer, M. Guadalupi, R. Ferrus, A. Calveras and J. A. Ruiz-de-Azua, "Deployment of NB-IoT NTN core network functions on Software Defined Radio (SDR) nanosatellites: approach and performance assessment," in *74th International Astronautical Congress*, Baku, Azerbaijan, 2023.

[36] H. Manninen, V. Jääskeläinen and J. O. Blech, "Performance Evaluation of Containerization Platforms for Control and Monitoring Devices," in *2020 25th IEEE International Conference on Emerging Technologies and Factory Automation (ETFA)*, Vienna, Austria, 2020.

[37] V. Noronha, E. Lang, M. Riegel and T. Bauschert, "Performance Evaluation of Container Based Virtualization on Embedded Microprocessors," in *2018 30th International Teletraffic Congress (ITC 30)*, Vienna, Austria, 2018.

[38] L. M. Marrero, J. C. Merlano Duncan, J. Querol, S. Kumar, J. Krivochiza, S. K. Sharma, S. Chatzinotas, A. Camps and B. Otterstern, "Architectures and Synchronization Techniques for Distributed Satellite Systems," *IEEE Access,* pp. 45375-45409, 2022.

[39] C. &. M. E. Rao, "Minimum-hop Constellation Design for Low Earth Orbit Satellite Networks.," in *IEEE INFOCOM 2025 - IEEE Conference on Computer Communications, 1-10.*, 2025.

[40] B. Shang, X. Li, Z. Li, J. Ma, X. Chu and P. Fan, "Multi-Connectivity Between Terrestrial and Non-Terrestrial MIMO Systems," *IEEE Open Journal of the Communications Society,* vol. 5, pp. 3245-3262, 2024.

[41] S. Liu, C. Dong, J. T. X. Zhu and L. Zhang, "Performance Evaluation of BATMAN-adv Protocol on Convergecast Communication in UAV Networks,," in *GLOBECOM 2022 - IEEE Global Communications Conference,*, Rio de Janeiro, 2022.

[42] J. Acosta, H. Rouzegar, A. Augé and J. Ruiz-de-Azua, "Spatially-Aware NFV Orchestration for Dynamic LEO Satellite Management in 6G Networks," in *EUCNC 6G summit*, Poznan, 2025.

[43] A. Rouhani, "Linux in Depth," [Online]. Available: https://hrouhani.org/linux-in-depth/. [Accessed 25 June 2025].

[44] B. Tsai, "PODMan introduction," 25 June 2025. [Online]. Available: https://darumatic.com/blog/podman_introduction.

[45] Microsoft, "Development workflow for Docker apps," 25 June 2025. [Online]. Available: https://learn.microsoft.com/en-us/dotnet/architecture/microservices/docker-application-development-process/docker-app-development-workflow.

[46] Yocto Project Members, "The Yocto Project," 25 June 2025. [Online]. Available: https://www.yoctoproject.org/.

[47] ITU-R, "Radio Regulations, Chapter VI, Provision of Services and Stations, Art. 22 Space services," August 2024. [Online]. Available: https://www.itu.int/pub/R-REG-RR-2024.

[48] ITU-R, "Reference FSS earth-station radiation patterns for use in interference assessment involving non-GSO satellites in frequency bands between 10.7 GHz and 30 GHz," Recommendation S.1428-1, February 2021. [Online]. Available: https://www.itu.int/rec/R-REC-S.1428/en.

[49] J. M. P. a. J. M. A. Hills, "Feasibility of Using Beam Steering to Mitigate Ku-Band LEO-to-GEO Interference," *IEEE Access,* vol. 10, pp. 74023-74032, 2022.

[50] F. Ö. a. A. Kara, "Exclusion zone minimization and optimal operational mode selection for co-existent geostationary and non-geostationary satellites," *International Journal of Satellite Communications and Networking,* Vols. vol. 40, no. 3, pp. 191-203,, May June 2022.

[51] C. [Online], "Celestrak," [Online]. Available: https://celestrak.org/.

[52] MathWorks, "Satellite Communications Toolbox," [Online]. Available: https://www.mathworks.com/help/satcom/index.html. [Accessed November 2024].

[53] E. Delfani and N. Pappas, "Semantics-Aware Updates from Remote Energy Harvesting Devices to Interconnected LEO Satellites," *IEEE Communications Letters,* 2025.

[54] R. Yates, "The age of gossip in networks," in *IEEE International Symposium in Information Theory (ISIT)*, 2021.

[55] T. Kellermann, R. Pueyo Centelles, D. Camps-Mur, R. Ferrús, M. Guadalupi and A. Calveras Augé, "Novel Architecture for Cellular IoT in Future Non-Terrestrial Networks: Store and Forward Adaptations for Enabling Discontinuous Feeder Link Operation," *IEEE Access,* vol. 10, pp. 68922-68936, 2022.

[56] R. Pueyo Centelles, "UE context dissemination for LEO-based multi-satellite store-and-forward NTN NB-IoT," September 2024. [Online]. Available: https://www.youtube.com/watch?v=aY-wBOgB0pE. [Accessed November 2024].

[57] 3GPP, "Study on satellite access Phase 3," 2023.

[58] 3GPP, "Study on New Radio (NR) to support non-terrestrial networks," 3rd Generation Partnership Project, Technical Report TR 38.811, ver. 15.4.0, October 2020. [Online]. Available: https://portal.3gpp.org/desktopmodules/Specifications/SpecificationDetails.aspx?specificationId=3234.

[59] O. e. a. Kodheli, "Satellite Communications in the New Space Era: A Survey and Future Challenges," *IEEE Communications Surveys & Tutorials,* vol. 23, no. 1, pp. 70-109, 2021.

[60] V1.1.1 and E. G. E. 009, "AI and Networking: Use Cases of Artificial Intelligence Applied to 5G and Beyond," 2020.

[61] G. Giambene and e. al., "Resource Management and Mobility Handover in 5G Satellite-Terrestrial Networks," *IEEE Network,* vol. 32, no. 5, pp. 70-77, 2018.

[62] NSNAM, "NS3 Network Simulator," [Online]. Available: https://www.nsnam.org/. [Accessed November 2024].

[63] OMNeT++, "OMNeT++ Discrete Event Simulator," [Online]. Available: https://omnetpp.org/. [Accessed November 2024].

[64] SNS3, "Satellite Network Simulator 3," [Online]. Available: https://www.sns3.org/. [Accessed November 2024].

[65] OMNeT++, "OS³ - The Open Source Satellite Simulator," [Online]. Available: https://omnetpp.org/download-items/OS3.html. [Accessed November 2024].

[66] HUAWEI, "5G Power: Creating a green grid that slashes costs, emissions & energy use," [Online]. Available: https://www.huawei.com/en/huaweitech/publication/89/5g-power-green-grid-slashes-costs-emissions-energy-use.

[67] Xilinx Wiki, "Solution ZynqMP PL Programming," [Online]. Available: https://xilinx-wiki.atlassian.net/wiki/spaces/A/pages/18841847/Solution+ZynqMP+PL+Programming.

[68] P.-D. Arapoglou, S. Cioni, E. Re and A. Ginesi, "Direct Access to 5G New Radio User Equipment from NGSO Satellites in Millimeter Waves," in *2020 10th Advanced Satellite Multimedia Systems Conference and the 16th Signal Processing for Space Communications Workshop (ASMS/SPSC)*, Graz, Austria, 2020.

[69] A. Goldsmith, Wireless Communications, Cambridge University Press, 2005.

[70] L. Bai, C.-X. Wang, G. Goussetis, S. Wu, Q. Zhu and W. Zhou, "Channel Modeling for Satellite Communication Channels at Q-Band in High Latitude," *IEEE Access,* vol. 7, pp. 137691-137703, 2019.

[71] V. M. Baeza, E. Lagunas, H. Al-Hraishawi and S. Chatzinotas, "An Overview of Channel Models for NGSO Satellites," in *2022 IEEE 96th Vehicular Technology Conference (VTC2022-Fall)*, London, United Kingdom, 2022.

[72] H. Bischel, M. Werner and E. Lutz, "Elevation-dependent channel model and satellite diversity for NGSO S-PCNs," in *Proceedings of Vehicular Technology Conference - VTC*, Atlanta, GA, USA, 1996.

[73] E. Juan, I. Rodriguez, M. Lauridsen, J. Wigard and P. Mogensen, "Time-correlated Geometrical Radio Propagation Model for LEO-to-Ground Satellite Systems," in *2021 IEEE 94th Vehicular Technology Conference (VTC2021-Fall)*, Norman, OK, USA, 2021.

[74] E. Juan, M. Lauridsen, J. Wigard and P. E. Mogensen, "A Time-correlated Channel State Model for 5G New Radio Mobility Studies in LEO Satellite Networks," in *2021 IEEE 93rd Vehicular Technology Conference (VTC2021-Spring)*, Helsinki, Finland, 2021.

[75] N. Okati and T. Riihonen, "Nonhomogeneous Stochastic Geometry Analysis of Massive LEO Communication Constellations," *IEEE Transactions on Communications,* vol. 70, no. 3, pp. 1848-1860, March 2022.

[76] K. Zhang, S. Yang, Y. Wang, J. Huang and C.-X. Wang, "Ray-tracing Based Channel Modeling and Characteristics Analysis for LEO Satellite-to-Ground Systems," in *2024 18th European Conference on Antennas and Propagation (EuCAP)*, Glasgow, United Kingdom, 2024.

[77] N. Cenni, V. Degli Esposti, E. M. Vitucci, F. Fuschini and M. Barbiroli, "A study on Satellite-to-Ground Propagation in Urban Environment," in *2024 18th European Conference on Antennas and Propagation (EuCAP)*, Glasgow, United Kingdom, 2024.

[78] M. M. Azari, S. Solanki, S. Chatzinotas, O. Kodheli, H. Sallouha, A. Colpaert, J. F. M. Montoya, S. Pollin, A. Haqiqatnejad, A. Mostaani, E. Lagunas and B. Ottersten, "Evolution of Non-Terrestrial Networks From 5G to 6G: A Survey," *IEEE Communications Surveys & Tutorials,* vol. 24, no. 4, pp. 2633-2672, 2022.

[79] D. Tuzi, T. Delamotte and A. Knopp, "Satellite Swarm-Based Antenna Arrays for 6G Direct-to-Cell Connectivity," *IEEE Access,* vol. 11, pp. 36907-36928, 2023.

[80] I. Dagres, A. Polydoros and A. Moustakas, "Performance Analysis of Distributed Beamforming in Wireless Networks: The Effect of Synchronization and Doppler spread," in *MILCOM 2021 - 2021 IEEE Military Communications Conference (MILCOM)*, San Diego, CA, USA, 2021.

[81] H. Ochiai, P. Mitran, H. V. Poor and V. Tarokh, "Collaborative beam-forming for distributed wireless ad hoc sensor networks," *IEEE Transactions on Signal Processing,* vol. 53, no. 11, pp. 4110-4124, November 2005.

[82] J. A. Nanzer, S. R. Mghabghab, S. M. Ellison and A. Schlegel, "Distributed Phased Arrays: Challenges and Recent Advances," *IEEE Transactions on Microwave Theory and Techniques,* vol. 69, no. 11, pp. 4893-4907, November 2021.

[83] J. A. Nanzer, R. L. Schmid, T. M. Comberiate and J. E. Hodkin, "Open-Loop Coherent Distributed Arrays," *IEEE Transactions on Microwave Theory and Techniques,* vol. 65, no. 5, pp. 1662-1672, May 2017.

[84] J. C. Merlano Duncan, V. N. Ha, J. Krivochiza, R. Palisetty, G. Eappen, J. A. Vasquez, W. A. Martins, S. Chatzinotas and B. Ottersten, "Harnessing the Power of Swarm Satellite Networks with Wideband Distributed Beamforming," in *2023 IEEE 34th Annual International Symposium on Personal, Indoor and Mobile Radio Communications (PIMRC)*, Toronto, ON, Canada, 2023.

[85] R. Mudumbai, G. Barriac and U. Madhow, "On the Feasibility of Distributed Beamforming in Wireless Networks," *IEEE Transactions on Wireless communications,* vol. 6, no. 5, pp. 1754-1763, May 2007.

[86] G. Bacci, R. De Gaudenzi, M. Luise, L. Sanguinetti and E. Sebastiani, "Formation-of-Arrays Antenna Technology for High-Throughput Mobile Nonterrestrial Networks," *IEEE Transactions on Aerospace and Electronic Systems,* vol. 59, no. 5, pp. 4919-4935, October 2023.

[87] A. Guidotti, A. Vanelli-Coralli and C. Amatetti, "Federated Cell-Free MIMO in Nonterrestrial Networks: Architectures and Performance," *IEEE Transactions on Aerospace and Electronic Systems,* vol. 60, no. 3, pp. 3319-3347, June 2024.

[88] A. Al-Jumaily, A. Sali, V. P. Gil Jiménez, F. P. Fontán, M. J. Singh, A. Ismail, Q. Al-Maatouk, A. M. Al-Saegh and D. Al-Jumeily, "Evaluation of 5G Coexistence and Interference Signals in the C-Band Satellite Earth Station," *IEEE Transactions on Vehicular Technology,* vol. 71, no. 6, pp. 6189-6200, June 2022.

[89] C. She, Z. Chen, C. Yang, T. Q. S. Quek, Y. Li and B. Vucetic, "Improving Network Availability of Ultra-Reliable and Low-Latency Communications With Multi-Connectivity," *IEEE Transactions on Communications,* vol. 66, no. 11, pp. 5482-5496, November 2018.

[90] A. Maatouk, S. Kriouile, M. Assaad and A. Ephremides, "The Age of Incorrect Information: A New Performance Metric for Status Updates," *IEEE/ACM Transactions on Networking,* vol. 28, no. 5, pp. 2215-2228, October 2020.

[91] F. d. G. Ortiz Gómez, R. Martínez Rodríguez-Osorio, M. A. Salas Natera and S. Landeros Ayala, "On the use machine learning for flexible payload management in VHTS systems," in *Proceedings of 70th International Astronautical Congress 2019*, Washington, DC, USA, 2019.

[92] A. Papoulis and S. U. Pillai, Probability, Random Variables, and Stochastic Processes, McGraw-Hill Europe, 2002.

[93] J. Shi, Z. Li, J. Hu, Z. Tie, S. Li, W. Liang and Z. Ding, "OTFS Enabled LEO Satellite Communications: A Promising Solution to Severe Doppler Effects," *IEEE Network,* vol. 38, no. 1, pp. 203-209, January 2024.

[94] W. Peeters, "The Paradigm Shift of NewSpace: New Business Models and Growth of the Space Economydoi," *New Space,* vol. 12, no. 3, pp. 202-213, September 2024.

[95] R. Murray, "The NewSpace market: Capital, control, and commercialization," Atlantic Council, April 2023. [Online]. Available: https://www.atlanticcouncil.org/in-depth-research-reports/issue-brief/the-newspace-market-capital-control-and-commercialization/.

[96] M. Á. Vázquez, P. Henarejos and A. Pérez-Neira, "Learning to Optimize Satellite Flexible Payloads," in *2022 30th European Signal Processing Conference (EUSIPCO)*, Belgrade, Serbia, 2022.

[97] N. Font, C. Blosse, P. Lautier, A. Barthère and P. Voisin, "Flexible payloads for telecommunication satellites - a Thales perspective," in *32nd AIAA International Communications Satellite Systems Conference*, San Diego, CA, 2014.

[98] Jiang, Weiwei, "Software defined satellite networks: A survey," *Digital Communications and Networks,* vol. 9, no. 6, pp. 1243-1264, December 2023.

[99] P. S. Khodashenas, H. Khalili, D. Guija and S. Siddiqui, "TALENT Towards Integration of Satellite and Terrestrial Networks," in *2019 European Conference on Networks and Communications (EuCNC)*, Valencia, Spain, 2019.

[100] R. Akeela and B. Dezfouli, "Software-defined radios: Architecture, state-of-the-art, and challenges," *Computer Communications,* vol. 128, pp. 106-125, September 2018.

[101] M. Raho, A. Spyridakis, M. Paolino and D. Raho, "KVM, Xen and Docker: A performance analysis for ARM based NFV and cloud computing," in *2015 IEEE 3rd Workshop on Advances in Information, Electronic and Electrical Engineering (AIEEE)*, Riga, Latvia, 2015.

[102] B. Đorđević, N. Maček and V. Timčenko, "Performance Issues in Cloud Computing: KVM Hypervisor's Cache Modes Evaluation," *Acta Polytechnica Hungarica,* vol. 12, no. 4, pp. 147-165, 2015.

[103] C. Ssengonzi, O. P. Kogeda and T. O. Olwal, "A survey of deep reinforcement learning application in 5G and beyond network slicing and virtualization," *Array,* vol. 14, p. 100142, July 2022.

[104] J. A. Ruiz de Azua, U. López Fernandez, J. L. Ávila Acosta and D. Rincón Rivera, "Virtual Satellite Network Simulator (VSNeS) - A Simulation Engine to Virtualize Non-Terrestrial Networks," in *74th International Astronautical Congress (IAC-23)*, Baku, Azerbaijan, 2023.

[105] A. Stoddard, A. Gruwell, P. Zabriskie and M. Wirthlin, "High-speed PCAP configuration scrubbing on Zynq-7000 All Programmable SoCs," in *2016 26th International Conference on Field Programmable Logic and Applications (FPL)*, Lausanne, Switzerland, 2016.

[106] Y. Su, Y. Liu, Y. Zhou, J. Yuan, H. Cao and J. Shi, "Broadband LEO Satellite Communications: Architectures and Key Technologies," *IEEE Wireless Communications,* vol. 26, no. 2, pp. 55-61, April 2019.

[107] B. Shang, X. Li, C. Li and Z. Li, "Coverage in Cooperative LEO Satellite Networks," *Journal of Communications and Information Networks,* vol. 8, no. 4, pp. 329-340, December 2023.

[108] M. López, S. B. Damsgaard, I. Rodríguez and P. Mogensen, "Connecting Rural Areas: an Empirical Assessment of 5G Terrestrial-LEO Satellite Multi-Connectivity," in *IEEE 97th Vehicular Technology Conference (VTC2023-Spring)*, Florence, Italy, 2023.

[109] A. Hasan and J. G. Andrews, "Scheduling Using Near-optimal Guard Zones for CDMA Ad Hoc Networks," in *2006 IEEE International Conference on Communications*, Istanbul, Turkey, 2006.

[110] U. Tefek and T. J. Lim, "Interference Management Through Exclusion Zones in Two-Tier Cognitive Networks," *IEEE Transactions on Wireless Communications,* vol. 15, no. 3, pp. 2292-2302, March 2016.

[111] F. Öztürk and A. Kara, "Exclusion zone minimization and optimal operational mode selection for co-existent geostationary and non-geostationary satellites," *International Journal of Satellite Communications and Networking,* vol. 40, no. 3, pp. 191-203, May/June 2022.

[112] A. Hills, J. M. Peha and J. Munk, "Feasibility of Using Beam Steering to Mitigate Ku-Band LEO-to-GEO Interference," *IEEE Access,* vol. 10, pp. 74023-74032, 2022.

[113] Z. Chen and J. Yang, "A Database-Assisted Spectrum Sharing for Satellite System and Terrestrial Cellular Network," in *2019 IEEE 5th International Conference on Computer and Communications (ICCC)*, Chengdu, China, 2019.

[114] Z. Qiu, W. Wang, J. Geng and Y. Liu, "Interference Analysis of Multi-tier NGSO Based on Stochastic Geometry," in *2023 IEEE Wireless Communications and Networking Conference (WCNC)*, Glasgow, United Kingdom, 2023.

[115] A. Hills, J. M. Peha, J. Munk and S. Pogorelc, "Controlling Antenna Sidelobe Radiation to Mitigate Ku-Band LEO-to-GEO Satellite Interference," *IEEE Access,* vol. 11, pp. 71154-71163, 2023.

[116] J. Zhong, R. D. Yates and E. Soljanin, "Two Freshness Metrics for Local Cache Refresh," in *2018 IEEE International Symposium on Information Theory (ISIT)*, Vail, CO, USA, 2018.

[117] M. A. Abd-Elmagid, N. Pappas and H. S. Dhillon, "On the Role of Age of Information in the Internet of Things," *IEEE Communications Magazine,* vol. 57, no. 12, pp. 72-77, December 2019.

[118] Q. Liu, C. Li, Y. T. Hou, W. Lou, J. H. Reed and S. Kompella, "Ao2I: Minimizing Age of Outdated Information to Improve Freshness in Data Collection," in *IEEE INFOCOM 2022 - IEEE Conference on Computer Communications*, London, United Kingdom, 2022.

[119] E. Delfani, G. J. Stamatakis and N. Pappas, "State-Aware Timeliness in Energy Harvesting IoT Systems Monitoring a Markovian Source," 2024. [Online]. Available: https://doi.org/10.48550/arXiv.2405.03628. [Accessed November 2024].

[120] R. D. Yates, "The Age of Gossip in Networks," in *2021 IEEE International Symposium on Information Theory (ISIT)*, Melbourne, Australia, 2021.

[121] S. Kaul, R. D. Yates and M. Gruteser, "Real-time status: How often should one update?"," in *2012 Proceedings IEEE INFOCOM*, Orlando, FL, USA, 2012.

[122] M. L. Puterman, Markov Decision Processes: Discrete Stochastic Dynamic Programming, John Wiley & Sons, 2014.

[123] G. Sciddurlo, A. Petrosino, M. Quadrini, C. Roseti, D. Striccoli, F. Zampognaro, M. Luglio, S. Perticaroli, A. Mosca, F. Lombardi, I. Micheli, A. Ornatelli, V. Schena, A. Di Mezza, A. Mattioni, D. Morbidelli, G. Boggia

and G. Piro, "Looking at NB-IoT Over LEO Satellite Systems: Design and Evaluation of a Service-Oriented Solution," *IEEE Internet of Things Journal,* vol. 9, no. 16, pp. 14952-14964, August 2022.

[124] R. Brandborg Sørensen, R. Ferrús, N. Hernandez, M. Guadalupi, J. Ferrer, I. Llorens Aymerich, H. Krogh Moeller and R. van der Pool, "System level performance analysis for 3GPP NB-IoT NTN solutions with small satellites and sparse LEO constellations," in *73rd International Astronautical Congress (IAC-2022)*, Paris, France, 2022.

[125] I. Rahman, S. M. Razavi, O. Liberg, C. Hoymann, H. Wiemann, C. Tidestav, P. Schliwa-Bertling, P. Persson and D. Gerstenberger, "5G evolution toward 5G advanced: An overview of 3GPP releases 17 and 18," *Ericsson Technology Review,* pp. 2-12, October 2021.

[126] M. M. Saad, M. A. Tariq, M. T. R. Khan and D. Kim, "Non-Terrestrial Networks: An Overview of 3GPP Release 17 & 18," *IEEE Internet of Things Magazine,* vol. 7, no. 1, pp. 20-26, January 2024.

[127] A. Warrier, L. Aljaburi, H. Whitworth, S. Al-Rubaye and A. Tsourdos, "Future 6G Communications Powering Vertical Handover in Non-Terrestrial Networks," *IEEE Access,* vol. 12, pp. 33016-33034, 2024.

[128] Ericsson, "6G spectrum - enabling the future mobile life beyond 2030," May 2023. [Online]. Available: https://www.ericsson.com/49ac9c/assets/local/reports-papers/white-papers/2024/6g-spectrum.pdf. [Accessed November 2024].

[129] E. Project, "Architectures, services, and technologies towards 6G Non-Terrestrial Networks," February 2023. [Online]. Available: https://www.eagerproject.eu/wp-content/uploads/sites/82/2023/02/EAGER_White_Paper_long_version_v3.pdf. [Accessed November 2024].

[130] P. B. de Selding, "Intelsat orders 2 flexible-payload satellites from Airbus," Space Intel Report, January 2021. [Online]. Available: https://www.spaceintelreport.com/intelsat-preparing-for-gogo-acquisition-orders-2-flexible-payload-satellites-from-airbus/. [Accessed November 2024].

[131] European Space Agency, "4th ESA Workshop on Advanced Flexible Telecom Payloads," March 2019. [Online]. Available: https://atpi.eventsair.com/QuickEventWebsitePortal/advanced-flexible-telecom-payloads/website/ExtraContent/ContentPage?page=4. [Accessed November 2024].

[132] Asia Pacific Satellite Communications Council (APSCC), "The Industry Impact of Flexible Satellites," (summary: https://www.hughes.com/resources/insights/satellite-broadband/promise-flexible-satellites), September 2020. [Online]. Available: https://www.youtube.com/watch?v=MxK_ANaZuHA. [Accessed November 2024].

[133] S. Grant, "Memory Management and Virtual Memory," [Online]. Available: https://slideplayer.com/slide/13277282/. [Accessed November 2024].

[134] Programmer All, "ARMV8 MMU and Linux page mapping," [Online]. Available: https://www.programmerall.com/article/6386706502/. [Accessed November 2024].

[135] G. Pearson, "Deep Dive: MMU Virtualization with Xen on ARM," February 2020. [Online]. Available: https://www.starlab.io/blog/deep-dive-mmu-virtualization-with-xen-on-arm. [Accessed November 2024].

[136] Guisselquist Technology, LLC, "AXI Verification, the story so far," September 2019. [Online]. Available: https://zipcpu.com/formal/2019/09/06/axi-story.html. [Accessed November 2024].

[137] Xilinx, "Unleash the Unparalleled Power and Flexibility of Zynq UltraScale+ MPSoCs," June 2016. [Online]. Available: https://docs.amd.com/v/u/en-US/wp470-ultrascale-plus-power-flexibility. [Accessed November 2024].

[138] T. Collins, "Open-Source, Reusable Software Stack Enables Real-Time Processing and Algorithm Development for CbM," August 2021. [Online]. Available: https://embeddedcomputing.com/technology/software-and-os/ides-application-programming/open-source-reusable-software-stack-enables-real-time-processing-and-algorithm-development-for-cbm. [Accessed November 2024].

[139] AMD, "FPGA Manager architecture," July 2021. [Online]. Available: https://docs.amd.com/r/2021.1-English/ug1137-zynq-ultrascale-mpsoc-swdev/FPGA-Manager-Architecture. [Accessed November 2024].

[140] Federal Communications Commission, "FCC Partially Grants SpaceX Gen2 Broadband Satellite Application," December 2022. [Online]. Available: https://www.fcc.gov/document/fcc-partially-grants-spacex-gen2-broadband-satellite-application. [Accessed November 2024].

[141] ETHER Project, "D2.4: Final report on ETHER network architecture, interfaces and architecture evaluation," August 2024. [Online]. Available: https://www.ether-project.eu/wp-content/uploads/sites/100/2024/10/ETHER_Deliverable_D2.4_V1.0_final.pdf. [Accessed November 2024].

[142] ETSI, "ISG NFV Activity Report," European Telecommunications Standards Institute, 2023. [Online]. Available: https://www.etsi.org/committee-activity/activity-report-nfv. [Accessed November 2024].

[143] ETSI, "Network Functions Virtualisation (NFV) Release 4; Management and Orchestration; Requirements for service interfaces and object model for container cluster management and orchestration specification," European Telecommunications Standards Institute, ETSI GS NFV-IFA 036 V4.3.1, September 2022. [Online]. Available: https://www.etsi.org/deliver/etsi_gs/NFV-IFA/001_099/036/04.03.01_60/gs_NFV-IFA036v040301p.pdf. [Accessed November 2024].

[144] 3GPP, "Study on channel model for frequencies from 0.5 to 100 GHz," 3rd Generation Partnership Project, Technical Report TR 38.901 version 18.0.0, April 2020. [Online]. Available: https://portal.3gpp.org/desktopmodules/Specifications/SpecificationDetails.aspx?specificationId=3173.

[145] 3GPP, "Discussion on Ka-band NTN-TN NR adjacent band coexistence scenarios," 3rd Generation Partnership Project, TSG-RAN WG4 Meeting #104e-bis-e, R4-2215352, October 2022.

[146] 3GPP, "Handling of satellite Ka-band for NR-NTN exemplary band in Rel-17," 3rd Generation Partnership Project, TSG-RAN Meeting RP-91-e, RP-210439, March 2021.

[147] ITU-R, "Effects of building materials and structures on radiowave propagation above about 100 MHz," Recommendation P.2040-3, August 2023. [Online]. Available: https://www.itu.int/rec/R-REC-P.2040/en.

[148] ITU-R, "Prediction of clutter loss," Recommendation P.2108-1, September 2021. [Online]. Available: https://www.itu.int/rec/R-REC-P.2108/en.

[149] ITU-R, "Propagation data and prediction methods required for the design of Earth-space telecommunication systems," Recommendation P.618-14, August 2023. [Online]. Available: https://www.itu.int/rec/R-REC-P.618/en.

[150] ITU-R, "Attenuation by atmospheric gases and related effects," Recommendation P.676-13, August 2022. [Online]. Available: https://www.itu.int/rec/R-REC-P.676/en.

[151] ITU-R, "Propagation data required for the design systems in the land mobile-satellite service," Recommendation P.681-11, August 2019. [Online]. Available: https://www.itu.int/rec/R-REC-P.681/en.

[152] ITU-R, "Characteristics of precipitation for propagation modelling," Recommendation P.837-7, June 2017. [Online]. Available: https://www.itu.int/rec/R-REC-P.837/en.

[153] ITU-R, "Specific attenuation model for rain for use in prediction methods," Recommendation P.838-3, March 2005. [Online]. Available: https://www.itu.int/rec/R-REC-P.838/en.

[154] ITU-R, "Rain height model for prediction methods," Recommendation P.839-4, September 2013. [Online]. Available: https://www.itu.int/rec/R-REC-P.839/en.

[155] E. Delfani and N. Pappas, "Version Age-Optimal Cached Status Updates in a Gossiping Network with Energy Harvesting Sensor," *IEEE Transactions on Communications,* (early access), 2024.

[156] Y. Liu, M. Chen, C. Pan, T. Gong, J. Yuan and J. Wang, "OTFS vs OFDM: Which is Superior in Multiuser LEO Satellite Communications," *IEEE Journal on Selected Areas in Communications,* (early access), 2024.

[157] G. Maral, M. Bousquet and Z. Sun, Satellite communications systems: systems, techniques and technology, John Wiley & Sons, 2020.

[158] G. A, M. A. ElBahaay, A. M. Mohamed, M. M. Zaki, A. S. Abdo and N. AbdelBaki, "5G and Satellite Network Convergence: Survey for Opportunities, Challenges and Enabler Technologies," in *2nd Novel Intelligent and Leading Emerging Sciences Conference (NILES),*, Giza, Egypt, 2020.